Trinity College Dublin
Coláiste na Tríonóide, Baile Átha Cliath
The University of Dublin

DEPARTMENT OF CIVIL, STRUCTURAL AND ENVIRONMENTAL ENGINEERING

DEVELOPMENT OF SUSTAINABLE, ALKALI-ACTIVATED BINDERS FOR CONSTRUCTION

by

Omar Abdullah Alelweet

Supervisor: Dr. Sara Pavía

Thesis submitted to the University of Dublin, Trinity College for the degree of

Doctor of Philosophy

2023

DECLARATION

I declare that this thesis has not been submitted as an exercise for a degree at this or any otheruniversity and it is entirely my own work.

I agree to deposit this thesis in the University's open access institutional repository or allow the library to do so on my behalf, subject to Irish Copyright Legislation and Trinity College Library conditions of use and acknowledgement.

Author: _____   Date:

        Omar Alelweet

ABSTRACT

This work contributes to the design and production of alkali-activated materials (AAMs) of lower environmental impact than Portland cement (PC) products. AAM binders result from the reaction of an activator and a precursor. They do not require clinkering and can be produced at ambient temperature using waste precursors as the principal constituent. Hence, they reduce energy consumption, CO_2 emissions, and the use of unrenewable resources for their production.

Aluminosilicate precursors not investigated to date such as Saudi Arabian red mud (RM) and bauxite are studied. Their particle size, specific surface area, water demand, carbon content, composition and amorphousness are studied, and their reactivity measured with the Chapelle test, setting times, conductivity, mechanical index and microscopy. The quality and durability of AAMs made with these, FA and GGBS precursors, activated with NaOH and Na_2SiO_3 are investigated to optimize the mix design for a given precursor.

All the precursors are pozzolanic and successfully activate with alkali solutions forming AAMs. The FA and GGBS comply with standard requirements for use as PC replacement. GGBS has excellent quality being highly reactive, basic ($CaO+MgO/SiO_2=1.56$) and amorphous, with ratios ($CaO/SiO_2=1.41$; $SiO_2/Al_2O_3=0.34$) suitable for alkali activation.

The RM is reactive due to its layered phases of high surface area (gibbsite and boehmite inherited from the parent bauxite), and its zeolite/feldepathoid phases (cancrinite, chantalite and sodalite) formed during the refining (Bayer) process. It is suitable for the production of AA and pozzolanic materials. It has high SiO_2 and high alkalinity, the chloride and carbon contents are low and contains no toxic elements. The RM sintered at 300-400°C sets the fastest, combines the most lime and reaches the greatest strength. The RM's activity is mainly due to the reaction of feldspathoid cancrinite and formation of zeolitic/feldspathoid-based hydrates.

The bauxite is highly reactive due to the layered atomic structures of its main components gibbsite, boehmite and kaolinite, which provide high specific surfaces and active hydroxyls that enhance dissolution and subsequent geopolymerization. Calcination, even at 300°C, dehydroxylates kaolinite increasing reactivity. The 550°C bauxite (highest surface area) is

the most active initially (hours-2 days) but at later ages, the 700°C -800°C bauxites (highest amorphous alumina content) are the most reactive reaching the greatest strengths.

Some of the AAMs are fit for structural purposes, having strengths and durability superior to their CEM II equivalents at a much lower environmental impact.

In AA GGBS materials, the right activator procured similar strength, but much lower embodied energy (EE) and carbon emissions (E_{CO2}) -39.51 % and 78.57 % lower respectively-, than equivalent CEM II materials. The (Na_2SiO_3+NaOH activated) GGBS materials show the greatest strengths and microstructure. When cured at 60°C, they develop hydrogarnet–gehlenite cements responsible for their high strength (94 MPa at 270 days). The materials cured at 20°C are suitable for many applications. Curing at 60°C enhances early strength (3-7 d.), but ultimate strength (28-270 d.) can lower. The rheology and setting times of AA GGBS materials are within practical limits, and cracking is hindered by the high calcium in the slag. The GGBS is too reactive (too fine and amorphous) for a successful activation with high hydroxide concentration: the best activator is Na_2SiO_3 combined with low molarity-6M- hydroxide.

Some of the AA materials made with RM alone reach significant flexural (5 MPa) and compressive strength (7 MPa), but failed during cycling, being particularly vulnerable to frost. Replacing RM with FA increased strength and durability, and GGBS substitution enhanced quality further. When blended with FA/GGBS, N-A-S-H hydrates are common which improve strength and microstructure. The best AA RM materials (50%GGBS) show the highest density, shortest setting time, greatest strength (39 – 41 MPa activated with Na_2SiO_3 / 6M NaOH = 1 and 2.5 respectively), and superior durability than their CEM II equivalents, due to the high-Ca forming strong C-S-H/C-A-S-H cements. The RM needs silica and NaOH in the activator to dissolve and form a strong geopolymer structure: Na_2SiO_3 alone lowers strength and undermines the structure.

The DOE (Design of Experiments) proved suitable to predict optimum mixes for AA bauxite materials in the range studied, and it validated the experimental methods.

Bauxite creates outstanding AAMs (compressive strength -CS = 72-90 MPa) of low environmental impact. The bauxite alone produced quality geopolymers (CS=35MPa). Replacing bauxite with FA or GGBS enhances strength and density lowering porosity, and the effect is more pronounced with increasing replacement. Cementing geopolymers are

scarce in the AA bauxite, but with FA/ GGBS, the main cementing phase in a low-Ca, aluminate–silicate gel with some sodium substitution. The best materials include 50%GGBS, activated with Na_2SiO_3/8M NaOH=1, cured at 60°C. A formulation that reached 90 MPa -90 d- and 72 MPa -28 d- and agrees with the optimum mix forecasted by the DOE. The best experimental bauxite and bauxite-FA materials are cured at 20°C and activated with high silica (Na_2SiO_3/NaOH=3) and medium molarity (8M NaOH). However, the DOE forecast optimum mixes activated with less silica (Na_2SiO_3/NaOH=2) and higher molarity (NaOH 10M) -with 50%FA, cured at 20°C.

The activator must fit the precursor: an excessive activator content or too high concentration escalates environmental impact simultaneously lowering strength and undermining microstructure. Using higher impact precursors such as GGBS, offsets impact on account of increasing the strength and durability in the resultant AAMs. Pyro-processing precursors reports great strength increase with low rise in environmental impact: sintering bauxite at 800°C slightly raised environmental impact but doubled strength. In the AAMs developed, even the highest impacts (EE=0.62-0.64 MJ/kg which correspond with strengths of 15-22 MPa) are small when compared with those of common construction materials.

ACKNOWLEDGEMENTS

TABLE OF CONTENTS

\

LIST OF FIGURES

LIST OF TABLES

NOMENCLATURE AND ABBREVIATIONS

PC	Portland cement
GHGs	Greenhouse gas emissions
AAMs	Alkali-activated materials
AAS	Alkali-activated slag
FA	Fly ash
GGBS	Ground granulated blast furnace slag
RM	Red mud
MK	Metakaolin
CEM II A/L	Portland limestone cement
LCA	Life cycle analyses
DOE	Design of experiments
EE	Embodied energy
E_{CO2}	Embodied carbon footprint
N-A-S-H	Alkaline aluminosilicate hydrate gel
C-A-S-H	Calcium aluminum silicate hydrate gel
C-S-H	Calcium silica hydrate
NaOH	Sodium hydroxide
Na_2SiO_3	Sodium silicate
SEM	Scanning electron microscope
SSA	Specific surface area
XRD	X-ray crystallography (X-ray diffraction)
XRF	X-ray fluorescence
w/b	Water binder ratios
P	Porosity
BD	Bulk density
WA	Water absorption
FC	Flexural strength

CS   Compressive strength

Temp.   Temperature

M   Molarity

Ms   Silica modulus (SiO_2/Na_2O)

1. INTRODUCTION & OVERVIEW

1.1 CONTEXT

The search for alternative binders with a lower environmental impact than Portland cement (PC) is much needed in construction to protect the environment and reduce greenhouse gas emissions such as carbon dioxide, which are responsible for the greenhouse effect. It is widely acknowledged that climate change adversely affects earth and endangers human and animal life. Economic losses due to climate change in Europe amounted to approximately EUR 453 billion between 1980 and 2017 (EEA, 2019), and annually, $2,245 billion losses are attributed to climate-related disasters (Wallemacq and House, 2018).

The construction industry is one of the largest contributors to greenhouse gas emissions, and a great consumer of energy and non-renewable natural resources (Cole, 1998). The production of certain building materials such as aluminium, steel and PVC involves great energy consumption and carry strong environmental impacts (EC, 2010). As a result of severe environmental problems, the construction industry needs to adapt. Using construction materials of low environmental impact worldwide would considerably lower the greenhouse gas emissions (GHGs) and would improve the sustainability of construction.

PC is the binder most widely used in construction. It is held responsible for major contributions to greenhouse gas emissions worldwide in multiple publications. Most of the environmental impact of PC is due to clinker production, which requires burning rocks at 1400°C, releasing abundant CO_2 from the fuel combustion and the decarbonization of the carbonate rocks used as raw material. An estimated 12–15% of the total industrial energy consumption is attributed to cement production, which contributes about 5-7% of the total worldwide CO_2 emissions into the atmosphere from burning fossil fuels to produce the energy required for cement production (Ali *et al.,* 2011). Producing one tonne of cement emits 900 kg of CO_2 into the atmosphere (Benhelal *et al.*, 2013). According to CEMBUREAU (2020), the top four cement-producing countries in 2020 were China, the major cement producer in the world with 2377 Mt (57.2%), India, the second largest in the world with 290 Mt (7%), the EU with 171.5 Mt (6.1%), and the USA with 89 Mt (2.1%). Over the past few years, PC production has rapidly increased

worldwide, contributing to increased CO_2 emissions. In 1990, the global PC industry emitted 576 million tons of CO_2 (Boden *et al.*, 2011). In the 24 years between 1992 and 2014, emissions increased more than threefold, reaching 2.083 billion tons. It is estimated that global PC emissions will reach 2.34 billion tons in 2050 if the current rate of CO_2 emissions is sustained and no further reduction strategy is implemented (Cement roadmap, 2012). Figure 1-1 shows the worldwide CO_2 emissions of the cement industry from 1997 to 2023 and the predicted CO_2 emissions afterwards. Therefore, there is a need to develop alternative sustainable binders.
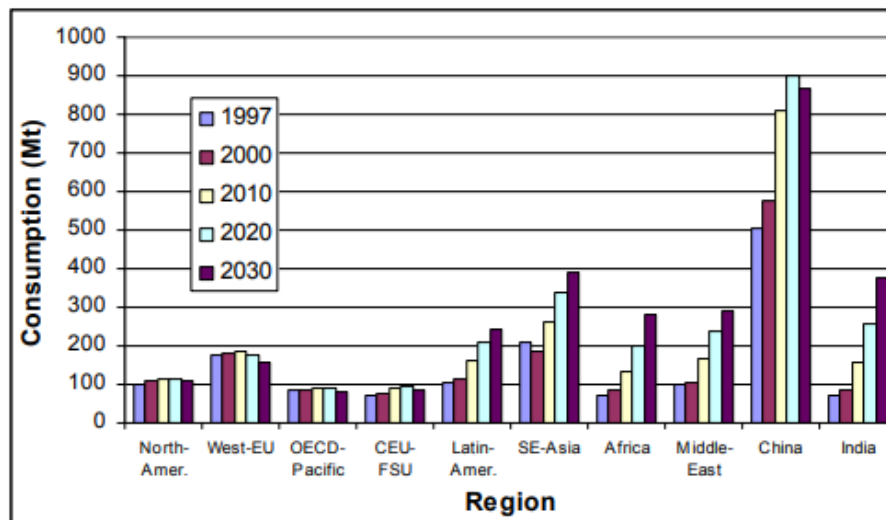
Figure 1-1 Global cement industry CO_2 emissions trends (Szabó *et al.*, 2003).

Most of the environmental impact of PC is due to clinker production, which requires burning rocks at 1400°C, releasing abundant CO_2 from fuel combustion and the decarbonization of the carbonate rocks used as raw materials. Alkali-activated materials (AAMs) do not require clinker manufacturing but are produced at low temperatures, usually ranging from ambient to 100°C. Most alkali-activated cements are produced at ambient temperatures, and others with a small energy input, usually ranging from 60°C (curing) to 100°C (drying) or 400-600°C (thermal activation of certain wastes) (Shi *et al.,* 2003). Hence, they yield low carbon emissions and have low embodied energy (EE). Furthermore, most AAMs are made with industrial waste which further lowers their EE as well as the raw material and fuel consumption for their making. This research investigates AAMs as an alternative to PC materials to lower the environmental impact of construction.

1.2 ALKALI-ACTIVATED MATERIALS AND GEOPOLYMERS

Alkali-activated materials (AAM) and geopolymers are synthesized from two basic components: an activator and a silicate precursor. The precursor material is frequently powdered and mineralogically amorphous (Buchwald *et al.,* 2003; Shi *et al.,* 2003). The precursor can be a calcium-rich aluminosilicate such as metallurgical slag, or a calcium-poor aluminosilicate such as fly ash or bottom ash. Activators are alkalis in the form of hydroxides, silicates, sulfates, carbonates, aluminates and oxides. They essentially include any soluble substance that can raise the pH of the mix and speed the dissolution of the solid precursor (Van Deventer *et al.,* 2010).

Davidovits first used the term 'geopolymer' to describe the products of alkali activation of calcined clays (metakaolin) in the 1970s. The technology of alkali-activation predates this terminology by over 60 years, with a patent granted to in the early 1900s (Kuhl 1908). During the 1940s and 1950s, Purdon and Glukhovsky conducted major research on AAMs that they named "soil cements" which used abundant slag-based aluminosilicates as a substitution for PC (Shi *et al.,* 2006). Geopolymers are often considered a subset of AAMs, in which the binding phase is almost entirely aluminosilicate with a high degree of coordination (Rahier *et al.*, 1997; Duxson *et al.*, 2005). The term is often used in the context of clays or FA based systems, either calcium-free or with low-calcium content. This classification is illustrated schematically in Figure 1-2, where geopolymers are shown as a subset of AAMs with the highest Al and the lowest Ca content.

Alkali-activated materials are usually produced with lower carbon emissions and less raw material and fossil fuel consumption than PC products. In general, AAMs have a lower environmental impact than traditional PCs (Provis and Van Deventer, 2013). The reduction in emissions, and the use of waste for their production, may now become the trigger for their wide uptake in the markets. The wastes or by-products used as precursors in AAMs can contain toxic elements which can leach when exposed to rainwater, surface water or groundwater. This research studies the chemical composition of the waste precursors and investigates their composition against current toxicity limits.

Ouellet-Plamondon and Habert (2015) state that the environmental impact of current mixes is lower than cement/concrete made with 100% PC (CEM I), saving up to 75% CO_2 emissions and having additional environmental benefits such as the reduction of water use, and no

requirement for superplasticizer admixtures. The authors reviewed and standardized sustainability calculations based on life cycle analyses (LCA), highlighting the disparity of results and discussing the critical points that need to be addressed in order to improve the LCA of AA cements and concretes.

As aforementioned, AA mortars and concretes consist of a silicate precursor activated with an alkali-metal and mixed with aggregate. Therefore, it is important to use precursors that do not require calcination or any other high-energy processing for production. Also, certain activators such as sodium silicate solution are responsible for a significant portion of the environmental impact of an AA material (Habert *et al.,* 2011).

Mellado *et al.* (2014) reports that AA mortars made with rice husk ash activated with sodium silicate, result in a 63% reduction in carbon footprint compared with an equivalent CEM I mortar. AA binders derived from waste materials such as ground granulated blast furnace slag (GGBS) and fly ash (FA) show an 80% reduction in CO_2 emissions compared with PC (Duxson *et al.*, 2007). Other AA mixes have shown a 60% reduction in CO_2 emissions compared with PC made with 70% CEM I and 30% FA (Habert *et al.* 2010), and some AA FA materials have shown a 45% reduction compared to CEM I equivalents (Habert *et al.* 2011).

As well as having lower CO_2 emissions and a lower energy demand, some AAMs have been claimed to have superior durability than PC materials, including resistance to seawater and sulphate and acid attack (Shi *et al.,* 2003). However, disadvantages in AAM production can include unpleasant handling, skin irritation, inconvenience of having to mix more than two components and a sticky consistency (Moranville-Regourd, 1998). Some of the challenges of AA cements, and concretes are comprehensively summarized in Shi *et al.,* (2003) including: the appearance of alkali carbonate efflorescence due to the leaching of alkalis and their reaction with atmospheric CO_2 and cracking due to drying shrinkage (which increases as the lime content in the system decreases and reduces the binder's strength limiting application).
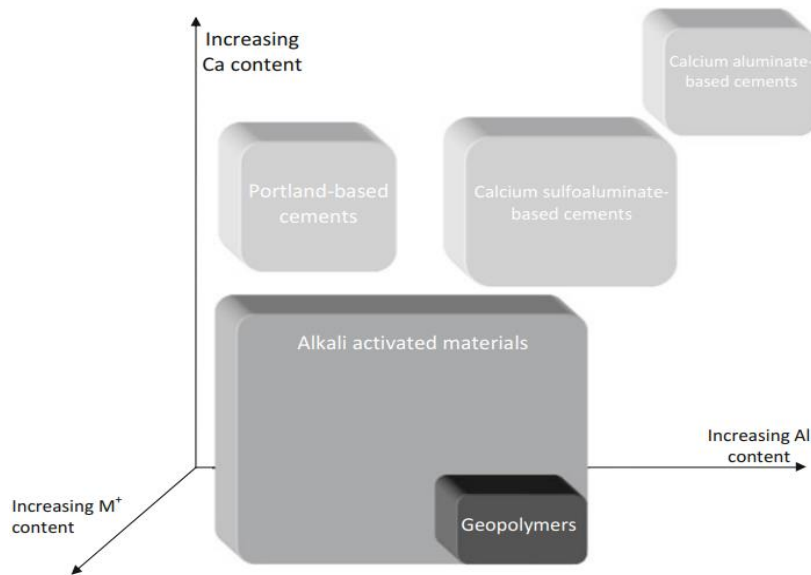
Figure 1-2 Comparisons of AAMs with PC and calcium sulfoaluminate binders (Provis *et al.,* 2014).

1.3 SCOPE OF RESEARCH

This research studies the reactivity of some materials not investigated to date, such as the Saudi Arabian red mud (RM) and bauxite. In addition, these materials are used as precursors to fabricate AAMs, and the quality and durability of the resultant products are tested. The nature of the resultant cements is also investigated. The research intends to contribute to the design and production of construction binders of low environmental impact.

The precursors are well characterized, and tested with activators of variable nature with different concentrations, with the purpose of optimizing the mix design for a given starter precursor. The evolution of the mineralogy and microstructure of AA cements with increasing temperatures and varying conditions are also established. The AAMs' potential to reduce environmental impact (Embodied Energy (EE) and carbon footprint – (E_{CO2})) is studied.

This research emphasizes design and durability to optimize the production of AAMs of low environmental impact. The materials investigated are largely made with waste, hence they reduce the energy consumption and CO_2 emissions and the use of natural unrenewable resources for their production.

Objectives are as follows:

- Assessing the potential of innovative waste materials RM and bauxite for the design of AA materials, both as the only precursors and in blends with better known precursors, namely GGBS and FA.

- Investigate the properties and reactivity of industrial waste materials and bauxite to produce cements.

- Examine the properties and durability of AAMs made with waste materials and bauxite and determine their optimal activator and formulation for sustainable binder production.

- Optimize AAMs made from bauxite using the design of experiments (DOE) Minitab-19 software.

- Assess the environmental impact of AAMs made with GGBS, RM and bauxite compared with equivalent CEM II products.

1.4 STRUCTURE OF THE THESIS

This thesis consists of eight chapters and appendices. Chapter 1 includes the introduction and objectives of this study. Chapter 2 is a literature review. Chapter 3 presents details of the materials and methods. Chapter 4 comprises the characterization of precursors. Chapter 5 includes the properties of the alkali-activated materials designed and produced in the laboratory. Chapter 6 shows an optimum mix design for alkali-activated bauxite materials using design of experiments (DOE) modelling. Chapter 7 includes a comparative study of the environmental impact of some alkali-activated and traditional materials. Finally, Chapter 8 includes the conclusions and recommendations.

2. LITERATURE REVIEW

This chapter reviews the ingredients of AAMs, the process of alkali activation and the reaction mechanisms and products in the alkali activation process. It also studies how the design variables involved in the production of alkali-activated materials (AAMs) can affect their final properties.

2.1 ALKALI-ACTIVATED MATERIALS (AAM): HISTORY AND DEVELOPMENT

Alkali-activated materials (AAMs) are inorganic polymers that are produced when alkaline solutions react with aluminosilicate precursors to create cementitious material (Davidovits, 1991; Duxson *et al.*, 2007).

The concept of AAMs relates to the patent by German chemist (Kuhl, 1908), stating that ordinary blast furnace slag can be interspersed with lime and sodium sulfate or carbonate and then mixed with water to create a slag binder. The scientific basis of alkali-activated binders was developed in more detail in the 1940s by Purdon. He used slag activated with sodium hydroxide in a two-step process. First, Si and Al dissolve alongside the calcium hydroxide, followed by the generation of hydrates. Feret (1939) worked on blast furnace slag, PC, and alkali-activated binders.

Glukhovsky (1959) investigated ancient Roman and Egyptian binders, and was the first author to study the possibility of producing binders using aluminosilicate wastes. Ancient civilizations did not use alkali-activation technology as established today. However, some historic mortars, made with hydraulic limes and/or pozzolanic additions, contain cementing hydrates similar to those found in AAMs and produced on PC hydration (Pavía and Caro 2006, 2007, 2008; Pavía 2008).

Finally, Davidovits and Cordi (1979) invented and patented binders derived from alkali-activated metakaolin and created the word "geopolymer" to describe them back in 1978.

Research has been increasing since the 1990s, involving over 100 active research academics and commercial research centres (Torres-Carrasco and Puertas, 2017). Table 2-1summarises historic events in the evolution of AA materials.

Table 2-1 History of developments in alkali-activated binders (Roy, 1999; Shi *et al.,* 2003).

Author	Year	Significance
Kuhl	1930	Investigated setting behaviour of slags in the presence of caustic potash
Chassevent	1937	Measured reactivity of slags using caustic potash and soda solution.
Feret	1939	Slags used for cement
Purdon	1940	Alkali-slag combinations
Glukhovsky	1957	Synthesized binders using hydrous and anhydrous alumina-silicates (glassy rocks, clays, metallurgical slags, etc.) and alkalis, proposed Me_2O–MeO– Me_2O_3–SiO_2–H_2O cementing system and called the binder "soil cement".
Glukhovsky	1959	Theoretical basis and development of alkaline cements
Glukhovsky	1965	First called "alkaline cements"
Davidovits	1979	''Geopolymer'' term
Malinowski	1979	Ancient aqueducts characterized
Davidovits	1982	Mixed alkalis with a burnt mixture of kaolinite, limestone and dolomite, and used several trademarks such as Geopolymer, Pyrament, Geopolycem, Geopolymite.
Forss	1983	F-cement (slag-alkali-superplasticizer)
Langton and Roy	1984	Ancient building materials characterized
Davidovits and Sawyer	1985	Patent of "Pyrament" cement
Krivenko	1986	DSc thesis, R_2O–RO–SiO_2–H_2O
Malolepsy and Petri	1986	Activation of synthetic melilite slags
Malek. et al.	1986	Slag cement-low level radioactive wastes forms
Davidovits	1987	Ancient and modern concretes compared
Deja and Malolepsy	1989	Resistance to chlorides shown
Kaushal et al.	1989	Adiabatic cured nuclear wastes forms from alkaline mixtures
Roy and Langton	1989	Ancient concretes analogs
Majundar et al.	1989	$C_{12}A_7$ – slag activation
Talling and Brandstetr	1989	Alkali-activated slag
Wu et al.	1990	Activation of slag cement
Roy et al	1991	Rapid setting alkali-activated cements
Roy and Silsbee	1992	Alkali-activated cements: an overview
Palomo and Glasser	1992	CBC with metakaolin
Roy and Malek	1993	Slag cement
Glukhovsky	1994	Ancient, modern and future concretes
Krivenko	1994	Alkaline cements
Wang and Scrivener	1995	Slag and alkali-activated microstructure

The chemical and physical characteristics of the precursors (which vary from source to source) need to be determined and controlled to ensure the quality and consistency of AA materials. One of the restraints that inhibit the worldwide production of AA cements is the uneven nature of the precursor required to manufacture them (Shi *et al.,* 2003; Fernando *et al.,* 2014; Bernal *et al.,* 2014).

The first AAMs ever made were slag-based. Subsequently, slags were used for the production of AAMs for decades. They were patented in 1958 and used in construction, in 1960 in the USSR, and as precast products in Eastern Europe, Finland, and France (Moranville-Regourd, 1998). Some AA slag materials show advantages over PC products including: early hardening, high strengths, lower hydration heat, better resistance to water solubility, chemical attack (resistance to sulfates and chlorides) and carbonation, higher resistance of interfaces, and higher resistance to frost action (Bernal *et al.,* 2014).

2.2 PRECURSORS: POZZOLANS AND SCMs

Any reactive aluminosilicate can be used as a precursor in an alkali-activated (AA) system. Both pozzolanic materials and Supplementary Cementitious Materials (SCMs) contain reactive aluminosilicates that can generate cements when properly activated, hence they can be used as precursors in the alkali activation process. Many precursors are waste materials generated as by products from industrial and agricultural processes. The use of waste constitutes an environmental credential for AAMs, as it avoids the use of non-renewable raw materials and energy for their processing and preparation.

A pozzolan is a siliceous or siliceous and aluminous material which in itself possesses little or no cementitious value but, in finely divided form and in the presence of moisture, reacts with calcium hydroxide at ordinary temperatures to form compounds with cementing properties (ASTM C618). In the absence of an activator such as calcium hydroxide (lime), i.e., with water only, pozzolans do not exhibit cementing properties. The low-medium, alkali phase brough about by the lime activates pozzolanic materials. However, when activated with stronger alkalis such as alkali hydroxides or alkali silicates, some pozzolanic materials such as metakaolin and coal fly ash can produce significant cements that provide high strength (Shi *et al.,* 2003).

SCMs are a wider group of materials that, not only contain pozzolans, but also other materials such as GGBS that, on their own, possess cementitious properties. GGBS comprises a small amount of reactive calcium silicates that hydrate when water is added without needing any alkali medium or any other activation (Lawrence and Hewlett, 1988).

A pozzolanic reaction is the chemical reaction between reactive siliceous and/or silicoaluminate components in the pozzolan, and calcium hydroxide (lime) in the presence of water (Dodson, 1990). Several factors influence the pozzolanic reaction including the type and proportion of active phases, the particle's specific surface area, the lime to pozzolan ratio, the mineralogical and chemical composition of the pozzolan, the water content, and the curing time and temperature (Massazza, 2002, 2007). In addition, reactivity increases in the presence of sulfates such as gypsum and Na_2SO_4 and other chemicals such as $CaCl_2$ (Massazza, 2002). Amongst the parameters that affect reactivity the most are: the amorphous silica content, fineness, specific surface area and carbon content (Walker and Pavía, 2010). It is widely accepted that an increase of specific area and/or decrease in particle size will expose a greater surface to chemical reaction enhancing reactivity, and that amorphous structures are more reactive than crystalline ones, on account of the greater mobility and superficial location of their atoms (Walker and Pavía, 2011). SCMs and pozzolans have been added to PC and lime-based materials for thousands of years. The first instance is usually attributed in the literature to the Romans, who built entire structures using concretes made with pure lime and pozzolans, where the pozzolans were usually natural volcanic ash or ceramic dust (Pavia and Caro, 2008). SCMs and pozzolans react with portlandite ($Ca(OH)_2$- lime) forming cementing hydrates that strengthen the microstructure of composites. It has been reported that this enhances durability, mainly due to lowering the porosity and permeability of the paste which minimises the penetration of harmful substances that may be present in destructive environments such as sewage systems, acid sulphate soils and sea water (Maso *et al.,* 1995; Chandra, 1996).

In most instances, incorporating pozzolans/SCMs into lime composites produces a series of general effects including a densification of the structure (or physical filler effect), a refinement of the pore system usually coupled with a reduction of permeability, and an enhancement of both the mechanical strength and the resistance to salt attack including sulfates and chlorides (Mehta, 1977; Walker and Pavía, 2011, 2010; Pavía *et al.*, 2014; Arif, Clark and Lake, 2016; Figueiredo and Pavía, 2017, 2018, 2020; Aly and Pavía, 2019; Pavía and Aly, 2019).

In PC materials, pozzolans positively influence the interfacial transition zone. The interfacial transition zone consists mostly of calcium hydroxide and ettringite. It is a weak area due to the

water film around the aggregate, which leads to higher porosity, ultimately unbalancing the stress distribution causing crack propagation (Maso, 1996). Pozzolanic materials strengthen this zone by reducing the amount of $Ca(OH)_2$, consequently lowering the width of the interfacial zone and reinforcing the microstructure around the aggregate (Scrivener *et al.,* 1988; Zhang *et al.,* 1996). It has also been reported that pozzolans can enhance resistance to sulphate attack. In general, PC materials suffer sulphate attack when the excess CH and aluminate reacts with H_2SO_4 producing expansive gypsum and secondary ettringite which crack and spall the material. However, if the CH is combined with the pozzolan, these reactions would not take place, consequently increasing the durability of materials (Chandra, 1996)**.**

The replacement of PC clinker with pozzolanic materials carries important environmental and economic benefits. Today, most of the PC-based materials used in construction, include some SCM and/or pozzolan aimed at lowering environmental impact. As Lima and Pavía (2020) note, most of the 27 members of the family of cements in EN 197-1 include either SCMs or pozzolans; and CEM I is the only cement consisting nearly entirely of clinker (calcium silicates). As a result, the use of SCMs and pozzolans is escalating.

According to Lima and Pavía, (2020), in 2011, the European cement industry used 47.8 million tons of alternative materials in cement production, and in the CEMBUREAU countries, blended cements corresponded to 72% and CEM I only 28% of the total cement production.

The properties and composition of the precursors (SCMs and pozzolans) determine their reactivity, therefore the nature and the amount of cementing hydrates formed, as well as the time at which they appear, and these govern the properties of the resultant materials. The chemical and physical characteristics of the precursors vary from source to source, affecting their pozzolanic and hydraulic activity, consequently the properties of the resultant materials. Therefore, to determine the mineral and chemical composition as well as the physical properties of the precursors is very important. This was the first step in this research and, as aforementioned, it is included in Chapter 4.

The precursors most commonly used in alkaline activation are vitreous blast furnace slags (calcium-rich), fly ash from coal combustion (calcium-poor), and thermally activated clays (metakaolin), or blends of them. These precursors can be grouped, based on their composition, as shown in Figure 2-1 in a ternary graph ($CaO-SiO_2-Al_2O_3$). In summary, the precursors are split in two groups: calcium poor and calcium rich precursors.

- $(Na,K)_2O-Al_2O_3-SiO_2-H_2O$ system (also known as geopolymer system): the materials in this model are rich in aluminosilicates and low in calcium, e.g. metakaolin, fly ash class-F. The activator must be more aggressive to start the chemical reactions, and the main reaction product is alkaline aluminosilicate hydrate gel (N-A-S-H) (Grutzeck, 1999; Provis and Deventer, 2009; Pacheco-Torgal *et al.,* 2008; Duxson *et al.,* 2007).

- $(Na,K)_2O-CaO-Al_2O_3-SiO_2-H_2O$ system: Ca-rich precursors such as GGBS $(SiO_2 + CaO > 70\%)$ need moderate alkaline conditions to harden at ambient temperature. They have a shorter setting time, and their main reaction product is calcium aluminum silicate hydrate gel (C-A-S-H), which is identical to the gel obtained during PC hydration (Palomo *et al.,* 1999; Duxson *et al.*, 2007; Provis *et al.,* 2009).
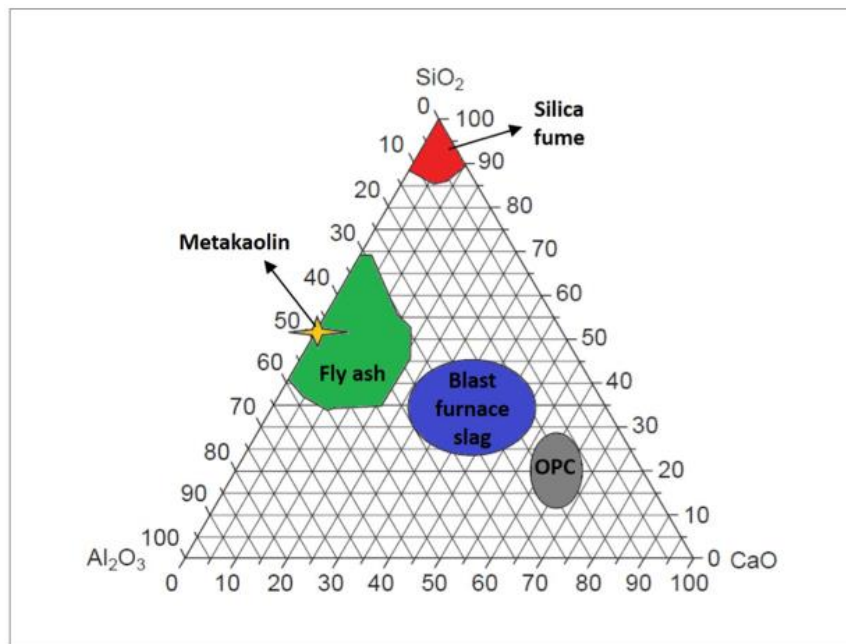
Figure 2-1 Composition of some of the precursors used in alkaline activation compared with PC (Torres-Carrasco et al., 2017).

2.2.1 GGBS

GGBS is a vitreous material formed by rapid cooling of a melt of iron ore in a blast furnace. The method of rapid cooling is known as quenching. Quenching the molten slag in the furnace with water and air at high-pressure creates glassy, granulated particles that are then dried and ground into a fine powder (Hewlett 1988). It usually consists of at least two-thirds by mass of

glassy slag, showing hydraulic properties when suitably activated EN 15167-1:2006. GGBS contains some calcium silicates (similar to those in PC clinker) so it is not strictly a pozzolan but a supplementary cementitious material - SCM. However, the rate of reaction is slow and needs alkalis or sulfates to fully activate. Generally, the main chemical composition of GGBS is CaO, SiO_2, Al_2O_3 and MgO, with additional components including MnO, SO_2 and TiO_2 which depend on the type of iron ore used (Osborn et al., 1969). Shi et al., (2006) studied the differences in the composition of furnace slag from several countries, concluding that slags have similar SiO_2 and CaO contents but the Al_2O_3, MgO and TiO_2 contents vary.

Due to their physical properties and composition, slags have been used as cements for hundreds of years. They are still widely used today as partial PC replacement around the world. GGBS is a typical supplementary cementitious material in PC products such as CEM II and III EN 197-1: 2011 , where cement clinker is blended with GGBS at content ranging from 6 to 95%.

Slag, on its own, has a slow hydration rate and low early strength which is usually overcome by chemical activation. PC is the most commonly used activator for GGBS (Wang and Scrivener, 1995; Song et al., 2000; Shi et al., 2006). A two-phase reaction occurs when slag is blended with PC. The early stages of hydration are dominated by alkali hydroxide, while the subsequent stages are dominated by calcium hydroxide (Hogan, 1982). In PC materials, the hydraulic calcium silicates hydrate quickly, to form C-S-H and $Ca(OH)_2$. As aforementioned, the low-crystallinity C-S-H cement provides strength, while the (usually large) hexagonal plates of $Ca(OH)_2$, scattered in the matrix and the interface, are sometimes considered a flaw in the microstructure of PC composites. However, in slag-PC materials the slag reacts with the $Ca(OH)_2$ released upon PC hydration to form additional C-S-H, which densifies the matrix enhancing strength (SCA, 2013).

GGBS generally improves the workability of PC materials due to the high fineness and great specific surface area of its particles. GGBS is typically finer and has a greater specific surface area (SSA) than PC. PC has usually a SSA of 300 m^3/kg versus 375-435 m^3/kg with a fineness of 460 Blaine (m^2/kg) for GGBS.

For decades, slags such as ground granulated blast furnace slag (GGBS) have been used heavily, as PC replacement, to reduce the environmental impact of PC production. As PC replacement, GGBS has been proven to decrease chloride diffusion (Luo et al. 2003), reduce creep and drying shrinkage (Jianyong and Yan, 2001), increase sulfate resistance (Higgins, 2003; Binici and Aksoğan, 2006), enhance strength (Barnett et al. 2006), reduce the heat of

hydration and bleeding (Wainwright and Rey, 2000) and increase durability in the aggressive environment of farming silos (Pavía and Condren, 2008). According to Ecocem Ireland, CEM I blended with 0% and 50% of GGBS achieved a compressive strength of 58 and 59.5 MPa respectively. Lawrence and Hewlett (1988) highlight the lower environmental impact of blends of GGBS with PC.

In addition, slags have been successfully activated with lime and other alkalis by many authors. Lime activates GGBS forming C-S-H and the AFt ettringite phases (Häkkinen, 1993; Aly and Pavia, 2015). Slags have also been activated with alkali solutions of hydroxides and silicates to produce AAMs for decades.

AAMs made with slags were patented in 1958 and used in construction, in 1960 in USSR, and as precast products in Eastern Europe, Finland and France (Lawrence and Hewlett, 1988). Some AA slag materials show advantages over PC products including: early hardening, high strengths, lower hydration heat, better resistance to water solubility, chemical attack (resistance to sulfates and chlorides) and carbonation, higher resistance of interfaces and a higher resistance to frost action (Bernal, Provis, Fernández-Jiménez, *et al.*, 2014).

Alkali activated blast furnace slag materials have been used in applications requiring high resistance to chemical attack. From the 60s onwards, they were used in Ukraine in the construction of apartment buildings, railway sleepers, road sections, pipes, drainage and irrigation channels, flooring for dairy farms, pre-cast slabs and blocks (Provis and Van Dementer 2014).

The amorphousness and the basicity of the slags impact reactivity (Lawrence and Hewlett, 1988). The more basic the slag, the greater its hydraulic activity in the presence of alkali activators (Lawrence and Hewlett, 1988). Generally, glassy slags with CaO/SiO_2 ratios between 0.50 and 2.0 and Al_2O_3/SiO_2 ratios between 0.1 and 0.6 are considered suitable for alkali-activation (Provis and Van Deventer, 2013).

2.2.2 Fly ash (FA)

Fly ash is a by-product of power generation at coal-fired power plants. It is collected by filters or electrostatic precipitators, which remove the solid particles from the smoke, making the smoke less harmful to the environment (Helmuth, 1987).

The composition of FA depends on the type of coal used and on the various substances injected into the coal or gas stream to reduce gaseous pollutants or to improve the efficiency of the particulate collectors (Fisher *et al.*, 1978; Shi, Krivenko and Roy, 2006; Elsayed and Swan, 2007; Yao *et al.*, 2015). For example, when limestone or dolomite are used for desulphurization of the exit gases, CaO and MgO contents increase in the FA. Conditioning agents such as sulphur trioxide, sodium carbonate and bicarbonate, sodium sulphate, phosphorus, magnesium oxide, water, ammonia and triethylamine are often used to improve the collection efficiency and can alter the composition of the FA (Shi *et al.,* 2006).

FA usually consists of small, spherical particles of high surface area, but it can also contain irregular or angular mineral particles and unburned coal remnants. FA is often highly amorphous and consists predominantly of silicon dioxide (SiO_2), aluminium oxide (Al_2O_3) and iron oxide (Fe_2O_3) (Abdullah *et al.,* 2018; Ismail *et al.,* 2007; Nizar *et al.,* 2014).

Due to their physical properties and composition, FAs are valuable raw materials for binder production, and they have been used as supplementary cementitious materials in PC materials for several decades. FAs have been used as partial clinker replacement in PC production since the 1930s (Provis *et al.,* 2009; Massaza, 1998; Thomas, 2007; EN 197-1, 2011).

The use of FA results in lower carbon emissions and lower energy and raw material consumption binders. Currently, in the European standard, there are three types of Portland-fly-ash cements in the CEM II group, with clinker substitution by FA up to 35% (EN197-1, 2011).

FAs have also been used successfully for the production of alkali-activated materials (AAMs), being the most commonly used aluminosilicate precursors in alkali activation due to their low cost and wide availability (Bouaissi *et al.,* 2018; Torres-Carrasco and Puertas 2017).

Depending on their composition, FAs can be either pozzolanic or cementitious. Low-CaO, fly ashes have very little or no cementitious properties. They are pozzolanic and display no significant hydraulic behaviour. Hence, they need either lime or an alkali solution to activate and produce cementing minerals. In contrast, in high-calcium ashes, the calcium forms hydraulic silicates that produce hydraulic cements upon contact with water. As well as calcium, other elements can also affect the performance of the FA, including alkalis (Na_2O and K_2O), carbon (usually measured as a loss on ignition-LOI) and sulfates (SO_3) (Thomas, 2007).

As aforementioned FA cements with PC clinker substitution by FA up to 35% are well established. Therefore, the role of fly ash in the construction industry has been important, over the last decades, to lower the environmental impact and cost of PC materials. However, with the move towards renewable and sustainable energy sources, the production of FA will lower and may come to an end in the near future.

The attainment of strength and durability of most FA-blended, PC materials rely on the pozzolanic action of the FA particles which is a relatively slow process. To overcome this drawback, hydrated lime is sometimes added to FA-blended PC products (George and Sofi, 2017). The effect of FA in PC has been highlighted by several authors

The general beneficial effects of SCMs and pozzolans in composites aforementioned, also apply to FA materials. Scheetz and Earle (1998) summarise these effects as follows: benefits of blending FA with PC include decreasing water demand by 15–25%, reducing the shrinkage of concrete; saving PC and reducing costs; better durability; acting as a filler and improving capillary pores in concrete, hence reducing permeability. The reaction of FA with lime forms C-S-H, which is responsible for strength development (Watt and Thorne, 1965). The improved sulfate resistance of FA-PC materials was noted decades ago (Hughes, 1985).

2.2.3 Red Mud (RM)

Red mud (RM) waste is produced in large volumes when refining bauxite for aluminium production. Bauxite is mainly a mixture of hydrated aluminium oxides and iron phases. The refining (Bayer) process involves the digestion of crushed bauxite in a concentrated, caustic, sodium hydroxide solution at temperatures up to 270°C. Under these conditions, the majority of the aluminum containing species in the bauxite – such as gibbsite and boehmite– dissolve, leaving an insoluble residue (RM) composed of iron oxides, quartz, sodium aluminosilicates, calcium carbonate/ aluminate and, generally traces of titanium dioxide (Hind *et al.,* 1999).

The composition of the RM residue depends on the composition of the parent bauxite and the conditions of the alumina refining (Bayer) process such as the addition of lime and the washing efficiency. The lime addition is determined by the type of bauxite ore. The washing efficiency dictates the amount of soluble soda remaining in the RM and hence its alkalinity. The RM

mainly consists of Al_2O_3, Fe_2O_3 and SiO_2, but the composition widely varies around the world, a comparative table is included in Chapter 4.

According to previous authors (Hind *et al.,* 1999; Klauber *et al.,* 2011) during the refining process, silica can dissolve to form silicate as follows:

$$2\ NaOH + SiO_2 \rightarrow Na_2SiO_3 + H_2O$$

RM typically includes sodalite, cancrinite, dawsonite and calcium-containing phases resulting from the Bayer process, and gibbsite ($Al(OH)_3$) and boehmite (γ-AlOOH) as undigested material inherited from the bauxite (Klauber *et al.,* 2011). The organic compounds present in RM can form sodium oxalate- $Na_2C_2O_4$ - in the alkaline (pH=14), high ionic strength (6–7 M [Na^+]) liquors typical of the Bayer process (Hind *et al.,* 1999).

Between 1 and 1.5 tons of RM waste are generated to obtain 1 ton of aluminum oxide (Khairul *et al.,* 2019). Annually, 150 million tons of red mud are produced (Khairul *et al.,* 2019; Kumar *et al.,* 2006; Evans, 2016), and it is estimated that 30 billion metric tons are already accumulated worldwide (Mishra and Gostu, 2017). The high alkalinity of the RM can pollute water, land and air, and high costs are associated with the large areas required for storing the residue. The management of this residue can pose a complex environmental impact and requires the development of technological solutions that use the residue on a large scale. The disposal of RM represents a significant proportion of the overall alumina production cost, and it has been a concern for alumina refiners worldwide for decades (Hind *et al.,* 1999).

RM is usually pozzolanic but can be hydraulic. Therefore, it is important that RM waste is characterised prior to use. In the literature, RMs from different bauxite refineries in the world has been compared indiscriminately by previous authors. However, some of these RM residues are distinctively cementitious, they widely differ from their pozzolanic counterparts and should not be directly compared. This is the case of the Chinese Shandong Aluminium Plant, where the RM waste includes highly reactive minerals, C_3A and C_2S, hence having significant hydraulic properties. The Chinese process of sintering alumina is differs from the Bayer process which is applied in most bauxite refining plants. Here, due to the low Al_2O_3/SiO_2 of the Chinese bauxite ore (average 5–6), the bauxite is calcined at 1200°C before extracting the alumina with caustic soda, and reactive hydraulic phases C_3A and C_2S form as a result of the high temperature of the refining process. The presence of 50 and 56 wt.% β-C_2S has been reported

due to the special processing of this Chinese bauxite (Yang and Xiao, 2008). As it is well known in cement technology, β-C_2S is the most hydraulic belite polymorph. Liu et al. (2011), also found a strong cementitious activity in the Shandong RM: besides the high amount of C_2S initially present, additional poorly-crystallised C_2S is formed with the CaO derived from the decomposition of aragonite (500-600°C) and SiO_2 derived from the decomposition of amorphous aluminosilicates, a metastable phase that transforms into highly crystallised, less active, Ca_2SiO_4 by increasing the temperature from 700°C to 900°C. Similarly, Yalçın and Sevinç (2000) report the formation of sodium ferrite ($NaFeO_2$) in Turkish red mud at 500°C.

Due to its composition, RM can be used in the cement and ceramic industries. When fired, it becomes a viable ceramic material that can be used to manufacture tiles, bricks and insulating materials (Hind *et al.,* 1999). The use of RM in Portland cement (PC) production has attracted the attention of researchers since the 1970s. Pontikes and Angelopoulos (2013) reviewed existing literature where various authors used RM (as a source of Fe and Al oxide) in cement manufacturing, concluding that the majority of iron and alumina-rich phases in the RM, participate in the production of hydraulic phases tricalcium aluminate (C_3A), which accelerates cement hydration and tetracalcium aluminoferrite (C_4AF); and that the addition of 2-10 wt.% of RM improved the burnability of the clinker, reducing the temperature at which melt formation occurred by 200 $^{\circ}$C. RM was also used in calcium sulfoaluminate cement production (Pontikes and Angelopoulos, 2013). However, the alkalinity of RM limits its application as a PC clinker replacement. RM has also been used to neutralize acidic soils, as a treatment for iron-deficient soils, and to remove toxic heavy metals from solutions (Hind *et al.,* 1999). The recovery of alumina and soda, iron, titanium dioxide and other minor elements such as vanadium and rare earths from bauxite residues has been attempted without commercial success (Hind et al. 1999).

This research investigates the RM residue from aluminium producer Ma'aden. In Ma'aden, to recover alumina and soda from RM through sintering and hydrothermal routes involve billion-dollar capital costs, hence these are not realistic options. According to the Ma'aden Mining Industries, an economically viable disposal option has not yet been found, and at least 5-10% RM recycling needs to be achieved to make a disposal option economically viable. To date, due to its high alkalinity, only small quantities RM (3 wt.%) have been incorporated into PC. The pozzolanic activity of the Saudi RM has not yet been studied. This work explores the properties, composition and reactivity of the Saudi RM with a view to replace traditional non-sustainable binders in construction.

2.2.4 Bauxite

Bauxite is a natural sedimentary rock composed mainly of aluminium and iron minerals. It is the main ore for aluminium production. The majority of mined bauxites are lateritic, and mainly consist of hydrates of alumina. Laterite bauxites (industrial grade) are deposits of bauxite overlying alumosilicate rocks. They are generated by silica leaching from aluminosilicate rock (Bardossy, 1982; Mustafa *et al.,* 2019; Bárdossy and Aleva, 1990). The main mineral component of bauxite is usually gibbsite $Al(OH)_3$, with smaller amounts of boehmite, γ-$AlO(OH)$, and often diaspore α-$AlO(OH)$. Clays such as kaolinite $Al_2Si_2O_5(OH)_4$ as well as iron oxides (hematite Fe_2O_3, goethite $FeOOH$), silica (quartz SiO_2), and titania (rutile TiO_2 or anatase TiO_2) are usually present in lesser amounts.

The layered atomic structures of the alumina hydrates (or aluminum oxyhydroxides) gibbsite and boehmite in bauxite are comparable to the structures of clays such as kaolinite: their high specific surfaces and active hydroxyl surfaces makes them highly reactive, and hence suitable for a wide range of applications such as adsorbents and catalysis supports. Their high specific surfaces enhance adsorption (accumulation of matter at the solid/water interface) which affects the rates of nucleation, precipitation and dissolution, and the catalysis of redox processes (Rosenqvist, 2002).

The surface hydroxyl groups (adsorbed water molecules in dissociated form) of gibbsite and boehmite are active centres in many reactions (Hadjiivanov, 2014). Their amount and nature affect the physicochemical properties of the surface and the efficiency as a catalyst or adsorbent (Lagauche *et al.*, 2017). The bonds between adjacent hydroxyl ions can weaken, increasing layer separation and causing their breakup, producing an enhanced reactivity. This has been evidenced in boehmite -n-$AlO(OH)$- by (Brühne *et al.*, 2008). As a result, bauxites have industrial applications, and their transitions have been studied by former authors.

Former authors have studied the atomic structures of gibbsite and boehmite and their transformation in detail. However, most studies refer to mineral phases in synthetic form, as laboratory-synthesized, structurally and chemically precise, pure, nanoplates of gibbsite and boehmite with no detectable structural defects or impurities. However, in natural bauxites such as the one in this study, the alumina hydrates are mixed with alkalis and other phases such as gypsum and iron oxides which are soluble, and hence affect reactivity. Furthermore, former authors studied the structures of gibbsite and boehmite for industrial applications, but they do

not establish a correspondence between microstructural changes and the variation in the physicochemical properties of the surface that determine adsorption and reactivity. This research intends to measure the pozzolanic and hydraulic capacity of raw and thermally activated Saudi bauxite with a view to bridge this gap, and establish a relationship between the nature of the forming phases and the resultant reactivity/end-material properties.

The world's bauxite resources are estimated to be over 75 billion tons, with the majority of them located in Africa (33%), Oceania (24%), South America and the Caribbean (22%), and Asia (15%) (Survey, 2009). The Saudi bauxite is extracted from two mines' sites where bauxite is extracted, i.e., the Az Zabirah Mine and Al Ba'itha Mine in Saudi Arabia. Bauxite annual production is 1.086 million tons from the Az Zabirah mine (Ma'aden, 2014). In 2017, bauxite's ore annual production was 308 million tons and 461 million tonnes in 2016 from the Az Zabirah mine, and 35 million tons from the Al Ba'itha mine (Ma'aden, 2017).

One of the applications of bauxite is the production of calcium aluminate cements (CAC) which are made from limestone and bauxite. Their current production is very small when compared with the member of the family of PCs. The standard composition of CAC is Al_2O_3 (ranging from 38% to 40%), silica (<6%) and iron oxide (>20%). The principal hydraulic phase of CACs is $CaAl_2O_4$ (or CA) in amounts from 40% upwards. The hydration of CACs is different from the hydration of calcium silicate cements such as PC: in CACs, hydration is strongly dependant on the temperature, and metastable hydrates can form that may persist for many years before they convert into stable phases. The time between the initial and final set is much shorter for CACs than PCs, and hence early the heat of hydration evolved is much greater between 6 hours and 5 days. (Lawrence and Hewlett, 1988). CACs exhibits rapid strength gain even at low temperature, excellent durability and refractory properties (they resist high temperature) (Lawrence and Hewlett, 1988).

2.3 PRECURSOR TREATMENTS TO ENHANCE REACTIVITY

Pozzolans and SCMs can be treated to enhance their reactivity. As aforementioned, when pozzolans are mixed with lime, they undergo pozzolanic reaction producing cements. However, the pozzolanic reaction can be augmented by treating the pozzolans with thermal or chemical treatments.

Thermal activation (calcination) is usually applied to clay mineral-based precursors (aluminosilicates) such as bauxite, RM or kaolin. Heat alters the clay mineral structure, increasing the content of amorphous phase and hence favouring the dissolution of aluminates and silicates (Ferone *et al.*, 2015). Shi (2001) found that calcination changed crystalline structures into amorphous ones, significantly increasing pozzolanic activity. This is a common treatment in mainstream industrial processes such as the activation of kaolinite into metakaolin. Thermal activation breaks Si–O–Si and Al–O–Al bonds enhancing reactivity.

It is well known that calcination also eliminates organic matter (carbon) impurities which would otherwise interfere with the cementing reactions and would undermine the mechanical strength and the rheology of the resultant materials. This is important in precursors with high carbon content including agricultural waste such as rice husk ash (RHA) and sugar can bagasse ash (SCBA) (Pavía *et al.*, 2014; Lima Figueiredo and Pavía, 2020).

Calcination parameters including dwelling time, temperature and environment affect the specific surface area, amorphous silica, and carbon content of the precursor greatly affecting reactivity. The temperature is very important on pyroprocessing because, above a certain threshold, the amorphous phases become crystalline declining reactivity. In general, the temperature should be high enough to burn the carbon and increase the content of amorphous phase, but low enough to avoid the sintering of unreactive crystalline phases. However, in some precursors, calcining at high temperature allows the sintering of reactive calcium silicates that readily hydrate producing C-S-H and other hydrates with great cementing ability, similar to those formed on PC hydration.

Thermal activation works best in materials including layered phases such as clay minerals. The RM and bauxite in this study conform with this composition. The layered atomic structures of gibbsite and boehmite in bauxites are comparable to the structures of clays such as kaolinite. Their high specific surfaces and active hydroxyl surfaces make them highly reactive, and bonds between adjacent hydroxyl ions can weaken, increasing layer separation and causing their breakup, producing an enhanced reactivity. Generally, thermal activation breaks Si–O–Si and Al–O–Al bonds enhancing reactivity.

However, the outcome of thermal activation i.e., the degree of activation produced by heat to a given precursor, vary in different authors, probably due to the varying starting compositions.

For example Hind *et al.* (1999); Pontikes and Angelopoulos (2013) attempted to increase pozzolanic activity of RM through heat treatment, but the results differ, probably because the parent bauxite composition and the conditions of the Bayer process differ in different alumina plants around the world. Pera et al. (1997) found that RMs calcined at 600–800 °C were pozzolanic, but their activity was low, and the reaction started at 3 days. They claim that the aluminium hydroxides (boehmite and gibbsite) develop pozzolanic behaviour when calcined between 600 and 800 °C, and that RM reactivity increases over 700 °C. According to Manfroi *et al.* (2014), RM calcined at 600 °C has high pozzolanic activity, whereas (Shi *et al.,* 1999) obtained eminent pozzolanic activity by heating an RM with a high kaolinite content at 750 °C. RM can be inert up to 900 °C. According to Sglavo *et al.* (2000), up to 900 °C, the main components (Fe_2O_3 and TiO_2—which account for 50% of the original mass) maintain their original state, and nepheline and $Na_2Si_2O_5$ form in the 900–1100 °C interval.

Tchamba *et al.* (2010) investigated thermal transformations of a bauxite and concluded that dehydroxylation of bohemite and kaolinite takes place between 200 and 520 °C, and gibbsite dehydroxylates between 350 and 400°C. In the range of 1000 °C to 1200 °C, corundum and γ-alumina were evidenced; furthermore, hematite became magnetite, and ilmenite formed from the titanium oxides in the raw bauxite. Kloprogge et al. (2002) studied three major Al-minerals in bauxite: gibbsite, boehmite, and diaspore, over a temperature range of 200 to 750 °C. At 500°C, the gibbsite transforms into boehmite. The dehydroxylation of the gibbsite starts around 220 °C, which leads to the loss of the intensity of the OH^- stretching bands and dehydroxylation completes at around 350 °C, similarly to boehmite and diaspore.

2.4 ALKALI-ACTIVATION

2.4.1 Alkali activators

The type of activator is essential because it impacts the properties and durability of the final material. The type of alkali activator plays an important role in alkali activation because it determines the dissolution of the precursor (Nuruddin *et al.,* 2014). Hence, it needs to be chosen based on the precursor's chemical composition and physical-chemical properties (Fernando Pacheco-Torgal *et al.,* 2014; Bernal *et al.,* 2014). The most common alkali activators used for AAMs and geopolymers are sodium hydroxide (NaOH), potassium hydroxide (KOH),

potassium silicate (K_2SiO_3), and sodium silicate (Na_2SiO_3) (Glukhovsky *et al.,* 1980; Provis and van Deventer, 2014; Awoyera and Adesina, 2019).

An alkali activator may consist of Na^+ or K^+ and hydroxyl anions (OH^- ions), which stabilize charges, allowing the breakage of bonds of the silicate and aluminosilicate minerals in the precursors (Davidovits, 1991; Barbosa *et al.,* 2000). Theoretically, dissolution increases with increasing alkalinity. It has been shown that sodium hydroxide can release more silicate and aluminate monomers than potassium hydroxide (Li *et al.,* 2010). According to Xu and Deventer (2000), the ionic size of Na^+, smaller than K^+, enhances the dissolution of aluminosilicate minerals. However, sodium hydroxide solutions have other properties that must be considered including viscosity and heat released on dissolution (Nematollahi and Sanjayan, 2014; Provis *et al.,* 2009). NaOH is widely available and cheap, and it has low viscosity. Hence it is used extensively in alkali activation and geopolymer synthesis (Provis and Van Deventer, 2009; Sani *et al.*, 2016).

The second most frequently used alkali activators are silicate solutions, particularly sodium silicate. They can affect mixing, as well as the strength and microstructure of the formed material and gel structure (Pacheco-Torgal *et al.,* 2014). The soluble silica increases the growth of microstructures resembling glass. Nonetheless, a high silica concentration in the activating solution decreases the pH and increases viscosity, lowering the reaction rate (Duxson *et al.,* 2005). Therefore NaOH is typically blended with silicate to lower viscosity and increase the pH of the activator solution to optimise the reaction (Fernando *et al.,* 2014).

Most studies in geopolymers and AAMs use silicate blended with hydroxide as the alkaline solution for activation (Canpolat and Naik, 2011; Görhan and Kürklü, 2014). The objective of this combination is to provide Si ions in the aqueous phase and help activating the precursor, therefore improving dissolution and enhancing the mechanical properties (Rees *et al.,* 2004; Nuruddin *et al.,* 2014).

2.4.2 Reaction mechanism of low calcium precursors

As aforementioned, geopolymers are a subset of AAM with high Al and low Ca contents, with an almost entirely aluminosilicate-based phase which is highly coordinated (Yang *et al.,* 2022). Glukhovsky initiated research on these materials in the 1950s and pioneered their introduction

(Shi *et al.,* 2003). Glukhovsky *et al.,* (1980) proposed a mechanism of alkali activation in three stages: destruction, coagulation (condensation) and crystallisation.

The first stage (destruction) involves a breakdown of the covalent bonds Si–O–Si and Al-O–Si, which occurs when the pH of the alkaline solution increases and the conversion into a colloidal phase. In the next stage of coagulation-condensation, the broken bonds accumulate and interact among themselves to form a coagulate structure, and this leads to the final stage in which a condensed structure (crystallization) is generated.

Another reaction mechanism model for the geopolymerisation reaction was proposed by Peter Duxson *et al.,* (2007) and it is shown in Figure 2-2. The model depicts the transformation of a solid aluminosilicate source into a synthetic alkali aluminosilicate as follows:

1. Dissolution
2. Special equilibrium
3. Gelation
4. Reorganization
5. Polymerization and hardening
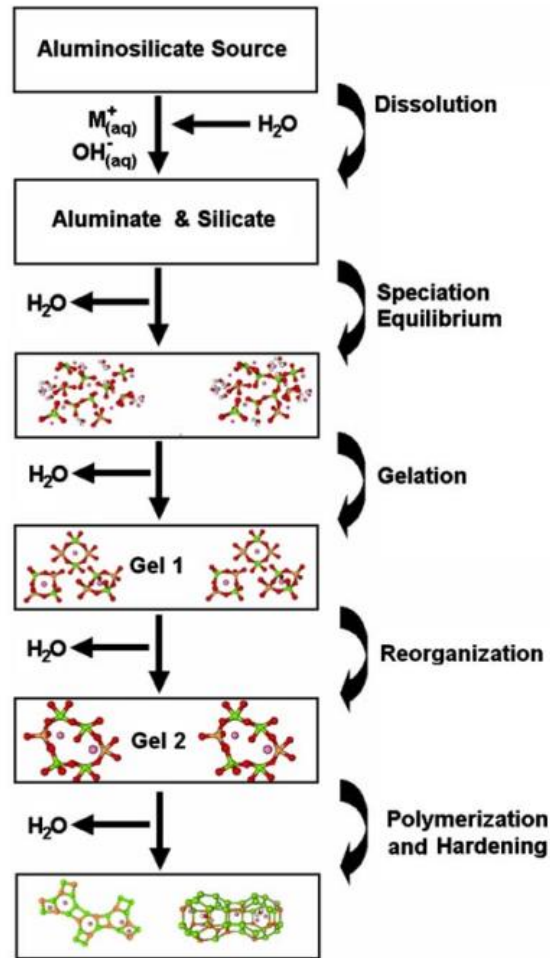
Figure 2-2 Geopolymerisation conceptual model (Duxson *et al.,* 2007)

According to Duxson, *et al.*, (2007), the first reaction of the geopolymerisation process is the dissolution of the aluminosilicate materials, resulting in the formation of reactive monomers of silicate and aluminate $[Si(OH)_4]^-$ and $[Al(OH)_4]^-$, which are atoms of silicon or aluminium in a tetrahedral configuration surrounded by four hydroxyls each (Ahmaruzzaman, 2010). The dissolution process commences when the covalent bonds Si-O-Si and Al-O-Al that characterize aluminosilicates are broken, and this can occur rapidly in the strongly alkaline medium of high pH provided by the activating solution. The alkaline solution dissolves the bonds that hold aluminosilicates together, resulting in the formation of a colloidad phase (Duxson *et al.,* 2007; Wu *et al.,* 2019).

The monomers form large networks of repeating units by condensation -or oligomers-, resulting in the gel stages referred to as "Gel 1" and "Gel 2" - Figure 2-2. The strength of geopolymers is developed due to the formation of these aluminosilicate gels. A gel rich in Al

is formed at an early stage of the alkali activation process known as "Gel 1". At a later stage, a gel rich in Si ("Gel 2") is formed which enhances the geopolymer's mechanical properties (Duxson *et al.*, 2007).

The process continues with an increase in the release of the water in the gels. The search for equilibrium continues, but load balancing is impossible due to the negative charges of both aluminates [Al (OH)$_4$]$^-$ and silicates [Si (OH)$_4$]$^-$. As a result, the availability of alkali metal ions such as Na$^+$ or K$^+$ is critical in the alkaline solution. The positive charge of these ions restores equilibrium to the charges of the unstable gels, resulting in a restructuring of the intermediate compounds, which initiates the synthesis of a stronger and more stable final compound (Marvila *et al.,* 2021). Komnitsas and Zaharaki (2007) provide the empirical formula (2.1):

$$M_n \left[- (Si - O_2)_z - Al - O\right]_n . wH_2O \qquad \text{Equation 2-1}$$

Where z=1, 2 or 3, represents the atomic relationship between Si/Al;
M= alkaline cation (K$^+$ or Na$^+$);
n= geopolymerization degree, and
(w) amount of bonded water.

In the final geopolymerisation stage, the gels undergo polycondensation and may or may not crystallize, resulting in the stable gels found in the geopolymer's final structure. Some authors state that amorphous gels are called N-A-S-H (sodium alumino-silicate hydrate), whereas crystalline or semicrystalline phases are zeolites (Rożek *et al.,* 2019). Finally, the material begins the process of hardening, acquiring the mechanical resistance and other final features associated with activated alkali materials (Duxson *et al.,* 2007; Wu *et al.,* 2019).

2.4.3 Reaction mechanism of high calcium materials

As summarised by Provis *et al.* 2015, the nanostructure of AAMs is strongly dependent on the available calcium content of the precursors: a high-calcium system such as alkali-activated GGBS is dominated by a calcium aluminosilicate hydrate (C–A–S–H) gel with a tobermorite-

like structure, while low-calcium systems such as those based on metakaolin or fly ash tend to generate an alkali aluminosilicate (N–A–S–H) gel with a highly crosslinked, disordered, zeolitic structure. As the authors note, these gels can coexist in binders based on blends of high-calcium and low-calcium precursors, although the final, most stable phase is still the subject of some discussion.

Precursors with a Ca/(Si+Al) ratio greater than 1 are considered calcium-rich precursors (Provis and Bernal, 2014). The alkali reaction generates reaction products that are similar to those produced on PC hydration (Provis and van Deventer, 2007; Provis et $al.,$ 2008). However, with less calcium than the C-S-H typical of PC, as well as more Al in the tetrahedral bonding locations. This results in a higher degree of polymerization and a significant crosslinking between the gel chains formed, which generates structures known as calcium alumina silicate hydrate (C-A-S-H) (Provis and Deventer, 2007; John et $al.,$ 2007). Marvila et $al.$ (2021) illustrated the difference in C-S-H and C-A-S-H gel structures (Fig. 2.3). The C-A-S-H structure, including interlayers with crosslinking and Al substitution, is known as Dreiketten structure (Marvila et $al.,$ 2021; Provis and Bernal, 2014). The net negative charge generated when Al^{3+} replaces Si^{4+} at the tetrahedral chains is balanced by some alkaline cations at the tetrahedral chain positions (Figure 2-3).
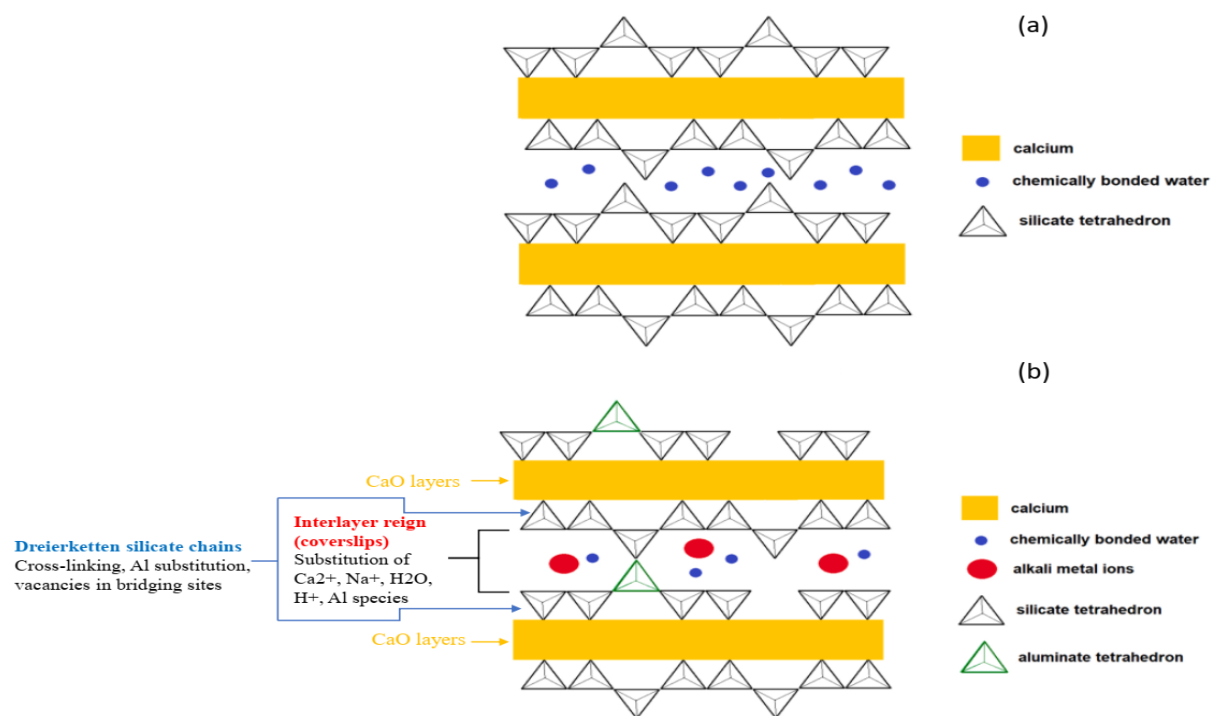
Figure 2-3 Structural differences between (a) C-S-H; and (b) C-A-S-H (Marvila et $al.$, 2021).

2.5 DESIGN VARIABLES FOR THE PRODUCTION OF AAMS

AAM's properties depend on the composition of the precursor and the activator, the dosage and concentration of the activator, curing, and other factors, as discussed below.

2.5.1 Type and concentration of alkali activator

The properties of the final AA material largely depend on the type and concentration of the alkali activator. As aforementioned, in the alkali activation process, the alkali solution is used to dissolve the precursors. Provis and Deventer (2009) report that increasing the molarity of an alkali solution improves the geopolymerization process by increasing the availability of hydroxide (OH^-) ions.

It has been proven by several authors that increasing or decreasing the NaOH concentration affects the mechanical properties of the resultant AAMs (Memon *et al.*, 2013; Livi and Repette, 2017; Nmiri *et al.*, 2017; Cornelis *et al.,* 2018).

The type and concentration of alkali activator must be chosen according to the composition of the precursor. Fernández *et al.,* (1999) experimentally proved that, in slag materials, the nature of the alkaline activator is the most significant factor that determines the strength, overriding the effects of the particle's specific surface area, curing temperature and activator concentration. When the alkali and the precursor are mixed, the pH controls reactivity because it determines the dissolution of the precursor. Previous authors state that silicates and hydroxides are the best activators for slags, because they generate the highest pH (or alkalinity), which accelerates the reaction between the activator and the precursor (Shi *et al.,* 2003; Fernández *et al.*, 2014; Pacheco-Torgal *et al.*, 2014). Hydroxide activators induce the hydrolysis of the Si-O-Si and Al-O-Al bonds, releasing Si^{4+} and Al^{3+} and providing more hydroxyls than other activators, which raise the PH further than other activators, quickly reaching the values required for the dissolution of the precursor, and hence the formation of hydrate cements. Similarly, when activating a slag with silicate, the glassy phases disintegrate, and the polycondensation reaction takes place whereby tobermolite and calcium silicate hydrate are generated at 1 day (Zhang *et al.*, 2008). However, it has been noted that silicate activators provide a higher level of available alkalinity over longer periods because, when a

moderate amount of silica dissolves, the PH does not drop rapidly (as it is the case with hydroxide activators) (Fernández-Jiménez, *et al.*, 2014).

A high pH is not considered suitable for Ca-rich precursors such as GGBS, because at very high OH^- concentrations, although silica and alumina increase solubility, calcium becomes less soluble (Pacheco-Torgal *et al.*, 2014). Conversely, a high pH may be suitable for low calcium, alkali-activated systems. Therefore, high-calcium slags (Ca=35-45%) are usually activated under moderated alkaline conditions (Fernandez *et al.,* 1999; Bakharev *et al.,* 2000; Shi *et al.,* 2003). Furthermore, high concentrations of hydroxide activator in GGBS have been reported to encourage efflorescence and increase the cost (Fernández *et al.*, 2014; Pacheco-Torgal *et al.*, 2014) *et al.*, 2014; Pacheco-Torgal *et al.*, 2014). It is considered in the literature that slags can be successfully activated with a combination of alkali hydroxide and silicate. The fluidity of the hydroxide activator maintains suitable rheology, while the silicate provides Si ions for the generation of cementing hydrates that contribute to strength (Pacheco-Torgal *et al.*, 2014).

Mohamed, 2019 states that the compressive strength of alkali-activated slag increases with increasing concentration of the alkaline activator solution. However, other authors have demonstrated that increasing alkaline concentration led to an inefficient reaction due to an excessive quantity of OH^- ions (Görhan and Kürklü, 2014). Nasr et al., (2018) demonstrated that the optimal ratio of Na_2O to the weight of GGBS was 8% to enhance compressive strength, whereas the compressive strength decreased with the increasing percentage of Na_2O to 10% and 12%. Gebregziabiher et al. (2015) observed that activating GGBS with 8 M NaOH exhibited strong hydrates forming around GGBS grains immediately after activation and showed high strength at 28 days.

In contrast, in high aluminosilicate and low-Ca materials such as FA, increased molarity of NaOH is necessary to start reactions (Palomo *et al.,* 1999; Puertas *et al.,* 2000; Provis *et al.,* 2009). Patankar and Jamkar (2017) indicate that the increase in concentrations of NaOH plays a significant role in increasing the mechanical strength of geopolymers. Wang *et al.* (2005) studied the synthesis and mechanical properties of metakaolinite-based geopolymer with different concentrations of NaOH (4,6,8,10, and 12 M). They reported that the flexural, compressive strength and apparent density increased when raising the concentration of the NaOH solution, due to the enhanced dissolution of metakaolinite and the enhanced production of monomer bonds. Ayeni *et al.* (2021) agree, stating that increasing NaOH concentration in metakaolin-based geopolymers increased the dissolution of Si and Al, improving

geopolymerization and producing a homogeneous dense gel that produced a dense microstructure enhancing strength.

Azzahran *et al.* (2018) also agree. They studied the effects of NaOH concentration (4M to 14M) on the bulk density, water absorption and compressive strength of FA geopolymers. The results show that the NaOH concentration significantly affects the geopolymerization process and the strength of the resulting geopolymer. The bulk density did not change significantly with increasing NaOH concentrations up to 12 M. However, the water absorption and porosity values decreased, and the highest NaOH concentration resulted in a denser microstructure. In addition, increasing NaOH concentration up to 12 M accelerated the dissolution of silicon and aluminum, increasing compressive strength to 56 MPa. The compressive strength results were consistent with bulk density, porosity and water absorption values. Huseien *et al.* (2016) studied the influence of NaOH molarity (2 M to 16 M) on water absorption in multi blend AAMs made with GGBS, FA, waste ceramic and waste glass. The growth in molarity contributed to decreasing the water content and enhancing the microstructure. The growth in molarity from 2M to 16M led to an enhancement of density and a reduction in the void content. It lowered water content and enhanced the microstructure. Most specimens cured at ambient temperature demonstrated lower water absorption than those cured in oven conditions.

2.5.2 Effect of sodium silicate to sodium hydroxide ratio (Na$_2$SiO$_3$/ NaOH)

Most studies agree that the presence of an alkali silicate in an alkali reactant solution is essential and leads to an improved microstructure and superior strength (Liew *et al.,* 2016). As aforementioned, the fluidity of the hydroxide activator maintains suitable rheology, while the silicate activator provides Si ions for the generation of cementing hydrates that contribute to strength (Pacheco-Torgal *et al.*, 2014). The relative proportions of Na$_2$SiO$_3$/NaOH are essential as NaOH acts as a dissolvent while Na$_2$SiO$_3$ acts as a binder (Liew *et al.*, 2016). Alkali silicates and hydroxides are combined during the reaction process to help dissolve the solid precursor and speed up the reaction rates (Samarakoon *et al.,* 2019). The presence of the alkali silicate in the solution provides a certain amount of soluble SiO$_2$ to form monomers, dimers and larger oligomers containing Si-O-Si bonds (Singh *et al.,* 2005; Wang *et al.,* 2005). In the activation of aluminosilicates by sodium silicate (waterglass - Na$_2$SiO$_3$), the soluble silica affects the growth of a microstructure resembling many glass types.

Previous authors state that the compressive strength of AA slag increases (from 56 to 60 MPa) with increasing the Na_2SiO_3/NaOH ratio from 1.5 to 2.5. For AA slag/FA (75/25) blends, increasing the Na_2SiO_3/NaOH activator 1.5 to 2.5 increased the compressive strength from 56 MPa to 70 MPa. An increase from 45 to 57 MPa is reported AA slag/FA (75/25) blends when increasing the Na_2SiO_3/NaOH activator 1.5 to 2.

Al Bakri *et al.* (2012) conducted a study on the effect of Na_2SiO_3/NaOH ratio (0.5, 1, 1.5, 2, 2.5, and 3) and NaOH concentration (6, 8, 10, 12, 14, and 16M) on the physical properties and compressible strength of FA geopolymers. The study shows that the geopolymer paste with NaOH at 12 M concentration and a Na_2SiO_3/NaOH ratio of 2.5 produces the highest compressive strength of 57 MPa, similar to that obtained in other studies (Abdullah *et al.*, 2011). Al Bakri *et al.* (2012) discovered that the compressive strength decreased at a higher Na_2SiO_3/NaOH ratio of 3, probably due to an excess of sodium causing calcium carbonate production in contact with the CO_2 in the air. Increasing the Na_2SiO_3 content in the activating solution enhanced the compressive strength and lowered porosity and water absorption, which agrees with (Huseien *et al.,* 2016), showing an improvement in the microstructure.

2.5.3 Curing temperature

The curing temperature of AAMs is considered an important parameter, and it is widely investigated. This is no surprise, as heat is a catalyser for most chemical reactions. However, onsite, to maintain a controlled high temperature during curing is not feasible, and increasing curing temperature has a detrimental effect on the environment. Furthermore, curing at high temperatures often improves strength at early ages at the expense of dropping values at a later age, for example in PC materials. Therefore, the AAMs in this research were mainly cured at ambient temperatures. However, several curing temperatures were applied to the AA slag materials in this research. Therefore, a review is presented below.

Several authors have noted that increasing curing temperature of AAMs enhances mechanical properties, and hence some authors promote curing at high temperature to enhance the mechanical properties of the resultant materials. Elevated curing temperatures enhance the rate of dissolution between the aluminosilicate source and the alkaline solution, significantly impacting the AAM's mechanical properties (Heah *et al.*, 2011; Cheng *et al.*, 2015).

Rovnaník (2010) investigated the effect of curing temperature (10-80 °C) on the development of a rigid structure in metakaolin-based geopolymers. The results show that the strength increases with elevated temperature at early ages due to the increased degree of geopolymerization. However, at a later age, the geopolymer developed at lower temperatures showed superior properties. In the low temperature geopolymers, the cements grew slowly leading to lower porosity and higher toughness. This agrees with PC, where high temperature enhances early strength at the expense of lowering the ultimate strength. In addition, the rate of hydration of PC increases with increasing temperature, but the composition of the calcium silicate hydrate (C-S-H) phase formed differs from that formed at ambient temperature and has lower strength. Furthermore, the amount of AFm increases at the expense of AFt, hence curing PC at ambient temperature shows better overall properties (Lawrence and Hewlett, 1988).

Al Bakria *et al.* (2011) observed an improved geopolymerization process and higher compressive strength in aluminosilicate precursors such as FA when curing with elevated temperatures. Heat curing produced fast geopolymerization and achieved significant strength at an early age (Jaarsveld *et al.,* 2002; Zhang *et al.,* 2018). Görhan and Kürklü (2014) agree, noting that FA geopolymers cured under 30 ^{0}C include more unreacted fly ash. They found that curing at ambient temperatures results in low strength development at an early age, while heat curing results in significant early strength improvement.

Curing temperature also influences the strength development of high calcium slags. Significant retardation at 5 °C and acceleration at 40 °C have been reported compared to curing at 20 °C (Brough and Atkinson, 2002). Heat curing typically enhances the early strength of AA slag materials, but the late strength is significantly reduced compared with ambient temperature curing (Bakharev *et al.,* 1999). Bakharev *et al.* (2003) note that curing at 60°C is the most effective method for Na_2SiO_3 activated slags. They also note that when slags are activated with a combination of Na_2SiO_3 and NaOH, curing at 70°C accelerates early strength development, but after 28 days, the strength is 35-45% lower than the strength of the ambient-cured specimens. However, Altan and Erdoğan (2012) observed that AA slags activated with a mixture of Na_2SiO_3 and NaOH, cured at room temperature for a sufficiently long time, will reach the same strength or more than when cured at 80°C.

Zhang *et al.* (2018) investigated the influence of elevated curing temperature on a red mud-(class F) fly ash geopolymer. The results showed that curing at 50 °C and 80 °C accelerated the raw material dissolution when compared to room temperature. This resulted in higher early

mechanical strength. However, the pore volume at 80 °C was higher than in the samples cured at room temperature and 50 °C. This was due to the faster formation of geopolymer gels at the early stage. Zhang *et al.* (2014) successfully synthesized a red mud-fly ash geopolymer at ambient temperature (23°C) and 40–50% relative humidity. The results showed a compressive strength of 11.3-21.3 MPa at 28 days. Furthermore, Le *et al.* (2018) synthesized an alkali-activated binder based on red mud at ambient temperature with a compressive strength of 14.25 MPa at 28 days. Görhan *et al.* (2016) investigated the effect of curing temperature on the porosity and water absorption of FA and metakaolin geopolymers. They state that water evaporated during curing at high temperatures resulting in microcracks or pores.

2.5.4 Effect of the [SiO$_2$]/[Al$_2$O$_3$] molar ratio of AAMs

One of the significant factors in the development of microstructure and engineering properties in AAM binders is the molar ratio of SiO$_2$/Al$_2$O$_3$ (Davidovits, 1991; Yip and Van Deventer, 2003; Khale and Chaudhary, 2007; Duxson *et al.*, 2007; Liu *et al.,* 2009).

The ratio of Si/Al differs due to the diverse chemical compositions of the precursors. However, the contribution of the activator to this ratio is very important, as the activator phase is usually considered more active than the silica phase in the precursor. Increasing the content of Na$_2$SiO$_3$ rises the ratio. In AA slag materials, this leads to increasing strength an improving the microstructure up to a certain threshold. Previous authors state that the compressive strength of AA slag increases (from 56 to 60 MPa) with increasing the Na$_2$SiO$_3$/NaOH ratio from 1.5 to 2.5. The effect and ratio are similar for AA slag/FA (75/25) blends: increasing the Na$_2$SiO$_3$/NaOH activator from 1.5 to 2.5, rises compressive strength from 56 to 70 MPa. An increase from 45 to 57 MPa is reported in AA slag/FA (75/25) blends when increasing the Na$_2$SiO$_3$/NaOH activator 1.5 to 2.

From the literature, it is not possible to determine the most appropriate Si/Al ratio that would render the best properties in the resultant AAMs. The values proposed by different authors vary greatly. In AA slag materials, Mustofa and Pintowantoro, (2017) note that an increase of Si/Al ratio enhances compressive strength and lowers water absorption, and the molar ratio of Si/Al that yields the best properties is 3.5. In aluminosilicate-based AAMs (such as FA and metakaolin), the Si/Al ratio plays a significant role in geopolymerization which affects mechanical properties (Singh, 2018), durability (Pacheco-Torgal *et al.*, 2014) and setting time

(Chindaprasirt *et al.,* 2012). The microstructure and mechanical properties of metakaolin geopolymers were examined by Duxson *et al.* (2005) at molar ratios ranging from 1.15 to 2.15. It was observed that the microstructure was highly porous at Si/Al ratios ≤ 1.40 but highly homogeneous at Si/Al ratios ≥ 1.65. He *et al.* (2016) studied metakaolin geopolymers for Si/Al ratios from 2 to 4. The result shows Si/Al ratios of 4 increased Si-O-Si links which improved mechanical properties with respect to the geopolymer with Si/Al of 2 (with more abundant, weaker Si-O- Al bonds). However, Zhang *et al.* (2014) suggest that to develop geopolymer from aluminosilicate-rich precursors such as FA and RM, the Si/Al molar ratio of 2 is a good starting point, and the author reported the optimum value of Si/Al ratio of 2.3.

For FA geopolymer binders, most authors report that the highest compressive strength is obtained at a SiO_2/Al_2O_3 molar ratio between 3.2 and 3.7 (Chindaprasirt *et al.,* 2012; Silva *et al.,* 2007). Xu and van Deventer (2003) developed a geopolymer binder with albite, FA and kaolinite. Their study found the optimum molar Si/Al ratio to be 2 for a gel phase of higher strength. In AA RM, the molar ratio of SiO_2/Al_2O_3 of 3.3 to 4.5 is considered adequate for geopolymerization (Yip and Van Deventer, 2003; Khale and Chaudhary, 2007; Lahoti *et al.*, 2007; Liu, Yang and Xiao, 2009; Gräfe, Power and Klauber, 2011).

2.6 PROPERTIES OF ALKALI-ACTIVATED MATERIALS

There are no common properties to AAMs because of the varying properties of the precursors as well as the nature of the activators and, sometimes, the curing regime. However, there are some ordinary tendencies that are summarised below. As the Ca content increases, the resultant AAMs usually show a greater strength and a denser microstructure. However, the properties of AAM have been reported to be adversely affected by excessive Ca content (Xing *et al.*, 2019).

With respect to durability, former authors indicate that AA slag materials display a high resistance to aggressive conditions, and they can remain structurally intact, without any expansion or material loss, for longer than PC materials. However, variability in the chemical composition of the slag might have an effect on durability, and AA materials prepared using different slags might have different resistance to aggressive conditions (Bakharev *et al.,* 2002).

Former authors also report that AA slag materials as sulphate resistant. They have better resistance to sulfate attack than PC, which has often been associated with the lower content or

absence of tricalcium aluminate (C$_3$A) in the slag materials (Bakharev *et al.,* 2002; Puertas *et al.*, 2002; Rodríguez *et al.*, 2008). Sulfate attack to PC concrete is often considered the most common cause of concrete degradation (Marchand *et al.,* 2001). AAMs have been reported to be more resistant to the reaction of sulfate ions with hydration products (Bakharev, 2005). The main factor affecting the resistance of PC concrete to sulfate attack is tricalcium aluminate (C$_3$A). Sulfate ions react with C$_3$A in the presence of Ca(OH)$_2$ resulting in decalcification of calcium silicate hydrate (C-S-H) gel due to the formation of ettringite and gypsum which cause severe damage (Fernández *et al.,* 2007).

Puertas *et al.*, (2002) demonstrated that AA slag mortars are highly resistant to sulfate attack, having an outstanding resistance to seawater exposure, in particular waterglass-activated slag mortars. The authors also state that NaOH activated slag mortars were slightly sensitive to sulphate and sea water attack, forming some gypsum and ettringite, which slightly decreased mechanical strengths. Bakharev *et al.* (2002) agree on the high resistance to salt attack (magnesium sulfate and sodium sulfate solutions) of AA slag materials, and the higher sensibility of NaOH activated slag mortars to sulphate attack when compared to the Na$_2$SiO$_3$ activated ones. After 12 months of exposure to sulfate solutions, the strength decrease was 17-23% for AAS concrete vs 25-37% for PC concrete. The main degradation products were ettringite and gypsum in the PC and gypsum in AAS materials. Waterglass-activated slag mortars have been reported to undergo a negligible expansion following exposure to Na$_2$SO$_4$ solution (Puertas *et al.*, 2002). Similarly, Bakharev *et al.* (2002) found that AA slag materials did not expand but were only slightly cracked in sodium sulfate solutions.

Geopolymers with low calcium contain different cementing hydrates than PC systems. However, the mechanism of sulfate attack whereby external cations exchange Ca^{2+} in C-A-S-H gel is similar for AAMs than for PC materials (Karakoc *et al.*, 2016).

Several authors have observed that the interfacial transition zone, a weak area in PC materials, is highly dense and uniform in alkali-activated slag concretes (Shi and Xie, 1998; Provis *et al.*, 2007; San Nicolas *et al.*, 2014). Nicolas *et al.* (2014) illustrated two mechanisms in AA slag materials that develop a compact and homogeneous matrix at advanced ages: the reaction of slag particles through an Ostwald supersaturation nucleation-depletion cycle and the precipitation of Ca (OH)$_2$ from the pore solution in microcracks, closing cracks, hence avoiding the ingress of aggressive agents to ensure durability.

The literature tends to agree on that geopolymer mortars remain structurally sound for longer than PC materials under frost and wet-dry cycling. Several authors have determined a superior resistance for AA slag materials subject to wet-dry cycling (Luga, 2015; Yankwa Djobo *et al.*, 2016) and freeze-thaw cycling (Fu *et al.,* 2011). Fu *et al.* (2011) evidenced weight loss under 1%, a frost resistance coefficient of ∼90% after 300 cycles. In the literature, it is also relatively common to find instances of strength increase following durability cycling (Provis and van Deventer, 2014; Azarsa and Gupta, 2020).

With respect to porosity, Razak *et al.* (2020) note that the porosity of a FA geopolymers is lower than their equivalent PC materials (1.17% vs 2.36% for the PC material). In AA slag mortars, the pore structure characteristics depends on the activator type. Na_2SiO_3 usually provides the lowest porosity (5–9%) and the finest pore structure when compared to NaOH. The NaOH often provides higher porosities (13-17%) and a coarser pore structure, similar to equivalent PC materials (porosity = 10-13%) (Shi, 1996).

Setting times vary widely depending on the formulations. Some AA slag materials activated with NaOH and Na_2SiO_3 set significantly faster than standard equivalent PC mixes (Atiş *et al.* 2009). The initial setting time for a PC is usually equal to or over 45 minutes and the final setting time is no longer than 12 hours (Barnes and Bensted, 2002). In slags, the setting time depends on the slag basicity (CaO+ MgO / SiO_2). Higher basicity results in shorter setting times regardless of the activator (Krivenko, 1994). The more basic the slag, the greater its hydraulic activity in the presence of alkali activators (Lawrence and Hewlett, 1988). Hence, the highest CaO contents in GGBS lead to shorter setting times (Shi and Qian, 2000).

In general, AAMs of high-Ca content such as GGBS, set faster than those made with precursors of low CaO (Lee *et al.,* 2016; Huseien *et al.*, 2018). Results show that the final setting time of AA GGBS (40-60 min) is faster than AA FA (200-330 min) when activated with NaOH (8M, 12M, 16M) / Na_2SiO_3 = 2.5 (Mallikarjuna et al, 2015). Some AA slag pastes can begin to set as early as after 15 minutes of reaction (Wang *et al.*, 1995).

For AA slags Andersson and Gram, (1987) report 2h 20min and 4h 45min setting times (initial and final respectively) when activated with Na_2SiO_3 (3h 40min and 4h 40 min, when activated with NaOH). In contrast, a much longer set is expected for low Ca systems such as AA metakaolin, with 923 minutes and 1200 minutes (initial and final set respectively) when cured at ambient temperate and activated with Na_2SiO_3 and 8 M NaOH (Liew *et al.*, 2013). Similarly, Chowdhury *et al.* (2021) state that FA-based geopolymers take over 24 hours to set due to the

slower reaction rate at ambient temperature. However, increasing GGBS content in geopolymer pastes significantly improves the initial and final setting times from 290 min at 10% GGBS to 94 min and 41 min after increasing the slag content to 20% and 30%. The properties of metakaolin-based geopolymer are often improved by adding GGBS because AAS has a positive fast setting time, early strength, and corrosion resistance (Sakulich *et al.*, 2009; Ye *et al.*, 2017). In addition, it has been shown that blending GGBS with metakaolin increases the amount of Si and Ca in the geopolymer system, which is conducive to the formation of two hydrates interwoven (N-A-S-H and C-A-S-H gels), thereby improving the strength of metakaolin-based geopolymers (Buchwald *et al.,* 2009).

3. MATERIALS AND METHODS

3.1 MATERIALS

The silicate materials evaluated as precursors include, fly ash (FA), metallurgical slag (GGBS), Saudi bauxite and Saudi red mud (RM). CEM II, binders and activators were also used in these investigations.

3.1.1 Ground granulated blast furnace slag

The GGBS investigated is widely used as a partial PC replacement in Ireland. It was produced in Ringsend, Co. Dublin, with a raw molten slag imported from Europe. For decades, slags such as ground granulated blast furnace slags (GGBS) have been used heavily, as PC replacement, to reduce the environmental impact of PC production. In Ringsend, manufacturing produces 40 kilos of CO_2 per ton of GGBS, but this is offset by carbon credits (Reddy, 2010). The GGBS is imported in Dublin from blast furnaces located in Belgium and Spain (MRPI, 2013). Ecocem Ireland produces two different products with this slag: Ecocem CEM III/C contains up to 95% GGBS, and Ecocem CEM III/A contains up to 65% GGBS (EPD Ireland).

3.1.2 Fly ash

Fly ash (FA)-class F, from a coal-burning power plant in Moneypoint, Co. Clare, Ireland, was also used as a precursor. Due to their particle size distribution, chemical composition, generally spherical particle shape and low cost, FAs are widely used as supplementary cementitious material in concrete. Former authors have used several FAs for the production of AAMs. Due to their physical properties and composition, FAs are valuable raw materials for binder production, and they have been used as supplementary cementitious materials in PC materials for several decades. FAs have been used as partial clinker replacement in PC production since

the 1930s (Lawrence and Hewlett, 1988; Provis and Van Deventer, 2009; EN 197-1, 2011). In Ireland , the FA is used as a minor additional constituent to CEM II (A/L) (EPD Ireland).

As aforementioned, FA is probably the precursor most widely used to produce AA binders. Results were commercialized in 1997, as a product known as Siloxo, used to produce ready-mix concrete and a range of pre-cast products from both Class-F and Class-C FA (Provis & van Deventer, 2014).

3.1.3 Bauxite

The bauxite was quarried from a deposit located in a remote desert area of central/northern Saudi Arabia, predominantly in the province of Ha'il Figure 3-1. The Ma'aden's exploration area covers approximately 6,000 km^2, centered in the town of Az Zabirah (northwest of Riyadh), with elevations of 535-600 meters above sea level (Al-Dubaisi, 2011; Al-Mutairi, Galmed and Aldamegh, 2015) indicate that the bauxite layers have a similar mineralogy, and that their main textures are microooliths, ooliths and pisoliths which are composed largely of boehmite and often have gibbsitic rims. They also refer to calcite as a significant secondary mineral in the bauxite, found in cavities and cracks as a cementing material.

The Az Zabirah and Al Bai'tha mines are open-pit operations located approximately 20 km apart, North of the city of Qibah, in the Al Qassim and Hail provinces of central Saudi Arabia Fig.3.1. Al-Mutairi *et al.,* (2015) carried out a comprehensive study of the area. According to the authors, the Az Zabirah bauxite is a Cretaceous paleolaterite, and the Mesozoic sediments were deposited on a stable platform without any major tectonic disturbances. However, they were later uplifted, exposed and eroded due to Quaternary activity (Al-Mutairi *et al.,* 2015). The bauxite deposits are discontinuous, uplift associated with the faulting has caused the erosional loss of the bauxite sequence (Al-Mutairi *et al.,* 2015) Figure 3-1. The bauxite is ovelaid by the Upper Cretaceous Wasia Formation and the Aruma Limestone, and the area has a NW-SE strike over a length of approximately 105 km, with succession of dips of approximately 5° towards the NE (Al-Mutairi *et al.,* 2015).

In the Az Zabirah bauxite subject to study, gibbsite, boehmite, and kaolinite are predominant minerals, and the bauxite has low iron and low organic matter contents (Al-Dubaisi, 2011; Al-Mutairi *et al.,* 2015)
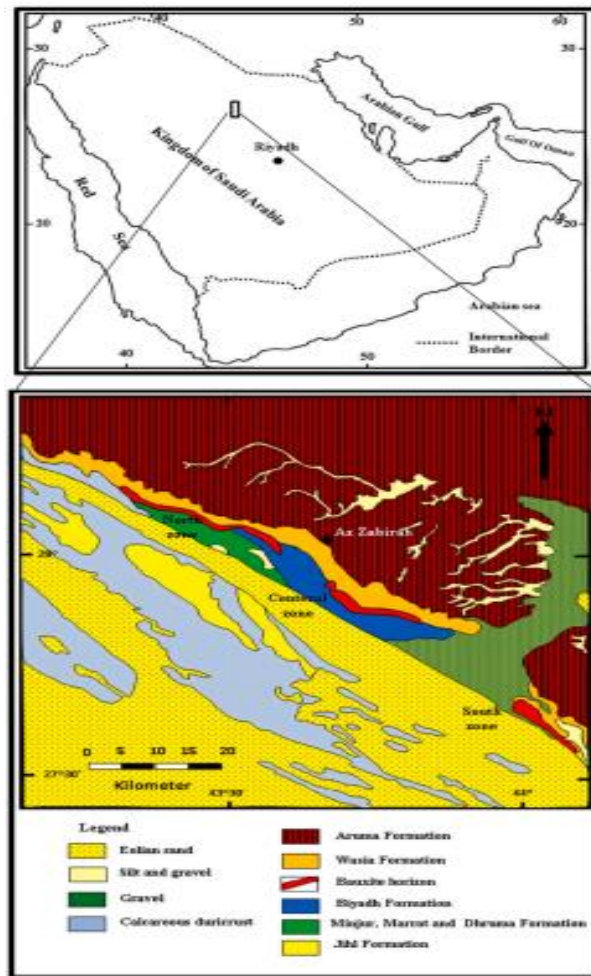
Figure 3-1 Location of the Az Zabirah area and geological map of the Az Zabirah bauxite deposits by (Al-Mutairi *et al.,* 2015).

3.1.4 Red mud (RM)

The RM used in this research was produced, as a by product of aluminium production, by the Ma'aden Mining Industries of the Kingdom of Saudi Arabia which are one of the main world producers. They generate circa 6,000 tonnes of RM per day (over 2 Mtpa) which results in disposal problems and high land decommissioning costs for landfill disposal. This research intends to establish the potential of this RM waste for sustainable binder production.

The composition of the RM residue depends on the conditions of the refining process, such as the addition of lime and the washing efficiency. Lime addition is determined by the type of bauxite ore. The washing efficiency dictates the amount of soluble soda remaining in the RM and hence its alkalinity. In Ma'adem, temperatures between 260 and 270 °C are used, and quick lime -CaO - is added twice during the process. The lime transforms the iron compounds from

goethite (which interferes with the separation of Al) into hematite, and helps transform the unstable Al oxides in solution, in the high-temperature digestion units, into stable phases. Lime is also added in the clarification stage, to separate the solid phase (RM) from the liquid phase (Sglavo *et al.*, 2000). RM residues worldwide are pozzolanic but the pozzolanic activity of the Saudi RM has not yet been studied.

3.1.5 Lime

A hydrated lime - $Ca(OH)_2$ - or calcium lime of European designation CL90s complying with EN 459-1: 2015 manufactured by Clogrennane Lime, with a pH 12.4, specific gravity 2.24 g/cm^3, and bulk density ranging from 200 to 800 kg/m^3.

3.1.6 Portland Cement

CEM II/AL 32,5 N, complying with EN 196-1, produced by Irish cement, was used to produce control mixes to which the properties of the alkali-activated materials were compared. The cement´s particle size ranges from 5 to 30 µm. It has a pH range of 11-13.5, and its chemical composition is shown in Table 3-1.

Table 3-1 Chemical composition by XRF (wt%) of the CEM II (Appendix C).

SiO_2	Al_2O_3	Fe_2O_3	CaO	SO_3	Na_2O	LOI
17.30	4.68	2.89	62.10	2.47	0.59	6.50

3.1.7 Sand

Limestone sand from a Roadstone's quarry in Belgard and standard CEN sand were used. The particle size distribution was determined according EN 933-2:2020 and it is included in Fig. 3.2. The standard CEN sand was used to produce control specimens.
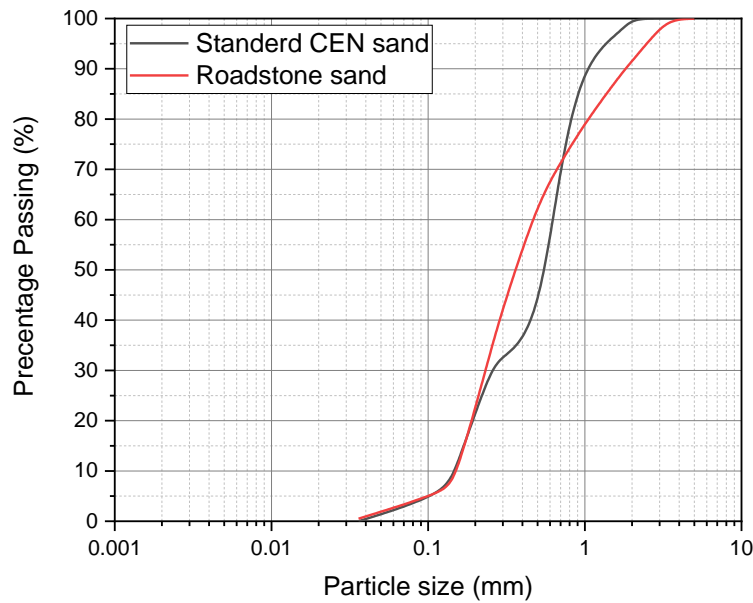
Figure 3-2 Sand particle size distribution.

3.1.8 Activators, precursor processing, mixing, and curing

The precursors (GGBS, FA, RM and bauxite) were activated with sodium hydroxide (NaOH) or/and sodium silicate (Na_2SiO_3). The sand to precursor ratio is constant for all the materials at 3: 1.

The precursors were dry mixed for 3 min, and the activator solution was added and mixed for a further 5 minutes. The sand was then added and mixed for 6 min. The mortars were cast into prismatic molds of 160 * 40 * 40 mm, vibrated for 1 min, and sealed with plastic sheets to prevent moisture loss during curing. The specimens were demolded after 72 hours. Some were cured in ambient conditions, in isothermal chambers at (20 ± 2 °C) for 28 and 90 days. Some AA GGBS materials and AA bauxite were cured in an oven of 40°C to 60 °C for 24 h.

The CEM II A/L -based control materials were fabricated according to EN 196-1. The standard mix in EN 196-1 made with CEM II A/L was used to compare the results.

Both activators (NaOH, Na_2SiO_3) were mixed in liquid form. The sodium hydroxide activator (NaOH) was used in pellet form with 98% purity. It was mixed with distilled water to attain different molarities to suit the different AAMs: a 6 M solution was used for the red mud materials, 8 M solutions for the GGBS, and 8-12M solutions for the bauxite materials. A

commercial solution of sodium silicate activator (Na_2SiO_3) in liquid form was used, with a viscosity ranging from 800 to 1400 cps: PH 11-14, the chemical composition of 15.5% Na_2O, 33% SiO_2, and 47.5% of H_2O and a silicate modulus (MS = SiO_2/Na_2O) of 2.21.

The silicate waste precursors were selected so that they required minimum processing and preparation. The bauxite required grinding to enhance fineness and specific surface area. It was oven-dried at 105 °C for 24 hours and ground in a digital ball mill at 150 r.p.m with 20 mm Ø stainless steel balls. Finally, it was calcined at 800 °C to enhance reactivity. For the same reason, the RM was oven-dried at 105 °C for 24 hours, ground using a digital ball mill at 150 r.p.m with 20 mm Ø stainless steel balls before being calcined at 400 °C. The GGBS and FA were unprocessed.

3.2 METHODS FOR STUDYING THE PRECURSORS

3.2.1 Particle size distribution

The particle size distribution was measured by laser diffraction, using a Mastersizer 2000, composed of a Mastersizer 2000 unit; a Hydro 2000G wet dispersion and an Autosampler 2000 unit. This method measures the angular distribution and intensity of the light by particles in suspension and utilizes the Mie theory of diffraction in the prediction of laser particle size results. Statistics (D-Values) were applied to understand the particle size distributions whereby the distribution width is defined with three values on the x-axis: the D10, D50 and D90. The D50 (median) is the diameter where half of the population lies below this value. Similarly, 90% of the distribution lies below the D90 diameter, and 10% of the population lies below the D10 diameter.

3.2.2 Specific Surface Area (BET)

Surface chemistry is essential to the alkali activation process. Geopolymerization and, in general, any alkali solution reaction begins on the surface of the alumino-silicate precursor particles, where the chemical reactions that result in the formation of geopolymers and hydrates take place. Therefore, the amount of particle surface available for reaction or specific

surface area of the precursors determines their reactivity. The specific surface area was measured with a Quantachrome Nova 4200e and the Brunauer–Emmett–Teller (BET) method, which records the specific surface area based on the physical adsorption of gas molecules by the precursors. The BET theory correlates the physical adsorption of gas molecules on a solid surface with the specific surface area of the particles.

3.2.3 Chemical and mineral composition and amorphousness

Composition and amorphousness (amount of vitreous material) are essential as they control reactivity. The chemical composition was determined by XRF analysis, with an Epsilon 4 Energy Dispersive X-ray Fluorescence (EDXRF) spectrometer. The results were reported as percentage weight by oxides. The mineral composition was determined by X-Ray Diffraction (XRD) using an apparatus including a PW1050/80 goniometer and a PW3313/20 Cu k-alpha anode tube. Measurements were taken from 3 to 60 degrees (2θ), and the detection limit is approximately 5%. An indication of the amorphousness of the precursors was provided by assessing the lifting of the difractogram at c.20 degrees (2θ) which correlates with the vitreous character of the minerals (Bish and Post, 2018).

3.2.4 Loss on Ignition

The loss on ignition (LOI) was measured at 450 and 1000 °C to determine the thermal decomposition of organic matter and the carbonate content. The percentage LOI was calculated from the differences in weight based on EN 1377-3:1990.

3.2.5 Thermal analyses

The Thermal Gravimetric Analysis (TGA) and the Differential Scanning Calorimetry (DSC) of the bauxite, RM, FA and GGBS were carried out using refractory alumininum crucibles, calcined at temperatures ranging from 0 to 1000 °C, in a fibre-chamber, 10 L furnace reaching up to 1300 °C. The DSC analyses indicate thermal events (crystallization, dehydroxilation,

combustion), as exothermic or endothermic peaks, while TGA shows the weight loss, or change in mass due to dehydration, decarbonation or oxidation, over a temperature range.

3.2.6 Devitrification

The phase composition of the most vitreous precursors (GGBS and FA) was studied by investigating the phase transformation during calcination in a kiln at 500°C, 800°C and 1000°C. Following calcination, the ashes and slag were cooled in a desiccator, and their mineralogical composition and glass content were studied with XRD.

3.2.7 Evaluation of reactivity with mechanical methods: strength and mechanical index

Reactivity indicates how quickly a pozzolanic material would combine lime (calcium hydroxide) to form cementing hydrates that provoke setting and eventually hardening. The reactivity measured with these methods closely relates to the speed of dissolution of the material in an alkali media. Therefore, informing on the ability of the material to produce cementing hydrates and hence the speed of setting and hardening. Measuring reactivity is complex and dependent on the methodology. In this research, reactivity is determined with chemical and physical methods. These include setting times, the Chapelle method, and strength development of standard mortars and pastes. The mechanical index (which measures reactivity by monitoring the compressive strength development of lime: RM mixes in relation to a standard lime mix) was also calculated and compared with other pozzolanic materials.

The compressive strength (mechanical activity index) is not only dependant on the amount of hydrates formed but also on their type and microstructure. Mechanical tests were carried out to compare the strength of standardized prismatic specimens of dimensions 160 x 40 x 40 mm. The specimens were demoulded after three days and cured under damp hessian to maintain humidity, in a curing chamber at ambient temperature and 60±5% relative humidity. The flexural and compressive strengths were assessed following EN 196-1:2016. The results are the arithmetic mean of six specimens for compressive strength and three for flexural strength.

The mechanical index (MI) evaluates reactivity by measuring the compressive strength of the lime: (bauxite or RM) mixes in relation to a standard lime mix after 28 days of curing. The MI

is adapted from EN 450-1-Fly ash (FA) for concrete EN 450-1:2012. The prisms were produced with a ratio by mass of 1:1:3 (lime: bauxite or RM: sand) with w/b = 0.90±0.20. The 1:1 (lime: bauxite or RM) content was chosen to be able to compare the results with former literature on pozzolan reactivity (Figueiredo & Pavía, 2020).

3.2.8 Evaluation of pozzolanic activity with chemical methods: conductivity variation

This method indirectly evaluates reactivity as it measures the pozzolanic reaction of the raw and pyro-processed precursors (Bauxite, RM, FA and GGBS) by monitoring the changes in the conductivity of a saturated lime / precursor solution.

It follows the method by Luxan *et al.,* 1989; Borrachero *et al.,* 2001. The fixation of dissolved Ca (OH)$_2$ reduces portlandite concentration in solution, leading to a decrease in conductivity. The conductivity variation of the lime - precursor suspension was measured over time to examine the ability of precursors to combine lime, and therefore their reactivity.

The conductivity loss (%) was calculated according to the following equation:

$$C(\%) = \frac{C_i - C_t}{C_i} \times 100 \qquad \text{Equation 3-1}$$

Where,

C_i is the electrical conductivity of the lime suspension

C_t is the electrical conductivity at the time intervals

Continuous stirring took place using a magnetic stirrer, and conductivity and temperature were measured over time using an WTW LF 197 conductivity meter with a Tetracon 325 probe. The solutions were kept in sealed flasks to avoid water evaporation and carbonation. The reaction was monitored for over 170 hours. The flasks containing the solutions were kept in a thermostatic bath to maintain a constant temperature of 20 °C. The temperature was maintained constant because very small variations in temperature (as low as 0.3 °C) induce considerable

conductivity variation (Luxan *et al.,* 1989). The conductivity loss over time was plotted, and the conductivity variation was calculated as a percentage.

3.2.9 Direct measurement of pozzolanic activity with the Chappelle test

The pozzolanic activity was directly quantified by measuring the amount of calcium hydroxide (portlandite-$Ca(OH)_2$) fixed by the precursors (pozzolanic index) in accordance with the test methods in Gava and Prude, (2007); NBR 15895:2010. The test results were compared with other pozzolanic and cementitious materials previously studied. Solutions were fabricated with the precursors, and a blank test containing only CaO was also included. Sucrose was added to the solutions and stirred, and the resultant solution was titrated with 0.1 M hydrochloric (HCl). The portlandite content that was not consumed was determined by sucrose extraction and HCl titration. The HCl volume consumed in titration (V_2) was noted, alongside the volume consumed by the blank test (V_3). The pozzolanic activity index ($I_{Ca\ (OH)2}$) or amount of portlandite (mg) fixed per gram of (bauxite /or RM), was calculated using Equation 3-2:

$$I_{Ca(OH)2} = \frac{28\ (V_3 - V_2)\ Fc}{m_2} \qquad \text{Equation 3-2}$$

Where: m_2 is the mass of (bauxite /or RM) (g),

V_2 is HCl 0.1 M volume consumed by titration (ml),

V_3 is the HCl 0.1 M volume consumed in the blank test,

Fc is a correction factor (Fc = 1.32 - for a HCl concentration of 0.1 M).

3.3 METHODS FOR STUDYING THE AAMs

3.3.1 Workability by Initial Flow: Water Demand of the Precursors

The amount of water required for the precursor to provide suitable workability for handling and placing was measured with the initial flow diameter test using a flow table. The flow diameter was selected according to EN 1015-3:1999, and the water required for each of the

silicate materials to reach this flow is recorded. The water demand of the precursors is essential as it affects drying, setting and hardening and, if too high, it can cause shrinkage fracturing or strength loss by increased porosity.

3.3.2 Setting times

The setting times of AAM pastes were measured with the Vicat test EN 196-3:2016, which determines the stiffening rate of a paste by dropping a needle from a fixed height and measuring its penetration. The initial and final setting times are standard references which provide comparative data.

3.3.3 Flexural strength (FC)

Flexural strength tests were performed using the centre point loading method According to EN 196-1:2016. The prisms (160 x 40 x 40 mm) were mounted on fixed supports with the longitudinal axis perpendicular to them when the load was applied. The flexural strength was determined using the following equation:

$$R_f = \frac{1.5 \times F_f \times l}{b^3} \qquad \text{Equation 3-3}$$

where

$R_f = is\ the\ flexural\ strength, in\ (MPa);$

$F_f = $ is the load applied to the middle of the prism at fracture, in (N);

$l = $ is the distance between the supports, in (mm).

$b = $ is the distance between the supports, in (mm).

3.3.4 Compressive strength (CS)

The compressive strength refers to the maximum, compressive, uniaxial, unconfined load per unit area that the material withstands before failure occurs. The compressive load is applied to the half prisms by loading the sides. EN 196-1 : 2016 was used to test this property. The compressive strength was determined using the following equation:

$$R_c = \frac{Fc}{1600}$$
<div align="right">Equation 3-4</div>

Where

$R_c =$ is the compressive strength, in (MPa);

$Fc =$ is the maximum load at fracture, in (N);

$1600 =$ is the area of the platens $(40 \text{ mm} \times 40 \text{ mm})$, in (mm^2).

3.3.5 Porosity (P)

The open porosity was measured according to RILEM recommendations (RILEM, 1980). The specimens were dried to constant mass (M_1) and kept in a desiccator at low pressure (2667 Pa) for 24 hours. After that, the specimens were saturated with distilled water under vacuum for 24 hours. Finally, the saturated samples were weighed and the hydrostatic mass (M_2) and the weight at atmospheric pressure (M_3) measured. The porosity (%) was determined using the following equation:

$$P = \frac{(M_3 - M_1)}{(M_3 - M_2)} \times 100$$
<div align="right">Equation 3-5</div>

Where;

M_1 the dry mass (g),

M_2 the hydrostatic mass (g),

M_3 the saturated mass (g).

3.3.6 Bulk Density (BD)

The bulk density is defined as the mass of a material divided by its bulk volume. The bulk density was measured using the same procedure as the porosity based on RILEM recommendations. The bulk density (kg/m^3) is calculated using the following equation:

$$BD = \frac{(M_1)}{(M_3 - M_2)} \times 10^3 \qquad \text{Equation 3-6}$$

Where;

M_1 the dry mass (g),

M_2 the hydrostatic mass (g),

M_3 the saturated mass (g).

3.3.7 Water absorption (WA)

According to ASTM C642, the water absorption of a mortar is the ratio of the mass of water it can retain to its dry mass. The water absorption (WA %) was calculated according to the equation below:

$$WA = \frac{(M_3 - M_1)}{(M_1)} \times 100 \qquad \text{Equation 3-7}$$

Where;

M_1 the dry mass (g),

M_3 the saturated mass (g),

3.3.8 Durability

A material must show resilience under salt crystallization, wet-dry cycles and freeze-thaw cycles. The cycles were performed according to RILEM recommendations (RILEM, 1980). These tests aimed to assess the resistance of the materials to weathering agents and quantify the extent of damage caused. To this end, the variation in strength after cycling and macroscopic damage was evaluated, and the performances were compared with a standard CEM II mix. After each cycle, the condition of the specimens was recorded, and the results were reported in terms of weight loss (expressed as a percentage of the initial dry weight) and the number of cycles required to induce any failure (Pavia Santamaria & Bolton, 1997). Therefore, the durability was determined by measuring the strength loss, mass loss and macroscopic damage after cycling.

3.3.8.1 Salt crystallization

The specimens were immersed in a 14% sodium sulphate decahydrate ($Na_2SO_4 \cdot 10H_2O$) solution for 4 h. The density of this solution at $20°C$ is 1055 kg/m^3. They were then removed and left to dry in an oven pre-heated to $105 °C$ for a period of 15 hours and later left to cool to room temperature for 6 hours. Their masses were noted before recommencement of the soaking in the salt solution. Each material was subjected to 15 such cycles. At the end of cycle 15, the flexural and compressive strengths were tested and compared with the values reached by the unweathered material.

3.3.8.2 Hygrothermal expansion (wet-dry cycles)

Hygrothermal expansion can damage materials through differences in the drying shrinkage and coefficient of thermal expansion of binder and aggregates. All specimens went through 20 wet-dry cycles. The specimens were immersed in water at a constant temperature of $20 \pm 0.5 °C$ for a period of 16 hours. They were then placed in an oven pre-heated to $105 °C$ to dry for 6 hours. All specimens were subjected to 15 wet-dry cycles. At the end of cycle 15, the flexural and compressive strength were tested and compared with the values reached by the unweathered material.

3.3.8.3 Freeze-thaw

The freeze-thaw resistance was evaluated with standard cycling. Frost action typically causes cracking and scaling as water absorbed by the materials expands on freezing. The specimens were immersed in water at a constant temperature of 20 ± 0.5 °C for a period of 6 hours. They were then removed from the water and placed in a freezer at a temperature of -20 °C for 15 hours. All specimens were subjected to 15 freeze-thaw cycles. At the end of cycle 15, flexural and compressive strength were tested and compared.

3.3.9 Microstructure by scanning electron microscopy (SEM)

The microstructure of the materials, and the quality of their cementing hydrates, and other phases such as salt minerals which can affect material quality and durability, were assessed with a scanning electron microscope (SEM). The qualitative analyses focussed on the cementing phases, the general structure and porosity and the quality of the interfacial zone. Specimens sized approximately 1 cm^3 were embedded in an epoxy resin and carbon-coated to provide observation surfaces of approximately 1.5 cm^2. SEM micrographs and elemental chemical composition spectrums were acquired, using an SE2 detector. The elemental chemical composition spectrums of specific mineral phases and general areas in the matrix were acquired at 5- 20kV, with an energy dispersive X-ray microanalysis (EDXR) system with an Oxford INCA X Max detector.

3.4 ANALYSIS AND OPTIMIZATION OF ALKALI-ACTIVATED BAUXITE MATERIALS USING DESIGN OF EXPERIMENT (DOE) SOFTWARE

The design of experiment (DOE) is a useful statistical tool to simulate experimental results (Rafidah et al., 2014). It allows us to observe the interaction between the variables and the results. A minimum number of experiments can provide a maximum quantity and quality of information (Narayanan *et al.*, 2007). The results allow to determine the effect of each factor (or design variable) over an output of interest or response (material property) (Alshalif *et al.*, 2021).

The DOE software was applied to the AA bauxite materials to optimize the mixes for superior strength and durability.

To undertake the DOE analysis: first the response that we are interested in analyzing was determined followed by a list of factors that can affect the response, and the levels that we are interested in testing.

The five responses or outputs of interest are flexural strength, compressive strength, porosity, bulk density and water absorption at 28 and 90 days.

According with the experimental results in this research and the literature, 4 main factors (i-iv) affect these properties of AAMs, and three different levels (minimum, centre, maximum) were selected for each factor as follows:

i. NaOH 8 M (minimum level),10 M (centre level) and 12 M (maximum level);
ii. Na_2SiO_3/NaOH ratio = 1 (minimum level), 2 (centre level) and 3 (maximum level);
iii. temperatures at 20 ^{0}C (minimum level), 40 ^{0}C (centre level) and 60 ^{0}C (max. level);
iv. FA% and GGBS% at 0% (minimum level), 25% (centre level) and 50% (max. level).

The Minitab 19 software was used to undertake the DOE analysis. It generates different statistical reports and plots that illustrate the effects of the factors (or variables) on the outputs (or properties). Therefore, it determines the optimum variables that enhance the properties. The Minitab contributes the following statistics:

1- ANOVA (Analysis of Variance) is used to evaluate the fitness of the generated mathematical models of the five responses. The F-value is used to calculate the P-value, which determines whether the factors are statistically significant, and whether the factors are associated with the response. The higher the F-value, the more significant the factors' coefficients (Montgomery, 2017). The P-values refer to the variance. The final subset of variables was selected based on the P-value with a 95 % confidence level (Biglarijoo *et al.,* 2017).

2- The effective coefficient (R^2) was used to assess the model's fit. The adjusted (R^2) is the percentage of the variation in the response that is explained by the model. It is calculated as 1 minus the ratio of the mean square error (MSE) to the mean square total (MS Total) (LLC, 2005).

3- The magnitude and significance of an effect can be determined using a Pareto chart. A reference line on the chart refers to the absolute value of the effects, and any effect that

extends beyond the vertical reference line is treated as statistically significant (Mathews, 2005; Arnold, 2006; Newton, 2014).

4- The probability plot shows the normal distribution of the data when the points are relatively close to the fitted normal distribution line (the solid middle line of the graph and the points are not out of the other two red lines), and the P-value is greater than the significance level of 0.05 (LLC, 2005; Mathews, 2005; Arnold, 2006;Al-Shalif, 2020).

5- The main effects and main interaction plots show the corresponding mean response values at each level of factors (Lesik, 2018).

3.5 SUSTAINABILITY OF THE AAMs

The embodied energy (EE) and the embodied carbon (E_{CO2}) of some of the AAMs designed and produced were calculated to determine their environmental impact, and compared with traditional materials. Only the production stage is included in the calculations. Therefore, the life stages included in the EE and E_{CO2} calculations are the raw materials extraction, manufacturing and related transport, which in a LCA is equivalent to the cradle to gate system boundary. The scenarios for the production stage are usually defined in environmental product declarations (EPD's). However, no EPDs were found for some of the AAMs components. Therefore, some values are taken from the literature and others calculated with data provided by the producers (Table 3-2).

Table 3-2 EE and E_{CO2} of the materials used to fabricate the AAMs found in the literature.

	Embodied Energy (MJ/kg)	Embodied Carbon (kgCO$_2$/kg)	References
PC (CEM II A/L)	4.5	0.799	(ICE, 2014) (Hammond and Jones, 2011)
FA	0.10 0.10	0.010 0.008	(Hepworth and Goulden, 2008) (ICE, 2014) (Hammond and Jones, 2011) (Adesina, 2020)
GGBS	1.60	0.083	(ICE, 2014) (Hammond and Jones, 2011) (Adesina, 2020)
Bauxite	0.05	0.003-0.005	(Alelweet and Pavia, 2022)
NaOH	3.50	0.632	(Thannimalay et al., 2013)
Na$_2$SiO$_3$	4.60	0.430	(Fawer, Concannon and Rieber, 1999) (Davidovits, 2015)
Water	0	0	(Jones, McCarthy and Newlands, 2011) (Mathew et al., 2013) (Adesina, 2020)
sand	0.081	0.0048	(Hammond and Jones, 2011)

The embodied energy was measured, as Mega-Joules (MJ) per unit area (m^2) or per unit weight (kg or ton), according to (Anvekar *et al.*, 2014). The embodied energy and carbon were calculated with equations 3.8 and 3.9 (Adesina, 2020).

$$EE = \sum_{i=1}^{n}(EE_i \times m_i)$$
<div align="right">Equation 3-8</div>

$$E_{CO_2} = \sum_{i=1}^{n}(E_{CO_{2\,i}} \times m_i)$$
<div align="right">Equation 3-9</div>

Where:

EE_i is the embodied energy of each material component (MJ/kg)

$E_{CO_{2i}}$ the embodied Carbon (kgCO$_2$/kg)

m the mass of each component.

As aforementioned, some components were processed (milled or heated). According to (Kim, 2014), ball milling is a grinding method of low environmental impact because it uses no chemical catalysts or any other substances. A ball mill of 200 watts power capacity was used for grinding the RM and bauxite. However, the oven capacity was used of 2000 watts with a max temperature of 220 ^{0}C. The EE of the heating and calcination processes were calculated (Table 3-3) based on Equation (3-10-3-11) (Unklesbay *et al.,* 1988):

$$EE_{oven}\ (MJ) = E \times PF \times 3.6$$
<div align="right">Equation 3-10</div>

Where:

E is the energy monitor readings (kWh),

PF = power factor (0.80 for gas oven and for fan and lights, 1.00 for electric oven),

3.6 = conversion factor (1 kWh = 3.6 MJ).

The E (kWh) value is calculated based on Equation 3-11.

$$E \text{ (kWh)} = \frac{P \times t}{1000}$$ Equation 3-11

Where:

P is the oven power (watts),

t is the time (hours).

The embodied energy of the grinding process $EE_{ball\ mill}$ is calculated based on Equation 3-12 (Petrakis and Komnitsas, 2022):

$$EE_{ball\ mill}(MJ) = \frac{(P \times t)}{1000} \times 3.6$$ Equation 3-12

Where:

P is the power capacity of the ball mill (watts),

t is the time (hours).

Table 3-3 EE of the dry and calcined RM and bauxite.

	T (°C)	Time (h)	*Power (w)	E (kWh)	EE (MJ)
RM dry	105	24	954.55	22.90	82.43
RM sintered	400	3	3636.36	10.91	39.27
Bauxite dry	105	24	954.55	22.90	82.43
Bauxite sintered	800	3	7272.73	21.82	78.54
Bauxite calcination	60	24	545.45	13.08	47.09
Bauxite calcination	40	24	363.64	8.71	31.36
GGBS (G4-G6) calcination	60	24	545.45	13.08	47.09

* $P \text{ (watts)} = oven\ power \times \frac{temperature\ required}{maximum\ temperature\ of\ the\ oven}$, i.e., $P_{\text{RM dry (105 °C)}} = 2000 \times \frac{105}{220} = 954.55\ watts.$

4. CHARACTERIZATION OF PRECURSORS

The chapter studies the physical properties and composition of the precursors. It measures their pozzolanic and hydraulic activity and their potential for use as binders in construction. It also studies the possibility of activation with thermal treatments.

4.1 PARTICLE SIZE, DENSITY AND SPECIFIC SURFACE AREA

It is well known and widely accepted that, in general, chemical reactivity increases at small particle sizes and high surface areas. Similarly, the alkaline activation of a precursor is usually enhanced at small particle sizes and high surface areas (Provis *et al.,* 2014; Li and Wu 2005). The particle density has been related to the strength and porosity of the resultant AAMs. In general, high density, low porosity and a fine-grained microstructure contribute to enhancing strength (Steveson and Sagoe-Crentsil, 2005).

According to the particle size parameters measured (Figure 4-1 and Table 4-1), the RM and GGBS are the finest with medians of c.3.80, and 11.67 microns respectively (the size of half of the particles is below these diameters). The RM is the finest (10% are under 0.40 microns) while the bauxite is the coarsest. However, the bauxite contains a much wider range of particle sizes than the GGBS whose particles are more consistent in size (90% under 31 microns).

The bauxite has the highest specific surface area followed by the RM. The RM particles are the densest closely followed by the bauxite at 2.43 mg/m^3. The GGBS particles are the lightest (1.80).

The bauxite's surface area is much greater than any of the other precursors due to the presence of abundant minerals with layered structures. The high specific surface area should enhance the rate and intensity of the alkali activation reaction.

The raw, unmilled bauxite, despite being coarser that typical pozzolanic and cementing materials (90% of the particles are smaller than 464 µm and only 10% are under 1.22 µm), it has the greatest specific surface area, superior to commercial PC (CEM II) and other pozzolanic

and cementing materials such as FA and GGBS. The high SSA of the bauxite is due to the layered atomic structures of its main components (gibbsite, kaolinite and boehmite). The grounded bauxite is much finer, as 90% of its particles are under 116 μm, 50% under 21.6 μm and 10% under 0.96 μm.
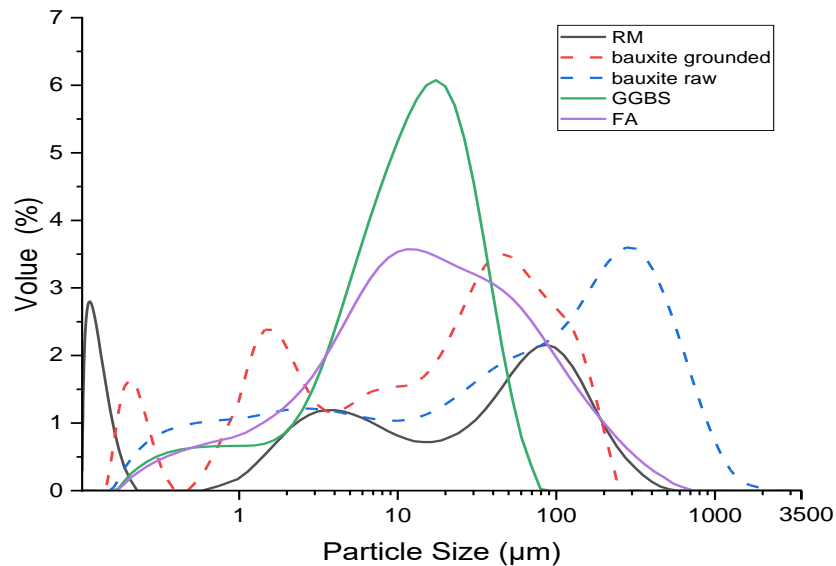
Figure 4-1 Particle size distribution of the silicate precursors by laser grading.

Table 4-1 Specific surface are (SSA), particle size and density of the precursors compared with CEM II A-L 32,5N (6-12% limestone and 5% minor addition).

	(SSA) m²/g	(SSA) m²/kg	particle density mg/m³	particle size				rating	
				mean μm	D90 μm	D50 μm	D10 μm	Finest on top	SSA-greatest on top
Bauxite raw	17.92	17920	2.43	0.10 to 3000				RM	bauxite
				300	463.94	74.1	1.22		
Bauxite grounded	32	32000		0.01 to 2080					
				40.9	116	21.6	0.96		
FA	6.50	6500	2.28	0.20 to 650				GGBS	RM
				15	100.63	14.96	1.95		
GGBS	1.95	1950	1.80	0.25 to 75				FA	FA
				18	31.62	11.67	2.35		
RM	9.35	9357	2.94	0.01 to 516				bauxite	GGBS
				33.6	8.42	3.80	0.40		
CEM II	1.88	1880	-	-				-	CEM II

4.2 WORKABILITY AND LOSS OF IGNITION (LOI)

Workability is an essential criterion that must be taken into consideration in the design of AAMs (Heah *et al.*, 2012; Liew *et al.*, 2012, Liew *et al.* 2016). It is well known that the water requirement is influenced by the fine particle fraction and the carbon content which binds water lowering workability and increasing water demand (Hewlett 1988). It is also well known that a high LOI (carbon content) obstructs chemical reactions such as pozzolanic reaction, hydration, and alkali activation, adversely affecting reactivity, and that it can disturb strength development and enhance fracturing, which can in turn accelerate carbonation, chemical attack and the corrosion of steel reinforcement (Hewlett 1988; Chindaprasirt *et al.,* 2008).

As FA and GGBS have been used in blended cements for decades, the influence of carbon in their reactivity has been previously studied. Ha *et al.* (2005) indicate that FA containing 8% unburned carbon can accelerate the corrosion of steel reinforcement. Previous authors have found carbon to adversely affect the compressive strength of AAMs (Lee *et al.*, 2010). The carbon particles absorb the activator solution, thus obtaining a workable mixture requires a volume of activator solution far beyond what is necessary to activate the source material. This can result in unreacted and partially reacted precursor particles, leading to lower compressive strength, which can accelerate carbonation, chemical attack and the corrosion of embedded steel reinforcement (Fernandez-Jimenez and Palomo, 2003; Diaz *et al.,* 2010).

All of the precursors have low carbon contents (0.30-5.04%). The small LOI of the bauxite (Table 4-2) was expected due to the typical lack of organic matter and carbonates of deposits of lateritic bauxite overlying aluminosilicate rocks. The LOI of the Saudi RM is slightly higher, either comparable or lower to others worldwide (Table 4-2). The LOI indicates the presence of carbonates in the RM, due to the lime used (twice) during the aluminium refining (Bayern) process.

As shown in Table 4-2, the GGBS and RM show the worst workability (highest water demand at 36 and 35% respectively, followed by the bauxite (30%). The water demand of the GGBS is likely due to its fineness and the hydraulic nature of some of its components (calcium silicates) binding water molecules as they hydrate. While in the RM, the water demand is enhanced by its carbon content (5% - Table 4-2). It was expected that the bauxite and RM would present a high-water demand due to the nature of their layered minerals. However, despite their water demand, polymers made with precursors of layered minerals such as metakaolin, can exhibit

comparable or superior mechanical properties to PC (Davidovits, 1991).

The FA displays the best workability (lowest water demand at 15%), probably assisted by the spherical shape of its particles. It was expected that the FA would enhance workability due to the characteristic shape of its particles. According to previous authors, FA-based AA materials are of particular interest as they can display superior workability with less water than other precursors such as metakaolin which may result in improved mechanical properties (Keyte, 2009).

The LOI values indicate that the GGBS contains neither organic matter nor carbonates. According to EN 15167-1: 2006, the maximum carbon allowed for GGBS is ≤ 3 %. Therefore, the GGBS meets the standards - the carbon content is 0.41%. The negative value at 1000 ^{0}C indicates that the GGBS absorbed some moisture during testing. In addition, The slag had a superior low carbon content because it was formed on top of molten steel at high temperatures (1500–1600 °C), which led to the evaporation of most of its moisture and impurities (organic compounds, sulphate, and carbonate) (Ter *et al.*, 2016).

According to the LOI results, the residue of unburnt carbon of FA is 1.67% (Table 4-2) which conforms with the category of European standard EN450-1 and AST C618.

Table 4-2 Water demand to reach a given initial flow diameter and LOI.

	water (%)	Flow diameter (mm) (EN 1015-3)	LOI (%)	
			450 ºC	1000 ºC
RM	35	170	5.04	11.51
Bauxite	30	170	0.30	1.10
FA	15	170	1.67	4.92
GGBS	36	170	0.41	-0.77
CEM II	24	173	-	-

Table 4-3 LOI of the Saudi RM compared with others previously studied.

Country	Reference	LOI (%)
Belgium	(Singh, Aswath and Ranganath, 2018)	10.20
France	(Toniolo, 2019)	10.77
Canada	(Hairi *et al.*, 2015)	10.51
China	(Gong and Yang, 2000)	17.42
Minas Gerais	(Manfroi *et al.,* 2014)	13.00
China	(Liu *et al.*, 2011a)	20.07
Korea	(Choo *et al.*, 2016)	9.10
China	(Ye *et al.,* 2017)	13.74

The LOI for the Irish FA is to either be comparable or lower than others previously studied and satisfies the requirements of ASTM C618:2014 (Table 4-4). However, the FA obtained from different coal-fired power plants often has very different LOI values, which could be attributed to the source of coal and the combustion processes used in power plant boilers to burn pulverized coal (Hurt and Gibbins, 1995; Pedersen *et al.,* 2010).

Table 4-4 LOI of FA from different coal-fired power plants

Country	Reference	LOI (%)
USA	ASTM C618	< 6
Vietnam	(Ngo *et al.*, 2018)	15.8
Taiwan	(Chen *et al.*, 2019)	5-8
North American	(Velandia *et al.*, 2016)	12
Slovakia	(Sisol, Drabová and Mosej, 2014)	10
Japanese	(Sagawa *et al.*, 2015)	9
Taiwan	(Huang *et al.*, 2013)	5-8

4.3 COMPOSITION AND REACTIVITY OF THE GGBS

4.3.1 Chemical composition

The amorphousness and the basicity of the slags impact reactivity. The basicity of the slag in this study is slightly greater than in other slags previously reported (Table 4-7). The chemical composition (Table 4-5) evidence that the GGBS has a basicity (CaO+ MgO / SiO_2) of 1.56, hence it is basic (>1).

The more basic the slag the greater its hydraulic activity in the presence of alkali activators (Moranville-Regourd, 1998). In general, glassy slags with CaO/SiO_2 ratios between 0.50 and 2.0, and Al_2O_3/SiO_2 ratios between 0.1 and 0.6 are considered suitable for alkali-activation (Provis *et al.,* 2014). The ratios in the slag investigated are 1.41 and 0.34 respectively, therefore suitable for alkali activation. In addition, the slag complies with the standard chemical requirements for the use of slags in concretes mortars and grouts EN 15167-1:2006 (Table 4-6).

Table 4-5 Chemical composition as a percentage by weight. [a] same GGBS analysed by (Walker and Pavía, 2010).

	SiO_2	Al_2O_3	CaO	Fe_2O_3	Na_2O	K_2O	MgO	P_2O_5	SO_3	Cl	TiO_2	MnO	LOI %	
													450 ºC	1000 ºC
GGBS	31.71	10.83	44.9	0.51	0.03	0.71	7.50	0.42	2.08	0.03	0.95	0.17	0.41	-0.77
GGBS[a]	34.14	13.85	39.27	0.41	0	0.26	8.63	-	2.43	-	0.54	0.25	-	-
Mean	32	12	42	0.45	0.03	0.5	8	0.42	2.2	0.03	0.75	0.20	-	-

Table 4-6 Compliance of the GGBS with chemical standard requirements.

	$SO_3 - S^{2-}$ (%)	MgO (%)	Cl^- (%)	LOI (%)	Fineness (m^2/kg)
EN 15167-1: GGBS requirements for use in concretes, mortars and grouts	≤ 2-2.5	≤ 18	≤ 0.10	≤ 3	≥275
GGBS	2.2	8	0.03	0.41	1950

Table 4-7 Chemical composition of the slag investigated compared with others in the literature.

	(Collins and Sanjayan, 2001, 2001)	(Puertas et al., 2002; Pavía and Condren, 2008)	(Altan and Erdoğan, 2012)	(Bakharev et al., 1999; Bakharev et al., 2002)	(San Nicolas et al., 2014)	(Qureshi and Ghosh, 2014)	slag investigated, Ringsend IRELAND
SiO_2	35.04	35.5	39.9	35.04	33.7	32.5	32
Al_2O_3	13.91	12.15	11.13	13.91	12.8	18.5	12
CaO	39.43	41.45	34.56	39.43	45.4	33.5	42
MgO	6.13	8.34	9.37	6.13	1.00	8	8
Fe_2O_3	0.29	1.01	0.26	0.29	1.00	0.4	0.45
Na_2O	0.34	0.58	0.35	0.34	0.10	0.7	0.03
K_2O	0.39	0.64	1.18	0.39	-	0.4	0.50
P_2O_5	<0.10	-	-	<0.10	-	-	0.42
SO_3	-	2.47	0.09	-	-	0.50	2.20
TiO_2	0.42	-	-	0.42	0.50	1.01	0.75
MnO	0.43	-	-	0.43	-	0.55	0.20

4.3.2 Mineral composition and amorphousness

The mineralogy of the precursor, mainly its amorphous or vitreous phase content determines the formation of alkaline cements which, in slags, are mainly C-A-S-H gels that define the mechanical strength and durability of the resultant materials. The X-Ray diffraction pattern

(Figure 4-2) shows that the GGBS is largely amorphous with no crystalline phases evident. Therefore, the silica and alumina in the slag are reactive.
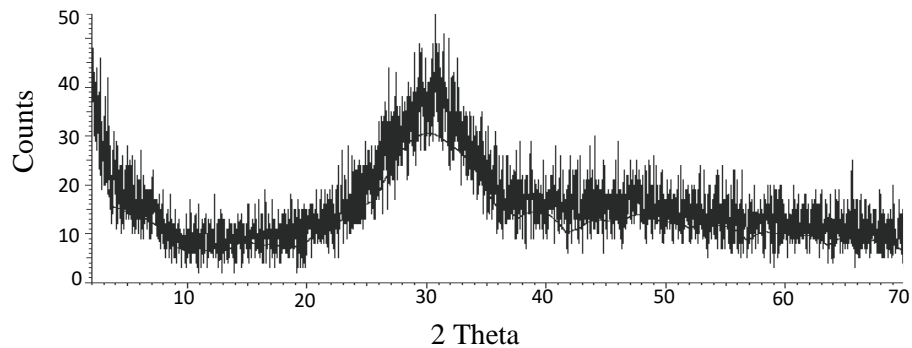
Figure 4-2 XRD trace of the slag with no crystalline phases and a marked halo which indicates that the slag is highly amorphous.

4.3.3 Devitrification

The thermal treatment caused phase transformation. According to the results, the transformation of the amorphous phases into crystals begins at c. 500°C. The glassy nature of the unheated slag is evidenced in the extended halo (Figure 4-2). At 500°C, the GGBS is still mostly glass, but a small amount of crystalline merwinite $Ca_3Mg (SiO_4)_2$ has begun to form (Figure 4-3). At 800°C (Figure 4-4) there is a significant crystalline fraction: the amount of merwinite has increased and significant gehlenite $Ca_2Al [AlSiO_7]$ has formed. At 1000 °C, the GGBS is crystalline (Figure 4-5). The new crystalline phases are a representation of the amorphous phases and include merwinite $Ca_3Mg (SiO_4)_2$ and gehlenite $Ca_2Al [AlSiO_7]$. Merwinite begins to appear at 500°C and it is abundant at 800°C, however over this temperature, it is no longer stable and transforms into gehlenite and, at 1000°C, it has completely disappeared (Figure 4-5). This mineral composition agrees with the literature (Moranville-Regourd, 1998).
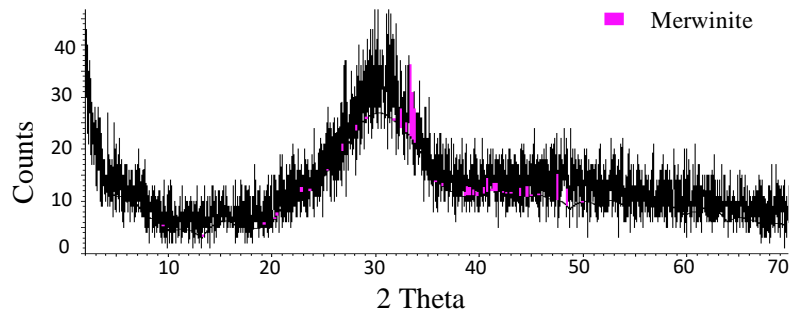
Figure 4-3 XRD trace of the slag at 500°C, the halo indicates that the slag is highly amorphous but a small amount of crystalline merwinite $Ca_3Mg(SiO_4)_2$ has begun to form.
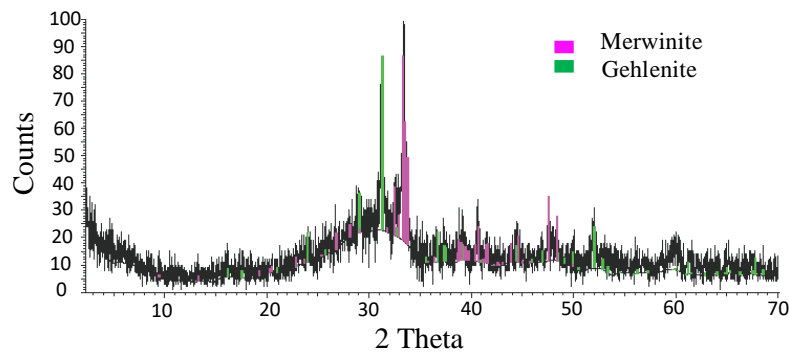
Figure 4-4 XRD trace of the slag at 800°C, the amount of merwinite has increased and gehlenite $Ca_2Al\,[AlSiO_7]$ begins to form.
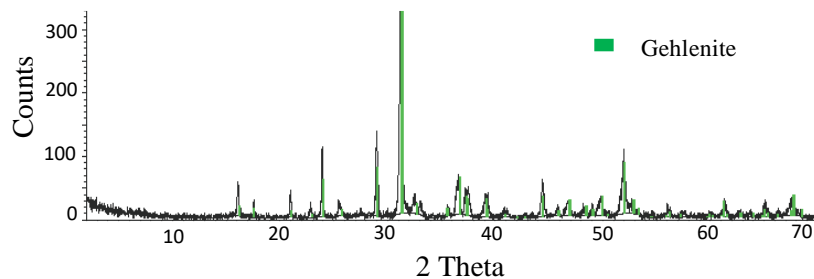
Figure 4-5 At 1000°C, the GGBS is completely devitrified, only gehlenite is stable, and merwinite has transformed into crystalline gehlenite.

The glass content of the GGBS at increasing temperature was calculated, as a percentage, based on the background area determined by the lifting of the difractogram's baseline between 15 and 35 (2Θ) which indicates the presence of amorphous materials (Table 4-8). The relative amounts of the crystalline phases were calculated using the relative intensities of their main reflexions: merwinite: 2Θ=33.38 with d-spacing= 2.68; and gehlenite: 2Θ=31.20 with d-spacing= 2.85 Å.

Table 4-8 Mineral composition and amorphousness of the GGBS. (*) calculated using the intensities of main reflexions: merwinite: $2\Theta=33.38$ / d-spacing= 2.68; gehlenite: $2\Theta=31.20$ / d-spacing= 2.85 Å.

Material	% Glass	% Crystalline	Mineral composition
GGBS 0°C	>90	<7	Glass. No crystals recorded.
GGBS 500°C	80-85	>7	Glass + traces of crystalline phases.
GGBS 800°C	c.11	50*	Merwinite $Ca_3 Mg (Si O_4)_2$
		38*	Gehlenite $Na_{0.05} Ca_{1.96} Mg_{0.24} Fe_{0.12} Al_{1.25} Si_{1.39} O_7$
GGBS 1000°C	<7	>90	Gehlenite $Na_{0.05} Ca_{1.96} Mg_{0.24} Fe_{0.12} Al_{1.25} Si_{1.39} O_7$

4.3.4 Thermal analyses

The DSC (Figure 4-6) indicates thermal events (crystallization, dehydroxilation, combustion), as exothermic or endothermic peaks while TGA shows the weight loss over the temperature range. According to the DSC results, the GGBS releases heat up to approximately 500°C (a progressive exothermic DSC curve can be observed between 0 and c.500°C). The devitrification test demonstrates that, during this heat evolution, only a small amount of crystals appear and no major changes occur in the GGBS which remains amorphous (Figure 4-2 - Figure 4-3 and Table 4-8). After 500°C, the DSC curve becomes endothermic, and the GGBS keeps absorbing heat until it reaches c. 800°C. Endothermic peaks are usually associated with a decomposition reaction. The devitrification test proves that the steady heat absorbed between 500 and 800°C is due to the decomposition of most of the glass to form crystalline merwinite and gehlenite (Figure 4-4 and Table 4-8). There is a direct correspondence between the results of the devitrification test and the DSC events. Therefore, as indicated by the phase evolution on devitrification, the marked exothermic peak at 850°C corresponds to the transformation of merwinite into gehlenite, while the steady endothermic branch that follows (up to 1000°C) corresponds to the decomposition of the remining glass into crystalline gehlenite (Figure 4-5 and Table 4-8). The main events agree with (Moranville-Regourd, 1998) who identified main endothermic peaks at 800°C and 1000°C, and attribute this to the devitrification of the mineral phases in the GGBS. When compared with the heat evolution in other GGBS (Sha and Pereira, 2001), the crystallization

reactions are more progressive and steady, taking place over a longer temperature range rather than suddenly at a specific temperature.
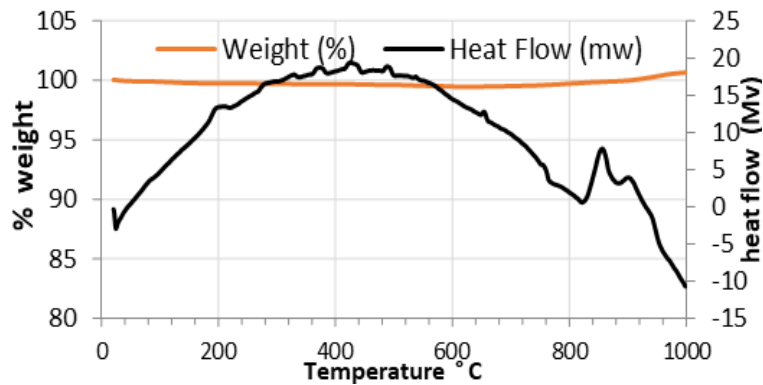
Figure 4-6 TGA / DSC analysis of the GGBS.

The TGA measures changes in mass such as dehydration, decarbonation or oxidation. The mass of the GGBS remains nearly constant up to 1000°C, with a slight mass loss (1%) and a final slight mass increase. This indicates that the GGBS does not include either constitutional water or organic carbon or carbonates, supporting the LOI results (Table 4-5) and the chemical and mineralogical analyses (Table 4-5 and Table 4-8). After reaching 850°C, the GGBS gains a slight mass. The devitrification experiment indicates that this is probably due to the conversion of merwinite $Ca_3Mg (SiO_4)_2$ into denser gehlenite $Ca_2Al [AlSiO_7]$ (Table 4-8).

4.4 COMPOSITION AND REACTIVITY OF THE FA

4.4.1 Chemical composition

As it can be seen from above, the FA is ultrafine, significantly finer than limestone cement (CEM II). The mean particle size is 15 microns, and 90% of the particles are smaller than 100 microns. The high specific surface area of the particles, at 6500 m^2/kg, lies above the typical values reported in the literature, agreeing with the grading range and suggesting that some of

the particles might be porous. Also as seen above, the density of the FA particles is high, at the high end of the common FA densities reported by previous authors which vary between 1900 to 2800 kg/m^3 (Minnick *et al.*, 1971).

As expected, the silica and alumina contents are high (Table 4-10)**.** In contrast, the calcium content is low (c.3%) and $\Sigma\ SiO_2 +\ Al_2O_3 + Fe_2O_3 > 70\%$ by mass (Table 4-11). According to this chemical composition, the FA belongs to Class F in the ASTM C618 standard. Therefore, the FA is pozzolanic, it has very little or no cementitious properties, and its pozzolanic reactivity is mainly determined by the characteristics of the aluminosilicate glass and the fineness of the particles.

The FA composition, especially the iron and carbon contents, cause differences in density (Minnick *et al.*, 1971). Therefore, the significant iron content (Table 4-10) evidenced by XRF, coupled to the low carbon content recorded by calcination (LOI= 1.67%) are partially responsible for the high density of the FA particles. The nature of the cooling process may have also enhanced density, as internal voids in the ash particles are mainly produced during cooling. The FA investigated meets the European standard chemical requirements for the use of FA in concrete, mortar and grout (Table 4-11). According to the LOI results, the residue of unburnt carbon is 1.67% (Table 4-10) which classifies the FA in the category A ash of the European standard EN 196-2: 2013 with unburnt carbon not greater than 5% by mass of ash (Table 4-11).

Table 4-9 Specific surface area and particle size distribution of the FA.

	Specific surface area		Particle density mg/m^3	Particle size range & dominance			
	(m^2/kg)	(m^2/g)		Mean μm	D90 μm	D50 μm	D10 μm
FA	6500	6.50	2.28	0.20 to 650			
				15	100.63	14.96	1.95
CEM II	1880	1.88		-			

Table 4-10 Chemical composition as percentage by weight and LOI. * same FA analysed by (Walker and Pavía, 2011).

	SiO$_2$	Al$_2$O$_3$	CaO	Fe$_2$O$_3$	Na$_2$O	K$_2$O	MgO
FA	53.40	21.18	4.14	9.99	0.70	3.24	1.86
FA*	65.32	24.72	0.94	4.84	-	1.37	0.68
	P$_2$O$_5$	SO$_3$	Cl$^-$	TiO$_2$	MnO	LOI %	
						450°C	1000°C
FA	0.84	2.67	0.04	1.35	0.07	1.67	4.92
FA*	0.37	0.37	-	0.91	-	-	-

Table 4-11 Compliance of the FA with the chemical requirements in the European standard EN 450-1: FA requirements for use in concrete, mortar and grout EN 450-1, 2012. All results as % by mass of ash.

	$SiO_2 + Al_2O_3 + Fe_2O_3$ (% by mass)	SO_3 (%)	MgO (%)	Cl^- (%)	LOI (%)	Total alkalis (%)	Total phosphate (%)
FA requirements in EN 450-1	≥ 70	≤ 3	≤ 4	≤ 0.10	< 5 = Class A-EN196-2	<5.5	<5.5
FA	89	1.4	1.0	0.04	4.92	2.4	0.5

4.4.2 Mineral composition and amorphousness

As aforementioned, the reactivity of FA or any other material with cementitious or pozzolanic properties is largely determined by the amount of reactive silica and alumina in the material. The chemical analysis demonstrated that total silica and alumina in the FA are high (59% and 23% respectively- Table 4-10). However, it is necessary to measure how much of this material is amorphous (or reactive), as crystalline phases are essentially considered inert. To this aim, the mineral composition and glass content of the FA were investigated with XRD.

Previous studies have reported 316 individual minerals and 188 mineral groups as present in FA (Xu and Shi, 2018). Previous authors report that the most abundant phase in FAs is usually glass, while crystalline compounds account for 5-50% and include quartz, mullite, hematite, spinel, magnetite, melilite, gehlenite, kalsilite, calcium sulphate, alkali sulphate (Hemmings and Berry, 1987).

The XRD analysis evidenced that there is significant glass in the FA (Figure 4-7). A broad diffraction halo, which is attributed to the glassy phase, appears on the XRD traces. The glass content of the FA was roughly calculated as 40-60% based on the background area determined by the lifting of the difractogram's baseline between 15 and 35 degrees (2Ө) (Figure 4-7), which indicates the presence of amorphous materials. Small amounts of quartz (SiO_2) and mullite ($2Al_2O_3 . 2SiO_2$) were also determined with XRD, agreeing with Walker and Pavia [16] which, in a previous study, note the same FA as featuring intermediate amorphousness and quartz and mullite peaks. The lack of sulphates and calcium silicates in the Moneypoint FA is due to the composition of the sub-bituminuos coal used in the power station (low in sulphur) and the low calcium content in the coal and the processing method.

The results (Figure 4-7), also concur with former literature reporting quartz and mullite (3–24 wt%) as the two major crystalline phases in low-Ca (CaO< 8%) FA, and a content of crystalline minerals is in the 11–48 wt% range (Velandia *et al.*, 2016; Xu and Shi, 2018).
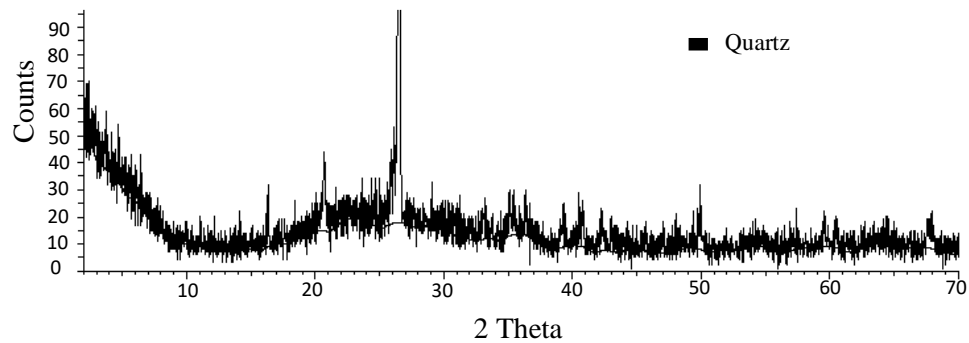
Figure 4-7 XRD trace of the FA with significant amorphous material and some crystalline phases including quartz (SiO_2) and a small amount of mullite ($2Al_2O_3. 2SiO_2$).

4.4.3 Devitrification

To produce power at the Moneypoint station, the sub-bituminous coal is burned at 1000 – 1150°C. At this temperature range, mullite is formed from the clay minerals in the coal: the dehydroxylation of the clay minerals is followed by reconstitution with nucleation and growth of mullite. Clay minerals usually decompose at temperatures from 550-800°C (although in non-carbonate materials they can stand higher temperatures) and mullite begins to form at 1100 °C (Grapes, 2006). The coal firing temperature agrees with the presence of mullite in the ash.

In order to determine the mineral composition of the glass comprising the FA, several specimens were devitrified at 500, 800 and 1000°C. The results appear in Figure 4-8 to Figure 4-10 and Table 4-12. According to these results, at 500°C, most of the glass has become crystalline however, some glass still remains even at 1000°C.
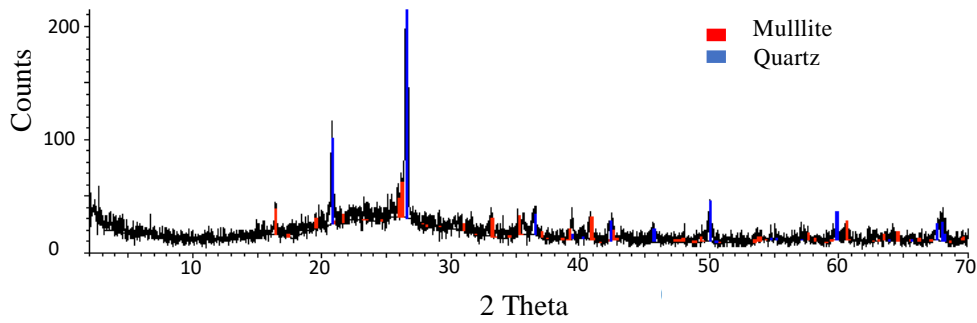
Figure 4-8 XRD trace of the FA at 500°C, there is still a background halo that indicates the presence of some amorphous material. The reflexions for the crystalline quartz and mulllite are clearer and the amount of mullite has increased.
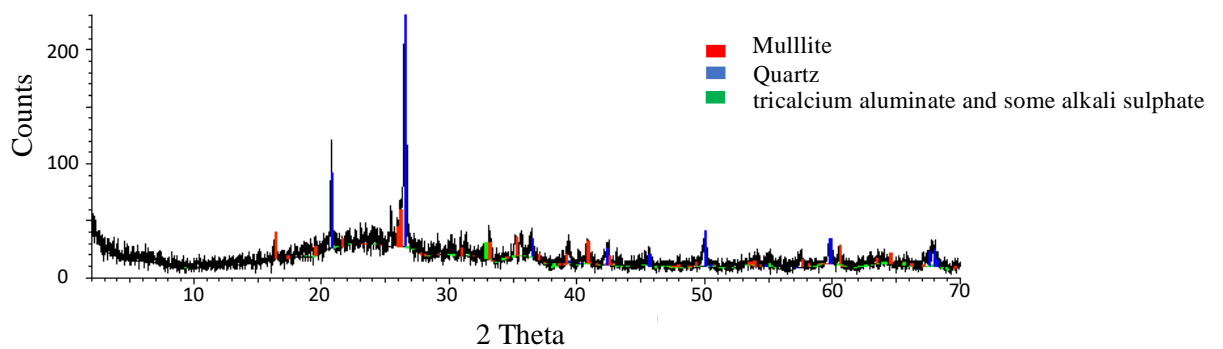
Figure 4-9 XRD trace of the FA at 800°C, no apparent difference exists between the traces of the FA at 500 and 800 degrees.
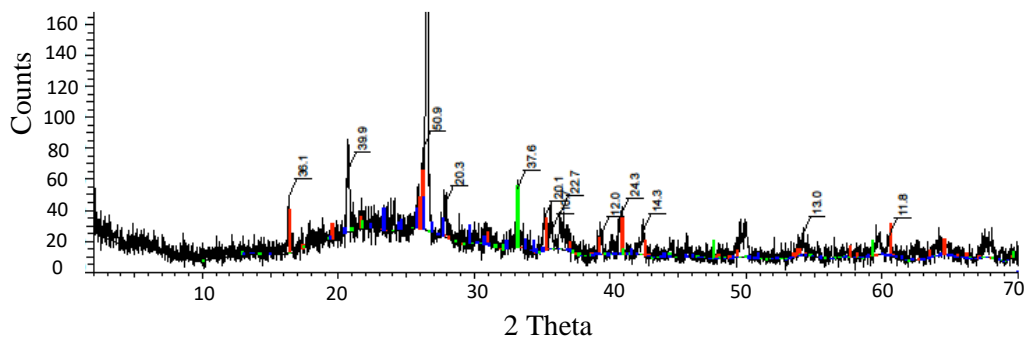
Figure 4-10 At 1000°C, the FA is still slightly amorphous, the amounts of mullite ($2Al_2O_3. 2 SiO_2$) and hematite (Fe_2O_3) are significant. It is likely that a small quantity of tricalcium aluminate ($Ca_3Al_2O_6$) and some alkali sulphate (at d-spacing=3.20) have appeared

The glass content of the FA was loosely calculated as a percentage based on the background area determined by the lifting of the difractogram's baseline between 15 and 35 degrees (2Θ) in Figure 4-7 to Figure 4-10, which indicates the presence of amorphous materials. The results were compared to a reference slag sample that was also devitrified. According to the results,

approximately half of the mass of the FA is amorphous therefore, a significant fraction of the total silica as well as most of the alumina are reactive.

Table 4-12 Mineral composition and amorphousness of the FA.

Material	% Glass	% Crystalline fraction	Mineral composition
FA 0°C	40-60	60-40	1 glass 2 quartz (SiO_2) 3 mullite ($2Al_2O_3$. $2 SiO_2$)
FA500°C	10-30	70-90	4 quartz (SiO_2) 1. mullite ($2Al_2O_3$. $2 SiO_2$) 2. glass
FA 800°C	10-30	70-90	5 quartz (SiO_2) 3. mullite ($2Al_2O_3$. $2 SiO_2$) 1. glass
FA 1000°C	10-30	70-90	6 quartz (SiO_2) 2. mullite ($2Al_2O_3$. $2 SiO_2$) 5. hematite (Fe_2O_3) 6. possible tricalcium aluminate ($Ca_3Al_2O_6$) and alkali sulphate 7. glass

4.4.4 Thermal analyses

The FA was studied with differential scanning calorimetry (DSC) and thermal gravimetric analysis (TGA) (Figure 4-11). The TGA analysis shows the weight loss over a temperature ranging from 0 - 1000°C, while the DSC displays thermal events such as crystallization, dihydroxylation, or combustion either as exothermic or as endothermic peaks. As can be seen form Figure 4-11, the FA progressively loses mass with increasing temperature: the mass of the FA drops suddenly and significantly between 1°C and 90°C, and then remains relatively stable until the temperature reaches approximately 500°C. At this point, there is a slight and gradual drop in mass (between 500 and 750 °C). The first sudden mass loss is likely due to dehydration, while the second gradual loss at c. 500°C is due to the evolution of organic carbon, agreeing with the LOI at 450°C which amounts to 1.67%. The slight steady mass loss at high temperature might be partly caused by the evolution of carbonates as CO_2, agreeing with the 4.92% LOI result at 1000°C.
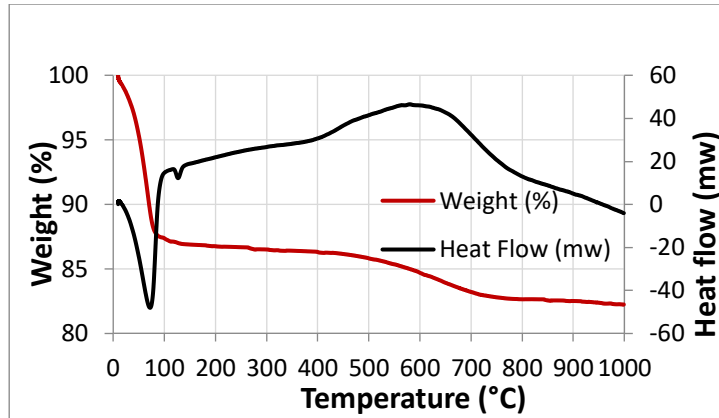
Figure 4-11 Results of the TGA and DSC of the FA.

In the differential scanning calorimetry (DSC) curve (Figure 4-11), the mass loss coincides with a marked endothermic peak just before 100°C, likely due to the ash absorbing heat in order to fully dehydrate.

There is also a broad exothermic area between roughly 100 and 600°C, after which the ash begins to absorb heat again and the DSC curve becomes markedly endothermic indicating the crystallization of the amorphous phase. According to the devitrification experiment above, the steady heat released between 600 and 1000°C is due to the progressive crystallization of mullite ($2Al_2O_3. 2 SiO_2$) and some hematite (Fe_2O_3).

4.4.5 Reactivity by electrical conductivity

The conductivity tests demonstrated that the FA reacts with lime, leading to a gradual decrease in electrical conductivity over time, hence showing reactivity (Figure 4-12). The initial conductivity was 3.07 ms/cm and the conductivity loss 20.19% over the time of the experiment.

The steep slope at stage I (3 to 6 hours), where the conductivity increased, is likely due to a lack of seal in the suspension flask, allowing evaporation and carbonation to take place. Phase II shows a slight drop in conductivity suggesting that, initially (up to approximately 20 hours), the FA combines lime at a slow rate, and hence there is marginal reactivity. However, at stages III and IV, there is an increase on the reaction rate, and the FA combines a greater amount of lime producing steep curves. The results are in agreement, with previous authors who evidenced the typical low speed of the pozzolanic reaction (Massazza, 1998).
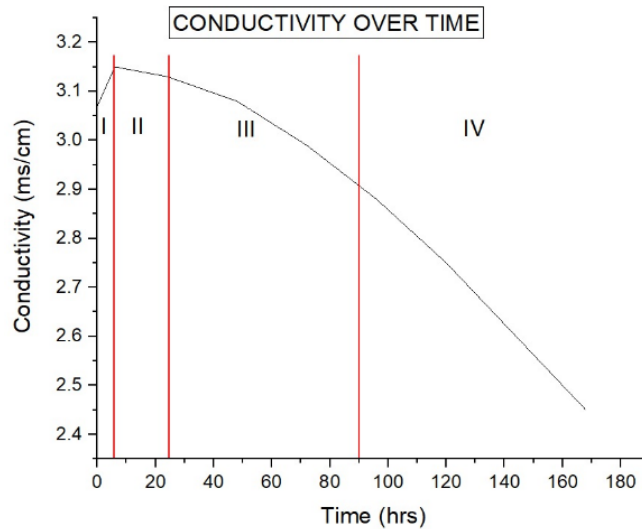
Figure 4-12 Electrical conductivity of the lime/FA suspension over time.

4.4.6 Conclusion

The results of the physical, chemical and mineralogical analyses concur on that the FA is reactive. It is ultrafine, it has a high specific surface area and is partially glassy. Furthermore, a substantial part of the total silica and alumina comprising the FA is amorphous, hence reactive and likely to form cements upon alkali activation. In addition, the reactivity with lime - $Ca(OH)_2$-, a low alkalinity activator is evident, for that reason the reactivity of the FA with any of the stronger alkalis generally used for alkali activation it is likely to be faster and greater.

Also, the FA is clearly pozzolanic, as the silica and alumina contents (> 70% by mass) complying with ASTM C 618 standard class F (ASTM C618 : 2014). The FA also complies with the chemical requirements in the European standards for the use of FA in concretes, mortars and grouts. The low unburnt carbon content is likely to enhance workability even with the most viscous alkali activators.

Combining all the results in this research (physical properties, chemistry and mineralogy/amorphousness), it can be concluded that the FA is suitable for alkali activation. The FA meets the requirements set by (Garcia-Lodeiro *et al.,* 2015) for a FA to be suitable for the production of AA cements (Table 4-13).

Table 4-13 Evaluation of the FA investigated against the requirements for a FA to be deemed suitable for the production of AA cements in (Garcia-Lodeiro *et al.,* 2015).

Properties	FA	Requirements in (Garcia-Lodeiro *et al.,* 2015)
Unburned C	1.7%	<5%
Fe_2O_3	4.8%	≤ 10%
CaO	1-4%	≤ 10%
Vitreous phase content	40-60%	>50%
SiO_2 reactive	Total SiO_2= 65% - includes a significant reactive fraction.	>40%
SiO_2 (reactive)/Al_2O_3 (reactive)	2.56	>1.5
Particle size	50% <15 μm; 90% <100 μm	80-90% <45 μm

4.5 COMPOSITION AND REACTIVITY OF THE BAUXITE

4.5.1 Physical properties of the bauxite

The specific surface area (SSA) measured with BET, laser grading, particle density and loss on ignition are included in Table 4-14. The properties are compared with those of other pozzolanic and cementitious materials such as GGBS, FA and Portland cement (CEM II). As it can be seen from the results (Table 4-14), the bauxite consists of dense particles of extremely high SSA, and the organic matter content is insignificant. As aforementioned, the bauxite was studied both raw and grounded in a digital ball mill with 20mm Ø stainless steel balls, and the grounded bauxite was calcined and tested.

In the case of the raw, unmilled bauxite, despite being coarser that typical pozzolanic and cementing materials (90% of the particles are smaller than 464 micrometers and only 10% are under 1.22 microns), the raw bauxite particles have a high specific surface area, superior to commercial PC (CEM II) and other pozzolanic and cementing materials such as FA (fly ash) and GGBS (ground granulated blast-furnace slag). The high SSA of the bauxite, even raw (unmilled), is due to the layered atomic structures of the bauxite's main components (gibbsite, kaolinite and boehmite). The grounded bauxite is much finer, as 90% of its particles are under 116 μm, 50% under 21.6 μm and 10% under 0.96 μm.

Table 4-14 Specific surface area of the raw and grounded bauxite compared with other pozzolanic and cementitious materials. (*) grounded.

	Specific surface area (SSA) m²/g	Particle density mg/m³	Particle size distribution			LOI %	
			D90 µm	D50 µm	D10 µm	450 °C	1000 °C
Bauxite	17.92	2.43	463.94	74.10	1.22	0.30	1.10
Bauxite (*)	32.00	2.43	116.00	21.60	0.96	0.30	1.10
RM	9.35	2.94	8.42	3.80	0.40	5.04	11.51
GGBS	1.95	1.80	31.62	11.67	2.35	0.41	-0.77
FA	6.50	2.28	100.63	14.96	1.95	1.67	4.92
CEM II	1.88	-	82.58	24.90	2.56	-	-

Heating significantly increases the SSA of the bauxite particles even at low temperature: at 300°C the SSA has increased by over 60%, due to the dihydroxylation of the layered atomic structures of the constituent particles. Thermal treatments of clay mineral structures cause dihydroxylation leading to the complete destruction of the structure with increasing temperature (Bergaya et al 2006). The results indicate that, at a certain point after reaching 800 °C, SSA lowers because the bauxite particles begin to significantly agglomerate.

The specific surface area of the bauxite particles increases with increasing calcination temperature up to 700°C and then lowers (Table 4-15). The bauxite displays the maximum SSA when calcined between 300 and 700°C. However, the SSA is also high at 800°C, showing a similar value. Therefore, the thermal treatment of the bauxite increases the surface available for reaction at least up to 700°C. A similar trend was obtained when sintering the red mud residue of this bauxite (Alelweet *et al.,* 2021). Other authors have also found similar trends in other bauxites. Vieira Coelho et al. (2002) observed the maximum specific surface area for a bauxite calcined between 300 and 400°C.

Table 4-15 Effect of increasing temperature on the specific surface area of the grounded bauxites.

Material	SSA (m²/g)
Bauxite 300 °C	81.81
Bauxite 550 °C	82.26
Bauxite 700 °C	82.53
Bauxite 800 °C	80.00
Bauxite 900 °C	67.00
Bauxite 1000 °C	40.38

4.5.2 Chemical and mineral composition of the bauxite

According to the XRF analyses (Table 4-16), aluminium is the most abundant element in the bauxite followed by silicon. Iron and titanium follow in much lower amounts. The rest of the elements are marginal except for the calcium and sulphur (2%). The variability in the XRF results reflects the extent of the outcrops and the timing of the analyses being wide apart.

Table 4-16 Chemical composition analysed by X-ray fluorescence (XRF) expressed as % wt. (*)- Arithmetic mean of the bauxite samples analysed 1 and the analyses provided by the producer 2. RM-Red Mud residue. ** (Alelweet *et al.,* 2021).

	SiO_2	Al_2O_3	CaO	Fe_2O_3	Na_2O	K_2O	MgO	P_2O_5	SO_3	Cl^-	TiO_2	MnO
Bauxite[1]	26.82	54.30	2.48	6.01	0.008	0.23	0.00	0.59	2.89	0.25	5.62	0.01
Bauxite[2]	14.85	52.53	1.15	4.00	0.19	0.06	0.13	0.13	1.57	-	4.78	<0.01
Bauxite (*)	21.00	53.00	2.00	5.00	0.10	0.10	0.06	0.40	2.00	0.25	5.00	0.01
RM (**)	19.66	29.79	5.09	12.97	24.05	0.09	0.40	0.29	1.65	0.32	5.12	0.02

The mineralogical composition of the bauxite is included in Figure 4-13 and summarised in Table 4-17. The XRD trace indicates high crystallinity, presenting clear and intense reflections for the main phases which include gibbsite, kaolinite and boehmite. The relative intensities of their main reflections suggest that the amount of gibbsite is close to the amount of kaolinite, and that the amount of boehmite is at least 50% lower. According to the XRD results, kaolinite, boehmite and gibbsite are major phases (40-15%) while goethite, gypsum, rutile/anatase and calcite are minor components (15-7%) and there are traces of quartz (<7%).
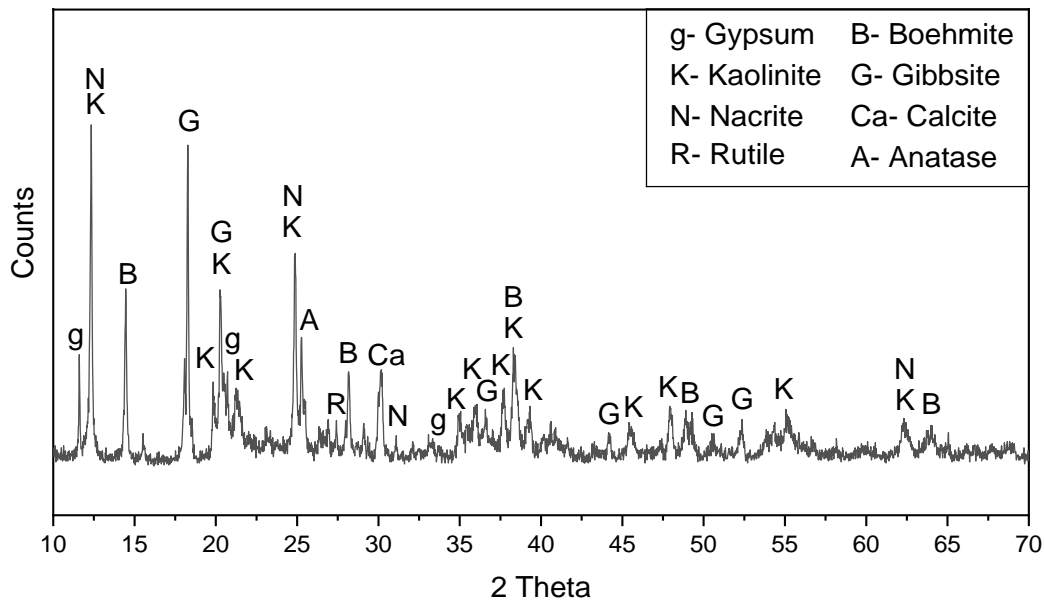
Figure 4-13 XRD trace showing the crystalline phases the raw bauxite including gibbsite, kaolinite and boehmite with minor gypsum, rutile/anatase, nacrite and calcite.

Table 4-17 Mineral composition of the bauxite by XRD.

	Major phases (40-15%)	Subsidiary (15-7%)	Traces <7%
Bauxite	Gibbsite - Al (OH)$_3$ Boehmite - Υ- AlO(OH) Kaolinite - Al$_2$Si$_2$O$_5$(OH)$_4$ / Nacrite	Goethite Fe$_2$O$_3$.H$_2$O Gypsum - CaSO$_4$·2H$_2$O Rutile/anatase - TiO$_2$ Calcite CaCO$_3$	Quartz SiO$_2$

The kaolinite polymorph nacrite [Al$_2$Si$_2$O$_5$(OH)$_4$] was identified. Similarly, to kaolinite, it is a 1:1 clay mineral, hence its primary structural unit is a layer consisting of one octahedral sheet (with the octahedral site occupied by aluminium) condensed with one tetrahedral silicon sheet, and these layers are regularly stacked. Nacrite is the rarest of the four kaolinite polymorphs and occurs mostly in hydrothermal environments (Poppe *et al.*, 2001; Kloprogge, 2019). Nacrite dehydroxylates similarly to kaolinite, but their atomic structures slightly differ. Nacrite has a greater interlayer separation and smaller lateral dimension than kaolinite, and the position of the basal O atoms differ. As a result, nacrite has a lower stability and it is more reactive than kaolinite (Brigatti *et al.,* 2006). Cahyono and Damayanti, (2014) report significant nacrite in Indonesian bauxite. The authors state that nacrite is highly reactive in an alkaline environment, and that its presence increases the refining (Bayer process) costs due to both, the high dissolution of the nacrite's silica increasing the consumption of caustic soda, and its subsequent re-precipitation requiring desilication.

In the context of the present study, the high kaolinite content and the presence and highly reactive, kaolinite-polymorph nacrite is likely an advantage, as these can enhance the reactivity of the bauxite in pozzolanic reactions.

The mineralogical analysis results agree with (Al-Dubaisi, 2011). According to the author, the Az Zabirah bauxite has a high alumina and silica content (average 56%, and 9% respectively), low iron content and a low organic matter content, and the alumina is boehmitic. The results also agree with Al-Mutairi *et al.* (2015) that report gibbsite, boehmite, diaspore, kaolinite, hematite, quartz and calcite as the predominant minerals, with anatase (0.3–3.5%), zircon and rutile as minor minerals in the in the Az Zabirah bauxites. However, unlike other bauxites, no diaspore was clearly evidenced. Al-Mutairi *et al.* (2015) state that diaspore can dissolve, and kaolinite recrystallize during the weathering of lateritic soils. The transformation of diaspore into kaolinite is probably the reason for the high kaolinite content and the lack of diaspore in the bauxite samples analysed.

4.5.3 Bauxite's phase changes with increasing sintering temperature

The mineralogy of the bauxite calcined at increasing temperature was analysed with XRD. Table 4-18 and Figure 4.14 include the mineral assemblages obtained at each temperature, and the phase changes in the assemblage caused by increasing activation temperature.

Transformation at 300°C. The main events at 300°C are as follows- Table 4-18 and Figure 4.14:

1- The gibbsite has disappeared transforming into boehmite agreeing with previous authors stating that, gibbsite dehydroxylation into boehmite occurs at ~300 °C (Alex *et al.*, 2014). According to Zhang *et al.* (2019), the transformation can be written simply as:

$$Al(OH)_3 \rightarrow AlOOH + H_2O$$

2- The main kaolinite diffraction peaks have lost approximately half of their original relative intensities hence the amount of crystalline kaolinite has approximately halved with respect to the raw bauxite (by dehydroxilation according to the equation below).

3- The lifting of the difractogram's baseline between approximately 19 and 22 degrees (2Θ) (reaching a relative intensity of 15 counts) indicates the presence of an amorphous phase.

According to previous authors, the dehydroxilation of kaolinite to form amorphous metakaolinite begins after 400 °C and is completed at ~ 650 °C, though some additional mass loss can be observed up to 800 °C according to the equation: (Ferreira , 2005)

$Al_2Si_2O_5(OH)_4 \rightarrow Al_2O_3 \bullet 2\ SiO_2 + 2\ H_2O$
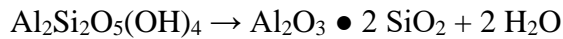
However, in this bauxite, the dehydroxylation begins at lower temperature (300°C), at 550°C most crystalline kaolinite has transformed, and at 700°C it has totally disappeared. The lowering of the kaolinite dehydroxylation suggests an increase in reactivity, and it is probably due to the lower particle size and crystallinity of the bauxite. Crystallinity and particle size strongly influence the kaolinite transformation temperature, with small, poorly crystallized particles presenting lower dehydroxylation temperatures than high ordered samples with larger particles (Brindley and Lemaitre, 1987).

g- Gypsum   K- Kaolinite   B- Boehmite   G- Gibbsite   A- Anatase
Q- Quartz   An- Anhydrite   C- Corundum   Ca- Calcite   Ge-Gehlenite
Al- γ-Aluminum Oxide   R- Rutile   N- Nacrite
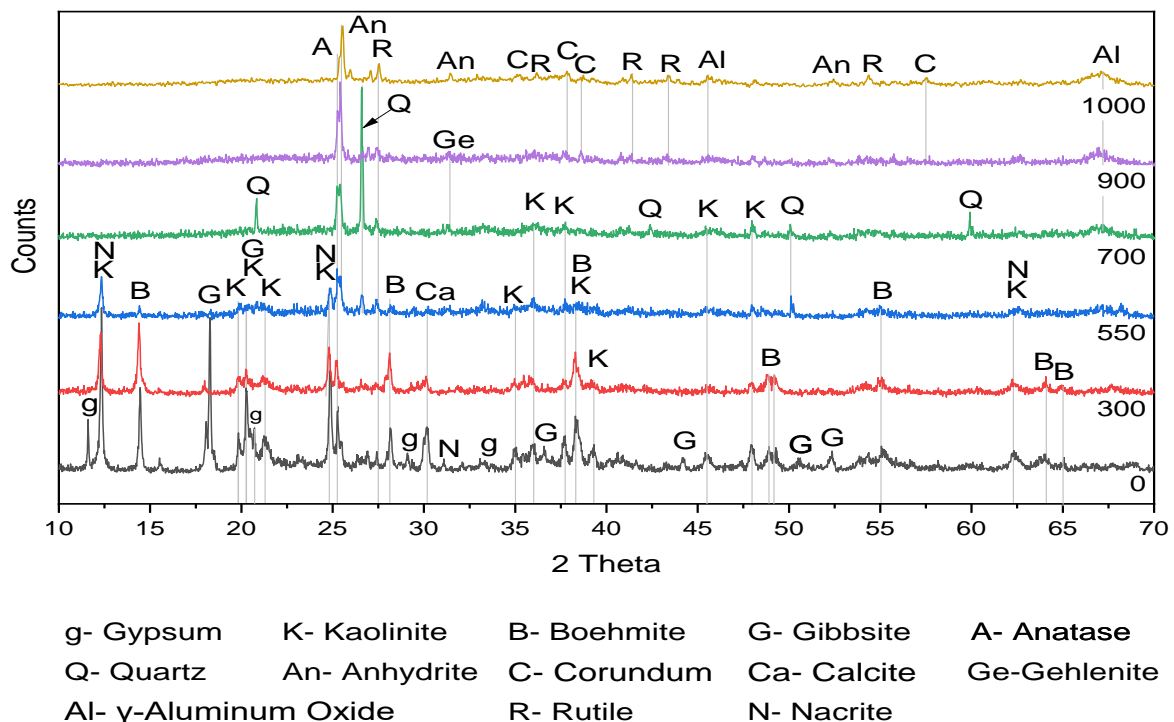
Figure 4-14 XRD traces showing the mineral composition of the bauxite at each temperature.

Table 4-18 Mineral assemblages of the raw and thermally activated bauxites analysed with XRD, and phase changes on increasing activation temperature. C_4AF = tetracalcium aluminoferrite = $4CaO \cdot Al_2O_3 \cdot Fe_2O_3$ (brownmillerite). C_3A = tricalcium aluminate.

Material	Phase composition by XRD			Phase evolution
	major (40-15%)	subsidiary (15-7%)	traces <7%	
Bauxite	Gibbsite Al (OH)$_3$ Boehmite Υ-AlO(OH) Kaolinite/Nacrite Al$_2$Si$_2$O$_5$(OH)$_4$	Gypsum CaSO$_4\cdot$2H$_2$O Rutile/anatase TiO$_2$ Calcite Goethite Fe$_2$O$_3$.H$_2$O	Quartz SiO$_2$	-
Bauxite 300°C	Kaolinite ↓ Boehmite ↑	Calcite Nacrite↓	Magnetite Fe$_2$O$_4$ Quartz (SiO$_2$) Gypsum CaSO$_4\cdot$2H$_2$O	Gibbsite has disappeared transforming into boehmite. The amount of crystalline kaolinite has approximately halved with respect to the raw bauxite.
Bauxite 550°C	Kaolinite ↓	Boehmite ↓	Quartz (SiO$_2$) Calcite Anhydrite Ca SO$_4$	The crystalline Al-containing phases lower but no new Al-containing phases appear. Hence, most of the Al is in amorphous form. Most of the crystalline boehmite and kaolinite have become amorphous Υ- Al$_2$O$_3$ and metakaolin respectively.
Bauxite 700°C	Quartz (SiO$_2$)	Kaolinite ↓ Rutile TiO$_2$ Anatase TiO$_2$	γ - Al$_2$O$_3$	Boehmite has disappeared. γ - Al$_2$O$_3$ peaks become evident.
Bauxite 900°C	Corundum α Al$_2$O$_3$	Rutile TiO$_2$ Anhydrite Ca SO$_4$	γ - Al$_2$O$_3$ C$_3$A C$_4$AF Gehlenite Ca$_2$Al$_2$SiO$_7$ Anatase-TiO$_2$	Kaolinite has disappeared. Gehlenite appears. Possible traces of hydraulic C$_3$A / C$_4$A.
Bauxite 1000°C	Corundum α Al$_2$O$_3$	Rutile/Anatase-TiO$_2$ Anhydrite Ca SO$_4$↓ Microcline	γ-Al$_2$O$_3$ C$_3$A C$_4$AF Gehlenite Ca$_2$Al$_2$SiO$_7$	Microcline appears. Possible traces of hydraulic C$_3$A / C$_4$A.

Bauxite transformation at 550°C. At 550°C, most of the aluminium is in amorphous form. This is deducted as follows:

1- The amount of crystalline, Al-bearing phases (kaolinite and boehmite) is very low: the relative intensities of their main reflections indicate than less than 30% of the original amount is present, ~70% of the boehmite has decomposed and ~37% of the kaolinite that was present at 300°C has disappeared. Most of the crystalline boehmite and kaolinite have become amorphous Υ- Al$_2$O$_3$ and metakaolin respectively. This agrees

with Novak *et al.* (1990) that state that boehmite is the thermodynamically stable phase up to approximately 300°C and, if heated further in air, dehydration to y-alumina occurs.

2- No new, crystalline, Al-bearing phases have formed.

3- Therefore, most of the Al (at least 2/3rd s of the total content) is in amorphous form at 550°C.

4- The lifting of the difractogram's baseline (2Θ=19-22°) reaching a relative intensity over 20 counts also indicates an increase in amorphous content.

Bauxite transformation at 700-1000°C. In the Saudi Arabian bauxite, γ-Al_2O_3 is present at 700, 900 and 1000°C with blunt peaks located at 2Θ = 67.0° and 45.8°. **At 700°C,** γ - Al_2O_3 peaks have become evident however, most of the Al is still in amorphous form as, except for the Υ- Al_2O_3 peaks, no other crystals of Al-bearing phases are present in the XRD pattern. At 900°C and 1000°C, the amorphous alumina phases crystallize, becoming mainly the alpha polymorph corundum - α Al_2O_3-, and small amounts of gehlenite- $Ca_2Al_2SiO_7$. Microcline appears at the highest temperature and there are possible traces of aluminate and ferrite C_3A /C_4AF.

The mineral transformation of the alumina phases evidenced with XRD agrees with Sglavo *et al.* (2000); Paglia *et al.* (2004) and others that studied the calcination path of transition aluminas, stating that boehmite transforms into γ-Al_2O_3 (present between 450 and 750 °C) and later into corundum according to the following sequence:

γ-Al_2O_3 → δ-Al_2O_3 (or gamma-prime-alumina (γ'-Al_2O_3) above 750 °C) → θ-Al_2O_3 → α-Al_2O_3 (corundum).

Gypsum -$CaSO_4 \cdot 2H_2O$- has become insignificant at 300°C and has disappeared at 550°C transforming into anhydrite -$CaSO_4$-. Gypsum enhances the pozzolanic reactivity of metakaolinite (Heller-Kallai, 2006). Therefore, the presence of anhydrite at 550°C (temperature at which metakaolinite content is maximum) may enhance the bauxite's reactivity.

The phase change, caused by increasing activation temperature, in the bauxite's mineral assemblage analysed with XRD, places the highest reactivity at around 550°C because, at this temperature, most of the aluminium is in amorphous form. However, even using advanced

structural characterization techniques such as XRD, it is difficult to distinguish between amorphous and finely grained crystalline solids due to their similar interatomic distances. Amorphous materials have some short-range atomic order and, in very small crystals, a large fraction of atoms are at or near the surface, distorting atomic positions and decreasing structural order (Varshneya, 1994). Therefore, reactivity at temperatures other than 550°C can be underestimated if based on the amorphous fraction only.

4.5.4 Thermal analyses by DSC and TGA

The mineral transformations resolved with XRD above, agree with the two endothermic peaks at ~300° and 520°C determined with TGA / DSC. The bauxite shows a marked endothermic peak at 300°C (Figure 4-14). As evidenced with XRD, this peak is due to the decomposition of gibbsite and its partial transformation into boehmite, and to the transformation of approximately half of the kaolinite into metakaolin. This is followed by a smaller endothermic peak at 520°C whereby the bauxite absorbs heat for the decomposition of crystalline boehmite (likely into amorphous Υ- Al_2O_3) and the conversion of the remining crystalline kaolinite into metakaolin. The small endothermic peak at approximately 150°C likely corresponds to the elimination of water molecules adsorbed to the external surfaces of the particles of the original aluminium hydroxides and kaolinite Figure 4-15.

The TGA analysis in Figure 4-15 shows two main episodes of mass loss with rising temperature. The first weight loss of ~ 7% of the original mass at around 300°C coincides with the endothermic peak of the decomposition of gibbsite and the conversion of kaolinite into metakaolin. Another significant weight loss coincides with the endothermic peak at 520°C marking the decomposition of crystalline boehmite and the conversion of the last kaolinite into metakaolin.
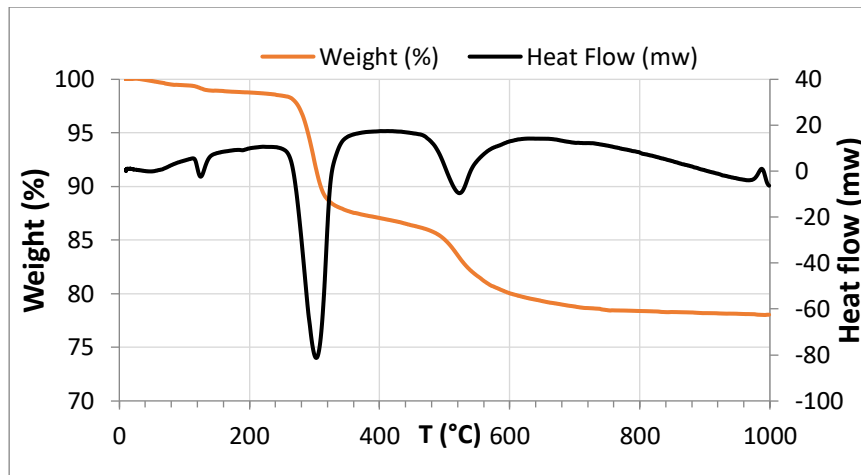
Figure 4-15 Differential scanning calorimetry (DSC) and thermal gravimetric analysis (TGA) of the bauxite.

4.5.5 Reactivity by the Chapelle Test

The Chapelle test measures the amount of lime fixed per gram of bauxite. Lime combination is due to cation exchange (between the ions on the bauxite minerals surfaces and the lime's Ca^{2+}) and pozzolanic reaction, hence it is a good indicator of reactivity. The results (Table 4-19) indicate that the bauxite calcined at 550°C combines the most lime, closely followed by the bauxite sintered at 700°C. Therefore, the bauxites sintered at 500 and 700°C have the greatest initial reactivity. At 800°C, the amount of combined lime slightly lowers, however it is still significant. The difference in the amount of lime combined by the bauxite calcined at 800 and 900°C is insignificant. In addition, the pozzolanic index of the bauxite is high, considerably superior to other pozzolanic or hydraulic materials previously studied (Alelweet and Pavia, 2019, 2020; Berenguer *et al.*, 2020; Alelweet *et al.,* 2021) (Table 4-20). The values are comparable to those in the literature. Ferraz *et al.* (2015) reached values of 920-1560 mg $Ca(OH)_2$/g for metakaolin, placing the minimum reactivity at 700 mg $Ca(OH)_2$/g metakaolin.

The high pozzolanic index for bauxite when compared with RM and FA is largely due to the mineralogy of the bauxite including major kaolinite, gibbsite and boehmite. The major components of the bauxite's red mud are hematite, cancrinite -$Na_6Ca_2[(CO_3)_2|Al_6Si_6O_{24}]\cdot 2H_2O$, gibbsite - $Al(OH)_3$ and sodalite $Na_4Si_3Al_3O_{12}Cl$ (Alelweet *et al.,* 2021) which, although reactive, combine less lime that the bauxite's aluminium phases in the short term.

The FA used for comparison (SiO_2=53-65%; Al_2O_3 = 21-24 %) contains significant amorphous material and some crystalline phases including quartz (SiO_2) and a small amount of mullite ($2Al_2O_3 \cdot 2SiO_2$) (Alelweet and Pavia, 2020). As it can be evidenced from the Chapelle results, these combine less lime than the aluminium phases in the bauxite. As expected, the GGBS shows a poor lime combination, because the Chapelle test is not designed for latent hydraulic materials such as GGBS which would release lime on hydration, rather than combining it.

Table 4-19 Amount of lime fixed per gram of bauxite and pozzolanic index (I Ca(OH)$_2$ of both raw and calcined (300-1000°C) bauxite specimens measured with the Chapelle test.

	Bauxite	Bauxite300	Bauxite550	Bauxite700	Bauxite800	Bauxite900	Bauxite1000
mg Ca(OH)$_2$/g	525	635	1034	996	819	808	425
mg CaO/g	397	481	783	755	620	612	322
I Ca(OH)$_2$	262	317	517	498	409	404	213

Table 4-20 Pozzolanic index -I Ca(OH)$_2$ – of the bauxite (B) compared with its red mud (RM) activated at temperatures ranging from 300 to 1000°C; GGBS- ground granulated blast furnace slag-, FA- fly ash-, MK – metakaolin- and SCBA- sugar cane bagasse ash-. (*)(Alelweet and Pavia, 2020); (**) (Alelweet and Pavia, 2019); ($^+$) (Berenguer *et al.*, 2020); ($^{++}$) (Alelweet *et al.,* 2021).

	B	B 300	B 550	B 700-800	B 900	B 1000	RM300-400 $^{++}$	RM750 $^{++}$	RM1000 $^{++}$	GGBS **	FA *	SCBA +	FA +	MK +
I Ca(OH)$_2$	262	317	517	498-409	404	213	203-229	127	140	104	286	293-337	382	1194

4.5.6 Reactivity by conductivity loss

This method follows the pozzolanic reaction indirectly by measuring the changes in the conductivity of saturated lime/bauxite solutions. The fixation of dissolved Ca(OH)$_2$ by the bauxite reduces the lime concentration in solution leading to a decrease in conductivity. The speed of consumption of portlandite Figure 4-16 was monitored over the first 170 hours, hence it corresponds to the early rate of pozzolanic reaction. According to the results Figure 4-16, all the sintered bauxites combine substantial lime early, except for the bauxite calcined at 1000°C, probably due to the presence of abundant crystalline corundum, and traces of hydraulic C_3A and C_4AF.
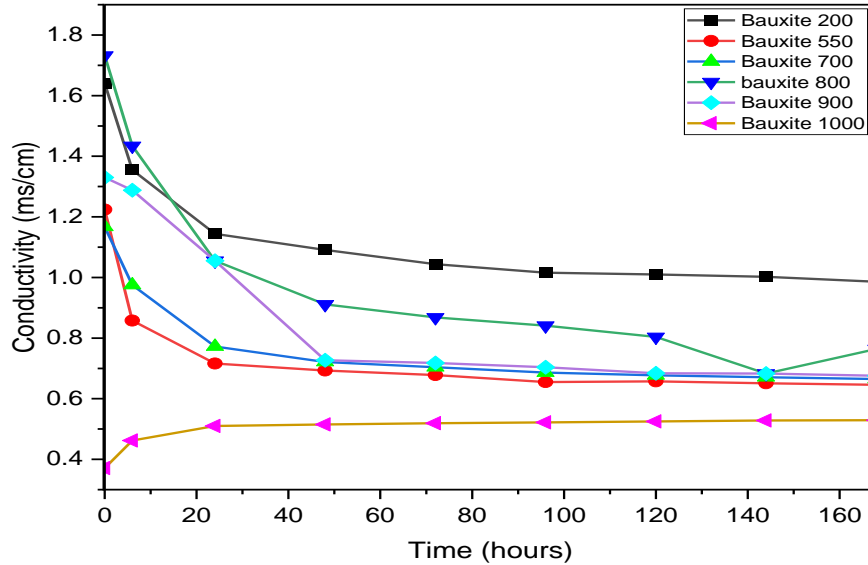
Figure 4-16 Pozzolanic activity of the bauxite as change in conductivity of a saturated lime/bauxite solution (caused by lime consumption) over time or chemical activity index.

A slow fall in conductivity indicates a reduced chemical activity in the solutions, hence the bauxite is not combining lime and pozzolanic activity is low. On the contrary, the curves of the bauxites burned at 550, 700 and 800°C show marked slopes in the first 6 hours, evidencing significant activity. The conductivity loss of the bauxite sintered at 300°C is significant, indicating that the bauxite calcined at lower temperature is also reactive. The curve of the bauxite burned at 900°C is less steep, indicating lesser lime combination and hence less reactivity. The higher crystallinity and the incipient hydraulic phases recorded with XRD in the bauxite burned at 900°C conform with this result.

The conductivity curves generally show that, within 48 hours, most of the lime in solution has been consumed, and lime combination has either stopped or reduced significantly. This roughly agrees with (Ferraz *et al.*, 2015) who established the reaction limit to 36 hours for pozzolans such as RHA, GGBS, FA and MS. However, the bauxite burned at 200°C reacts more slowly and activity ends after ~72 hours. With the exception of the 1000°C bauxite, the variation in conductivity over time is significant. According with this variation, the materials can be classified as having good pozzolanicity, as the variation in conductivity greater than 1.2 mS/cm (Luxan et al., 1989).

4.5.7 Setting times and water demand of the raw and sintered bauxite

It is well known that water demand is largely determined by the specific surface area (SSA) of the particles. This is evidenced from the results -Table 4-21- as the water demand is highest when the particles have greatest SSAs. As it can be seen from Table 4-21, sintering the bauxite up to 800°C doesn't affect significantly neither the particle SSA nor the water demand of the paste. However, at higher temperature, both the SSA and water demand lower. This agrees with the XRD mineral assemblage showing that, at around 800°C, the high SSA minerals such as kaolinite, boehmite and gibbsite have completely disappeared, and dense stable phases such as corundum have formed instead. The results -Table 4-21- roughly agree with the mineral composition placing the maximum content of layered, high-SSA minerals (kaolinite/nacrite and boehmite) between 300 and 550°C.

All the bauxites reduced the initial setting time of the hydrated lime, and they also shortened the final setting time (except for the 1000°C bauxite). The bauxites sintered at 700 and 800°C speed up the initial and final set of the hydrated lime significantly. The initial set of the 700°C bauxite is ~7 times shorter than that of the lime (4.5 times shorter for the 800°C bauxite). The final setting times also shorten significantly: the paste made with the bauxite sintered at 700°C sets 4.6 times faster than the lime alone, 3.7 faster for the 800°C bauxite paste. The bauxites sintered at 300 and 1000°C reach their initial set faster than the hydrated lime, and their final set is either similar (300°C) or slightly slower (1000°C). According with EN196-3:2016, the initial setting time shall be not less than 2 hours, and the final setting time not more than 8 hours. Therefore, all the final setting times comply with standard requirements. However, the initial set of the bauxites sintered at 700 and 800°C is too quick.

Typically, it takes approximately 1 hour for CEM I to achieve its final set. In contrast, all the bauxite pastes, except for 1000°C paste, have achieved their final set within an hour. This agrees with previous research stating that pozzolans with highest Al_2O_3 content initially set the fastest (Walker and Pavía, 2011) and that aluminates are responsible for the early set of a paste (Taylor, 1997). This was to be expected given the high aluminum content of the bauxite, and it is clearly evidenced in CACs which, even though they take similar time to initially set than PC, they reach their finial set much faster than PC due to their high aluminate content (Scrivener and Capmas, 1998).

Table 4-21 Relationship between the water demand to produce an initial flow diameter of 170±5 mm for a 1:1, bauxite: lime mix, setting times of the mixes, and specific surface area of the bauxite. (*) (Scrivener and Capmas, 1998).

	T ºC	W/b	SSA (m²/g)	Initial Setting Time (h)	Final Setting Time (h)
Bauxite	300	0.61	81.81	5.6	6.1
	550	0.73	82.26	4.0	4.3
	700	0.73	82.53	0.8	1.3
	800	0.71	80.00	1.3	1.6
	900	0.65	67.00	5.1	5.5
	1000	0.62	40.38	5.5	6.6
CL90s	-	0.52	-	6.0	6.1
CEM I*	-	-	-	3 ± 1.20	4 ± 1.10
CAC*	-	-	-	3.55 ± 0.35	4.10 ± 0.35

4.5.8 Reactivity by strength development and mechanical activity index

All the bauxites increased the 28-day compressive strength of the lime mix, and most of the bauxites surpassed the flexural strength of the hydrated lime (Table 4-22). The bauxites sintered at 800 and 900 ºC produced the highest mechanical activity indices, followed by the bauxites sintered at 700 ºC (37% MI reduction when compared to the 800 ºC bauxite). The MI of the bauxite sintered at 800 and 900 ºC is high. It compares well with highly-siliceous, pozzolanic materials such as rice husk ash and microsilica (Table 4-23), and it is lower than latent hydraulic materials such as GGBS and the eminently pozzolanic metakaolin.

As seen in the Chapelle test the bauxite has a higher pozzolanic index than its RM residue (Table 4-20), but their MIs are comparable (9-11 vs 7-8) – Table 4-23. This agrees with previous authors stating that compressive strength and hence the MI, is not only dependant on the amount of combined lime but also on the packing effect induced by the pozzolan and the microstructure of the hydration products formed (Walker and Pavía, 2011).

Table 4-22 Strength (28 d) and mechanical index of the bauxite at increasing temperature. SD- standard deviation.

Bauxite	Flexural strength (MPa)	SD	Compressive strength (MPa)	SD	Mechanical index	W/b
300 °C	0.26	0.01	0.55	0.05	1.80	0.85
550 °C	0.19	0.02	0.45	0.03	1.47	1.00
700 °C	0.33	0.04	0.93	0.05	3.05	1.05
800 °C	1.31	0.06	3.51	0.08	11.52	0.83
900 °C	1.17	0.14	2.83	0.26	9.29	0.77
1000°C	0.47	0.04	0.64	0.03	2.10	0.73
lime	0.17	0.05	0.30	0.05	-	1.07

Table 4-23 MI of the bauxite compared with the MI of the bauxite's red mud -RM- (sintered at 300-750°C) and other pozzolanic/cementing materials. * (Alelweet *et al.,* 2021). [+] (Walker and Pavía, 2011). RHA- Rice husk ash; MS- microsilica; MK-metakaolin; BD-brick dust.

	Bauxite 300	Bauxite 700	Bauxite 800/900	RM 300*	RM 400&750*	FA[+]	GGBS[+]	RHA[+]	MS[+]	MK[+]	BD[+]
MI	1.8	3	11.5/9.29	8	7	3.5	29	12	12	38	2-3

4.5.9 Microstructure by SEM/EDX

The microstructure of (1:1) pastes made with bauxite and hydrated lime (CL90s) are examined with SEM. The bauxites calcined at 550 and 700°C were selected because, according to the XRD results, most of the silica in the raw bauxite (which is forming part of kaolinite - $Al_2Si_2O_5(OH)_4$ / Nacrite) becomes amorphous in the 550-800°C interval.

According to the XRF results, in the bauxite: lime system studied, the silica content is medium to low, ranging between 27 and 15%. Generally, the reaction of lime-pozzolan mixes produces the same compounds as those formed upon PC hydration, since the overall chemistry falls within the same field (Massazza, 1998). Therefore, in the alkaline conditions created by the lime, the amorphous silica and alumina phases dissolve and combine with the lime's Ca^{2+} to produce cementing hydrates: calcium silicate hydrates (C–S–H), calcium aluminate hydrates (C–A–H), and calcium alumino– silicate hydrates (C-A–S-H).

According to the SEM results, there are no measurable differences between the bauxite pastes at 550 and 700°C. They both show relatively dense structures with abundant hydrates. However, rare unreacted alumina phases were observed in the 550°C pastes (Figure 4-17). The pozzolanic pastes show abundant pozzolanic hydrates and occasionally relics of pseudo-hexagonal plates and rhombic plates of very low crystallinity which are probably the remains of untransformed boehmite and metakaolinite (Figure 4-18). Metakaolinite is usually almost amorphous. However, the particles retain the pseudo-hexagonal morphology, and structural order persists within individual layers but not between them (Brindley and Lemaitre, 1987). Ghosts of hexagonal and rhombic habits covered by abundant pozzolanic hydrates of low crystallinity (Figure 4-19 - Figure 4-20) are also present. Their composition is consistent with the aluminosilicates aforementioned (Figure 4-21 - Figure 4-22).

The microstructure of the bauxite: lime pastes investigated show similarities with those of thermally-treated, clay sediments, activated in stronger alkaline media (such as NaOH solutions) to produce geopolymeric materials (Medri *et al.*, 2010; Ferone *et al.*, 2015).
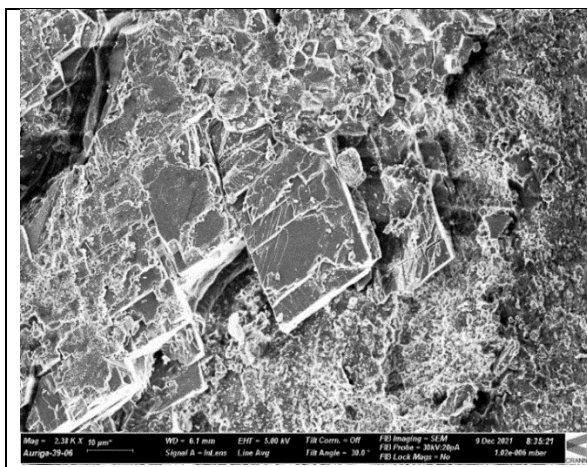
Figure 4-17 Microstructure of the (1:1) paste made with 550°C bauxite and hydrated lime (CL90s) showing un-reacted boehmite with a rhombic habit covered with hydrates.	Figure 4-18 Abundant pozzolanic precipitates and relics of pseudo-hexagonal plates of metakaolinite and rhombic plates (remains of boehmite not yet transformed), in the paste made with lime (CL90s) and bauxite calcined at 550°C.
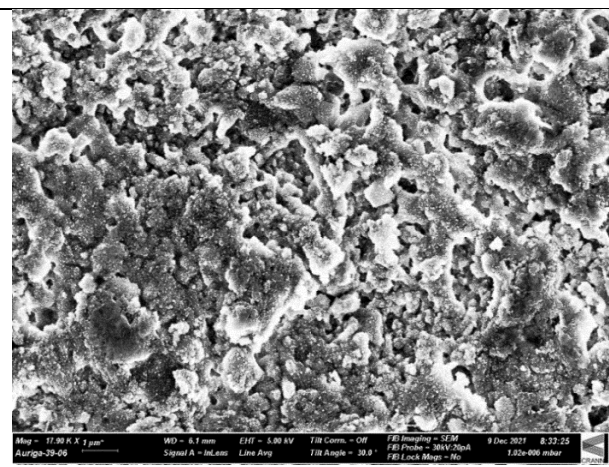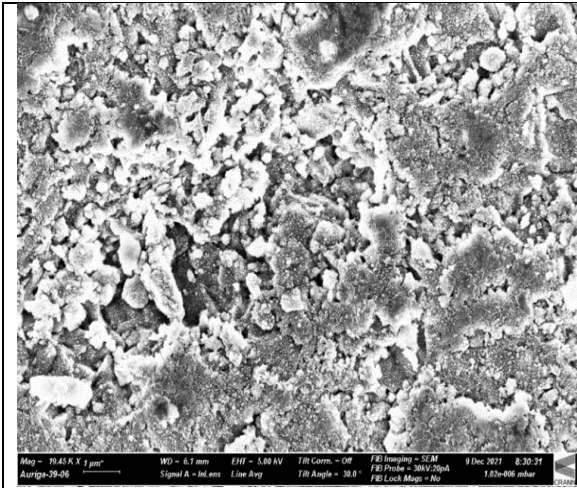
| Figure 4-19 Abundant pozzolanic precipitates leading to a lower porosity in the (1:1) paste made with lime (CL90s) and bauxite calcined at 700°C. | Figure 4-20 Ghosts of hexagonal and rhombic habits covered with abundant pozzolanic hydrates of low crystallinity- also seen in Figure 4-18. |

| Figure 4-21 Elemental composition analysis of the binder in Figure 4-18 by EDS. | Figure 4-22 Elemental composition analysis of hexagonal plates (Figure 4-18 and Figure 4-20) by EDS. |
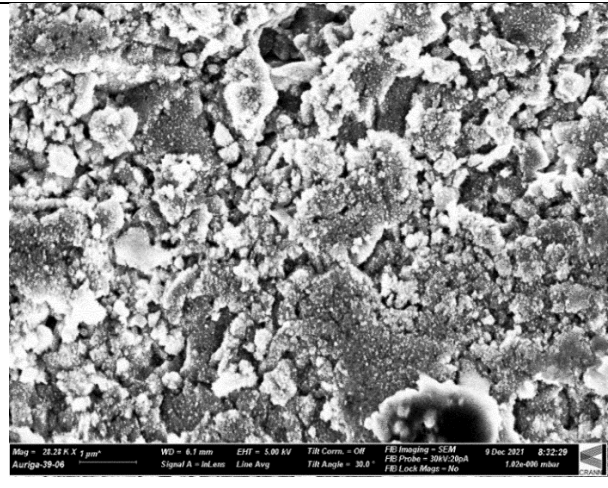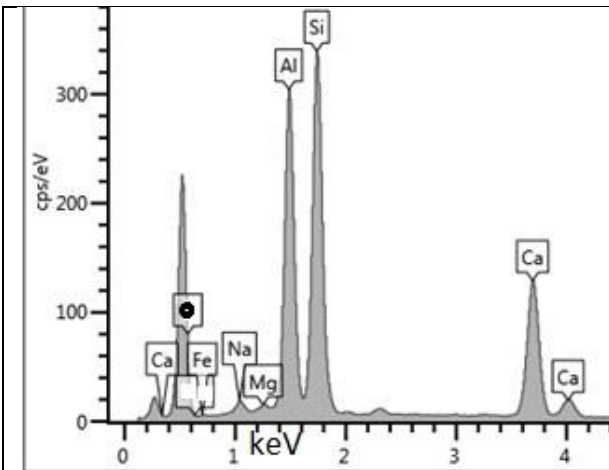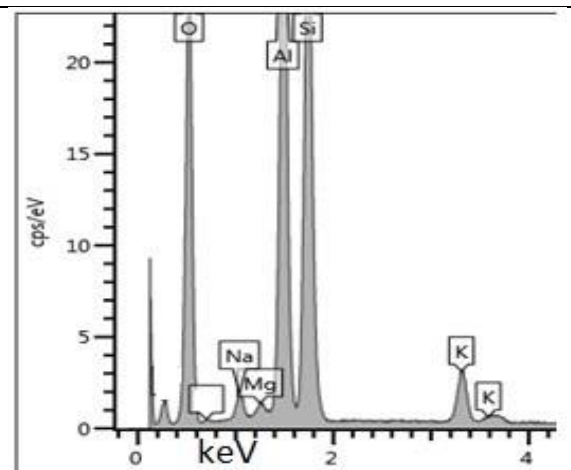
4.5.10 Discussion

The results (Table 4-24) show that the bauxite is remarkably pozzolanic, and that traces of hydraulic phases are only evidenced when the bauxite is sintered over 900°C.

The bauxite mainly consists of gibbsite, kaolinite and boehmite. The amount of gibbsite is close to the amount of kaolinite, and the amount of boehmite is at least 50% lower. The layered atomic structures of gibbsite, boehmite and kaolinite, with high specific surfaces and active surface hydroxyls that enhance adsorption, and hence nucleation, precipitation and dissolution, are the main drivers of the pozzolanic activity. The high reactivity of the bauxite is assisted by the great SSA of its particle constituents (superior to CEM II and other pozzolans), and by their high fineness produced with milling.

The early dehydroxilation of the kaolinite in the bauxite subject to study (beginning at 300°C and completed at 700°C), indicates high reactivity. The high kaolinite content of the bauxite, and the presence and the high-reactivity, kaolinite-polymorph, nacrite further enhanced the pozzolanic reactivity. According to Heller-Kallai (2006), sulphates improve the pozzolanic reactivity of metakaolinite. Therefore, the presence of sulphates (gypsum turning into anhydrite at 550°C) has probably improved the pozzolanic activity of the bauxite by increasing the activity of metakaolinite at ~700°C (temperature at which metakaolinite content is maximum).

Some of the results indicate initial activity (SSA, Chapelle test, conductivity variation and setting times) while others indicate later activity (28-day strength and mechanical index). A high SSA makes lime combination easier in the earlier stages of the pozzolanic reaction, whereas at longer ages, the pozzolanic reaction is mainly controlled by the active silica and alumina content (Massazza, 1998). The Chapelle, conductivity and setting times tests measure the ability to combine lime in the first hours hence the initial reactivity. In this research, the SSA, Chapelle and conductivity results agree. The Chapelle tests evidenced that the bauxite calcined at 550°C combines the most lime, hence showing the greatest initial activity, closely followed by the bauxite sintered at 700°C, and the bauxites sintered at 550 °C and 700 °C showed the greatest specific surface areas. The conductivity results agree, as the conductivity curves of the 550, 700 and 800°C bauxites show marked slopes in the first 6 hours evidencing high activity.

All the bauxites reduced the initial setting time of the hydrated lime, and they also shortened the final setting time of the lime (except for the 1000°C bauxite). The 550°C bauxite takes slightly longer to initially set when compared to the bauxites calcined at 800-900°C however, it reached its final set within 20 minutes (agreeing with the quick lime binding of the sample shown by the Chapelle and conductivity tests) and its setting times comply with current standard requirements.

Table 4-24 Summary of main results.

Bauxite	SSA (m^2/g)	Chapelle test $Ca(OH)_2/g$	Setting times (min)		CS (MPa)	MI	Phase evolution (XRD)
			Initial	Final			
300 °C	81.81	635	340	370	0.55	1.80	Gibbsite disappeared transforming into boehmite. 50% kaolinite disappeared becoming metakaolinite.
550 °C	82.26	1034	240	260	0.45	1.47	Most of the Al phases are amorphous. Most of the crystalline boehmite and kaolinite have become amorphous Υ-Al_2O_3 and metakaolin.
700 °C	82.53	996	50	80	0.93	3.05	Boehmite has disappeared (completely transformed into amorphous transition aluminas). γ - Al_2O_3 peaks become evident.
800 °C	80.00	819	80	100	3.51	11.52	
900 °C	67.00	808	310	330	2.83	9.29	Kaolinite has disappeared. γ - Al_2O_3 is present but some alumina phases have become corundum. Possible traces of C_3A, C_4AF and gehlenite
1000°C	40.38	425	330	400	0.64	2.10	Corundum increases. Microcline appears. Possible traces of C_3A, C_4AF and gehlenite.

The bauxites sintered at 800 and 900 °C produced the highest strengths and mechanical activity indices, followed by the 700°C bauxite (with a 37% reduction). This agrees with the XRD results whereby the bauxite sintered at 700-800°C, contains the highest amorphous/ active alumina content because the boehmite has totally disappeared, transformed into amorphous transition aluminas, and the kaolinite has completely turned into reactive metakaolin (kaolinite disappeared before 900°C). Therefore, the results agree with Massazza, (1998) who states that strength and mechanical index indicate late pozzolanic activity where the pozzolanic reaction is mainly controlled by the active silica and alumina content

The thermal analyses concur with the XRD results, indicating two main endothermic events at 300°C (marking gibbsite decomposition into boehmite, and transformation of approximately

half of the kaolinite into metakaolin) and at 520°C (decomposition of boehmite and transformation of the remining kaolinite into metakaolin).

At 900°C corundum is the main phase, and traces of hydraulic phases and gehlenite begin to appear. The sudden drop in SSA and the transformation of the alumina phases into stable, unreactive crystalline corundum lower pozzolanic activity and reduce strength.

4.5.11 Conclusion

The environmental impact of PC production (even with partial clinker substitution) is enormous when compared with the impact of bauxite mining. (CEM II releases 620-700 kg CO_2e/t *vs* 3-5 kg CO_2e/t for bauxite mining).

Gibbsite, boehmite and kaolinite are the main phases in the Saudi Arabian bauxite. The layered atomic structures of gibbsite and boehmite are comparable to the structure of clay mineral kaolinite, featuring high specific surfaces and active surface hydroxyls that enhance adsorption, and hence nucleation, precipitation and dissolution, which makes them highly reactive.

All the tests evidenced a high pozzolanic activity for the bauxite. The pozzolanic index (Chapelle method) is high, superior to other pozzolanic materials previously studied, and the mechanical index compares well with other pozzolanic and cementing materials. All the bauxites increased the 28-day compressive strength of the standard, hydrated-lime mix.

The high specific surface area of the bauxite particles, confirmed with laser diffraction, is superior to CEM II and other pozzolanic and cementing materials such as FA and GGBS. Heating, even at low temperature, significantly increases the SSA of the bauxite particles (at 300°C the SSA rises by over 60%).

The high kaolinite content (likely secondary from diaspore dissolution), and the presence of highly-reactive, kaolinite-polymorph nacrite, enhance the reactivity of the Saudi bauxite in pozzolanic reactions. The presence of sulphates (minor-traces) also contributes to the initial activity.

The kaolinite in the Saudi bauxite begins to dehydroxylate at 300°C, significantly earlier than reported by previous authors, evidencing an increased reactivity which is probably assisted by the presence of nacrite and sulphates, and the ultrafine particle fraction produced by milling.

The results of the SSA, Chapelle test, conductivity variation and setting time tests indicate the initial pozzolanic activity of the bauxite, while the results of the 28-day strength and the mechanical index indicate the amount of late pozzolanic activity.

The methods that determine the initial pozzolanic activity rate the 550°C bauxite as the most active, while the mechanical methods rate the 700-800°C bauxites as the most reactive. This is because the 550°C bauxite has one of the highest SSAs that makes lime combination easier in the earlier stages of the pozzolanic reaction, hence it combines the most lime in the Chapelle and conductivity tests. However, when sintered at 700-800°C, the bauxite contains the highest amorphous/ active alumina content (which control the late pozzolanic activity), because at 700-800°C the boehmite has totally disappeared, transformed into amorphous transition aluminas, and the kaolinite has completely turned into reactive metakaolin.

4.6 COMPOSITION AND REACTIVITY OF THE RM

The RM was studied both raw and sintered at several temperatures to enhance reactivity. The pozzolanic and cementing activity of the raw and sintered Saudi RM are investigated including the evolution of crystalline phases and their reactivity with increasing temperature. Reactivity determined with chemical and physical methods is compared with other pozzolanic materials.

4.6.1 Composition and reactivity of RM

RM is a mixture of hydrated aluminium oxides and iron phases produced as a residue when refining bauxite ore for aluminium production.

The refining (Bayer) process involves the digestion of crushed bauxite in a concentrated, caustic, sodium hydroxide solution at temperatures up to 270°C. Under these conditions, the majority of the aluminum containing species in the bauxite – such as gibbsite and boehmite– dissolve, leaving an insoluble residue (RM) composed of iron oxides, quartz, sodium aluminosilicates, calcium carbonate/ aluminate and, generally traces of titanium dioxide (Hind

et al. 1999). According to previous authors (Hind *et al.,* 1999; Liu *et al.,* 2009; Klauber *et al.,* 2011) during the refining process, silica can dissolve to form silicate as follows:

$$2\ NaOH + SiO_2 \rightarrow Na_2SiO_3 + H_2O$$

RM typically includes sodalite, cancrinite, dawsonite and calcium-containing phases resulting from the Bayer process, and gibbsite ($Al(OH)_3$) and boehmite (γ-AlOOH) as undigested material inherited from the bauxite (Klauber *et al.,* 2011). The organic compounds present in RM can form sodium oxalate- $Na_2C_2O_4$ - in the alkaline (pH=14), high ionic strength (6–7 M [Na^+]) liquors typical of the Bayer process (Hind *et al.,* 1999).

However, the composition of the RM residue depends on the composition of the parent bauxite and the conditions of the alumina refining (Bayer) process such as the addition of lime and the washing efficiency. Lime addition is determined by the type of bauxite ore. The washing efficiency dictates the amount of soluble soda remaining in the RM and hence its alkalinity. In Ma'adem, temperatures between 260 and 270 °C are used, and quick lime -CaO - is added twice during the process. The lime transforms the iron compounds from goethite (which interferes with the separation of Al) into hematite, and helps transform the unstable Al oxides in solution, in the high-temperature digestion units, into stable phases. Lime is also added in the clarification stage, to separate the solid phase (RM) from the liquid phase (Abdul Malik Shaheen, pers. Com. Ma'adem 2020).

Table 4-25 Composition of the RM investigated compared with other RMs from several Al producers worldwide.

Country	Reference	Major composition (wt.%)						Phase evolution (XRD)
		Fe_2O_3	Al_2O_3	TiO_2	SiO_2	Na_2O	CaO	
KSA	This research (Ma'adem)	12.97	29.79	5.12	19.66	24.05	5.09	Hematite, Cancrinite, Gibbsite,Sodalite, Boehmite Calcite,Quartz, Rutile Goethite, Chantalite
Canada	(Hairi *et al.*, 2015)	38.92	22.12	7.61	10.52	6.82	1.36	Hematite,Gibbsite, Boehmite Goethite,Quartz, Hydrated sodium aluminosilicate
Iran	(Bayat *et al.*, 2018)	20.54	15.41	4.97	13.26	5.87	19.87	-Calcite -Quartz - Phyllosilicates - K-feldespars - Plagioclase
China	(Zhang *et al.*, 2020)	24.9	21	6.19	20.15	9.7	7.30	-Hematite -Boehmite -Cancrinite -Gibbsite -Katotite -Muscovite
Australia	(Kumar and Kumar, 2013)	31.5	15.20	10.2	29.2	3.10	4.50	- Hematite - Goethite - Quartz - Cancrinite - Sodalite - Mullite
Australia	(Zhang *et al.*, 2014)	17.34	15.06	3.43	22.82	4.37	12.24	- Calcite - Hematite - Quartz
China	(Ye *et al.*, 2014)	9.48	24.5	2.92	20.38	11.46	12.86	-Muscovite -Cancrinite -katoite -Cibbsite -Hematite
China	(Dimas *et al.*, 2009)	18.15	20.77	4.29	19.41	3.78	12.11	- Hematite - Goethite - Gibbsite - Cancrinite - katoite
India	(Singh *et al.*, 2018)	53.75	16.07	4.24	8.25	3.82	1.48	- Quartz - Hematite - Calcite - Gibbsite - Geothite

RM waste from different bauxite refineries in the world has been compared indiscriminately by previous authors. However, some of these RM residues are distinctively cementitious, they differ widely from their pozzolanic counterparts and should not be directly compared. This is the case of the Chinese Shandong Aluminium Plant, where the RM waste includes highly reactive minerals, C_3A and C_2S, hence having significant hydraulic properties. The Chinese process of sintering alumina is different from the Bayer process which is applied in most bauxite refining plants. Here, due to the low Al_2O_3/SiO_2 of the Chinese bauxite ore (average 5–6), the bauxite is calcined at 1200°C before extracting the alumina with caustic soda, and reactive hydraulic phases C_3A and C_2S form as a result of the high temperature of the refining process. The presence of 50 and 56 wt.% β-C_2S has been reported due to the special processing of this Chinese bauxite (Yang and Xiao, 2008). As it is well known in cement technology, β-C_2S is the most hydraulic belite polymorph. Liu et al. (2011), also found a strong cementitious activity in the Shandong RM: besides the high amount of C_2S initially present, additional poorly-crystallised C_2S is formed with the CaO derived from the decomposition of aragonite (500-600∘C) and SiO_2 derived from the decomposition of amorphous aluminosilicates, a metastable phase that transforms into highly crystallised, less active, Ca_2SiO_4 by increasing the temperature from 700°C to 900°C. Similarly, Yalcin and Sevinc (2000) report the formation of sodium ferrite ($NaFeO_2$) in Turkish red mud at 500°C.

However, most of the RM residues worldwide are pozzolanic. Previous authors attempted to increase pozzolanic activity through heat treatment, but the results disagree, probably because the composition of the parent bauxite and the conditions of the Bayer process differ in alumina plants over the world. Pera et al. (1997) found that RMs calcined at 600-800°C were pozzolanic but their activity was low, and the reaction started at 3 days. They claim that the aluminium hydroxides (boehmite and gibbsite) develop pozzolanic behaviour when calcined between 600 and 800°C, and that RM reactivity increases over 700°C. Manfroi *et al.* (2014) account that RM calcined at 600°C has high pozzolanic activity, while Shi *et al.* (1999) obtained eminent pozzolanic activity by heating a RM of high kaolinite content at 750°C. However, RM can be inert up to 900°C. According to Sglavo *et al.* (2000), up to 900°C, the main components (Fe_2O_3 and TiO_2 - which account for 50% of the original mass) maintain their original state, and nepheline and $Na_2Si_2O_5$ form in the 900–1100°C interval.

4.6.2 Chemical composition of the Saudi RM

As noted by previous authors, the chemical composition of the RM is auspicious for the formation of cementing materials, having high silica and alumina contents (Table 4-26). The Saudi RM has a high SiO_2 when compared with other RMs (Table 4-27), and the content of chloride is low despite the use of sea water. The calcium content is high when compared with the parent bauxite due to the use of lime during the refining process.

The USA does not approve of the use of RM waste because the Environmental Protection Agency identified high levels of arsenic and chromium in some RM samples (Srikanth *et al.*, 2005). However, as it can be seen from Table 4-26, the levels of arsenic and chromium or any heavy metals in the Saudi RM are low, and hence no environmental toxicity is inferred from the chemistry of the Saudi RM. The only downside of the Saudi RM chemistry seems to be its high alkalinity when compared with other alumina plants where Na_2O usually varies between 3 and 11% wt% (Table 4-26 and Table 4-27). This is probably due to the use of sea water for dust control.

Table 4-26 Chemical composition of the Red mud and the parent bauxite as a % by wt oxide. ** traces of V_2O_5=0.138%; Cr_2O_3=0.074%; NiO=0.003%; ZnO=0.002%; Ga_2O_3=0.005%; As_2O3=0.005%; Y_2O_3=0.006%. [a] results by the producers. [b] Hazardous waste limit in construction products and materials.

	SiO$_2$	Al$_2$O$_3$	CaO	Fe$_2$O$_3$	Na$_2$O	K$_2$O	MgO	P$_2$O$_5$	SO$_3$	Cl$^-$	TiO$_2$	CuO	Zn	As	CrO$_3$	Cu	Ni
Red Mud**	19.66	29.79	5.09	12.97	24.05	0.09	0.40	0.29	1.65	0.32	5.12	0.00	0.002	0.005	0.074	0.001	0.003
bauxite	26.82	54.03	2.48	6.02	0.008	0.23	0.00	0.59	2.89	0.26	5.63	0.03	0.008	0.006	0.053	0.03	0.005
bauxite[a]	14.85	52.53	1.15	4.00	0.19	0.06	0.13	0.13	1.57	-	4.78	-	<0.01	-	0.04	-	-
(Wahlström et al., 2019) [b]	-	-	-	-	-	-	-	-	-	-	-	-	0.25	0.1	0.1	0.25	0.1
(Achternbosch et al., 2003) [b]	-	-	-	-	-	-	-	-	-	-	-	-	0.25	-	0.09	0.08	0.02

Table 4-27 Composition of the Saudi RM subject to study compared with other RMs generated from different alumina plants in various countries (Liu *et al.*, 2011; Mukiza *et al.*, 2019).

Country	Producer	Major composition (wt.%)					
		Fe_2O_3	Al_2O_3	TiO_2	SiO_2	Na_2O	CaO
KSA	MA'ADEM	12.9	29.7	5.1	19.6	24.0	5.1
India	HINDALCO	33.1	18.2	19.6	8.8	5.8	2.7
India	NARCO	51.0	18.0	9.8	4.6	5.3	1.8
Italy	Eurallumina	35.2	20.0	9.2	11.6	7.5	6.7
Turkey	Seydisehir	36.9	20.3	4.9	15.7	10.1	2.2
Greece	Al de Grece	40.8	19.9	5.8	6.8	2.7	12.6
Canada	ALCAN	31.6	20.6	6.2	8.8	10.2	1.6
China	-	27.9	22.0	2.3	20.9	10.5	6.2
China	Henan	11.7	25.4	4.1	20.0	6.5	13.9
China	Shandong	13.6	7.02	2.1	18.1	2.3	42.2
Australia	AWAAK	28.5	24.0	3.1	18.8	3.4	5.2
Australia	QAL	30.7	18.6	7.0	16.0	8.6	2.5
Germany	AOSG	44.8	16.2	12.3	5.4	4.0	5.2
Spain	Alcoa	37.5	21.2	11.4	4.4	3.6	5.5
Spain	San Ciprián	39.2	19.8	10.0	8.7	5.0	4.0
Brazil	Alunorte	38.0	19.0	3.8	19.9	8.5	0.8
Brazil	São Paulo	27.0	22.8	2.9	19.1	8.0	2.1
USA	RMC	35.5	18.4	6.3	8.5	6.1	7.7

4.6.3 Physical properties of the Saudi RM

According to the results (Table 4-28), the RM presents abundant specific surface area (SSA) available for reaction, superior to commercial Portland cement (CEM II) and other pozzolanic and supplementary cements such as FA (fly ash) and GGBS (ground granulated blast-furnace slag). The superior SSA of the RM is an outstanding quality with respect to reactivity, as it is widely accepted that reactivity increases proportionally to the specific surface available for reaction.

Table 4-28 Specific surface area and particle size distribution of the RM compared with PC (CEM II) and other supplementary cementitious materials including GGBS and FA.

	specific surface area (SSA) m^2/g	specific surface area (SSA) m^2/kg	particle density mg/m^3	Particle Size Distribution				LOI %	
				A. mean µm	D90 µm	D50 µm	D10 µm	450 °C	1000 °C
RM	9.35	9357	2.94	33.6	8.42	3.80	0.40	5.04	11.51
GGBS	1.95	1950	1.80	18	31.62	11.67	2.35	0.41	-0.77
FA	6.50	6500	2.28	15	100.63	14.96	1.95	1.67	4.92
CEM II	1.88	1880	-	-	82.58	24.90	2.56	-	-

The carbon content of the Saudi RM is either comparable or lower than others previously studied (Table 4-29). This constitutes a good quality with respect to reactivity, as it is well known that a high LOI (carbon content) adversely affects reactivity and increases water demand, and that it is associated to lowering strength and enhancing fracturing which could accelerate carbonation, chemical attack and the corrosion of embedded steel reinforcement. The negative value indicates that the GGBS absorbed some moisture during testing.

Table 4-29 Carbon content of the Saudi RM compared with others previously studied.

Country	Reference	LOI
Belgium	(Singh, Aswath and Ranganath, 2018)	10.20
France	(Toniolo, 2019)	10.77
Canada	(Hairi et al., 2015)	10.51
China	(Gong and Yang, 2000)	17.42
Minas Gerais	(Manfroi, Cheriaf and Rocha, 2014)	13.00
China	(Liu et al., 2011)	20.07
Korea	(Choo et al., 2016)	9.10
China	(Ye, Zhang and Shi, 2017)	13.74

4.6.4 Mineral composition of the Saudi RM

The mineralogical composition of the RM and the parent bauxite are included in Table 4-30. According to the XRD results, the bauxite consists of kaolinite, boehmite and gibbsite (major phases: 40-15%) while gypsum, rutile/anatase and magnetite are minor components (15-7%), and there are traces of goethite. The mineral composition of the RM appears in Table 4-30 and Figure 4-23. It is evident that gibbsite, boehmite and rutile are inherited from the bauxite ore, and that cancrinite, sodalite, chantalite, hematite and calcite have formed during the Bayer process.

Table 4-30 Mineral composition of the bauxite ore and the RM residue determined with XRD.

Material	Mineral composition by XRD		
	major phases (40-15%)	subsidiary (15-7%)	traces <7%
Bauxite	Kaolinite - $Al_2Si_2O_5(OH)_4$ Gibbsite - $Al(OH)3$ Boehmite - Υ- $AlO(OH)$	Gypsum - $CaSO_4 \cdot 2H_2O$ Rutile/anatase - TiO_2 Magnetite - Fe_2O_4	Goethite $Fe_2O_3.H_2O$
RM	Hematite - Fe_2O_3 Cancrinite - $Na_6 Ca_2[(CO_3)_2|Al_6Si_6O_{24}] \cdot 2H_2O$ Gibbsite - $Al(OH)_3$ Sodalite $Na_4 Si_3Al_3 O_{12}Cl$	Boehmite - Υ- $AlO(OH)$ Calcite $CaCO_3$	Quartz SiO_2 Rutile TiO_2 Goethite α-$FeOOH$ Chantalite - $CaAl_2(SiO_4)(OH)_4$

In the RM, the kaolinite from the bauxite has reacted with the NaOH and carbonated with the lime during the refining process, transforming into feldespathoids cancrinite and sodalite. This agrees with previous literature stating that kaolinite is not stable under highly alkaline conditions and various zeolite and feldspathoids can form (Breck and Breck, 1973). The transformation of kaolinite into cancrinite during the Bayer process agrees with Zhao *et al.* (2004), who obtained feldespathoids cancrinite and sodalite by reacting kaolinite with alkali solutions. Cancrinite is considered a feldspathoid rather than a zeolite due to the difficulty of molecular diffusion in its framework (Coombs *et al.* 1997 in Zhao *et al.* 2004). Similarly, sodalite is a tectosilicate without zeolitic water. The identification of cancrinite and sodalite in RM can be difficult. They have several common peaks located at 6.32, 3.65, 2.59 and 2.11 Å, but cancrinite can be identified by its characteristic diffraction peaks at 3.24, 2.74, 4.69 and 4.15 Å (Zhao *et al.*, 2004). In the Saudi RM, sodalite's unique peak at 2.84 Å and other characteristic peaks at 4.46 and 4.00 Å are concealed, but other characteristic and intense peaks such as 3.52 and 6.39 Å are evident (Zhao *et al.*, 2004).

The mineral composition of the Saudi RM also agrees with Castaldi *et al.* (2008) who reported the presence of cancrinite, hematite and sodalite making up 78% wt of the RM (with cancrinite and sodalite accounting for c.50%) and amorphous oxides accounting for 15-20% wt. However, the halo and the lifting of the trace indicating the presence of amorphous phases is minor in the Saudi RM indicating a higher crystallinity (Figure 4-23). The composition also agrees with Klauber *et al.* (2011) who found cancrinite, sodalite, dawsonite, and calcium-containing phases resulting from the Bayer process. The gibbsite ($Al(OH)_3$) and boehmite (γ-$AlOOH$) in the Saudi RM are undigested bauxite material, and the original goethite has been converted to hematite as previously highlighted by (Klauber *et al.,* 2011). The use of lime

(twice) in the Maa'dem refining process, has facilitated the occurrence of cancrinite, chantalite and calcite in the Saudi RM, and has also assisted the transformation of the original bauxite iron compounds (goethite and magnetite) into hematite.

4.6.5 Phase transformation on pyro-processing

The mineral phases produced when the RM was sintered at increasing temperature were determined with XRD analysis and are included in Table 4-31 and Figure 4-23. The main phase changes are as follows:

1- At 300°C. Gibbsite has disappeared turning into boehmite, and likely amorphous alumina polymorphs. Only boehmite was clearly detected, however, it is likely that some amorphous alumina polymorphs are present because the evolution of the XRD trace halo and the slight lifting of the base-line roughly indicate that the RM is most amorphous at 300°C. These changes agree with previous authors reporting the decomposition of gibbsite and the beginning and evolution of gibbsite dehydroxilation to form both boehmite and amorphous alumina polymorphs (Paglia *et al.*, 2004; Atasoy, 2005; Malki *et al.*, 2014). However, the temperature at which gibbsite disappears is lower than that reported by previous authors. Sglavo *et al.* (2000) state that the transformation of aluminium hydroxide phases (Bayerite, Gibbsite and Boehmite) into alumina polymorphs is the most important phenomenon up to 800°C, but in the Saudi RM, the decomposition of gibbsite takes place at a significantly lower temperature (<300°C).

2- At 400°C, the maximum cancrinite is recorded.

3- At 750°C boehmite, sodalite and calcite have disappeared and chantalite lowers, but there is still significant cancrinite.

4- At 1000°C cancrinite and chantalite disappear forming nepheline, C3A and gehlenite. This agrees with Sglavo *et al.* (2000) who also found nepheline in RM samples sintered between 900 and 1200°C. However, the authors report that the decomposition of chantalite and cancrinite produces alkaline oxides which in turn produce incipient nepheline at a slightly lower temperature (c.800°C).

Table 4-31 Phase evolution and mineralogical changes on pyro-processing of the RM determined with XRD.

Material	Mineral composition by XRD			Phase changes
	major phases (40-15%)	subsidiary (15-7%)	traces<7%	
RM 0°C-200°C	Hematite - Fe_2O_3 Cancrinite $Na_6Ca_2[(CO_3)_2|Al_6Si_6O_{24}]·2H_2O$ Gibbsite - $Al(OH)_3$ Sodalite - $Na_4Si_3Al_3O_{12}Cl$	Boehmite - ϒ- $AlO(OH)$ Calcite - $CaCO_3$	Quartz - SiO_2 Rutile TiO_2 Goethite α-$FeOOH$ Chantalite $CaAl_2(SiO_4)(OH)_4$	No appreciable changes in mineral composition between 0 and 200 degrees. Cancrinite increases up to 400°C, then it lowers.
RM 300°C	Hematite Fe_2O_3 Cancrinite $Na_6Ca_2[(CO_3)_2|Al_6Si_6O_{24}]·2H_2O$ Sodalite - $Na_4Si_3Al_3O_{12}Cl$	Boehmite - ϒ-$AlO(OH)$ Calcite-$CaCO_3$	Chantalite $CaAl_2(SiO_4)(OH)_4$	Gibbsite has disappeared. Likely turned into boehmite.
RM 400°C	Hematite Fe_2O_3 Cancrinite $Na_6Ca_2[(CO_3)_2|Al_6Si_6O_{24}]·2H_2O$ Sodalite - $Na_4Si_3Al_3O_{12}Cl$	Boehmite ϒ-$AlO(OH)$ Calcite $CaCO_3$	Chantalite $CaAl_2(SiO_4)(OH)_4$	Maximum cancrinite content. Chantalite slightly increases.
RM 750°C	Hematite Fe_2O_3 Cancrinite $Na_6Ca_2[(CO_3)_2|Al_6Si_6O_{24}]·2H_2O$	Perovskite-$CaTiO_3$	Chantalite $CaAl_2(SiO_4)(OH)_4$	-Boehmite, sodalite and calcite disappear. - Chantalite lowers. - Significant cancrinite.
RM 1000°C	Hematite Fe_2O_3	Nepheline $NaAlSiO_4$ C_3A-Tricalcium aluminate-$Ca_3Al_2O_4$	Gehlenite-$Ca_2Al_2SiO_7$	- Cancrinite and chantalite disappear
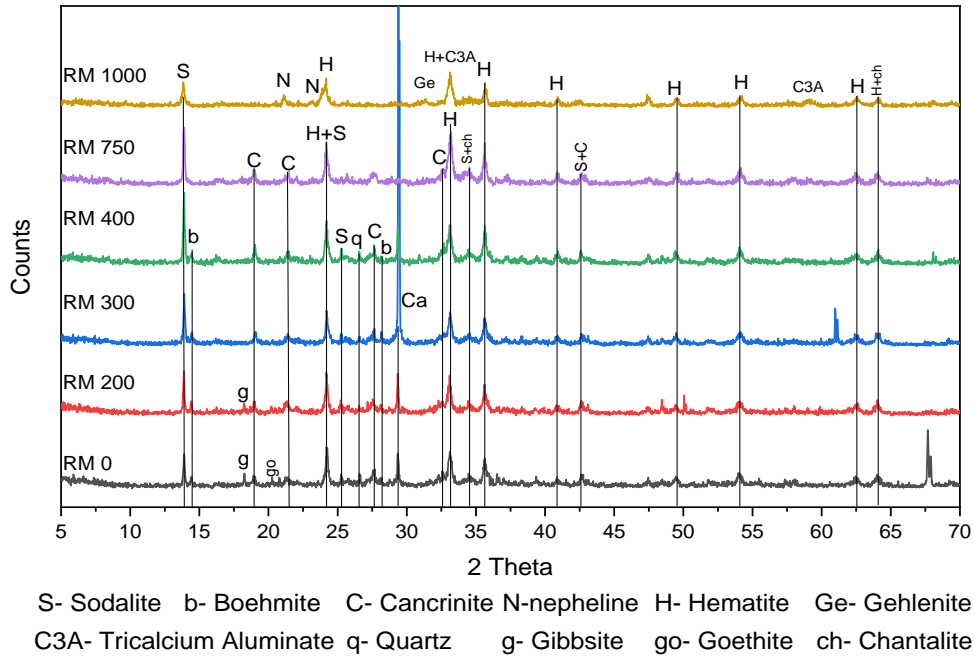
Figure 4-23 Phase transformation on pyro-processing of the RM.

4.6.6 Thermal analyses

The thermogravimetric analysis (TGA- Figure 4-24) shows a continuous weight loss as the temperature raises up to 1000°C. The total mass loss of the RM is 12% at 1000°C, it is slow and steady because the samples were previously dried at 100°C, and as expected, it coincides with the loss on ignition.

The differential scanning calorimetry (DSC- Figure 4-24) curve shows two marked endothermic peaks at 280 and 737°C where the samples take in heat to decompose. The endothermic peak at 280 °C is usually attributed to the decomposition of gibbsite and the beginning and evolution of gibbsite dehydroxilation (to form both boehmite and χ-alumina - Atasoy, (2005).

The endothermic peak at 737 °C corresponds to the decomposition of boehmite, sodalite and calcite because, according to the XRD results, at 750°C, they have disappeared. This agrees with Sglavo *et al.* (2000) who claim that the endothermic peak at around 800°C is due to the transformation of low temperature aluminium hydroxide phases (bayerite, gibbsite and boehmite) into η-, χ- and γ-Al₂O₃. It also agrees with Rivas Mercury *et al.* (2011) who

attributed this peak and the final descending (endothermic) branch to sodalite decomposition at c.700°C (965-1523K).

The endothermic DSC peaks are mirrored by two episodes of mass loss which are related to the evaporation of the water mechanically held, the gibbsite dehydroxilation, and the evolution of CO_2. These weight losses can also be related to the loss of water molecules located in the channels and cages of cancrinite and sodalite (Castaldi *et al.*, 2011).
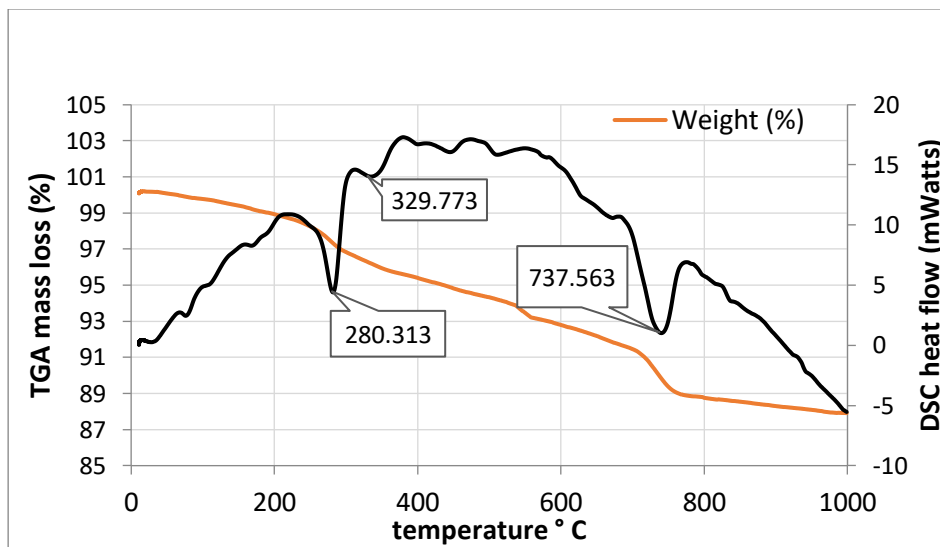
Figure 4-24 Thermogravimetric and differential scanning calorimetry analyses of the red mud.

4.6.7 Variation of specific surface area, water demand and setting with pyro-processing

As it can be seen from the results (Table 4-32), the specific surface area of the RM particles increases as the calcination temperature raises up to c.700°C, but after this threshold the surface area lowers. According to the XRD results, the main phase change above 750°C is the disappearance cancrinite. Therefore, the lowering of the SSA after 700°C is due to the melting and agglomeration of cancrinite.

An increase of fineness or surface area raises the water demand to reach a specific consistency. The water demand results agree with the variation of specific surface area, as the water demand increases with the calcination temperature up to 750°C, and lowers at 1000°C. These results

agree with the mineral composition results placing the maximum content of the cancrinite (a feldspatoid/zeolite characterized by its open microstructure) between 400 and 700°C.

As it can be seen from Table 4-32, all the RMs speed up the initial and the final set of the lime significantly. All the RMs reduced final setting time of the lime paste by over 50% except for the 300 RM where the reduction is less substantial. The slow set of the RM burned at 300 °C is inconsistent and it is due to the water content being too high for its SSA. The fastest set is achieved by the RM sintered at 400 and 750°C. This is consistent with the results above as these RMs have the greatest SSAs. It has been stated that the iron phases control the setting properties and the colour of RMs (Liu *et al.*, 2011). This disagrees, because the Saudi RM is a pozzolanic material, and the main iron phase (hematite) remains unchanged during the pyro-processing. Therefore, in the RM, the setting (or initial loss of plasticity) is not determined by the iron phases but by the evaporation of the mixing water, the carbonation of the lime, and the formation of pozzolanic hydrates.

Table 4-32 Variation of specific surface area, water demand and setting times with pyro-processing. Setting times for 1:1 (RM: lime) pastes to produce an initial flow of 170±5 mm. (*) Hydrated lime of European designation CL90s.

	T ºC	W/b	SSA (m²/g)	Initial Setting Time (min)	Final Setting Time (min)
RM	0	0.73	9.03	170	180
	200	0.70	8.87	150	130
	300	0.85	9.91	240	260
	400	0.83	11.47	140	150
	750	0.85	14.08	130	160
	1000	0.75	2.75	110	140
Lime *		0.52	-	360	370

4.6.8 Reactivity by the Chapelle test

According to the Chapelle test results (Table 4-33), the RM combines the most lime when burned at 400 ^{0}C, closely followed by 300 ^{0}C. The pozzolanic index values of the RM burned at 400 ^{0}C, compare well with some reactive, low-Ca (c.3%), class F (ASTM C618:2014), fly ashes (FA) previously studied (Alelweet and Pavia, 2019, 2020). As expected, the GGBS

pozzolanic index is low, as it is a cementitious material that needs less lime than pozzolans to activate and releases lime on hydration.

Table 4-33 Pozzolanic index or mg of lime fixed per gram of pozzolanic material (I Ca(OH)2) for the raw and thermally treated RM compared with GGBS and FA. (*) (Alelweet and Pavia, 2020); (**) (Alelweet and Pavia, 2019, 2020); (+) (Berenguer *et al.*, 2020). MK – metakaolin. SCBA-sugar cane bagasse ash.

Materials	RM	RM200	RM300	RM400	RM750	RM1000	GGBS**	FA*	SCBA⁺	FA⁺	MK⁺
mg Ca(OH)$_2$/g	251	277	406	457	254	280	209	572	-	-	-
mg CaO/g	190	209	308	346	192	212	158	433	-	-	-
I Ca(OH)$_2$	125.4	138.3	203.0	228.8	127.3	140.2	104.3	286.1	293-337	382	1194

4.6.9 Reactivity by strength development (mechanical method)

As it can be seen from the results in Table 4-34, the RM sintered at 300°C reached the highest mechanical index, closely followed by the RMs sintered at 400, 750 and 1000 °C. The reactivity of the RM (measured as the mechanical index at 28 days) is superior to other pozzolanic materials previously studied including Leca (4.6), FA (3.4) and ceramic dusts (1-3), and slightly inferior to microsilica (12.5) and rice husk ash (RHA=12) (Walker and Pavía, 2010, 2011).

Table 4-34 Compressive and flexural strengths and mechanical indices at 28 days. SD-standard deviation.

RM	Flexural strength (MPa)	SD	Compressive strength (MPa)	SD	Mechanical index-MI	SD
RM 0	0.73	0.10	2.02	0.25	6	0.15
RM 200	0.62	0.05	1.96	0.30	6	0.18
RM 300	0.86	0.06	2.50	0.19	8	0.12
RM 400	0.87	0.14	2.09	0.20	7	0.12
RM 750	0.85	0.09	2.02	0.20	7	0.13
RM 1000	0.88	0.01	2.18	0.10	7	0.08

From the long-term strength development results (Table 4-35) it can be stated that RM completes the pozzolanic reaction earlier that other pozzolans such as FA. The ultimate strength values of the GGBS materials are higher as expected from their cementitious nature.

Table 4-35 Ultimate strengths and mechanical indices of the RM sintered at 750°C compared with FA and GGBS. Standard deviation = 0.13-0.17. MI- mechanical index.

Material	Compressive strength (MPa)			Flexural strength (MPa)		
	4 months	5 months	MI	4 months	5 months	MI
RM 750	1.80	1.48	7.00	0.87	2.23	9.09
FA	3.43	4.55	18.56	1.82	1.93	7.88
GGBS	6.02	8.37	34.18	2.63	2.22	9.06

4.6.10 Microstructure and presence of hydrates

The SEM was used to investigate the quality and distribution of the hydrates in the lime/red mud pastes. The elemental composition of the hydrates was determined with EDXRA. The background search didn't reveal research work to which the results could be compared. The qualitative nature of the SEM analyses did not allow to determine clear differences in the microstructure of the type of hydrates produced by the different pastes. However, some trends could be established, and well-defined and representative hydrates are shown in the SEM micrograph results.

At 28 days, the general structure of the 1:1, RM: lime paste shows abundant hydrates in the RM sintered at 300°C (Figure 4-25 - Figure 4-26). The chemical composition indicates that these are pozzolanic hydrates resulting from the RM's cancrinite phase (Figure 4-27 - Figure 4-28). The morphology and composition of the hydrates is consistent (Figure 4-29 - Figure 4-30), and further investigation evidenced fan-shaped sprays of cancrinite crystals and hexagonal plates (Figure 4-31- Figure 4-32). After 3 months of curing, there seems to be a shift toward cubic hydrates (Figure 4-34 – Figure 4-36), probably due to the transformation of the metastable hexagonal hydrates. Manfroi et al. 2014 found calcium silicate hydrate (C-S-H) and C-A-H gel and AFm phase in RM pastes. AFm phases are also found upon pozzolanic reaction in the Saudi RM, however, the main pozzolanic hydrates seem to be of a zeolitic nature. Therefore, the reaction products of the Saudi RM can be better compared with those of natural pozzolans of zeolitic nature (Massazza, 1998).
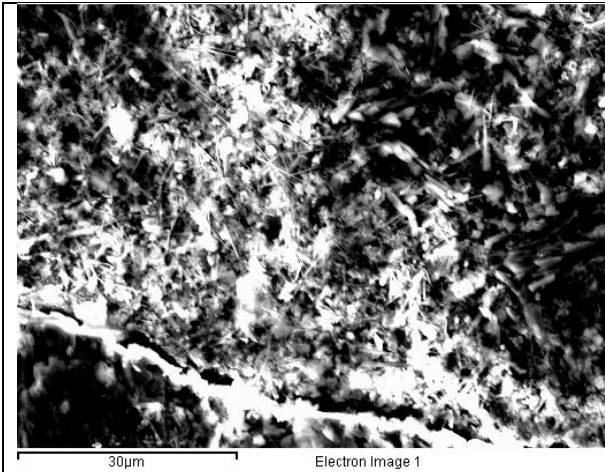
| Figure 4-25 General structure of the 1:1, RM: lime paste at 28 days showing abundant hydrates (RM sintered at 300°C). | Figure 4-26 General structure of the 1:1, RM: lime paste at 28 days showing abundant hydrates (RM sintered at 300°C). |

| Figure 4-27 Representative morphology of the hydrates in the RM/lime paste in Figure 4-26. | Figure 4-28 The chemical composition of the hydrates in Figure 4-27 indicates that these are pozzolanic hydrates derived from the RM's cancrinite phase $(Na_6Ca_2[(CO_3)_2|Al_6Si_6O_{24}]\cdot 2H_2O)$. |

| Figure 4-29 Further detail of the most abundant pozzolanic hydrates found in the RM/lime pastes. | Figure 4-30 Their chemical composition is consistent, and evidence that they are derived from the original cancrinite phase in the RM. |
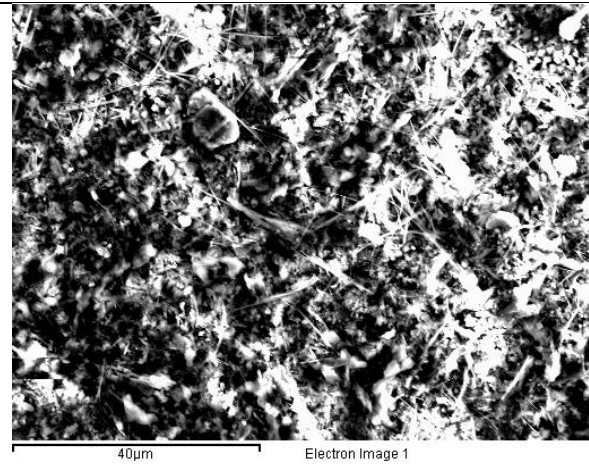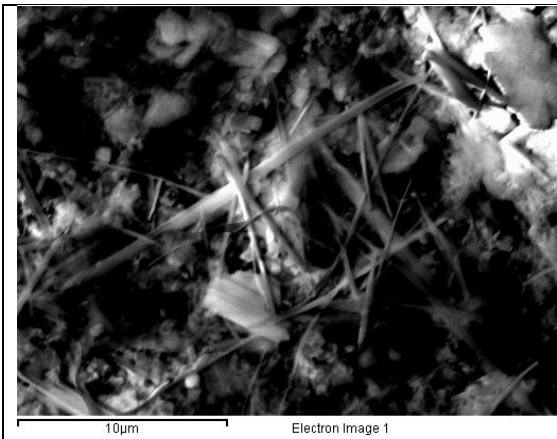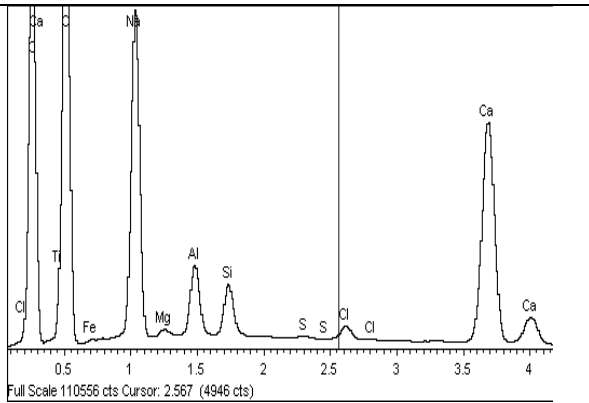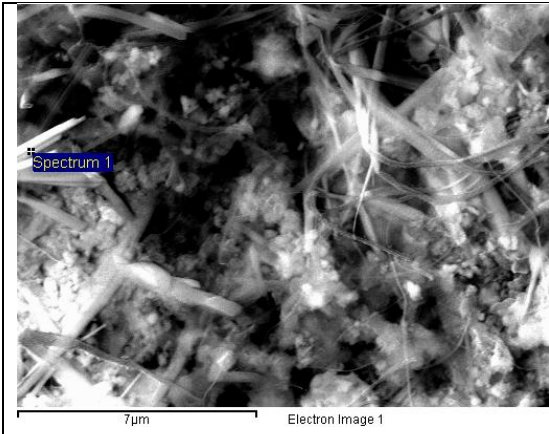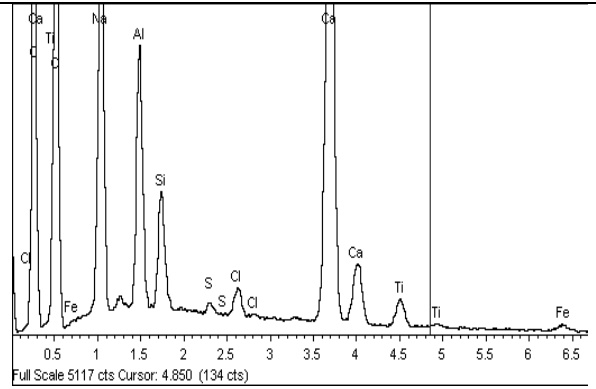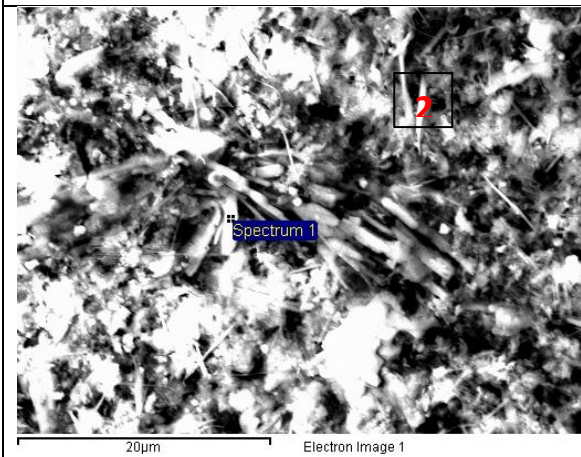
Figure 4-31 Hydrates formed in the RM /lime paste at 1 month, including fan-shaped sprays of cancrinite crystals and hexagonal plates. The elemental composition of these hydrates appears in Figure 4-32 - Figure 4-33.
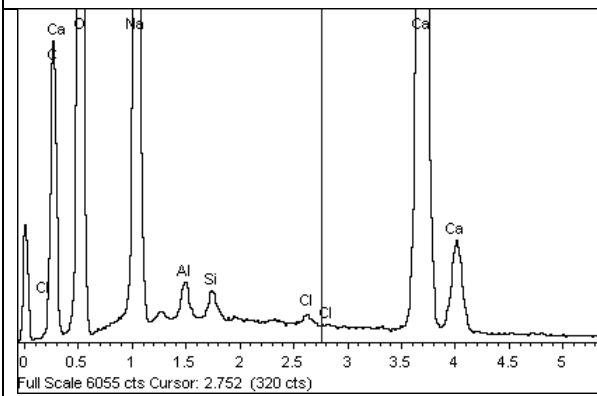
| Figure 4-32 The main pozzolanic hydrates, marked as spectrum 1 in Figure 4-31, are fan-shaped sprays of cancrinite crystals. | Figure 4-33 Hexagonal plates also appear. These are likely of the AFm type of hydrates (C_4AH_{13} / C_2AH_8). However, their composition shows the presence of Na picked up by the scattered X-Rays from the background and surroundings. |
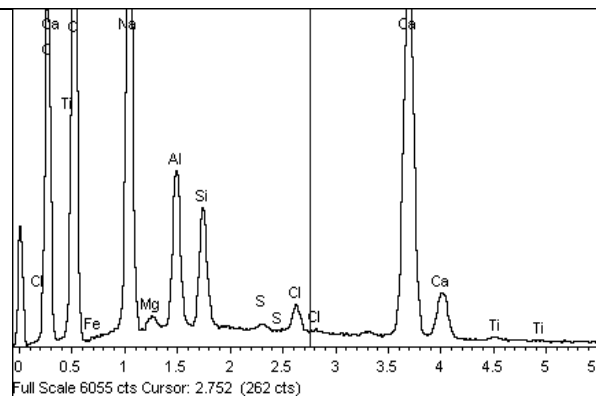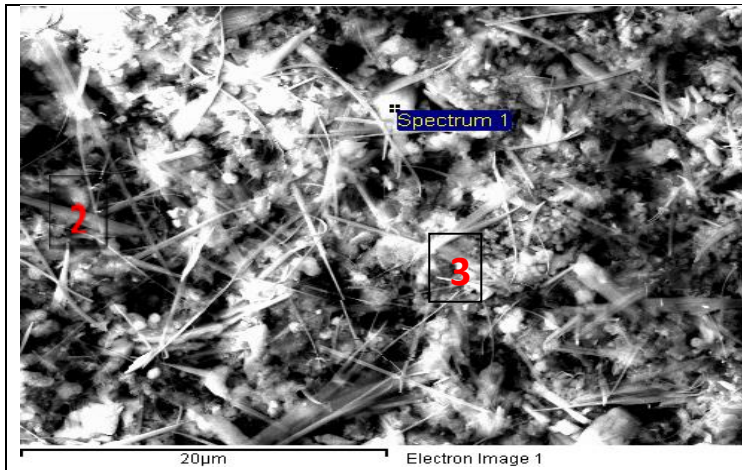
Figure 4-34 Detail of hydrates in the RM /lime pastes at 3 months. The elemental composition of the hydrates appears in Figure 4-35 – Figure 4-36.
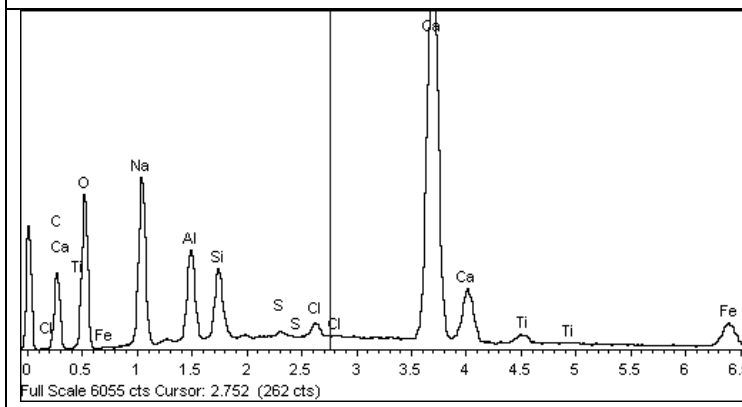
Figure 4-35 Elemental composition of the cubic hydrate phases (marked as spectrum 1 in Figure 4-33). These become more common over time, probably due to the transformation of the hexagonal hydrates.
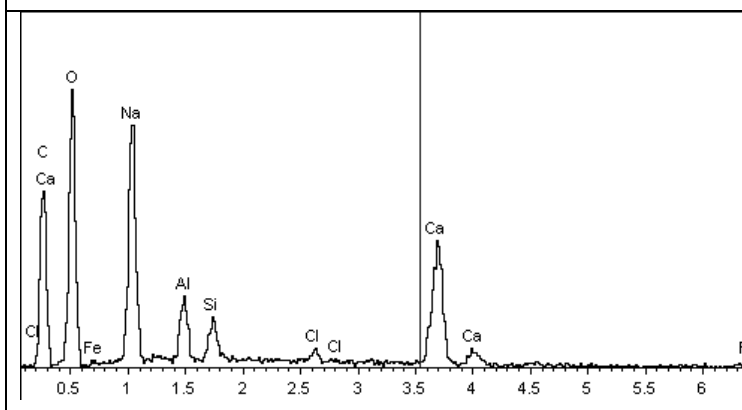
Figure 4-36 Elemental composition of the hydrates marked as 2-3 in Figure 4-34.

4.6.11 Discussion: Pozzolanic activity and cementitious properties

As aforementioned, the pozzolanic properties of the RMs reported in the literature vary considerably. According to Sglavo *et al.* (2000) RM is substantially inert up to 900°C, while (Pera *et al.* (1997) found that RMs calcined at 600-800°C were pozzolanic but their activity was low, and Shi et al (1999) obtained a RM of high pozzolanic activity by heating at 750°C a RM of high kaolinite content. Most authors attribute the pozzolanic activity of RMs to the transformation of the initial gibbsite into boehmite and transition aluminas (with reported

pozzolanic behaviour) at 600-800°. However, as evidenced by the XRD and DSC results, gibbsite transforms much earlier in the Saudi RM (280-300°C), agreeing with the greater activity for this RM found at a lower temperature.

The Saudi RM does not contain kaolinite. However, the Chapelle test and mechanical index results, and the comparison with other pozzolanic materials in the literature, indicate that the RM is moderately pozzolanic (Table 4-36). The SEM/EDXA and XRD analyses suggest that the main active phases are zeolites and feldespathoids. Therefore, the pozzolanic activity of the Saudi RM is mainly due to the presence and reaction of feldspathoids and zeolites, and the formation of zeolitic and feldspathoid-based hydrates. The SEM/EDXA evidenced that, at 300-400°C, cancrinite is clearly active and produces pozzolanic hydrates in the form of needle-shaped and fan-shaped sprays of crystals. The XRD results showed that the maximum cancrinite content is found at 400 °C. Therefore, the pozzolanic activity of the RM is mainly due to the presence and reaction of feldspathoids.

The results also indicate that the Saudi RM shows the greatest activity when sintered at 300 and 400°C. The RMs sintered at 300 and 400°C combine the most lime in the Chapelle test, and they reached the greatest strengths and mechanical index (Table 4-36). In addition, the RM at 400°C sets the fastest, closely followed by the RM sintered at 750°C which reached a comparable mechanical index and the greatest SSAs. Hence, the optimum thermal treatment that enhances pozzolanic activity lies c.400°C as evidenced by the highest lime combination and greatest mechanical indices.

At c.700°C, the specific surface area of the RM particles is still high, and the RM combines significant lime and has a mechanical index comparable to the lower temperature. According to the XRD and DSC results, at 750°C -boehmite, sodalite and calcite have disappeared but there is still significant cancrinite. This agrees with the main pozzolanic activity being driven by this mineral.

Negative effects of the thermal treatment are evidenced over 750°C. These are the decrease in specific surface area (Table 4-36), due to the melting and agglomeration of cancrinite (DSC results in figure 2), devitrification and crystallisation of nepheline, C_3A and gehlenite (1000°C) at the expense of cancrinite and chantalite which disappear (Table 4-31 and Figure 4-23).

Table 4-36 Summary of some of the principal physical properties and reactivity results. SD-standard deviation.

RM	SSA (m^2/g)	Chapelle test Ca(OH)$_2$/g	PH	Setting times (min)		Flexural strength (MPa)	Compr. strength (MPa)	Mechanical index
				Initial set	Final set			
0°C	9.03	251	10.64	170	180	0.73	2.02	6
200°C	8.87	277	10.23	150	130	0.62	1.96	6
300°C	9.91	406	10.34	240	260	0.86	2.50	8
400°C	11.47	457	10.96	140	150	0.87	2.09	7
750°C	14.08	254	11.75	130	160	0.85	2.02	7
1000°C	2.75	280	10.28	110	140	0.88	2.18	7

4.6.12 Conclusion

The Saudi RM is pozzolanic and not cementitious because, in Ma'adem, the Bayer process temperature (c.270°C) is not high enough for hydraulic calcium silicates to form. Thermal treatments enhanced reactivity. The heated RMs make hydrated lime set between two and three times faster than alone, hence they are pozzolanic. The RM is moderately pozzolanic, and its activity is mainly due to the presence and reaction of feldespathoids and the formation of zeolitic and feldspathoid-based hydrates. Cancrinite is active, and it produces pozzolanic hydrates in the form of needle-shaped and fan-shaped sprays of crystals. AFm phases were also found however, the main pozzolanic hydrates seem to be of a zeolitic nature. Despite the occurrence of nepheline, C$_3$A and traces of gehlenite at 1000°C, the formation of pozzolanic hydrates that result in setting and strength development is greater at lower temperature (300-400°C). The RM sintered at 300 and 400°C combines the most lime in the Chapelle test, and reached the greatest strengths and mechanical index. The (400°C) sets the fastest closely followed by the RM sintered at 750°C which reached a comparable mechanical index.

The positive effects of the thermal treatment can be seen below 750°C (loss of water in the zeolite/feldespathoids, and destruction of the crystal structures of the clay minerals inherited form the parent bauxite). Negative effects are evidenced over 750°C including a decrease in specific surface area, devitrification and crystallisation. The optimum thermal treatment that enhances pozzolanic activity lies c.400°C as evidenced by the highest lime combination and greatest mechanical indices.

The RM consists of gibbsite and boehmite, inherited from the bauxite, and cancrinite, chantalite and sodalite formed during the Bayer process. The CaO, added during refining, has transformed the original goethite into hematite, and caused the occurrence of cancrinite. The Saudi RM has high SiO_2 content and high alkalinity, the chloride and carbon contents are low, and no toxic elements were found. It presents abundant specific surface area available for reaction, superior to commercial CEM II and other pozzolanic and cementitious materials such as FA and GGBS.

5. PROPERTIES OF THE AAMS

Alkali-activated materials were designed and produced in the laboratory using RM, bauxite, GGBS and blends of RM and bauxite with FA/GGBS. Their physical properties and durability are studied in this chapter.

5.1 ALKALI-ACTIVATED MATERIALS MADE WITH A HIGH-CALCIUM, BASIC SLAG

This section studies the properties and durability of AA materials made with a ground granulated blast furnace (GGBS) from Dublin, activated with sodium hydroxide (NaOH), and sodium silicate (Na_2SiO_3), both combined and separately, and cured at 20 and 60 °C. The long-term strength and durability were assessed with accelerated weathering tests using thermal-moisture cycling, salt crystallization and freeze-thaw cycling. The mass loss and macro/microscopic changes after cycling were investigated. The 28-day strengths are compared to the 270-day strengths.

5.1.1 Mix design

The composition of the AA GGBS materials is included in Table 5-1 based on activator type and curing temperatures. The activators were selected according to previous authors who state that alkali silicate and hydroxide are the best activators for slags because they generate the highest PH (or alkalinity) which accelerates the reaction between the activator and the precursor (Shi et al., 2006; Provis et al., 2013; Pacheco-Torgal et al., 2014).

Hydroxide activators induce the hydrolysis of the Si-O-Si and Al-O-Al bonds releasing Si^{4+} and Al^{3+} and providing more hydroxyls which raise the PH to the values required for the dissolution of the precursor.

Silicate activators provide a higher level of alkalinity over longer periods because, when a moderate amount of silica dissolves, the PH does not drop rapidly (as it is the case with hydroxide activators) (Provis et al., 2013).

A high PH is not considered suitable for Ca-rich precursors such as GGBS, because at very high OH$^-$ concentrations, although Si and Al increase solubility, calcium becomes less soluble (Pacheco-Torgal *et al.*, 2014). Therefore, high Ca slags (Ca=35-45%) are usually activated under moderated alkaline conditions (Fernández-Jiménez *et al.,* 1999; Bakharev *et al.,* 2000; Shi *et al.,* 2006).

Furthermore, high concentrations of hydroxide activator in GGBS have been reported to encourage efflorescence and increase cost (Provis and Van Deventer, 2013; Pacheco-Torgal *et al.*, 2014). It is considered in the literature that slags can be successfully activated with a combination of alkali hydroxide and silicate. The fluidity of the hydroxide activator maintains a suitable rheology while the silicate activator provides Si ions for the generation of cementing hydrates that contribute to strength (Pacheco-Torgal *et al.*, 2014).

The ratio Na_2SiO_3/NaOH is essential as NaOH acts as dissolvent while Na_2SiO_3 acts as a binder (Liew *et al.*, 2016). Das *et al,* (2013) reported that the optimum value for Na_2SiO_3 to NaOH is 1.5, giving a higher compressive strength. Rajesh *et al.,* (2013) investigated the performance of alkali-activated slag with various alkali activators such as sodium silicate, sodium hydroxide and sodium carbonate. According to the results, NaOH ranked first for flexural strength and shear strength, Na_2CO_3 ranked second, and Na_2SiO_3 ranked third. Wang *et al.*, (1995) reported that Na_2SiO_3 was the most common and effective activator for slags providing the highest compressive strength values agreeing with Bakharev *et al.,* (1999). The Si ions contribute to the AAS's strength through effective silica gel formation, and the silica gel can react with calcium to form calcium silicate hydrates rich in silica.

Curing temperature is considered an important parameter. Bakharev *et al.,* (1999), reported improvements in early strength and reduced shrinkage in alkali activated slags (AAS) by curing at room temperature. Türker *et al.*, (2016) found that AAS mortar cured at 60 °C had a denser microstructure than AAS mortar cured at ambient temperatures.

Each slag responds differently to activation methods and curing temperatures as a result of variations in composition due to different raw materials and industrial processes (Wang *et al.,* 1994; Chen, 2020). There are considerable discussions among researchers in the literature regarding the most effective method for curing the AA slags.

Previous researchers have investigated curing temperatures from ambient to 60 degrees and higher. This research discusses the effect of curing temperature, up to 60 degrees, based on

mechanical strength, and accelerated weathering cycling. The curing temperature was not raised beyond 60 degrees due to environmental concerns and site application feasibility.

Table 5-1 Composition of the AA GGBS materials (3:1 - sand: GGBS).

	T	GGBS		Na_2SiO_3 /8M NaOH	Na_2O	Density	water		NaOH		Na_2SiO_3	
	^0C	(g)	(%)		%	(kg/m³)	(g)	(%)	(g)	(%)	(g)	(%)
G1	20	450	22.37	1.5	4.56	1676.26	124.36	6.18	20.52	1.02	66.63	3.31
G2	20	450	22.37	-	11.40	1676.26	160.21	7.96	51.3	2.55	—	—
G3	20	450	21.74	-	-	1725	128.25	6.20	—	—	141.75	6.85
G4	60	450	22.37	1.5	4.56	1676.26	124.36	6.18	20.52	1.02	66.63	3.31
G5	60	450	22.37	-	11.40	1676.26	160.21	7.96	51.3	2.55	—	—
G6	60	450	21.74	-	-	1725	128.25	6.20	—	—	141.75	6.85

*Sand is 1350 g (67%)

5.1.2 Mechanical strength of the AA GGBS mortars

Influence of activator. In general, the Na_2SiO_3 + NaOH activated slags tend to achieve the greatest compressive and flexural strengths (Table 5-2,Figure 5-1), agreeing with (Fernandez *et al.,* 1999). However, when cured at ambient temperature, the early strenghts (3 days) are superior for the NaOH activated slags. This has been previously reported and attributted to the slags reacting faster with the NaOH than the silica, hence reaching greater early strengths (Fernandez *et al.,* 1999). The early strengths of the Na_2SiO_3 + NaOH materials are lower than some in the literature, probably due to the slag's ultrafine nature and high SSA: an increment in the SSA of the slag has a negative effect on strength with Na_2SiO_3 + NaOH activators (A. Fernández-Jiménez and Puertas, 2003).

The Na_2SiO_3 activated slags result in poor strengths disagreeing with previous studies (Bakharev *et al.,* 2000; Fernández-Jiménez and Puertas, 2001, 2003; Krizan and Zivanovic, 2002; Atiş *et al.*, 2009; Altan and Erdoğan, 2012; Burciaga-Díaz and Escalante-García, 2013). The reason for the low strength is an excessive %Na_2O by mass of slag (the high reactivity of the slag would require a lower %Na_2O), as the optimum quantity lies between 3-6% by mass of slag, and the materials are over this threshold (Hewlett and Liska, 2019). The strength of the NaOH activated slags is lower than Talling and Krivenko, (1996), most likely due to an excessive alkalinity, produced by an undue high molarity of the NaOH solution (the alkalinity being excessive for the highly reactive nature of the slag). The sporadic efflorescence observed

in some of the materials conforms with the alkalinity being excessive, as efflorescence has been associated with high concentrations of hydroxide activator in slag materials (Pacheco-Torgal *et al.*, 2014; Provis *et al.,* 2014). The appearance of occasional microcracks also agrees with the high alkalinity.

In most instances, the strength tends to increase over time, raising significantly at late ages, between 28 and 270 days. The strength increase at late ages agrees with some authors, such as (Rodríguez *et al.*, 2008), who found strength increases up to 120 days, but does not conform with (Collins and Sanjayan, 2001), who found that the strength of alkali-activated slag concrete tends to reduce at late ages (360 days), and attributed the reduction to the occurrence of a network of interconnected microcracks with increasing age.
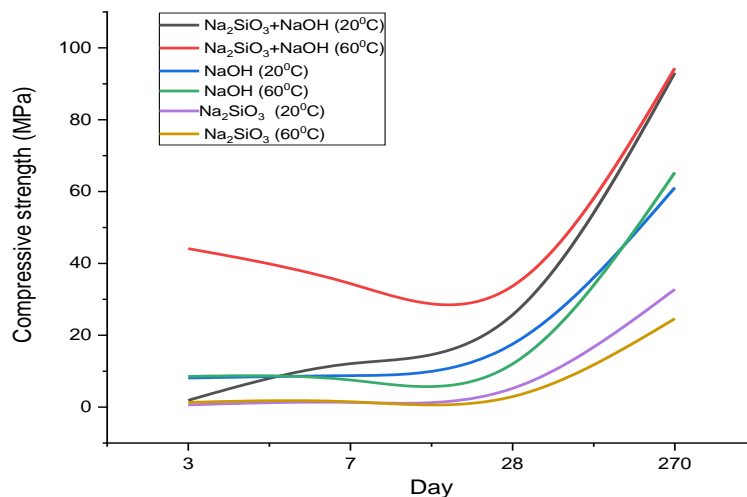
Figure 5-1 Effect of activator on compressive strength development.

Influence of curing temperature. A higher temperature is expected to increase the amount and rate of slag dissolution so that reactivity, and hence strength gain are favoured. The effect of increasing temperature for each of the activators is shown in Figure 5-2-Figure 5-4. Increasing temperature, enhances strength when Na_2SiO_3+NaOH is the activator (mainly at early ages, up to 28 days), agreeing with former authors (Fernandez *et al.,* 1999; Bakharev, Sanjayan and Cheng, 2000; Fernández-Jiménez and Puertas, 2001, 2003; Krizan and Zivanovic, 2002; Atiş *et al.*, 2009) but often lowers the ultimate strength when the NaOH and Na_2SiO_3 activators are used separately.

The general tendency is that raising the curing temperature enhances the strengths at early ages (3, 7 days) - except for the flexural strength of the NaOH activated slag which lowers. However, at late ages (28, 270 days) the strength increase with rising temperature is less significant, and sometimes the ultimate strength lowers (e.g. the compressive strength of Na_2SiO_3 activated slag at 270 days drops considerably when cured at 60 °C). Yet, the tendency is that the ultimate strength increase when rising the curing temperature is not significant, agreeing with former literature (Wang and Scrivener, 1995; Fernandez *et al.,* 1999). Similarly, (Bakharev *et al.,* 1999) report that heat initially accelerates the strength development of AA slag concrete, but at later ages, the compressive strength is reduced when compared with room temperature curing. They observed that curing at 70°C accelerates early strength but, after 28 days, the strength was reduced by 35 to 45%.

Most of the strength variation triggered by the higher curing temperature is within the values reported by Bakharev *et al.,* (1999), who studied the performance of AA slag materials up to the age of 540 days and report total strength variations of around 5 MPa, and no significant ultimate strength variation with increasing curing temperature from 20 to 60 °C.

The NaOH activator tends to perform best at room temperature agreeing with (Fernandez *et al.,* 1999) who note that an increase of temperature lowers the strength of NaOH- activated slags at all ages and with Altan and Erdoğan, (2012). The 0.77 MPa result of the NaOH-activated slag is unreliable, and likely due to a defective specimen with microcracks.

Table 5-2 Compressive and flexural strengths of AA GGBS materials: effect of the type of activator, curing temperature and age. 3:1 (sand:GGBS); Na_2SiO_3/NaOH=1.5; 8M NaOH.

	Flexural strength						Compressive strength					
Activator	Na_2SiO_3+NaOH		NaOH		Na_2SiO_3		Na_2SiO_3+NaOH		NaOH		Na_2SiO_3	
COVs	0.05-0.13		0.00-0.20		0.01-0.41		0.10-0.48		0.00-0.23		0.05-0.29	
Curing T	20°C	60°C	20°C	60°C	20°C	60°C	20°C	60°C	20°C	60°C	20°C	60°C
3 days	0.66	7.31	3.33	1.75	0.28	0.81	1.88	44.11	8.09	8.56	0.60	1.30
7 days	3.51	7.10	3.07	1.15	0.70	0.93	12.08	34.38	8.77	7.53	1.31	1.50
28 days	6.12	7.09	0.77	1.65	1.89	3.25	25.70	33.69	17.56	12.03	5.21	2.92
270 days	7.01	7.26	5.62	8.26	5.70	3.05	93.06	94.36	61.11	65.31	32.79	24.63
% Change 28-270 d	+12	+2	+86	+80	+66	-6	+72	+64	+71	+81	+84	+88
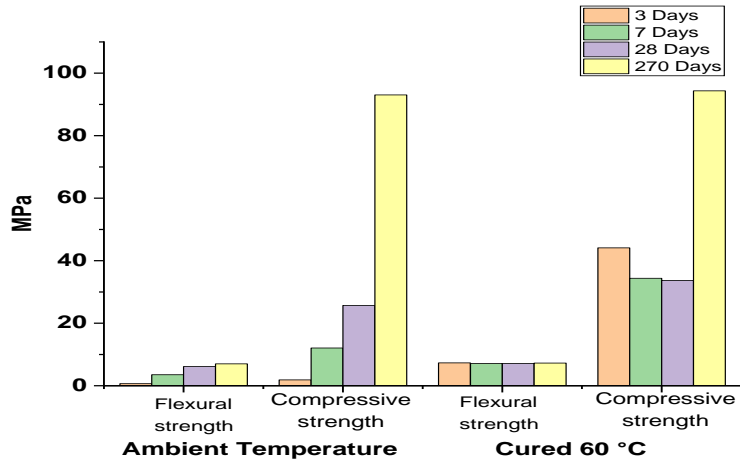
Figure 5-2 Strength development of the Na_2SiO_3+NaOH-activated, GGBS mortars.
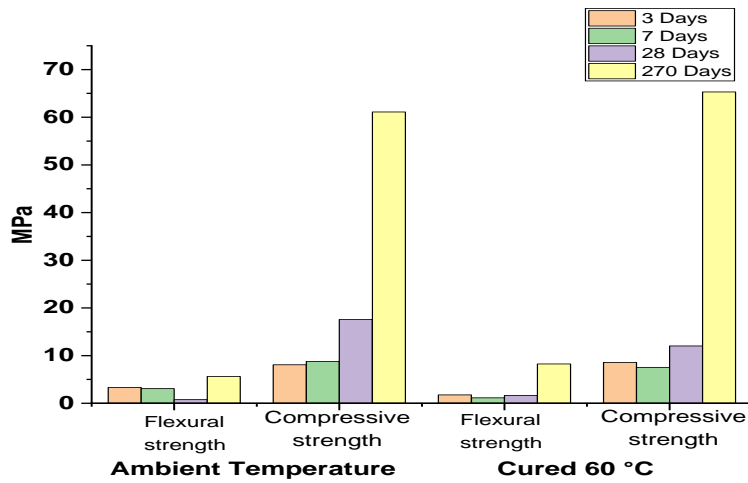
Figure 5-3 Strength development of the NaOH-activated, GGBS mortars.
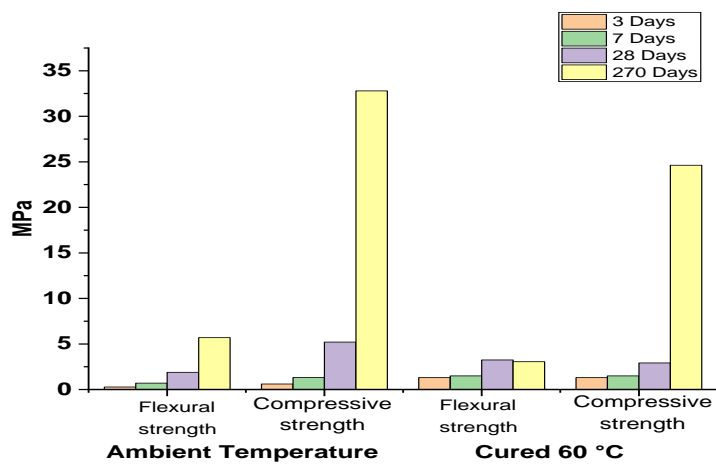
Figure 5-4 Strength development of the Na_2SiO_3-activated, GGBS mortars.

5.1.3 Effect of accelerated weathering on the mechanical strength of AAS materials

It was expected that the AAS materials would lose some strength as a result of weathering, but the results are inconsistent, and the strengths after weathering are sometimes higher than before (Table 5-3). This agrees with former authors: Bakharev *et al.,* (2002), following experiments with exposure to acid attack, found strength increase in AAS concrete. Similarly, (Luga, 2015) evidenced that slag geopolymers increased compressive strength by 14-24% following wet-dry cycles, and other authors found a compressive strength increase after freeze-thaw cycling (Kukko and Mannonen, 1982; Bernal *et al.*, 2014; Azarsa and Gupta, 2020). The strength increase have been attributed to the presence of smaller pores (Ellis *et al.*, 2015) but is likely the result of continuing hydration (Bakharev *et al.,* 2002).

In this research, raising the curing temperature of the AAMs does not seem to increase durability, as the strength losses of the room-cured specimens after cycling are comparable to those cured at high temperature. No consistent trend was found to help determine whether a certain weathering agent undermines the AAS materials further than another, as the strength losses after the three types of cycles are comparable. The Na_2SiO_3+ NaOH activated GGBS specimens lost the least strength as a result of performing durability cycles.

Table 5-3 Effect of accelerated weathering on the 270-day strength of the AAS materials (MPa).

	Na_2SiO_3+NaOH activated				NaOH activated				Na_2SiO_3 activated			
	Flexural strength		Compressive strength		Flexural strength		Compressive strength		Flexural strength		Compressive strength	
	20°C	60°C	20°C	60°C	20°C	60°C	20°C	60°C	20°C	60°C	20°C	60°C
Wet-dry	6.75	8.97	93.06	91.83	4.69	5.25	61.11	71.91	1.41	8.09	17.97	32.45
Salt crystallization	5.13	6.47	96.34	98.68	5.06	7.05	65.31	74.76	4.60	6.57	8.24	25.88
Freeze-thaw	5.51	6.59	77.43	87.41	3.56	2.47	38.50	40.33	0.54	3.06	20.40	16.63
Control (No cycles)	7.01	7.26	93.06	94.36	5.62	8.26	61.11	65.31	5.70	3.05	32.79	24.63
COVs	0.04- 0.35	0.04- 0.10	0.05- 0.50	0.03- 0.10	0.07- 0.17	0.02- 0.13	0.02-0.45	0.02-0.17	0.00-0.68	0.09- 0.24	0.06-0.50	0.15- 0.30

5.1.4 Mass loss and microscopic damage induced by accelerated weathering

Salt-crystallization cycling. The Na_2SiO_3+ NaOH activated GGBS showed the best durability after salt crystallization cycling. Some specimens lost/gained a small amount of mass (Table 5-4). However, no damage appeared after cycling. The Na_2SiO_3 activated GGBS lost insignificant material after 20 salt crystallization cycles. However, several specimens showed microcracks with no expansion or displacement and efflorescence (Figure 5-5). The NaOH activated GGBS displays the worst resistance to salt-induced damage, with efflorescence and slight swelling appearing after 15 cycles, and c.3% mass gain probably linked to the absorption and retention of salt solution inside voids and cracks (Figure 5-6).

Table 5-4 Mass loss of AAS materials after salt crystallization cycling.

	Mass loss (%)		
	Na_2SiO_3+NaOH activated	NaOH activated	Na_2SiO_3 activated
Cured at 20°C	-1.53	3.55	-0.33
Cured at 60°C	1.78	2.98	-0.36
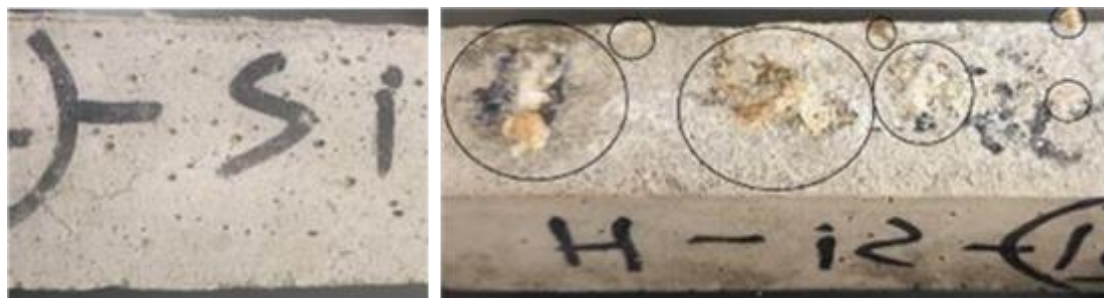
Figure 5-5 Na_2SiO_3 activated GGBS after salt crystallization cycles. Left: Microcracks in the 20°C- cured specimens. Right: efflorescence in the 60°C-cured specimens.

Figure 5-6 NaOH activated GGBS, 60°C-cured, after salt crystallization cycling showing cracks.

The intensity of sulphate attack has been related to the alumina content. The alumina content of the GGBS is c.12% wt which complies with the BS 8500 requirements for a high- resistance (+SR) PC concrete for aggressive ground conditions. It is a similar content than in other slags, but slightly higher than many PCs (usually 4-6%, the majority below 10%). Nevertheless, no gypsum or ettringite were recorded with the SEM (see section 5.1.5 microstructure and microscopic damage). In the AAS materials investigated, the slag is the only source for alumina therefore the content is within safe levels regarding durability.

Wet-dry cycling. The resistance to deterioration induced by thermal and moisture expansion was assessed by performing 15 wet-dry cycles. The specimens were immersed in water at a constant temperature of $20 \pm 0.5°C$ for 16 hours and dried in an oven preheated to $105°C$ for 6 hours. The best durability after wet-dry cycling is shown by the Na_2SiO_3+NaOH activated GGBS cured at 60°C and 20°C. The mass change (c.0.5%) is insignificant, and the specimens showed virtually no alteration after cycling. The worst resistance to wet-dry cycling is shown by the Na_2SiO_3 activated GGBS which shows the greatest mass variation at c.4% (Table 5-5). Cracks and efflorescence appeared after 15 cycles (Figure 5-7) indicating certain water absorption and retention.

Table 5-5 Mass loss of AAS specimens after thermal/moisture cycling.

	Mass loss (%)		
	Na_2SiO_3+NaOH activated	NaOH activated	Na_2SiO_3 activated
Cured at 20 (°C)	0.51	1.59	-3.57
Cured at 60 (°C)	0.42	0.86	-4.13

Figure 5-7 Na_2SiO_3 activated GGBS after 20 wet-dry cycles. Left image 20 °C cured, right 60 °C cured showing cracks, delamination and slight efflorescence.

The literature tends to agree on that AAMs and geopolymer mortars remain structurally intact without any visible cracks or deterioration for longer, while surface microcracks appear on PC

mortars following wet-dry cycles, due to the shrinkage. Djobo *et al.*, (2016) evidenced no visual deterioration after 20 wet-dry cycles in mortars made with alkali-activated volcanic ash, and small compressive strength reductions of 24% and 14% for specimens cured at 27 °C and 80 °C, respectively. The results agree with Luga (2015) who evidenced a high resistance to wet-dry cycles for slag/FA geopolymers, and an increase in compressive strength by 14% and 24% respectively for slag and FA/slag geopolymers.

Freeze-thaw cycling. The best durability after freeze-thaw cycling is shown by the Na_2SiO_3+NaOH activated GGBS with no degradation or efflorescence, and the highest mechanical strength (cured at 60 °C)- Table 5-3 and Table 5-6. It is well known that pore structure and saturation largely determine the amount of damage by frost action, as water held in pores expands on freezing, causing stresses and eventually disruption, which is usually evidenced as micro-cracks that finally cause material detachment. Their high performance is probably due to the dense microstructure and close pore structure observed with the SEM below. The results agree with Fu *et al.,* (2011) who showed experimentally that alkali-activated (Na_2SiO_3, NaOH) slag concrete has an excellent freeze-thaw resistance. They evidenced a high resistance, with slight weight loss (<1%) after 300 cycles and a frost resistance coefficient of $\sim$90%. The high resistance is attributed to the lack of $Ca(OH)_2$ (the hydration products were mostly C-S-H), resulting in a compact and homogeneous matrix with excellent freeze-thaw durability. The Na_2SiO_3 activated GGBS cured at 60 ^{0}C showed the highest weight loss after 15 cycles, and the NaOH-activated slag showed efflorescence (Figure 5-8).

Table 5-6 Mass loss of AAS specimens after freeze-thaw cycling.

	Mass loss (%)		
	Na_2SiO_3+NaOH activated	NaOH activated	Na_2SiO_3 activated
Cured at 20 (°C)	-1.53	-1.35	-1.69
Cured at 60 (°C)	-1.41	-1.90	-3.76

Figure 5-8 Efflorescence on NaOH activated GGBS after 20 freeze- thaw cycles (left 20°C-cured; right 60°C).

5.1.5 Microstructure and microscopic damage

The Na$_2$SiO$_3$+NaOH activated GGBS showed the best mechanical strength. Therefore, its microstructure was investigated with petrography and SEM analyses. The microscope analyses show a dense microstructure where macropores are virtually absent. Given the restricted and qualitative nature of these techniques, no direct correlation could be established between the microscopic analyses and the strength results. However, the results evidenced that the microstructure of the material is sound, the aggregate and the GGBS are evenly distributed and the bond at the interface is continuous (Figure 5-9-Figure 5-12). In the ambient cured materials (Figure 5-9), the petrographic microscope showed abundant unreacted GGBS grains in an opaque groundmass with occasional patches of cement. However, in the oven cured materials (Figure 5-10), the structure of the matrix is more crystalline, and the GGBS particles often show reaction and the formation of cementing hydrates. The petrographic microscope did not provide enough resolution to identify the nature of the hydrates. However, no alkali-aggregate reactions or alkali-silica reactions were evident (Figure 5-11-Figure 5-12), and none of the aggregates had reacted with the alkaline binder, not even the microsilica (chert) grains comprising the aggregate. The SEM analyses confirmed the petrographic analysis results. Furthermore, the SEM showed micro-cracks owed to shrinkage, that were invisible in the Na$_2$SiO$_3$+NaOH activated GGBS with the naked eye and with the resolution of the petrographic microscope (Figure 5-13). Cracking due to drying shrinkage is one of the challenges for alkali-activated slag materials, and it increases as the lime content in the system lowers (Shi *et al.,* 2006). Hence the high Ca content of this slag has probably reduced drying-shrinkage cracking and contributed to the sound microstructure of the materials.
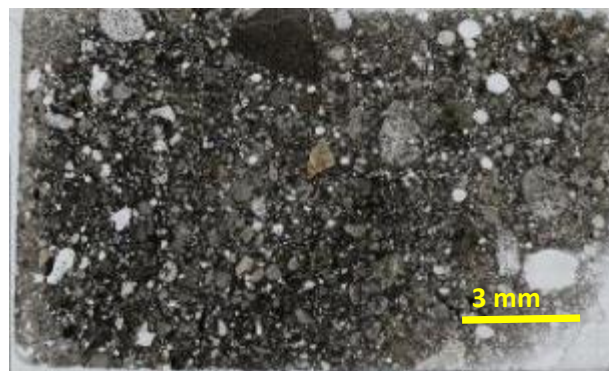
Figure 5-9 Na$_2$SiO$_3$ + NaOH activated GGBS cured at ambient temperature where abundant fine GGBS is still evident in the matrix.

Figure 5-10 Na$_2$SiO$_3$ + NaOH activated GGBS cured at 60°C shows stronger reaction, with a more homogeneous matrix where much of the GGBS has become cement.
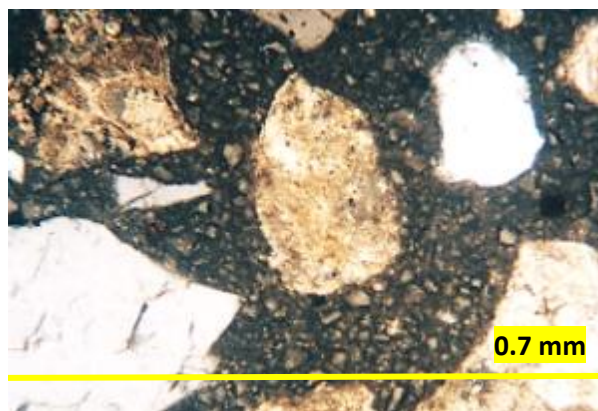
Figure 5-11 Representative image of the Na$_2$SiO$_3$ + NaOH activated GGBS, cured at ambient temperature, with abundant unreacted GGBS in the matrix and sound aggregate with no evidence of alkali reaction. X20 polarised light.
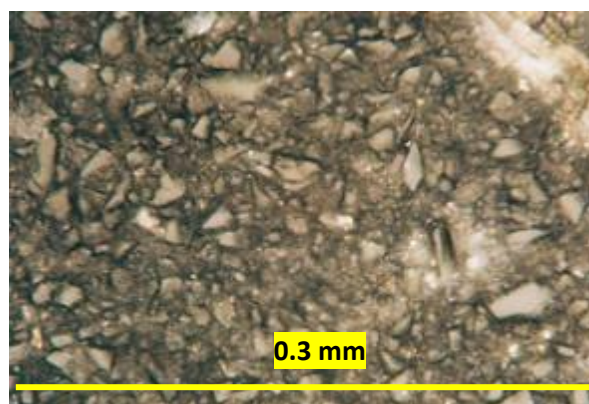
Figure 5-12 Detail of the GGBS reaction and the cement formed by alkali reaction in the oven-cured, Na$_2$SiO$_3$ + NaOH- activated, GGBS matrix. X40 polarised light.

Figure 5-13 SEM images of the Na$_2$SiO$_3$/NaOH activated GGBS, cured at ambient temperature, showing fractures and abundant unreacted GGBS.
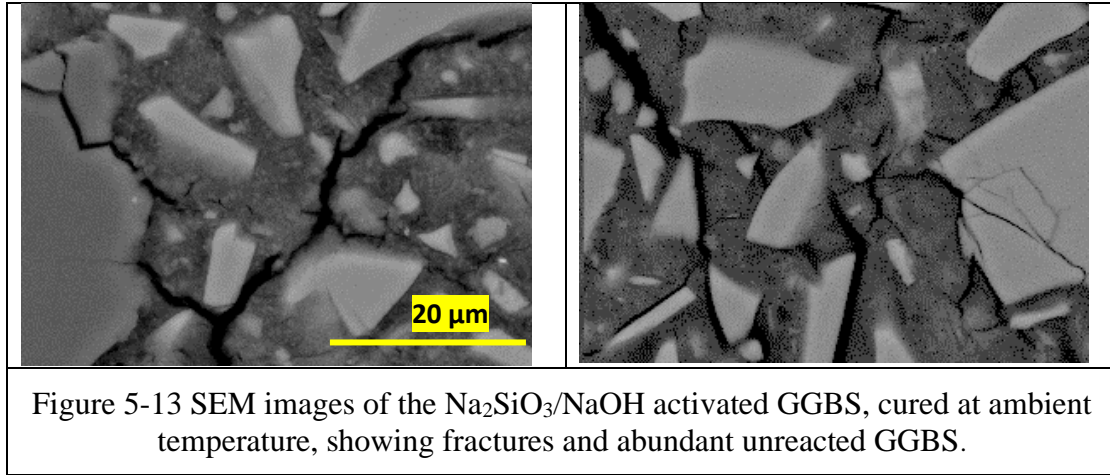
A slight surface precipitate known as efflorescence appeared after salt crystallization, wet-dry and freeze-thaw cycling in most of the specimens that were NaOH and Na$_2$SiO$_3$ activated. The formation of efflorescence in AA materials is relatively common. It has been associated with high concentrations of hydroxide activator in slag materials (Pacheco-Torgal *et al.*, 2014; Provis *et al.,* 2014), and with the depolymerization of cementing hydrate gels at advanced times of curing. In AA materials, Ke *et al.*, (2015) linked efflorescence to the loss alkali cations from cementing hydrate gels. Several authors state that it results from the leaching of alkalis in the AAMs and their reaction with CO$_2$ in the atmosphere i.e. unreacted sodium is mobile within the pore network, and that is prone to the form efflorescence when in contact with atmospheric CO$_2$ (Allahverdi *et al.,* 2008; Kani and Allahverdi, 2009; Škvára *et al.*, 2009; Temuujin and Riessen, 2009; Pacheco-Torgal and Jalali, 2010; Najafi *et al.,* 2012). The tendency towards efflorescence in AAMs has also been related to a high alkali concentration in the pore solution (Lloyd *et al.,* 2010) and to the relatively weak binding and exchangeability of the sodium in the aluminosilicate gel structure (Bortnovsky *et al.*, 2008; Szklorzová and Bílek, 2008).

On hand samples, the salts show a similar powdery habit, and do not seem to be associated to expansion, cracking or bulging of the specimens. However, this was further investigated microscopically with a scanning electron microscope. Under the microscope, the salts appear to cover areas erratically, hence it was not possible to conclude whether they originate from the cementing gel or not. However, the elemental composition shows that the salts are mainly soda (Na$_2$O) probably mixed with some sodium carbonates and sulphates (Figure 5-14-Figure 5-17).
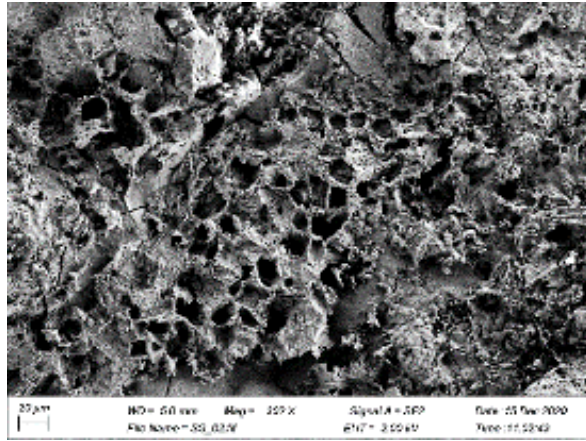
Figure 5-14 Alkali-activated GGBS after frost cycling, showing an area with erratic distribution of salt efflorescence.
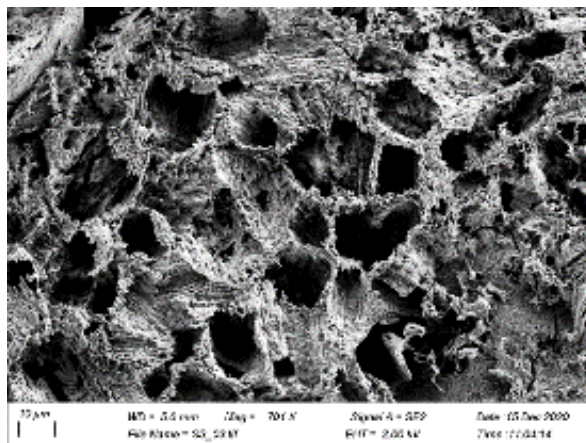
Figure 5-15 Detail of the salts in Figure 5-14; their composition appears in Figure 5-17.
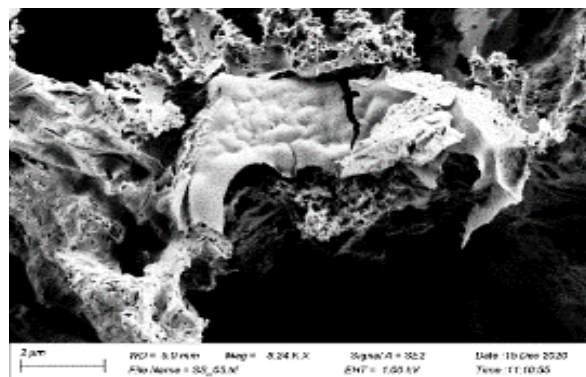
Figure 5-16 Detail of the salts after frost cycling.
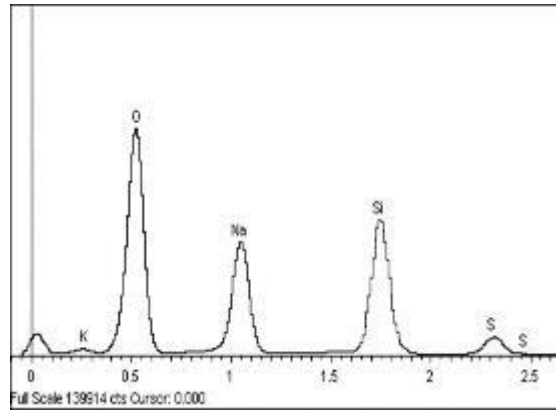
Figure 5-17 The elemental composition shows that the salt is mainly soda (Na_2O) probably mixed with some sodium carbonates and sulphates.

Sulfate damage to PC materials is usually associated to the presence of aluminates, as the reaction between sulfate and PC aluminates produces expansible ettringite and gypsum which lead to cracking and disruption, hence low aluminium PC materials have superior resistance to sulfate environments (Lawrence and Hewlett, 1988). Despite the Al content in the slag (12%) and the sulphur in the test solutions, neither expansive gypsum nor ettringite were recorded with the SEM. Hence, the salts can be partly attributed to the high alkalinity of the materials which, together with the high mobility of the sodium and the salt solution, have enabled efflorescence to precipitate on the surface of the specimens. The SEM examination confirmed the superficial distribution and the lack of expansive cracks or bulging associated to the efflorescence (Figure 5-18-Figure 5-20).

The microstructure of the best performers (Na_2SiO_3+NaOH activated GGBS cured at 60°C after 270 days of curing) seems unaltered after cycling. It varies from areas consisting of unreacted GGBS particles and scattered silica cements (Figure 5-18-Figure 5-20) to others featuring abundant silicates with different habits, mainly isometric and tabular (Figure 5-21).
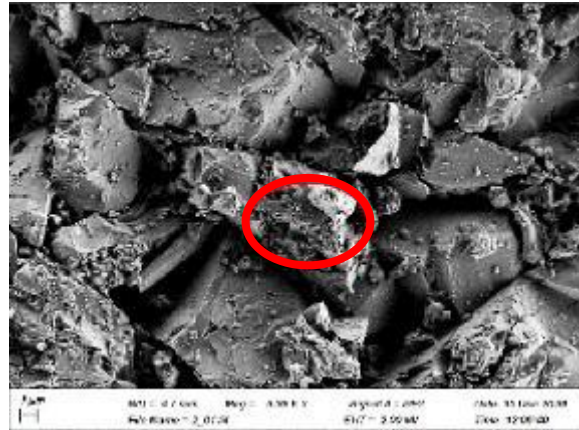
Figure 5-18 Microstructure of the Na$_2$SiO$_3$+NaOH activated GGBS cured at 60°C at 270 days showing unreacted GGBS particles and scattered cements.
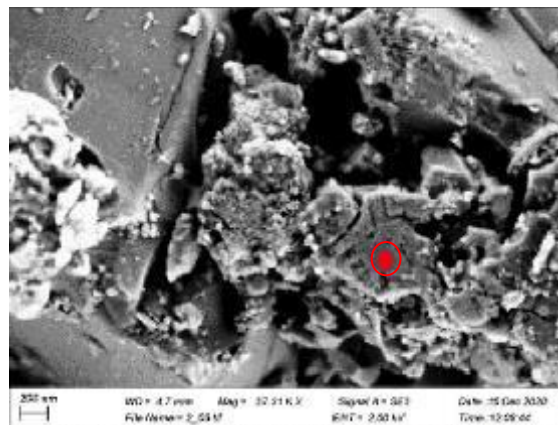
Figure 5-19 Detail of the cementing hydrates in Figure 5-18. The elemental composition of the cement (marked with a red dot) is shown in Figure 5-20.
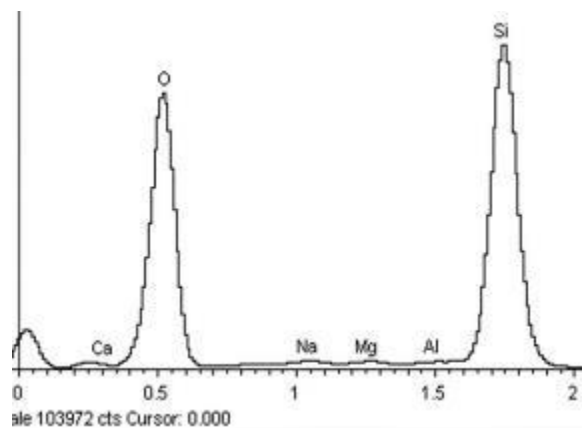
Figure 5-20 Elemental composition of the silica cement in Figure 5-19.
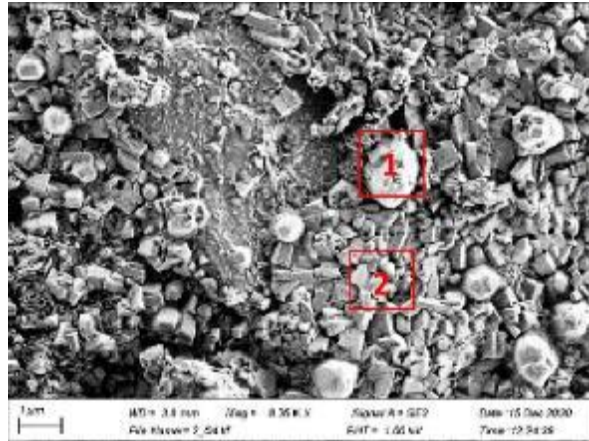
Figure 5-21 Microstructure of the Na_2SiO_3+NaOH activated GGBS cured at 60°C after 270 days, with abundant octahedral and tabular silicates (Figure 5-22-Figure 5-23).
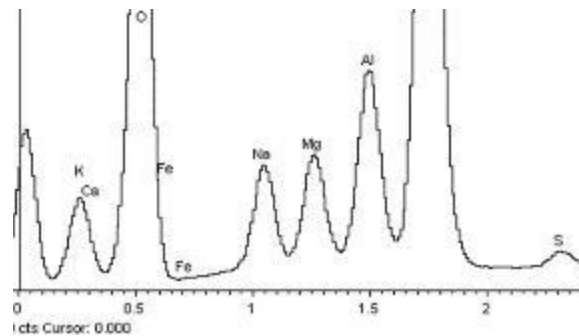
Figure 5-22 Elemental composition of the octahedral silicates. Spectrum 1 of Figure 5-21.
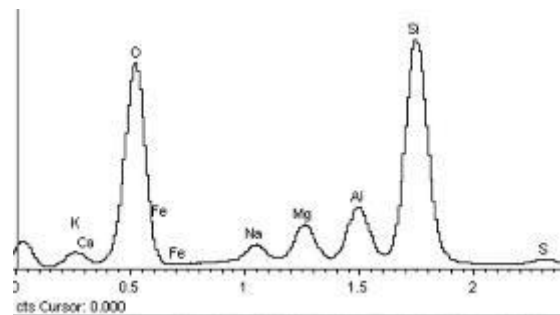
Figure 5-23 Elemental composition of the tabular silicates. Spectrum 2 of Figure 5-21.

This microstructure agrees with previous authors. It is well known that the main reaction product in alkali silicate activated slag binders is a poorly crystalline C-A-S-H type gel. However, hydrogarnets such as katoite have also been found (Bernal *et al.*, 2013). The

elemental composition of the abundant octahedral and tabular phases evidenced suggests that they are calcium alumino silicates (Figure 5-22-Figure 5-23), some including Mg. The Na content is provided by the activator and picked up by the scattered EDX beam. The presence of these phases agrees with the alumina content of the GGBS (approximately 12%). The octahedral crystals are likely the garnet katoite, a member of the $Ca_3Al_2(SiO_4)_3$- $Ca_3Al_2(SiO_4)_3$ $(OH)_{12}$, calcium aluminum silicate hydrate series of the hydrogrossular group. It is similar to the mineral identified by Passaglia and Rinaldi, (1984) in natural outcrops associated to lava flows. The appearance of this phase has been facilitated by the curing at 60 °C (Kyritsis *et al.,* 2009).

5.1.6 Setting time

All the activators produced similar setting times except for the NaOH activated slag which requires a significantly longer time to finally set (Table 5-7). The results agree with others reported in the literature. Previous authors have reported that, when finer than 450 m^2/kg, AA slag binders set in 1-3 minutes and hence the material is impossible to pour (Talling and Brandstetr, 1989). However, despite the slag being ultrafine, the setting times are over one hour for all the activators. The setting times are faster than others previously reported. Andersson & Gram, (1987) reported that, for AA slag pastes activated with Na_2SiO_3, the initial and final setting times were 2h 20min and 4h 45min respectively; and 3h 40min and 4h 40 min when activated with NaOH.

According to Andersson and Gram (1987), the fineness of the slag does not affect the setting time significantly between values ranging from 350-530 m^2/kg. However, the setting times are much shorter when fineness increases. The setting time also depends on the basicity (CaO+ MgO / SiO_2) of the slag. Higher basicity will likely result in shorter setting times regardless of the activator (Krivenko, 1994). The more basic the slag the greater its hydraulic activity in the presence of alkali activators (Lawrence and Hewlett, 1988). In general, glassy slags with CaO/SiO_2 ratios between 0.50 and 2.0, and Al_2O_3/SiO_2 ratios between 0.1 and 0.6 are considered suitable for alkali activation (Provis, and Deventer, 2014). Hence, the CaO content increases with the basicity of GGBS, leading to a shorter setting time (Shi and Qian, 2000).

Table 5-7 Setting time for alkali activated slags.

Activators	Initial time: t_i	Final time: t_f	$\blacktriangle t = t_i - t_f$	Slag properties	
				Fineness (m²/kg)	Basicity
Na_2SiO_3	1h11 min	1h31 min	20 min	1950	1.56
Na_2SiO_3/NaOH	1h 8 min	1h26 min	18 min		
NaOH	1h15 min	2h 8 min	53 min		
(Fernández-Jiménez and Puertas, 2001; A. Fernández-Jiménez and Puertas, 2003)					
Na_2SiO_3	1h16 min	1h46 min	20 min	460	1.51
80%Na_2SiO_3/20%NaOH	1h15 min	1h55 min	25 min		
NaOH	2h45 min	3h50 min	30 min		
80%NaOH/20%Na_2SiO_3	1h10 min	1h40 min	20 min		
(Andersson and Gram, 1987)					
Na_2SiO_3	2h20min	4h45min	2h25min	550	1.40
NaOH	3h40min	4h40 min	1 h		

5.2 PROPERTIES OF AA MATERIALS MADE WITH RM ALONE AND BLENDS OF RM WITH FA/GGBS

This section studies the feasibility of producing AAMs with RM and blends where RM is partially replaced with FA and GGBS at 30% and 50%. The RM was activated either with Na_2SiO_3 or with Na_2SiO_3/NaOH at varying ratios. The mechanical strengths, setting times, porosity, water absorption and density of the resultant materials were measured. In addition, their durability was assessed by measuring the strength loss, mass loss, and visual deterioration after accelerated cycling.

5.2.1 Mix design

The RM calcined at 400 °C was selected to produce the AAMs. As seen in chapter 4, at 400°C, the RM is most amorphous and shows the greatest reactivity (highest lime combination, greatest mechanical index and fastest set) due to the transformation of gibbsite (Al $(OH)_3$) into boehmite (Υ- AlO(OH)) and amorphous alumina polymorphs, and the presence of maximum cancrinite. At this temperature, the RM consists of hematite (Fe_2O_3), cancrinite ($Na_6Ca_2[(CO_3)_2|Al_6Si_6O_{24}]\cdot 2H_2O$) and sodalite ($Na_4Si_3Al_3O_{12}Cl$). High reactivity facilitates geopolymerisation. Previous authors noted that calcination of RM improves the dissolution of aluminosilicate phases enhancing geopolymerization (Ye *et al.*, 2012).

In general, the composition of the RM, namely the Si, Ca and Al reactive in an alkali media indicates potential for use in AA technology (Dimas *et al.,* 2009). Usually, RM is high in silica from bauxite impurities, and includes some residual Al (Provis *et al.,* 2014). Hence, the typically higher Si/Al ratio may result in a weak final product (Duxson *et al.*, 2007; Hajjaji *et al.*, 2013). According to Provis *et al.*(2014), the low Al in RM is the most significant challenge for the use of RM in AAMs. For this reason RM is usually blended with supplementary Al sources such as FA (Kumar and Kumar, 2013), and/or Ca sources such as GGBS (Pan *et al.*, 1998; Pan *et al.,* 1999) to produce AAMs. However, the RM in this research is high in Al (c.30%wt). As aforementioned, the Saudi RM has higher silica (20%) and alumina (30%) than most in the literature. Therefore, it is possible that the Saudi RM may produce AAMs alone.

Partially replacing RM with FA and GGBS

To produce some of the AAMs, the RM was partially replaced with FA or GGBS. As seen in the RM characterisation (chapter 4), the Saudi RM has higher silica and alumina and lower iron than most in the literature, and it is more alkaline than most. In summary, the RM is high in Al (30%) and silica (20%) and low in Ca (5%). When blended, the GGBS contributes abundant Ca (42%) and Si (32%), and some aluminium (12%), while the FA contributes abundant silica (62%) and Al (23%) – Chapter 4 and Table 5-8.

Therefore, the RM-FA combination results in a low calcium system which hence may lack calcium silicate hydrate cements. In contrasts, the RM-GGBS combination results in a high-calcium system, whereby the calcium would form hydraulic calcium silicate hydrates. Furthermore, as seen in Chapter 4, nearly the total mass of the GGBS is amorphous which means that the silica and alumina comprising the slag are reactive. Also as seen in chapter 4, the FA is highly reactive, including a high glass content of roughly 40-60%. Despite having a low-CaO, the FA is ultrafine, with 90% of the particles under 100 microns and high specific surface areas, at 6500m^2/kg.

Table 5-8. Chemical composition of the precursors used to make the AA RM materials (see Chapter 4). %wt

	SiO$_2$	Al$_2$O$_3$	CaO	Fe$_2$O$_3$	Na$_2$O	K$_2$O	MgO	SO$_3$	TiO$_2$	MnO
RM	*19.66*	*29.79*	*5.08*	*12.96*	*24.05*	*0.09*	*0.40*	*1.65*	*5.12*	*0.02*
GGBS	31.71	10.83	44.90	0.51	0.03	0.71	7.50	2.08	0.95	0.17
GGBS	34.14	13.85	39.27	0.41	0	0.26	8.63	2.43	0.54	0.25
FA	53.40	21.18	4.14	9.99	0.70	3.24	1.86	2.67	1.35	0.07
FA	65.32	24.72	0.94	4.84	-	1.37	0.68	0.37	0.91	-

Effect of activator

Previous authors have proven that the solid NaOH (or Na_2O) naturally occurring in RM can dissolve to provide an alkaline medium. According to several authors, the high alkalinity of RM contributes to geopolymerisation, but a NaOH activator solution is still required to achieve a desirable strength (Kumar and Kumar, 2013; Singh et al., 2016; Kulkarni, 2018; Kumar *et al.*, 2021). NaOH at 6M has been proposed as the optimum activator to enhance reaction and mechanical properties (Kumar and Kumar, 2013). In general, an increase in NaOH content increases alkalinity which enhances the dissolution rate of the aluminosilicate precursor (Ana Fernández-Jiménez and Puertas, 2003; Ke *et al.*, 2015) which boosts strength (Figure 5.24). However, an excess of OH^- and Na^+ produced at high NaOH concentration lowers mechanical strength. The Na^+ excess prevents the formation of oligomers at later stages which lowers strength (Aziz et al., 2020). The Na^+ excess can form sodium carbonate due to atmospheric carbonation which may disrupt the polymerization process (Barbosa *et al.,* 2000; Al Bakri *et al.,* 2013).

The UCS of RM geopolymers at RM contents 40–60% are comparable with those of other polymers made with one-part mix fly ash (with high unburned carbon particles) inorganic polymers activated with NaOH contents of 3–5%, indicating that the alkalinity (NaOH) supplied by RM contents of 40–60% could be equivalent to adding 3–5% NaOH activator Figure 5-24 (Choo *et al.*, 2016).

The Saudi red mud's pH was measured and found to be over 11. It contains significant Na_2O, which can act similarly to the NaOH activator or as a retarder on hydration.
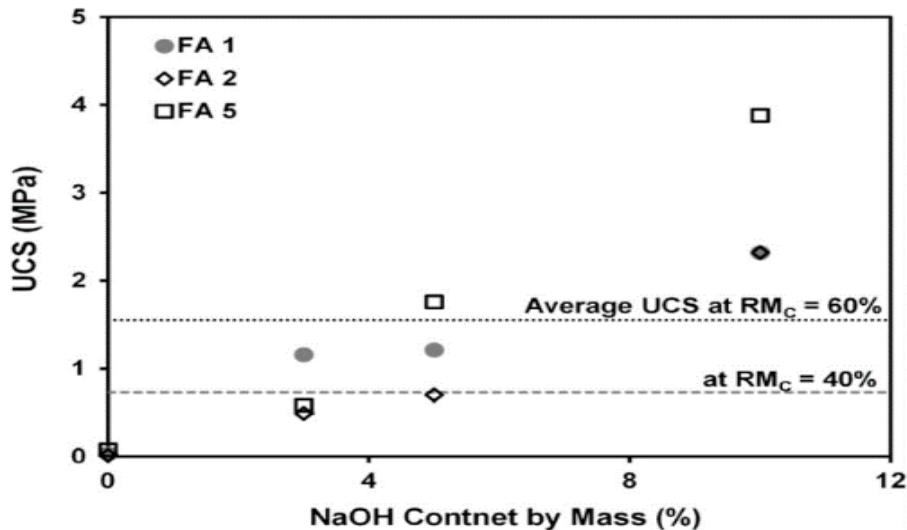
Figure 5-24 Unconfined compressive strength (UCS) of three different alkali-activated FAs as a function of NaOH content by mass (Choo *et al.*, 2016).

Dimas *et al.* (2009) studied the effect of NaOH activator concentration (3 to 10M) on the compressive strength of AA RM and metakaolin materials. The SiO_2 content of the activator was constant at 3M, the RM/metakaolin mass ratio of the solid phase was also constant at 85:15 and the solid/liquid ratio was 2.9 g/mL. The results (Figure 5-25) showed the compressive strength of the materials versus the initial NaOH activator concentration: between 3 and 6M NaOH concentration, the compressive strength was almost invariable at 7.7MPa. As the NaOH concentration increased from 6M to 8M, the strength increased substantially, reaching a maximum of 14.64MPa. A further increase of NaOH concentration to 10M caused substantial strength reduction. Therefore, polycondensation is best at intermediate NaOH concentration of around 8M. In general, high NaOH concentration promotes the dissolution of the silicon and aluminium in the precursors which normally facilitates polycondensation due to the increase of the SiO_2/Na_2O mass ratios in the aqueous phase. However, very high initial NaOH concentrations damage polycondensation because the amount of dissolved silicon and aluminum remains almost constant while the free NaOH increases, resulting in lower SiO_2/Na_2O mass ratios in the aqueous phase Dimas *et al.* (2009).

According to Provis and Van Deventer (2013), waterglass - Na_2SiO_3 - should be used as activator when synthesizing RM-GGBS polymers. In general Na_2SiO_3 activators are reported to introduce a volume of soluble SiO_2 to form monomers, dimmers, oligomers, and a growth of a better microstructure than the SiO_2 dissolved from the precursors (Singh *et al.,* 2005). It is widely acknowledged in AAM technology that soluble silica provides monosilicate species

in the liquid phase which are responsible for the formation of oligomers and their polycondensation, and that the higher the initial silica concentration, the greater the polycondensation rate and the compressive strength of the materials produced.
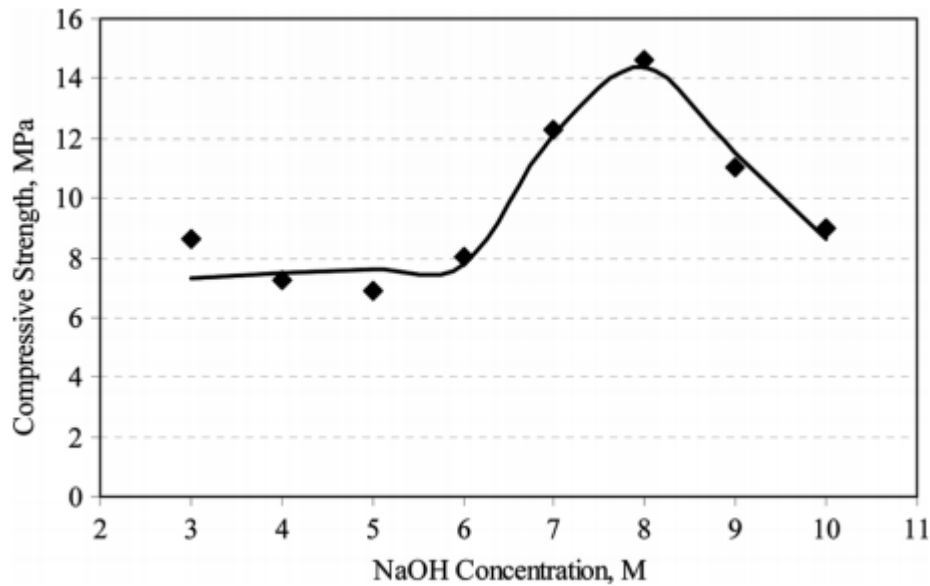
Figure 5-25 Compressive strength VS NaOH concentration (Dimas *et al.,* 2009).

Dimas *et al.* (2009) studied the effect of the initial soluble silica concentration in the activator, with the NaOH activator constant at 8M (S/L ratio =2.9 g/mL and RM/metakaolin wt = 85:15). Their results (Figure 5-26) show that increasing soluble silica concentration from 3M to 3.5M caused a substantial increase in compressive strength from 15MPa to 20MPa, but a further increase did not significantly affect strength. At higher silica concentration, cracks formed on the surface immediately after demoulding, which grew bigger as the silica concentration increased. However, despite the surface cracks, the materials displayed good mechanical properties, indicating a good degree of polymerization. The authors blamed the surface cracks on a high polycondensation rate forming an impermeable surface membrane that entrapped the free water of the aqueous phase which expanded during curing creating the cracks.
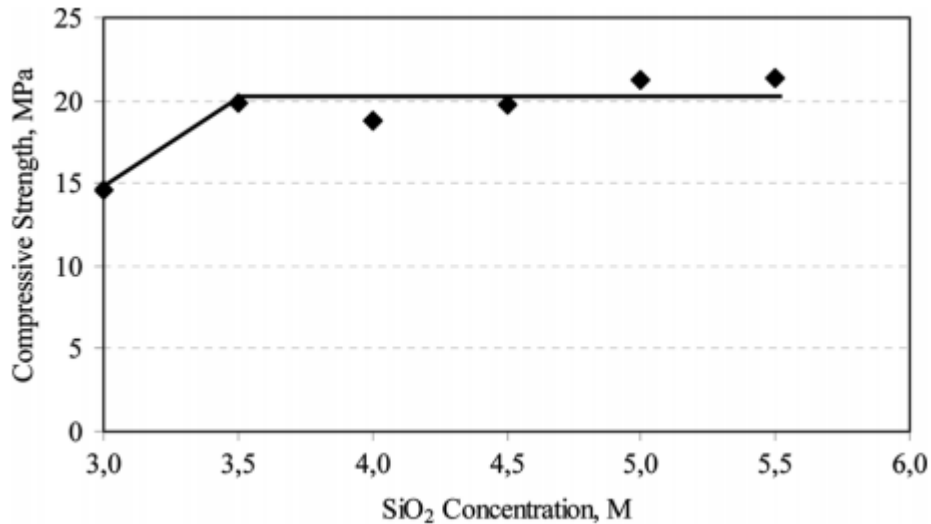
Figure 5-26 Compressive strength VS initial SiO_2 concentration (Dimas *et al.,* 2009).

With respect to blending activators for RM geopolymers, it is generally recommended to blend Na_2SiO_3 with NaOH to minimize the disadvantages of NaOH activation including heat generation. Cheng *et al.*, (2019) developed a 70% slag-30% RM geopolymer activated with a NaOH/Na_2SiO_3 at 1/3 ratio reaching 16.7 MPa compressive strength at 28 days. Singh *et al.*, 2016 developed a RM-FA geopolymer with NaOH/Na_2SiO_3 (1 /2.5). The RM content varied from 10 to 100% and the NaOH concentration from 6 to 12 M. The geopolymer containing 30% RM, activated with a 12M NaOH solution obtained the best 28-day strength at 38 MPa. Singh *et al.* (2016) studied 30-50% RM geopolymers, blended with FA and GGBS, activated with NaOH 6-10M and Na_2SiO_3/NaOH at 2.5. The results showed compressive strength ranging from 6 to 12 MPa, and that increasing RM substitution and NaOH molarity lowered strength. The optimum NaOH molarity was 6M for maximum strength. According to Singh et al. (2018) geopolymers made with 30% RM, FA (class-F) and 10% GGBS reached compressive strengths ranging from 35 to 43.8 MPa. Those activated with NaOH of 6 M exhibited maximum strength.

Effect of curing temperature

High temperatures can dissolve faster the silica-alumina in the precursor and produce a faster geopolymerization. However, previous authors preferred ambient temperature in RM-geopolymers, because a geopolymerization rate too fast can lead to insufficient dissolution and rapid setting that reduces strength (Muraleedharan and Nadir, 2021). The dissolution-

recombination–solidification of $[SiO_4]$ and $[AlO_4]$ from the aluminosilicate precursors in alkaline solutions can happen at room temperature (He *et al.*, 2013; Wan *et al.*, 2017; Ai *et al.*, 2021). Curing AA RM at room temperature shows a better microstructure and enhanced mechanical properties (Watling *et al.,* 1975; Kumar and Kumar, 2013; Singh *et al.,* 2016).

According to Singh et al., (2018) a 30% RM and 10% GGBS/FA geopolymer, cured at ambient temperature, reached its maximum strength (43.8 MPa) when activated with 6M NaOH. The strength reduced with increasing molarity, reaching 36.8 MPa at 8 M and 35 MPa at 10 M. This is attributed to the higher concentration of OH^- ions in high molarity solutions, leading to early precipitation of aluminosilicate gel which hinders geopolymerization (Singh *et al.*, 2016).

Taking all the above into consideration, it was decided to use NaOH 6M, a blended activator (Na_2SiO_3/NaOH) at varying concentrations, and curing at ambient temperature. The RM was blended with FA (to increase the content of Si and Al) and GGBS (to increase the Si, Al and Ca) according to Table 5-9.

Table 5-9 Composition of the AA RM materials (3:1 – sand: RM/FA/GGBS). Sand 750g (59-66%). Water 124-140 g (9.8-11.5%, CEM II 225g -11%).

	RM		FA		GGBS		Na_2SiO_3 / 6M NaOH	NaOH [a]		Na_2SiO_3 [b]		Activator / b	w/b
	(g)	(%)	(g)	(%)	(g)	(%)		(g)	(%)	(g)	(%)		
RM-1	250	100	—	—	—	—	1	21.19	1.74	57.47	4.71	0.88	0.43
RM-2	250	100	—	—	—	—	2.5	13.36	1.08	90.60	7.30	0.97	0.39
RM-3	250	100	—	—	—	—	Na_2SiO_3	—	—	141.37	11.14	1.08	0.33
RM-FA-1	175	70	75	30	—	—	1	20.52	1.69	55.67	4.59	0.85	0.42
RM-FA-2	175	70	75	30	—	—	2.5	12.97	1.05	87.94	7.12	0.94	0.38
RM-FA-3	175	70	75	30	—	—	Na_2SiO_3	—	—	137.45	10.89	1.05	0.32
RM-FA-4	125	50	125	50	—	—	1	19.86	1.65	53.88	4.47	0.82	0.41
RM-FA-5	125	50	125	50	—	—	2.5	12.57	1.02	85.27	6.95	0.91	0.37
RM-FA-6	125	50	125	50	—	—	Na_2SiO_3	—	—	88.86	8.16	1.08	0.34
RM-GGBS-1	175	70	—	—	75	30	1	21.19	1.74	57.47	4.71	0.88	0.43
RM-GGBS-2	175	70	—	—	75	30	2.5	12.97	1.05	87.94	7.12	0.94	0.38
RM-GGBS-3	175	70	—	—	75	30	Na_2SiO_3	—	—	137.45	10.89	1.05	0.32
RM-GGBS-4	125	50	—	—	125	50	1	20.52	1.69	55.67	4.59	0.85	0.42
RM-GGBS-5	125	50	—	—	125	50	2.5	12.57	1.02	85.27	6.95	0.91	0.37
RM-GGBS-6	125	50	—	—	125	50	Na_2SiO_3	—	—	137.45	10.89	1.05	0.32
CEM II	450	22.22	—	—	—	—	—	—	—	—	—	—	0.50

5.2.2 Mechanical strength of the AA RM materials

All the alkali activated RM materials achieved high strengths and some reached outstanding values - Table 5-10. Even the materials made with RM alone reached significant flexural and compressive strengths at 90 days, and the strengths increased significantly between 28 and 90 days. The significant strength upsurge between 28 and 90 days, can be related to the conversion of initial aluminate hydrates into stable phases of greater strength. During the hydration of calcium aluminates (e.g. in CACs) metastable hydrates can form that may persist for many years before they convert into stable phases (Lawrence and Hewlett, 1988). Risdanareni et al. (2015) and other authors also report that geopolymer binders do not reach full strength at 28 days.

Table 5-10 Mechanical strength of AA RM materials at 28 and 90 days. COVs=0.001-0.19 (flexural strength). COVs=0.015-0.22 (compressive strength).

Mix	%FA/ GGBS	Na_2SiO_3 / 6M NaOH	flexural strength (N/mm²)		compressive strength (N/mm²)	
			28d	90d	28d	90d
RM1	0	1	0.10	2.70	4.53	6.73
RM2	0	2.5	1.03	5.14	4.68	6.85
RM3	0	Na_2SiO_3	0.86	1.28	1.69	2.30
RM-FA1	30%FA	1	1.70	4.11	6.87	7.72
RM-FA2	30%FA	2.5	4.36	4.67	10.85	11.70
RM-FA3	30%FA	Na_2SiO_3	2.21	3.83	5.74	5.89
RM-FA4	50%FA	1	4.17	4.39	9.90	13.22
RM-FA5	50%FA	2.5	5.98	7.08	11.54	15.53
RM-FA6	50%FA	Na_2SiO_3	3.95	6.68	8.90	10.30
RM-GGBS-1	30%GGBS	1	1.85	4.24	13.21	19.43
RM-GGBS-2	30%GGBS	2.5	1.42	3.33	9.52	19.18
RM-GGBS-3	30%GGBS	Na_2SiO_3	1.72	6.57	8.02	21.53
RM-GGBS-4	50%GGBS	1	5.24	8.64	27.48	38.92
RM-GGBS-5	50%GGBS	2.5	5.52	9.20	33.65	40.64
RM-GGBS-6	50%GGBS	Na_2SiO_3	3.77	4.67	12.59	24.81
CEM II	-	-	6.02	7.33	37.18	46.67

Effect of RM substitution with FA and GGBS on strength.

FA substitution increased both the flexural and compressive strengths of the AA RM materials, and GGBS substitution increased the strengths further (Table 5-10 and Figure 5-27). The compressive strength of the AA RM materials with 30% FA (7 to 12 MPa) increased with 50% FA substitution (10-15.5 MPa). When the RM was replaced with GGBS, the compressive and

flexural strengths were the highest, increasing at 50% GGBS substitution (12.6 - 40.6 MPa). The results are comparable to those of Bayat *et al.* (2020) who obtained 33-50 MPa compressive strength values in AA RM-slag materials with 10-40% RM. They also agree with Cheng *et al.* (2019) who activated 30% RM / 70% slag with Na_2SiO_3/ $NaOH$ = 3 reaching a compressive strength of 16.7 MPa at 28 days.
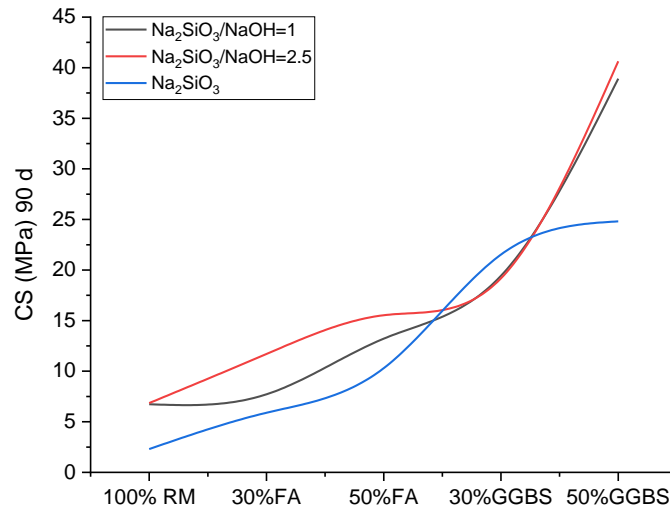
Figure 5-27 Variation of compressive strength of the AA RM materials with increasing substitution with FA and GGBS.

As seen in chapter 4, the RM has significant Al (30%) and silica (20%), and low Ca (5%), and GGBS contributes Ca (42%), Si (32%) and some Al (12%), while the FA contributes Si (62%) and Al (23%). Therefore, the RM-FA combination results in a low-Ca system which may lack C-S-H cements. In contrasts, the RM-GGBS combination results in a high-Ca system, where C-S-H cements of high strength should form. The superior strength of the GGBS materials is attributted to the combined effect of the latent hydraulicity of the GGBS and the high Ca content that activates with the alkali solution forming C-S-H and /or C-A-S-H cements of high strength. The higher Ca/Si of the GGBS materials results in stronger C-A-S-H gels with a more ordered structure. Singh *et al.* (2018) recorded C-S-H / C-A-S-H cement in high-Ca, RM-GGBS systems. Wang *et al.* (2021) investigated the polymerization of RM blended with FA and GGBS, and the effects of the $[AlO_4]^-$ content in the C-A-S-H structure.

The results show that the greatest Ca content (Ca/(Si+Al)>1) showed the highest polymerization, and hydrates with more abundant C-A-S-H gel. Also, secondary products were formed in this reaction, such as N-A-S-H and hydrotalcite as noted by (Marvila *et al.,* 2021).

The superior strength of the FA materials compared to the RM alone is probably related to the contribution of the Al in the FA to the production of calcium aluminate cements (Kumar and Kumar, 2013). Mudgal *et al.* (2021) confirmed the formation of a high dense structure in RM-FA geopolymer, with Al participating in the geopolymerization. Their lower values with respect to the RM GGBS materials is due to their lower Ca content: to synthesize C-A-S-H geopolymer cement, the Ca/Si ratio must be at least 0.6 (Martín-Garrido *et al.,* 2020) (in PC, the Ca/Si is generally over 2 -Wang *et al.*, 2021). The lower Ca/Si molar ratios of AAMs (generally 0.7- 0.3), are consistent with longer, more polymerised- (alumino)-silicate chains (Lecomte *et al.*, 2006).

In general, the flexural strength results (Figure 5-28) follow a similar trend: the strength of the RM materials with FA and GGBS replacements is higher than the RM alone, increasing the % replacement enhances strength and the AA RM materials with 50% GGBS replacement reached the greatest flexural strength. Activation with silicate alone lowers the ultimate strength of the 50%GGBS materials- see below.
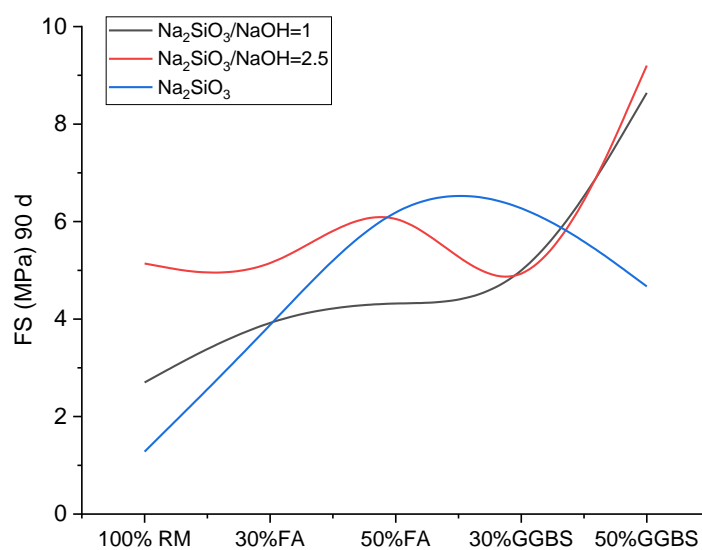
Figure 5-28 Variation of flexural strength of the AA RM materials with increasing substitution with FA and GGBS.

Effect of the activator on strength.

The activator type influences strength. In general, the combined activators yield better strength results than the silicate activator alone (Figure 5-27 and Figure 5-28).

In the RM-GGBS materials, the combined activator clearly provides the best mechanical properties. This agrees with AA-GGBS materials results, where it is clear that NaOH activator provides C-S-H cements with higher Ca/Si ratio, a more ordered structure and better strength than the C-A-S-H formed when activated with silicate alone (Escalante-García *et al.,* 2003; Fernández-Jiménez *et al.,* 2003).

The lower strength recorded when activating the RM with Na_2SiO_3 alone can be attributed to an excess of Si in the mix which results in unreacted Si that prevents the formation of large amounts of geopolymer cement. This agrees with Provis *et al.* (2014). The silica provided by the activator is more active in geopolymerization than the silica in the RM precursor (De and Brown, 1980; Hajjaji *et al.*, 2013). However, an excess of silica may hinder polymerisation, hence the optimum Si/Al ratio for a given geopolymer matrix varies with the amount of soluble silica in the raw material (Singh *et al.,* 2018). Similarly, Hameed *et al.* (2017) found that the compressive strength of AA metakaolin materials improved when increasing the Na_2SiO_3 / NaOH ratio up to 2, but over this threshold the compressive strength decreased because the excess of silicate hindered water evaporation and structure formation.

In addition, activating RM or RM- FA with Na_2SiO_3 alone did not increase strength. According to (Kumar and Kumar, 2013; Singh *et al.,* 2016; Kulkarni, 2018; Kumar *et al.*, 2021) the NaOH solution was necessary in order to achieve higher strength. Activation by Na_2SiO_3/NaOH at 1 resulted in the highest strength, while increasing FA to 50% increased Al and enhanced SiO_2/Al_2O_3.The higher strength was recorded when activated by Na2SiO3/NaOH at 2.5.

The results evidence that the high alkalinity of RM is not enough for the dissolution of aluminosilicate materials and geopolymer formation but an NaOH activator is needed to conform AA RM materials. This agrees with (Kumar and Kumar, 2013; Singh *et al.*, 2016; Kulkarni, 2018; Kumar *et al.*, 2021) which state that NaOH is necessary to achieve high strength.

5.2.3 Setting time

The setting times of the alkali activated RM materials appear in Table 5-11.

Table 5-11 Setting time of the alkali-activated RM materials.

	%FA/ GGBS	NaOH (6M)	Na$_2$SiO$_3$	initial setting	final setting
		(g)	(g)	(min)	(min)
RM-1	-	88.94	88.94	340	400
RM-2	-	52.78	131.97	400	490
RM-3	-	-	224.40	410	510
RM-FA-1	30%FA	82.10	82.10	400	460
RM-FA-2	30%FA	48.73	121.82	420	480
RM-FA-3	30%FA	-	246.84	440	500
RM-FA-4	50%FA	92.36	92.36	570	620
RM-FA-5	50%FA	58.88	147.20	610	660
RM-FA-6	50%FA	-	254.32	560	610
RM-GGBS-1	30%GGBS	95.78	95.78	140	150
RM-GGBS-2	30%GGBS	56.85	142.12	250	260
RM-GGBS-3	30%GGBS	-	254.32	370	380
RM-GGBS-4	50%GGBS	95.78	95.78	100	110
RM-GGBS-5	50%GGBS	54.82	137.04	110	150
RM-GGBS-6	50%GGBS	-	216.92	110	130
CEM II	-	-		130	140

In general, fast dissolution of highly active Al$_2$O$_3$ and SiO$_2$ sources in a high pH medium provides high initial concentrations of silicate (SiO$_2$(OH)$_2^{2-}$ or SiO(OH)$_3^{-1}$) and aluminate (Al(OH)$_4^{-1}$) to react with Ca^{+2} forming C-A-S-H or C-S-H phase that should result in shorter setting times. However, there is no agreement on the main contributor to the setting of AAMs. Some authors, state that the main responsible for setting is the soluble Si provided by the alkali solution, since the immediate availability of this silica expedites polymerization (Hardjito *et al.*, 2008; Nath and Sarker, 2014; Aldawsari *et al.*, 2022). However, others say that the setting time of geopolymer systems is mainly controlled by the alumina content (Komnitsas and Zaharaki, 2007), and that high CaO content in the precursor decreases setting time (Nath and Sarker, 2014). Overall, in calcium-based systems, a higher SiO$_2$ content and Al$_2$O$_3$ content appears to shorten the setting time and, in geopolymer systems increasing Al$_2$O$_3$ accelerates setting (Chindaprasirt *et al.*, 2012; De Silva *et al.,* 2007).

In PC, some authors say that set is the consequence of the formation of C-S-H resulting from C$_3$S hydration while according to others, setting is due to the hydration of the calcium aluminate C$_3$A (Ramachandran, 1976).

In the AA RM materials ettringite (AFt) has been held responsible for the setting of GGBS-RM polymers, where the appearance of C-S-H gel and ettringite (AFt) was followed by the polycondensation of C-S-H gels (Cheng *et al.*, 2019).

The initial setting time of the AA RM materials varied greatly ranging from 100 to 570 minutes. Compared to the CEM II (130 minutes), AA RM materials provide a more flexible range of initial setting times. The materials with the highest FA content take the longest to set whereas, on the contrary, the materials with the highest GGBS content set the fastest.

Blending GGBS with RM shortens the setting times consideraby. The final set follows a similar trend: AA RM materials take between 110 and 660 minutes to finally set. Most of the RM/50%GGBS blends set faster that the CEM II control material.

The RM materials tend to have a longer setting times than CEM II, possibly due to the fact that geopolymerization is generally slower that PC hydration. The initial and final setting times of the AA RM tend to increase when increasing the FA content. However, the setting times shorten when increasing the GGBS content.

The results agree with former authors working with AA, RM and FA materials. (Kumar and Kumar, 2013), using FA with 0–40% RM, showed that the initial and final setting times increased when increasing the FA content (210 and 310 minutes for the initial and final set respectively). Similarly, Lin *et al.* (2020) found that the initial setting time increased from 4.6 h to 5.5 h and the final setting time from 7.5 to 9.5 h when increasing FA content from 5% to 25% in RM. The author attributed this to the presence of inert FA cenospheres. According to (Kuenzel and Ranjbar, 2019), fly ash can be reactive, partially reactive and inert. The reactive FA cenospheres dissolve completely during geopolymerisation. In the partially reactive FA cenospheres, the outer vitreous Si shell dissolves gradually and the inert material remains un-reacted.

Blending RM with GGBS shortens the setting times considerably due to an increased reactivity produced by the additional soluble silica and alumina in the slag, which dissolves faster, accelerating the geopolymerization process. As a result, the setting time decreases with increasing substitution of RM with GGBS. The results agree with Hwang & Huynh (2017) who recorded that initial setting time drops from 6.2 to 1.8 hours, and the final setting time from 8.5 to 2.6 hours when RM replacement by GGBS rises from 10% to 30%.

5.2.4 Durability of the AA RM materials by accelerated cycling

The specimens were subject to cycling after 28 days of curing, and the strength and mass loss, as well as the physical damage, were assessed after cycling.

Despite reaching substantial strengths, many of the AAMs made with RM alone did not resist weathering cycles, and they were particularly vulnerable to frost action. The specimens suffered cracks and swelling after hydrothermal cycling, some after one cycle (RM-1) and others after 15cycles, as shown in Figure 5-29, and they lost considerable strength after cycling. The type of activator did not seem to make any difference, and neither the NaOH nor the silica activator seem to increase durability.

Dimas *et al.* (2009) also found insufficient the resistance of AA materials made with RM (plus little MK) activated with NaOH to freeze-thaw and flexure. They attribute this lack of resistance to the layered internal structure of the red mud-based inorganic polymers. Dimas *et al.* (2009) explain this mode of destruction by the absorption of water during the wetting phase of the freezing-thawing test. The entrapped ice between the surface layers exerts forces that break the bonds that link the layers. According to the authors, this indicates weak cross-linking between the layers which could also explain the inefficient flexural strength of synthesized inorganic polymers. As four-coordinated aluminum is the main cross-linking agent in inorganic polymers, the authors argue that the amount of aluminum dissolved during the synthesis was not enough to develop the stronger 3D structures and has developed weak cross-linked 2D structures instead.
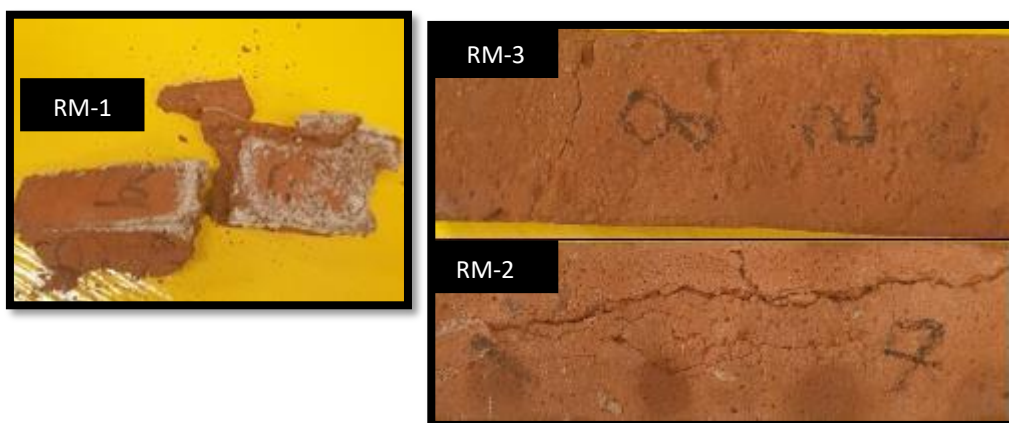
Figure 5-29 Specimens of alkali-activated RM alone following hygrothermal cycling.

Some of the FA-RM blends did not resist weathering cycles either, being particularly vulnerable to frost action. On the contrary, when blended with GGBS, the AA RM materials showed outstanding resistance to weathering. The durability of the alkali-activated RM materials dramatically improved when blended with GGBS, and most specimens improved their strength as a consequence of cycling, surpassing the strengths of their unweathered equivalent. This strength improvement is particularly significant during wet/dry cycling.

The AA RM materials blended with GGBS did not show any damage after cycling (Figure 5-30), most reached higher strengths after cycling than the unweathered control sample, and their performance improved as the amount of GGBS increased - Table 5-12. The increase in the resistance to weathering induced by the GGBS is probably due to the combined effect of its latent hydraulicity producing C-S-H and its high calcium content that activates with the alkali solution, forming ordered calcium silicate hydrate (C-A-S-H). These cements provide strength and lower porosity, which enhance durability. As shown in the SEM analyses in section 5.2.6, the quality of the hydrates changed in the RM-GGBS materials, with less needles and pores, and more abundant microcrystalline gels in denser microstructures (Figure 5-39- Figure 5-41). The effect is more pronounced with increasing GGBS content. Liang and Ji (2021) claim that the GGBS in AA RM materials forms chemical bonds through dehydroxylation which lower porosity and improve pore structure.

Figure 5-30 RM-GGBS-4, RM-GGBS-5 and RM-GGBS-6 undamaged after cycling.

After cycling, the strengths of the RM-GGBS materials activated with silicate alone (RM-GGBS-3 and RM-GGBS-6) are much lower than the strengths procured by the other activators. Therefore the use of silicate activator alone does not cause failure but lowers the resistance to weathering agents. There is no clear trend on the increase of NaOH activator enhancing durability as the use of Na_2SiO_3 / NaOH ratios 1 and 2.5 do not produce a consistent difference in the strength values. However, there is an enhancement in the resistance to weather when using NaOH activator. This may be related to an increase of C-A-S-H hydrates with a more ordered structure promoted by a higher Ca/Si ratio, as proposed by (Escalante-García *et al.*, 2003; Fernández-Jiménez *et al.*, 2003) in the case of NaOH-activated slag.

Table 5-12 Mass loss and strength after accelerated weathering (N/mm²).

Mix	wet-dry cycling			freeze-thaw cycling			salt-crystallization			Control un-weathered		Total SiO₂/Al₂O₃ molar ratio	Na₂SiO₃ / 6M NaOH
	Mass loss%	Fs	C s	Mass loss%	Fs	Cs	Mass loss%	F s	C s	F s	C s		
RM1	-	-	-	-	-	-	-	-	-	0.10	4.53	1.94	1
RM2	-14.50	0.60	1.41	-	-	-	1.30	2.65	4.05	1.03	4.68	2.42	2.5
RM3	-19.80	0.60	0.43	-	-	-	-	-	-	0.86	1.69	3.14	Na₂SiO₃
RM-FA1	-8.80	2.70	11.00	-	-	-	1.80	3.95	12.64	1.70	6.87	2.73	1
RM-FA2	-9.60	2.80	5.33	-1.30	0.76	3.41	1.70	8.14	14.69	4.36	10.85	3.24	2.5
RM-FA3	-	-	-	-	-	-	-6.50	2.22	4.97	2.21	5.74	4.01	Na₂SiO₃
RM-FA4	-8.30	3.10	13.07	-	-	-	2.20	3.60	21.04	4.17	9.90	3.33	1
RM-FA5	-8.60	2.70	8.20	-2.60	0.52	2.80	2.60	6.89	22.06	5.98	11.54	3.86	2.5
RM-FA6	-14.00	2.70	2.31	-	-	-	-16.10	1.15	4.70	3.95	8.90	4.8	Na₂SiO₃
RM-GGBS-1	-7.20	2.20	17.86	2.62	0.10	7.38	0.40	3.47	16.92	1.85	13.21	2.66	1
RM-GGBS-2	-9.00	1.70	20.58	-13.70	1.11	6.65	0.80	3.63	18.57	1.42	9.52	3.19	2.5
RM-GGBS-3	-9.80	1.50	13.88	0.50	1.70	8.47	0.60	3.40	9.60	1.72	8.02	4.07	Na₂SiO₃
RM-GGBS-4	-5.30	4.20	39.67	0.90	6.64	36.78	1.00	6.76	37.31	5.24	27.48	3.31	1
RM-GGBS-5	-4.00	4.40	44.34	-0.20	6.50	30.07	1.00	5.58	28.40	5.52	33.65	3.94	2.5
RM/GGBS-6	-7.40	2.20	20.76	-0.20	3.15	15.40	1.00	5.08	12.07	3.77	12.59	5.03	Na₂SiO₃
CEM II	-4.50	5.60	25.78	-0.70	6.08	23.39	-5.30	6.87	33.07	6.02	37.18	-	-

Out of all the FA-blended RM specimens, only those activated with Na_2SiO_3 / NaOH =2.5 survived all the cycles (both with 30%FA and 50%FA). Both lowering the silica activator to Na_2SiO_3 / NaOH = 1, and making the silicate the only activator, caused failure regardles of the amount of FA replacement. The RM-FA materials with Na_2SiO_3/NaOH ratio to 2.5 lost considerable strength on wet-dry and freeze-thaw cycling but reached significantly higher strengths than their unweathered, control equivalent after salt cycling.

When the RM was partially replaced with FA, the durability of most specimens improved after hygrothermal and salt cycling, but only c. 33% of the specimens survived frost action. Only

the AA RM-FA activated with Na_2SiO_3/NaOH 2.5 survived freeze-thaw cycling (RM-FA-2, carrying 30% FA, and RM-FA-5 with 50% FA), indicating that the percentage substitution with FA, has a lesser influence on durability than the activator's composition.

Similarly to the GGBS-blended RM materials, it seems that activation with sodium silica alone undermines durability (RM-FA-3 and RM-FA-6 failed after hygrothermal and frost cycling). The results also suggest that the total SiO_2/Al_2O_3 ratio (activator + precursor) is not essential for durability, as c.half of the materials with the highest ratios, (activated with silicate alone), failed during cycling unless the RM was partially replaced with GGBS.

Failure can be related to a longer time needed for geopolymerization in the RM and RM-FA blended materials and to the presence of microcracks resulting from geopolymerisation.

In general, salt crystallization cycling improves the strength of the blended RM specimens. However, this is likely due to the crystallization of sodium salts in the material. These salts are highly soluble; therefore, they cannot be considered a reinforcement of the structure but a weakness, as they can readily dissolve, causing damage.

Table 5-13 Deterioration of AA RM materials following water immersion for 24 hours and drying at 105 ^{0}C till constant mass.

RM-1 Spalling	
RM-2 Crazing surface+ swelling, cracks	
RM-3 Cracks + scaling, surface loss	
RM-FA-1 Small cracks + corner loss	

RM-FA- 2 Small cracks	
RM-FA-3 Delamination, cracks + surface loss	
RM-FA-6 Surface loss	

5.2.5 Porosity, water absorption and bulk density

Some authors state that hardened RM-slag pastes exhibit better microstructure, lower porosity and better resistance to weathering than hardened cement pastes (Pan *et al.*, 2003). Similarly, Liang and Ji, (2021) also state that the porosity and pore structure of RM-GGBS geopolymer are superior to PC materials (25.88 vs 33.35 respectively). The results do not agree, as the RM geopolymers have greater porosity than the CEM II control samples-Figure 5-31.

The porosity results (Figure 5-31) suggest that the GGBS lowers the porosity of the AA-RM materials: the GGBS-RM materials have lower porosities than the FA materials and the AA materials made with RM alone, and the porosity further lowers with increasing replacement. Replacement with FA shows a similar, however less marked trend. This is consistent with (Provis *et al.*, 2012), who determined that GGBS reduced the porosity of geopolymers further than FA, due to its chemical composition and higher fineness. Provis *et al.*, 2012 investigated the pore structure of sodium silicate-activated, FA-slag materials. They found that increasing GGBS replacement increased pore tortuosity and decreased porosity, which was particularly notable at slag contents of 50% or higher. The authors conclude that the formation of space-filling C-A-S-H gels begins to dominate the alkali-activated binder at slag content 25-50%, whereas the binders with slag content under 25% are dominated by N-A-S-H gels, which do not chemically bind water and therefore do not provide the same extent of pore network obstruction. Increasing GGBS content raises the Ca/Si ratio in the AAMs which causes the formation of hydrates of ordered structure (C-A-S-H) that lower porosity and enhance durability across all materials mixed with GGBS.

Some specimens of RM and FA-RM deteriorated during testing- Table 5-14- (only the AA RM specimens activated with Na_2SiO_3/NaOH at 2.5 survived). The deterioration evidenced that the silica alone is not a good activator for the system and that the best activator is Na_2SiO_3/NaOH = 2.5 for all the blended materials at all replacements, agreeing with the strength and durability results above.

The results revealed that the alkali-activated RM materials with partial GGBS substitution are the densest, and that the density increases and porosity lowers with rising substitution (Table 5-14). This agrees with the strength and durability results above. As seen above, the RM-GGBS materials are more resilient and have stronger structures than the RM aone or RM-FA materials.
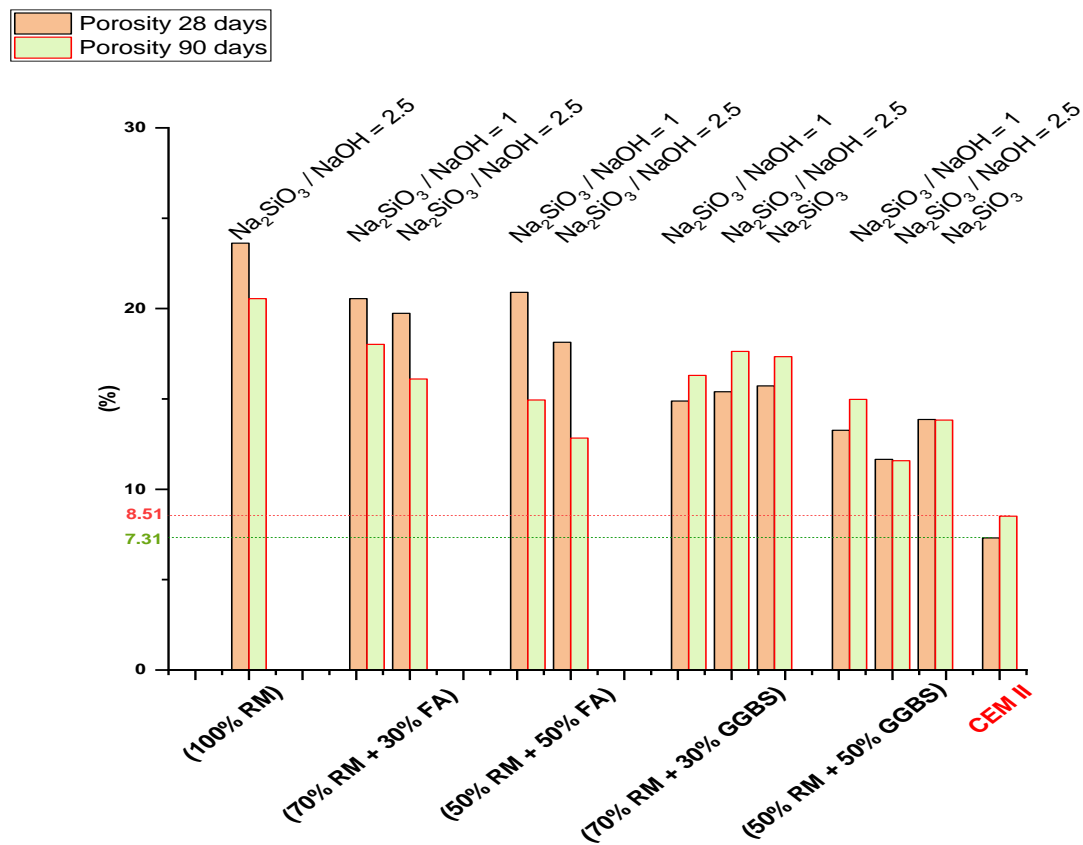
Figure 5-31 Porosity of AA RM materials.

Table 5-14 Porosity, water absorption and density.

Mix. Designation	Na$_2$SiO$_3$ / 6M NaOH	28 Days			90 Days		
		Porosity (%)	Bulk density (kg/m^3)	water absorption (%)	Porosity (%)	Bulk density (kg/m^3)	water absorption (%)
		COVs= 0.01-0.20	COVs= 0.01-0.20	COVs= 0.01-0.20	COVs= 0.01-0.03	COVs= 0.00-0.20	COVs= 0.00-0.20
RM-1	1	-	-	-	-	-	-
RM-2	2.5	23.62	1873.94	11.19	20.55	1942.80	9.58
RM-3	Na$_2$SiO$_3$	-	-	-	-	-	-
RM-FA-1	1	20.55	1995.82	9.33	18.02	2030.31	8.15
RM-FA-2	2.5	19.74	1992.34	9.01	16.10	2040.20	7.32
RM-FA-3	Na$_2$SiO$_3$	-	-	-	-	-	-
RM-FA-4	1	20.90	1973.04	9.58	14.94	2060.09	6.77
RM-FA-5	2.5	18.14	2019.31	8.24	12.84	2090.57	5.79
RM-FA-6	Na$_2$SiO$_3$	-	-	-	-	-	-
RM-GGBS-1	1	14.89	2051.75	6.77	16.30	2033.80	7.42
RM-GGBS-2	2.5	15.39	2056.36	6.97	17.63	2033.84	7.98
RM-GGBS-3	Na$_2$SiO$_3$	15.72	2041.23	7.15	17.34	2048.66	7.80
RM-GGBS-4	1	13.27	2095.31	5.96	14.98	2083.53	6.71
RM-GGBS-5	2.5	11.66	2096.48	5.27	11.58	2129.58	5.16
RM-GGBS-6	Na$_2$SiO$_3$	13.86	2097.20	6.20	13.83	2113.79	6.14
CEM II	-	7.31	2208.23	3.21	8.51	2125.83	3.85

5.2.6 Microstructure of the alkali activated RM materials by SEM/EDX

The SEM analysis was carried out in pastes aged 28 days. As shown in chapter 4, under the SEM, the RM consists of loose irregular particles and porous, irregularly-shaped aggregates of tiny particles - probably hematite and clays. As aforementioned, the AA RM materials were made with RM calcined at 400 °C to increase reactivity.

As seen in Chapter 4, the pozzolanic reaction of the feldspathoids and zeolites in the RM produced cementing zeolitic hydrates, AFm phases (ettringite needles) and hexagonal plates of portlandite, and the zeolite cancrinite produced pozzolanic hydrates in the form of needle-shaped and fan-shaped sprays of crystals.

Dimas *et al.* (2009) studied the mineralogical phases of RM+metakaolin polymers during geopolymerization. They observed that the initial RM phases did not change during geopolymerization. The authors conclude a negligible solubility of RM in caustic solutions, and that the RM acts as a filler in the process. On the contrary, they claim that the metakaolin changed during geopolymerization, and its components including illite and amorphous

aluminosilicates totally dissolved, providing Al and Si. The authors discovered a zeolite cement ($2\theta= 18°$) newformed during geopolymerization agglomerating the RM particles.

In the samples of **AA RM alone**, a scarce cementing phase (of similar quality to the product seen in the AA slag pastes) seems to grow on some grains, outwards into the pore space (Figure 5-32-Figure 5-33). However, these cements have very low crystallinity and their composition couldn't be recorded (Figure 5-33). Many of the typical particles and irregularly-shaped aggregates comprising the RM seem unchanged (Figure 5-34) agreeing with Dimas *et al.* (2009). No significant changes in the microstructure were apparent with varying Na_2SiO_3/NaOH.

Microstructure of the AA RM materials activated with Na_2SiO_3/NaOH at ratio 2.5	
Figure 5-32	Figure 5-33
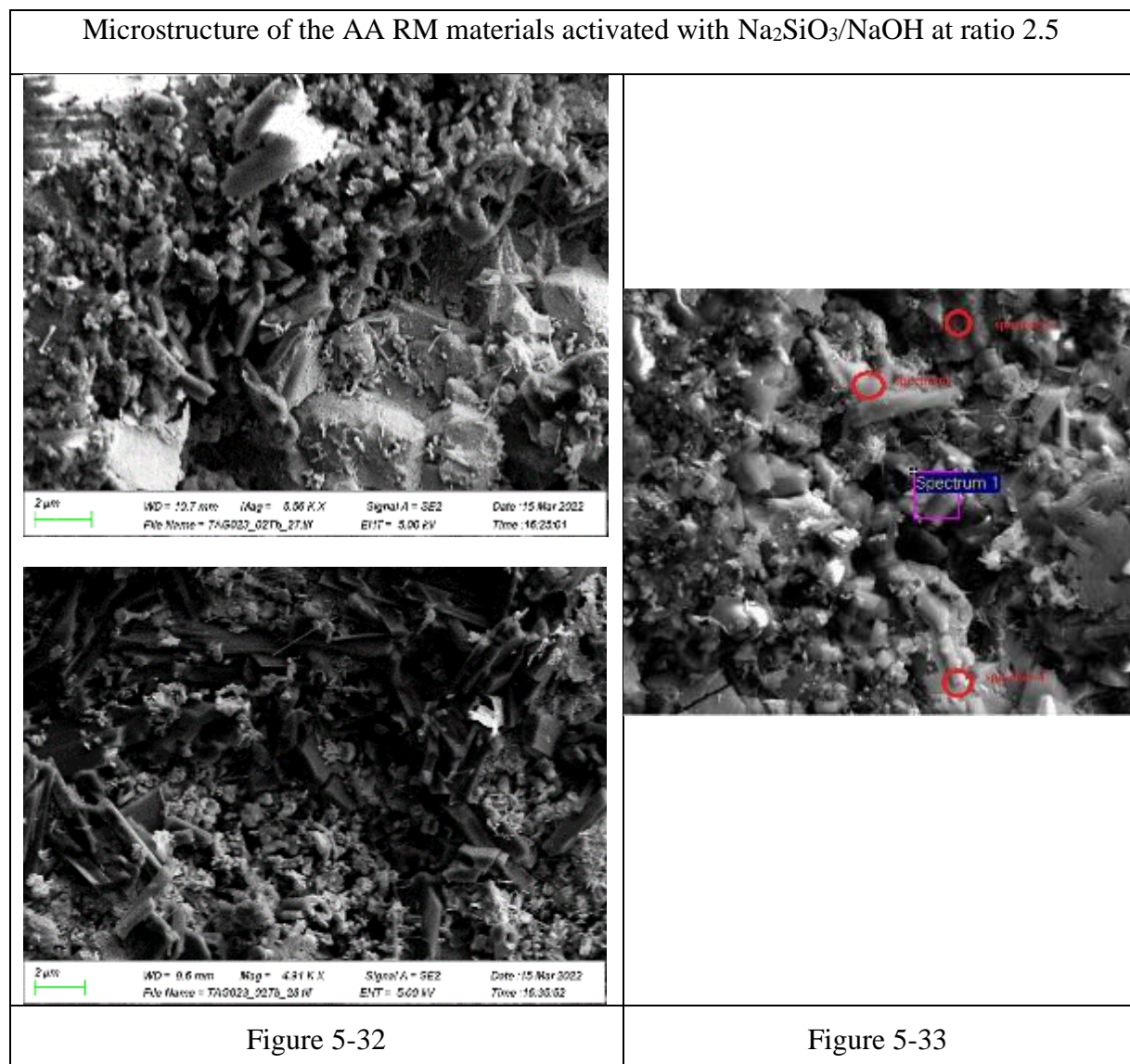
Elements	C	O	Na	Mg	Al	Si	Ca
Spectrum 1	17.98	55.6	20.21	-	0.59	0.11	5.5
Spectrum 2	17.05	56.53	19.09	-	1.06	0.32	5.94
Spectrum 3	20.82	46.78	1.16	0.27	0.63	0.44	29.9
Spectrum 4	20.98	53.15	3.87	-	1.47	-	20.52

Chemical composition (%wt) of Figure 5-33.
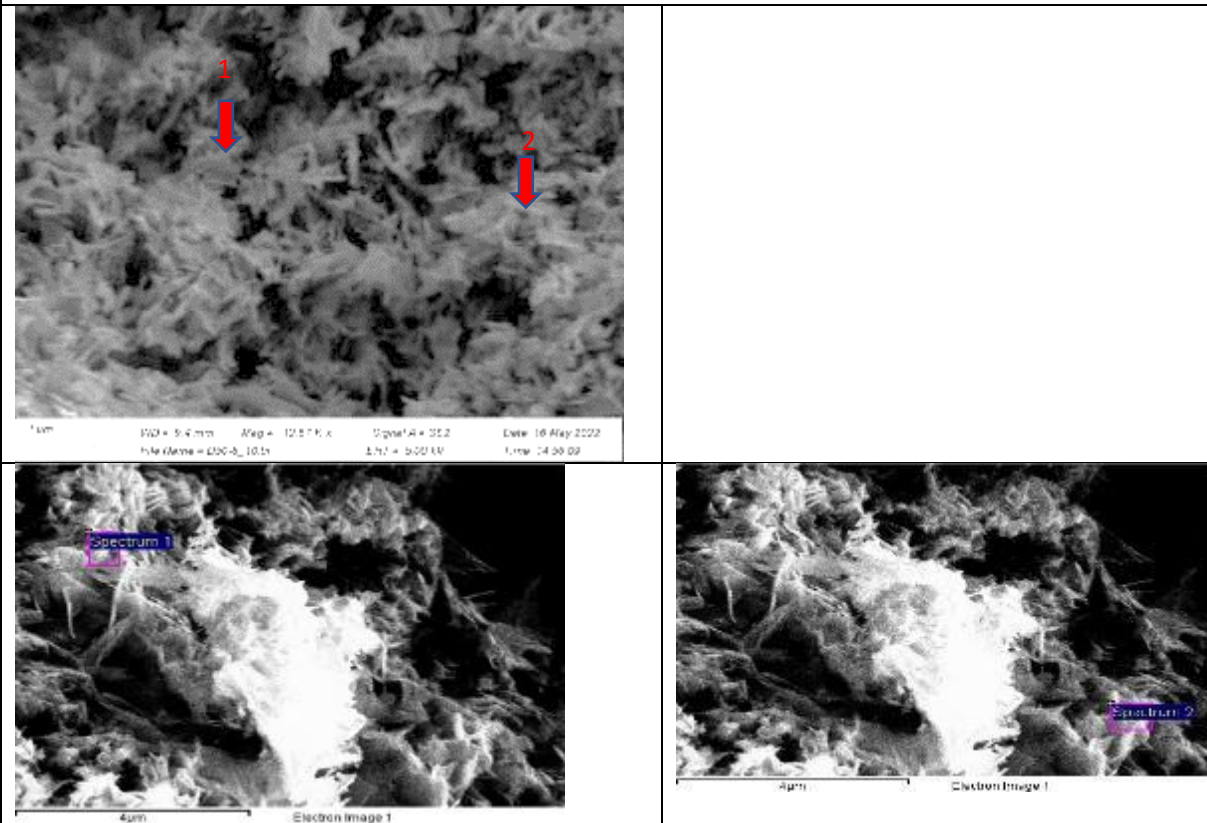
Figure 5-34 (top) and detail of Figure 5-34 with location of composition spectrums marked.

Elements	Na	Al	Si	Cl	Ca	Fe
Spectrum 1	2.98	1.43	1.32	0.25	1.24	47.90
Spectrum 2	2.69	1.38	1.12	-	0.92	39.46

Chemical composition of Figure 5-34- %wt.

AA RM materials blended with FA.

As seen in chapter 4, FA is a source for SiO_2 and Al_2O_3 while the GGBS contributes Ca and SiO_2. Both systems are high silica and alumina, but the RM-GGBS system has a much greater Ca content. Therefore, in the RM-FA system N-A-S-H hydrates and aluminates are expected whereas stronger C-S-H / C-A-S-H cements are expected in the RM-GGBS system.

In the AA RM materials blended with FA, cementing hydrates are abundant including low crystallinity gels, needle-shaped phases and fan-shaped sprays of zeolite crystals similar to the zeolitic cements found when on pozzolanic activation of the RM (Figure 5-35). The chemical

analyses by EDX indicate that the needles are AFm phases. The crystallinity of the gel is too low to obtain reliable EDX analyses, but the morphology reminds of C-S-H. However, the RM+FA material is a low Ca system. According to former authors this typically produces N-A-S-H hydrates, an alkali aluminosilicate structure different from the C-S-H gel of PC hydration (García-Lodeiro *et al.,* 2013) which agrees with the %wt Na in the spectrums of the gels. Increasing the amount of silica in the activator slightly raised the Si content of the hydrates, but the SEM didn't provide enough resolution to determine a clear change in the nature of the cementing hydrates – Figure 5-36.

Microstructure of the 70% RM -30% FA materials activated with $Na_2SiO_3/NaOH =1$.

Figure 5-35

Elements	C	O	Na	Al	Si	K	Ca	Ti	Fe
Spectrum 1	9.82	44.63	9.76	7.20	6.03	-	18.74	3.83	0
Spectrum 2	-	58.72	7.63	13.38	12.04	0.47	1.49	1.28	4.98
Spectrum 3	16.41	49.08	11.42	10.58	12.03	-	0.48	-	-
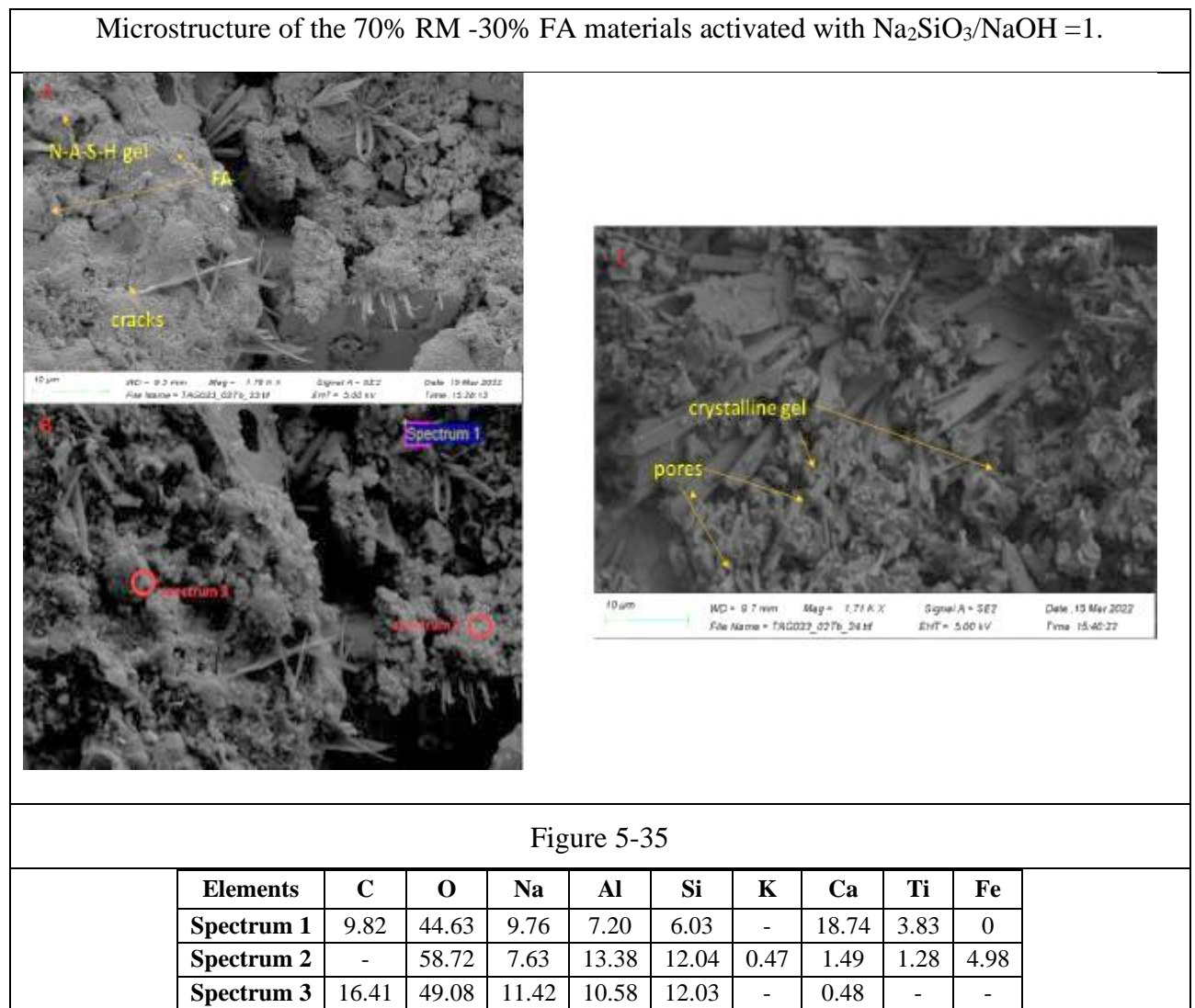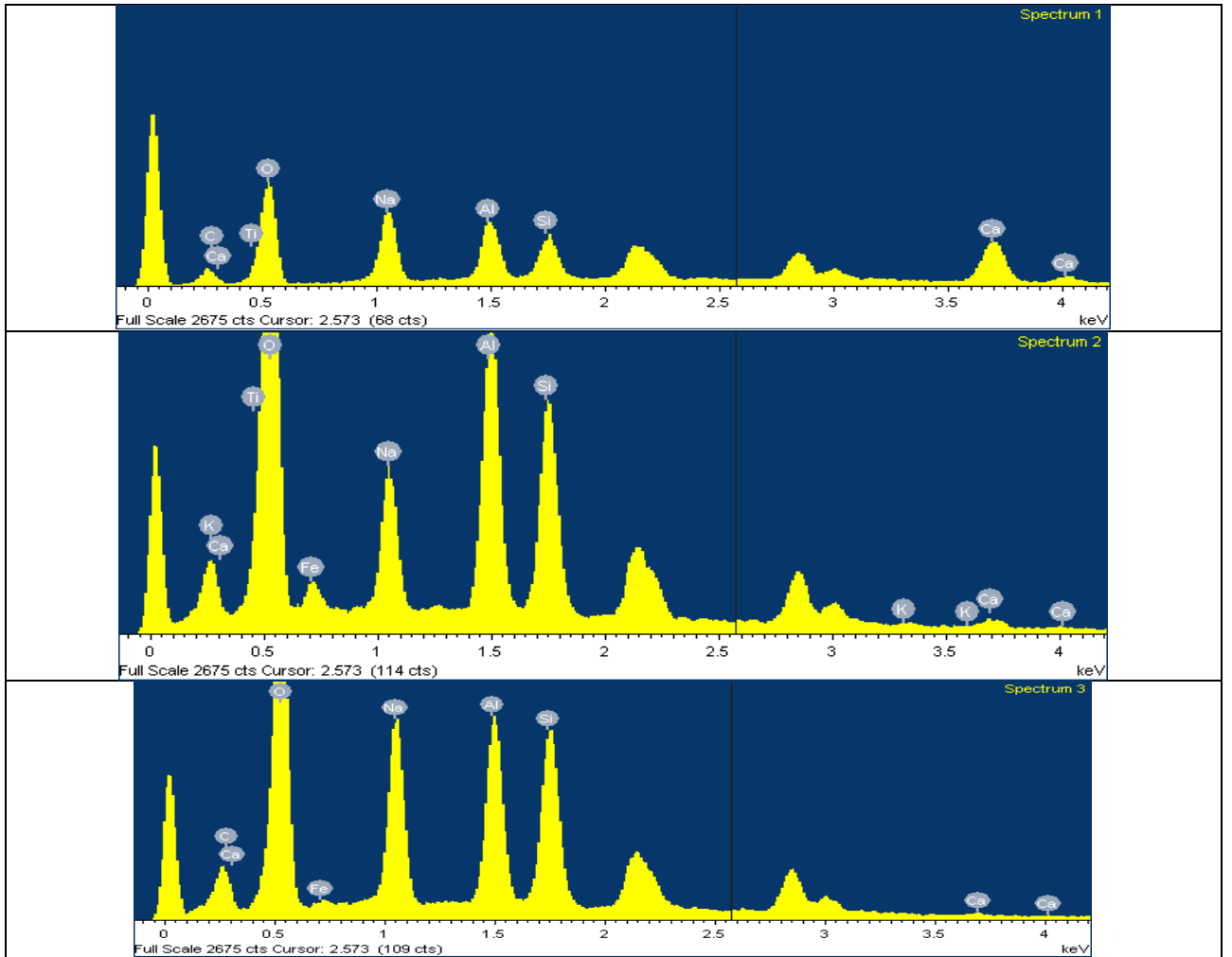
Chemical composition of Figure 5-35

Microstructure of the 70% RM -30% FA materials activated with $Na_2SiO_3/NaOH = 2.5$
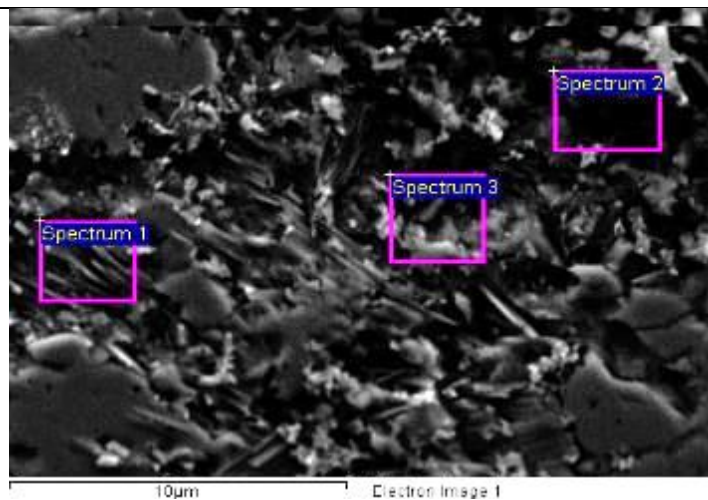
Figure 5-36
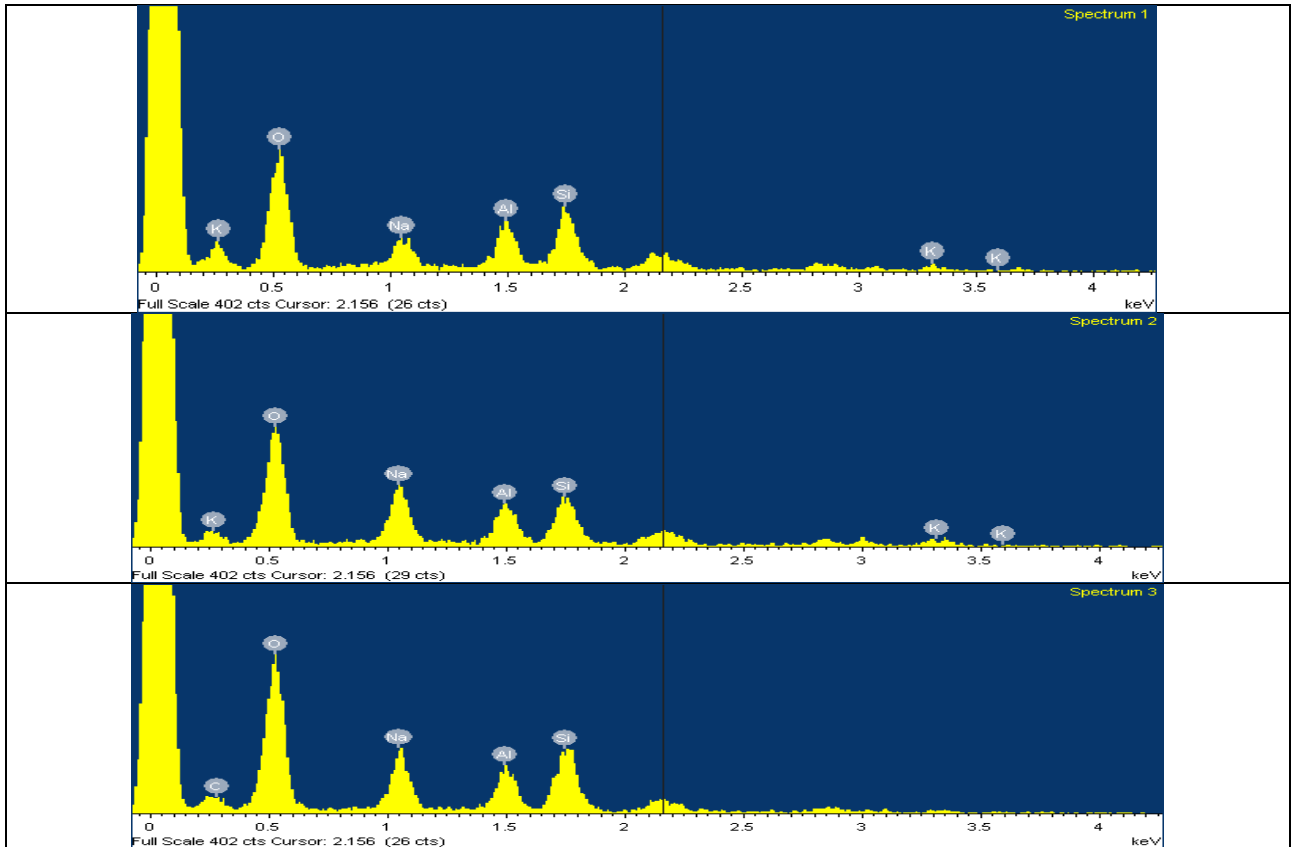
Elements	C	O	Na	Al	Si	K
Spectrum 1	9.82	49.98	7.63	13.75	22.82	5.82
Spectrum 2	-	48.06	15.20	11.75	18.16	6.84
Spectrum 3	17.08	44.43	11.11	9.37	18.02	-

Chemical composition of Figure 5-36 -weight %

Microstructure of the 50% RM -50% FA materials activated with $Na_2SiO_3/NaOH =2.5$.
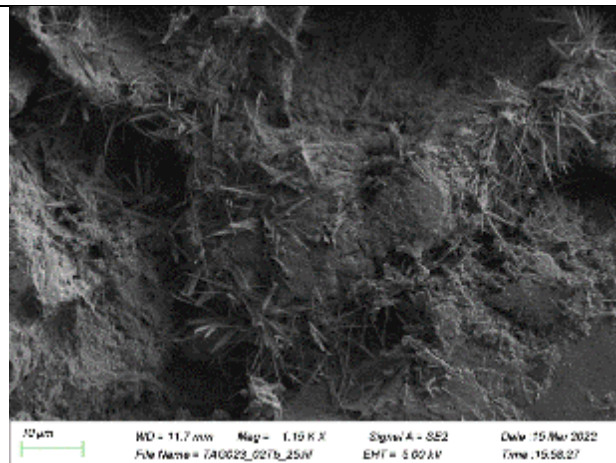
Figure 5-37 Needle-shaped hydrates, likely AFm phases.
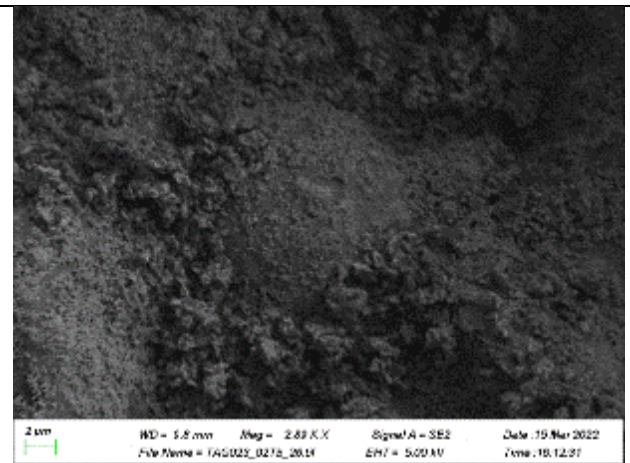
Figure 5-38. Low crystallinity hydrates, likely N-A-S-H

Elements	C	O	Na	Mg	Al	Si	K	Ca	Fe
Spectrum 1	-	65.95	10.88	0.29	10.24	10.40	0.52	0.96	0.76
Spectrum 2	-	61.73	12.63	-	13.12	10.72	0.60	1.20	0.00
Spectrum 3	16.58	57.47	10.22	-	8.22	6.27	-	1.23	0.00

Chemical composition (%wt) of the needles -AFm hydrates- in Figure 5-37.

Chemical composition (%wt) of the low crystallinity hydrates, likely N-A-S-H in Figure 5-38.

Elements	C	O	Na	Al	Si	Ca	Fe
Spectrum 1	31.97	49.16	5.08	8.41	3.54	0.60	1.26
Spectrum 2	33.40	48.54	4.99	7.28	4.02	0.40	1.37
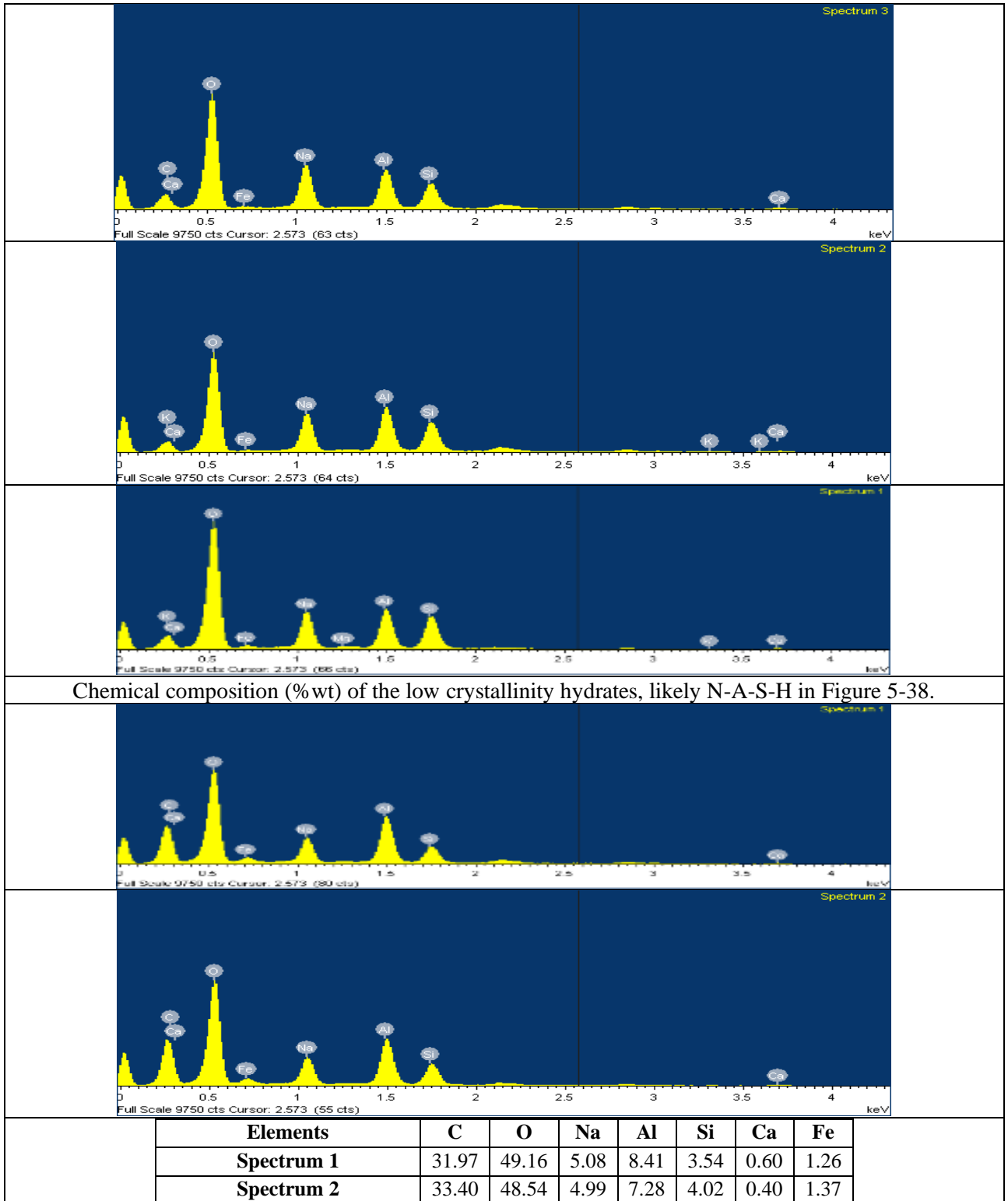
AA RM materials blended with GGBS.

The quality of the hydrates changed in the materials with GGBS, with less needles, low porosity, and more abundant microcrystalline gels in denser microstructures (Figure 5-39-

Figure 5-41). However, the chemical composition spectrums still record low Ca content in the cementing gels. It was not possible to determine a change in microstructure or the quality of the cements with increasing % GGBS (Figure 5-39-Figure 5-42). The SEM didn't evidence a change in microstructure however, the cements are richer in Ca in the 50% GGBS materials. According to Zhihua P *et al.,* (2002) the hydration product of AA, RM materials blended with GGBS is a nearly amorphous C-S-H, and coarse hydrates such as AFt and $Ca(OH)_2$ do not appear. In several areas, unreacted GGBS particles were common (Figure 5-41), and sodium salt were also recorded (Figure 5-42) due to the high alkalinity of the RM.

Microstructure of 70% RM-30% GGBS materials activated with Na_2SiO_3/NaOH =2.5

Figure 5-39

Typical spectrum of the needles (marked 2 in Figure 5-39) and %wt below
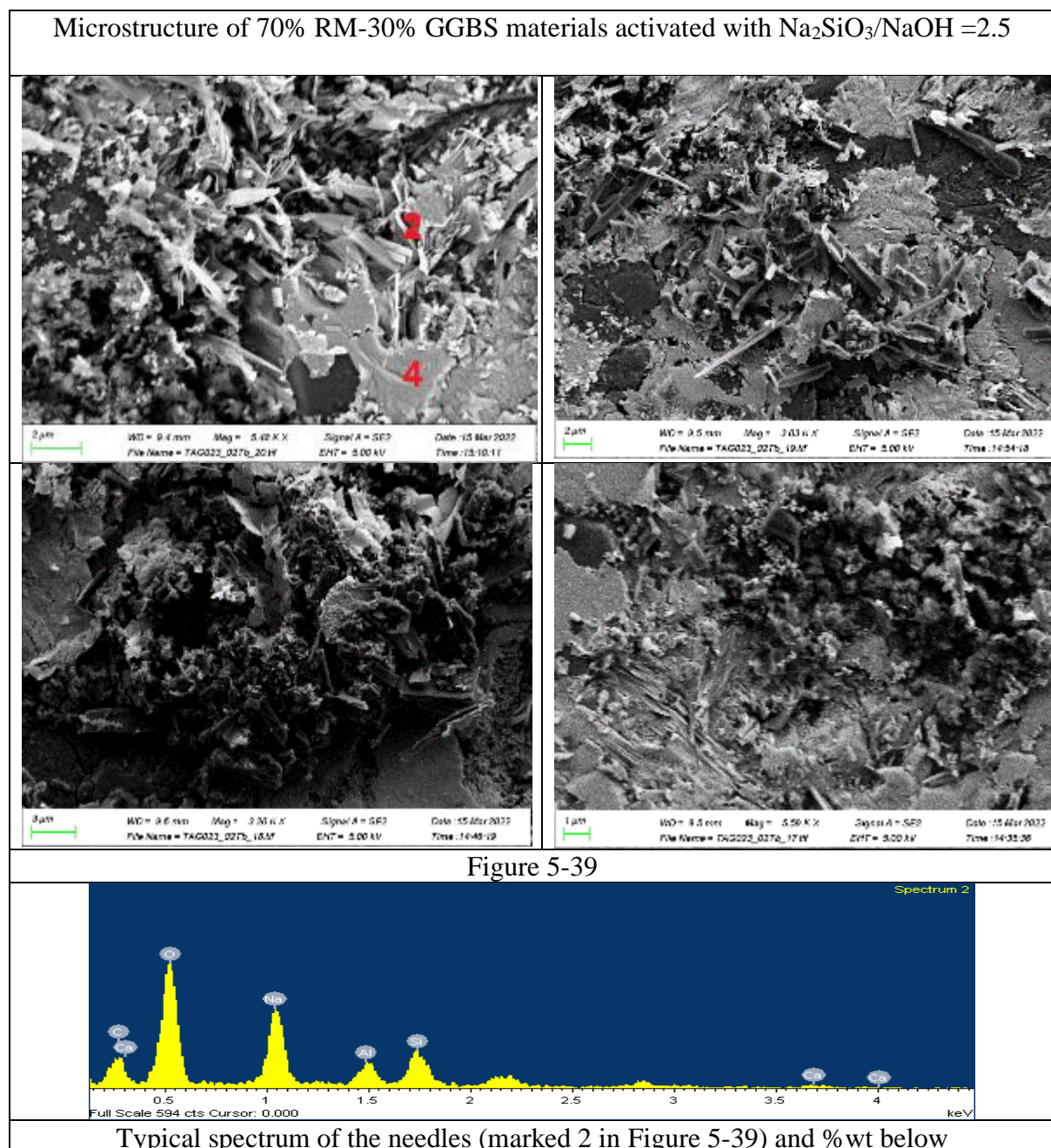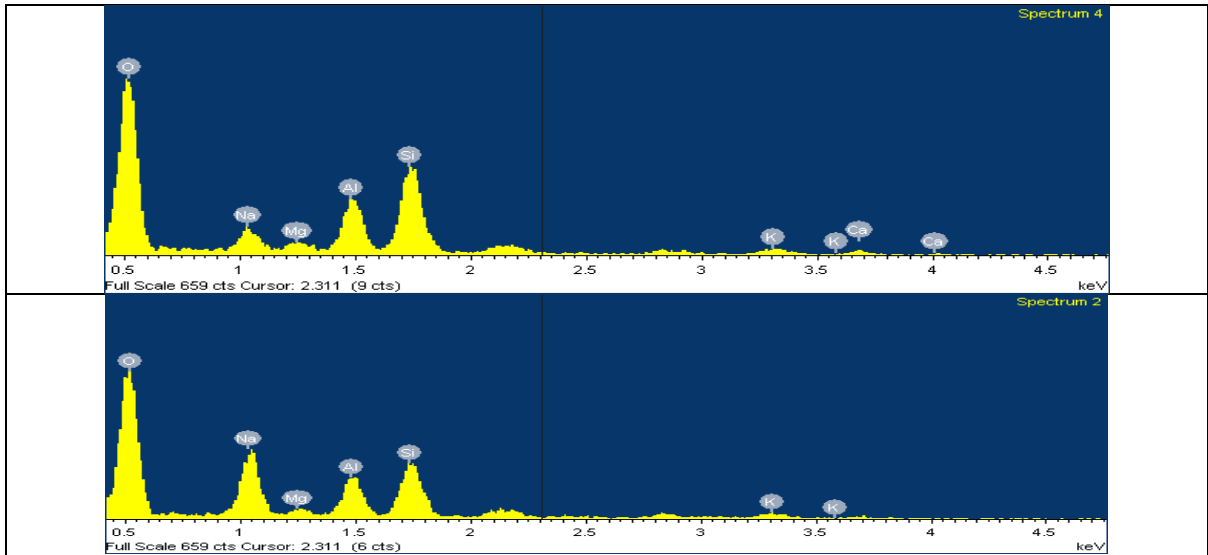
Typical spectrum of the continuos phase (marked 4 in Figure 5-39) and %wt below

Elements	C	O	Na	Mg	Al	Si	K	Ca
Spectrum 1	25.75	40.06	20.50	0	3.88	2.14	0	-
Spectrum 2	-	58.63	13.20	1.32	8.54	14.29	4.01	-
Spectrum 3	19.15	49.44	19.41	-	6.18	5.82	-	-
Spectrum 4	-	61.18	3.72	1.25	8.95	17.99	3.24	3.67

Microstructure of 50% RM-50% GGBS materials activated with Na$_2$SiO$_3$/NaOH =1.
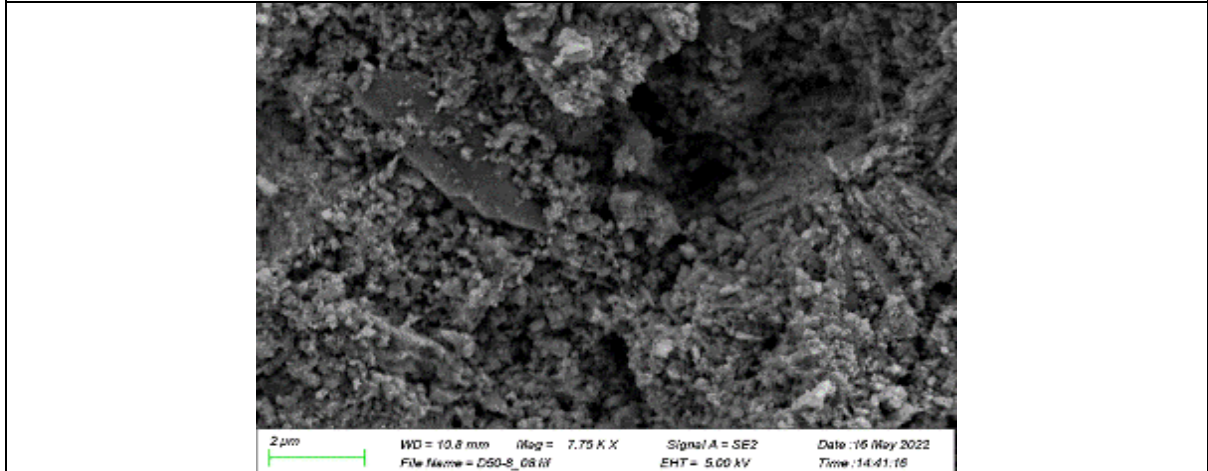
Figure 5-40
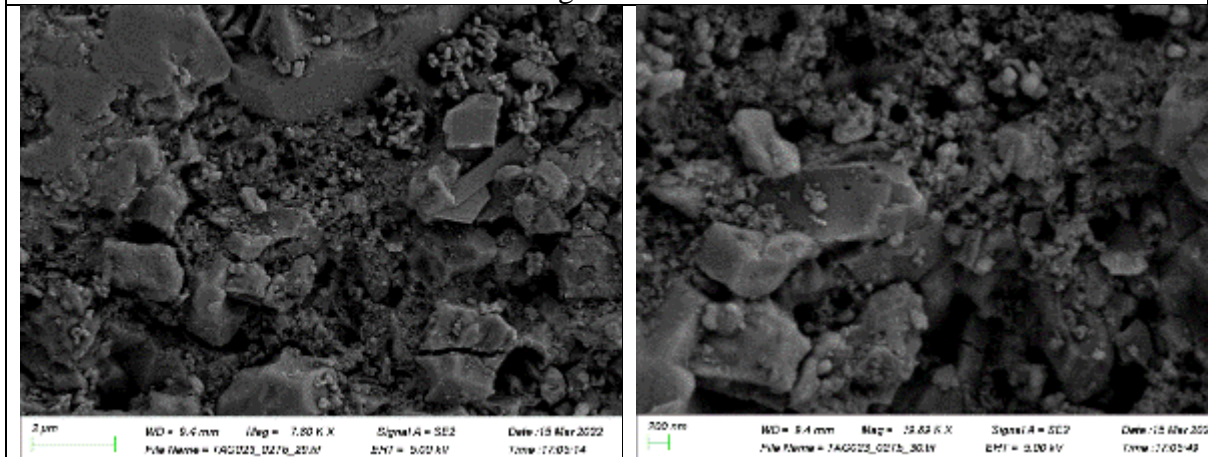
Figure 5-41

Chemical composition of cementing gels (% wt) in Figure 5-40-Figure 5-41.

Elements	C	O	Na	Al	Si	S	K	Ca	Fe
Spectrum 1	-	50.54	10.77	13.94	10.58	0.72	0.2	2.51	10.74
Spectrum 2	9.19	54.21	10.95	11.04	8.97	0.52	-	1.20	3.92
Spectrum 3	9.03	55.77	8.72	10.50	6.78	0.40	-	2.97	5.82
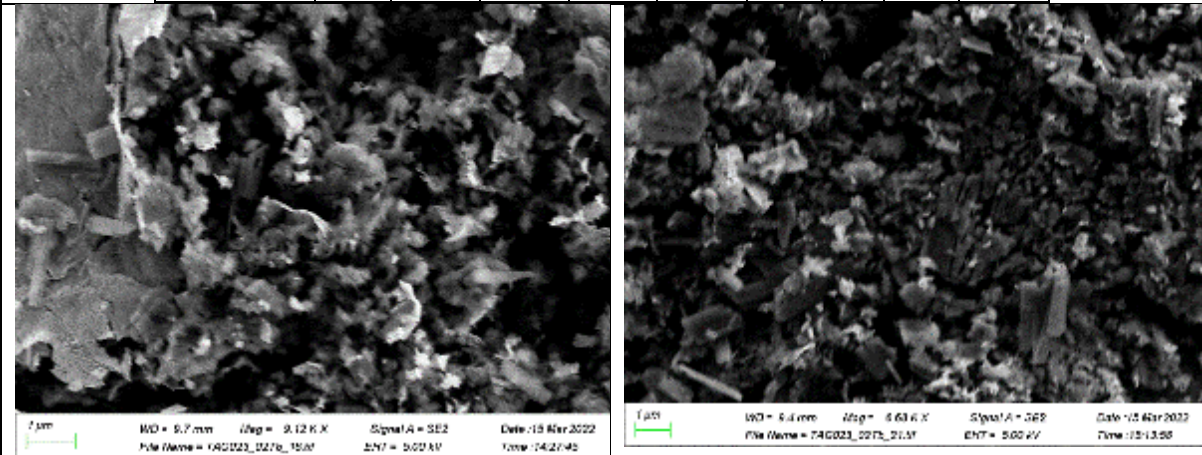
Figure 5-42
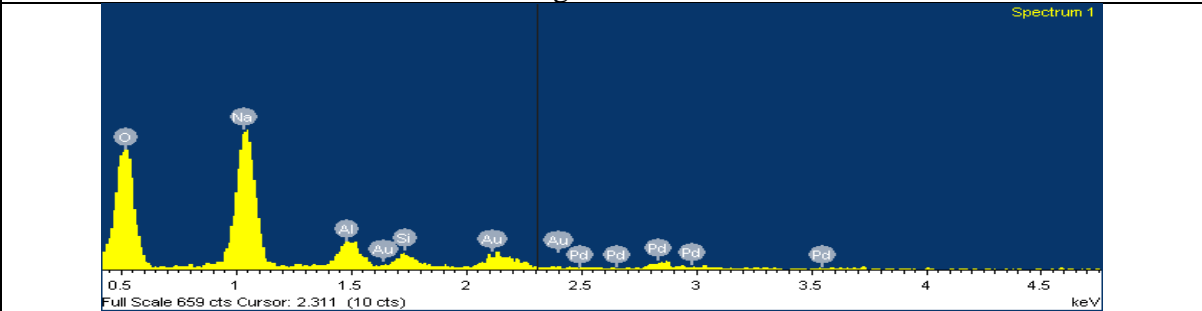
Chemical composition of the alkali salts in Figure 5-42

5.3 PROPERTIES OF AA MATERIALS MADE WITH BAUXITE AND BLENDS OF BAUXITE WITH FA AND GGBS

5.3.1 Mix design

The AA bauxite materials were made with bauxite calcined at 800 ^{0}C to enhance reactivity (chapter 4). At 800 °C, boehmite has disappeared, transformed into amorphous alumina, and kaolinite has completely turned into reactive metakaolin. No bauxite geopolymers were found in the literature. Therefore, the mix design was based on existing literature on metakaolin geopolymers and other low-Ca geopolymers systems such as FA. However, it was no possible to establish an optimum mix design based in the literature, due to the different composition of the precursors and varying activator solutions. There is no agreement in the activation temperature or the best activator concentration and composition. Therefore, bauxite mixes with

varying activator concentration and composition were investigated as well as curing at increasing temperatures according to the references below. Both FA and metakaolin appear to undergo similar reactions, but FA dissolution is slower than metakaolin during geopolymerization (Görhan *et al.,* 2016).

There is no agreement on the best curing temperature, some authors state that the dissolution of the metakaolin and FA precursors increases at 40-60 °C Najafi and Allahverdi (2009) and Zhang *et al.* (2014), while others state that curing metakaolin geopolymers at 40, 60, and 80 °C does not significantly affect strength (Pelisser *et al.*, 2013) . Strydom and Swanepoel, (2002) investigated FA blended with kaolinite activated with Na_2SiO_3 and NaOH. The samples were cured at 40, 50, 60 and 70 °C, and the results showed that the best temperature was 60 °C.

Wang *et al.,* (2005) studied metakaolin geopolymers cured at 20 ^{0}C, activated with a solution of NaOH 4 to 12 M and sodium silicate. The strength and apparent density increased with the rise in the concentration of the NaOH solution. Higher concentrations of NaOH dissolved metakaolin better and produced a more effective geopolymerisation increasing strength. According to Ayeni *et al.* (2021), for metakaolin geopolymers made with varying NaOH concentrations (8, 10 and 14M) and different curing temperatures (20, 60 °C), 10 M concentration and ambient temperature curing improved compressive strength due to an enhanced dissolution and polymerization of Al and Si. Manjunatha *et al.* (2014) also report an increase in compressive strength of geopolymer with increasing curing temperature. Görhan *et al.* (2016) claim that the optimum curing temperature for (60%FA 40% metakaolin) geopolymers was 60 °C reaching 25.1 MPa at 9 M NaOH and Na_2SiO_3/NaOH =2.

Metakaolins are usually more reactive than other pozzolans and SCMs such as FA or RHA. However, it is generally agreed that partly replacing metakaolin with GGBS improves the strength and microstructure of the geopolymers (Kumar and Ramesh, 2017; Praveen *et al.,* 2020). Previous studies investigated the effect of NaOH concentration, Na_2SiO_3/NaOH ratio, curing temperatures from ambient to 60 degrees, and FA/GGBS blended with metakaolin-based geopolymer. Many authors agree that a combined Na_2SiO_3/NaOH activator improves geopolymerisation (Abdullah *et al.*, 2011). According to Pelisser *et al.* (2013) a Na_2SiO_3/NaOH ratio of 1.6 showed the best performance in metakaolin geopolymer, with a compressive strength of 64 MPa and flexural strength of 17.6 MPa, and the lowest strength was recorded at a Na_2SiO_3/NaOH ratio of 1. As usual, the authors attributed this to the silicate activator improving geopolymerization.

Table 5-15 Composition of AA bauxite materials and bauxite-FA blends (3:1 – sand: bauxite/FA). Activator/binder = 0.86-1.05; water/binder = 0.32-0.44.

Mix	NaOH M	Na$_2$SiO$_3$/ NaOH	T ^{0}C	Bauxite %	FA %	Water %	NaOH g	NaOH %	Na$_2$SiO$_3$ g	Na$_2$SiO$_3$ %
1	8	1	20	100	0	13.69	62.29	2.69	134.90	5.83
2	12	1	20	100	0	12.99	85.39	3.67	137.94	5.93
3	8	3	20	100	0	12.24	31.54	1.36	204.89	8.83
4	12	3	20	100	0	11.85	42.53	1.83	206.57	8.89
5	8	1	60	100	0	13.69	62.29	2.69	134.90	5.83
6	12	1	60	100	0	12.99	85.39	3.67	137.94	5.93
7	8	3	60	100	0	12.24	31.54	1.36	204.89	8.83
8	12	3	60	100	0	11.85	42.53	1.83	206.57	8.89
9	8	1	20	50	50	11.66	50.90	2.29	110.22	4.97
10	12	1	20	50	50	11.19	70.48	3.15	114.10	5.11
11	8	3	20	50	50	10.51	26.02	1.17	169.03	7.58
12	12	3	20	50	50	10.41	36.07	1.61	175.19	7.80
13	8	1	60	50	50	11.66	50.90	2.29	110.22	4.97
14	12	1	60	50	50	11.19	70.48	3.15	114.10	5.11
15	8	3	60	50	50	10.51	26.02	1.17	169.03	7.58
16	12	3	60	50	50	10.41	36.07	1.61	175.19	7.80
17	10	2	40	75	25	10.98	34.74	1.56	150.50	6.75
20	8	2	40	75	25	11.33	36.13	1.61	156.50	6.96
21	12	2	40	75	25	11.18	50.60	2.23	163.81	7.22
22	10	1	40	75	25	11.46	44.65	1.97	164.08	7.23
23	10	3	40	75	25	11.65	45.59	2.00	167.53	7.35
24	10	2	20	75	25	10.70	40.95	1.84	150.50	6.75
25	10	2	60	75	25	10.70	40.95	1.84	150.50	6.75

Table 5-16 Composition of the bauxite-GGBS blends (3 sand: 1 RM-GGBS; water/binder = 0.31-0.47; activator/binder=0.83- 1.05.

NaOH M	Na$_2$SiO$_3$/ NaOH	T ^{0}C	Bauxite %	GGBS %	Water %	NaOH g	NaOH %	Na$_2$SiO$_3$ g	Na$_2$SiO$_3$ %
8	1	20	50	50	11.52	50.13	2.26	108.58	4.91
12	1	20	50	50	11.33	71.54	3.19	115.80	5.17
8	3	20	50	50	10.64	26.41	1.18	171.60	7.68
12	3	20	50	50	10.28	35.54	1.59	172.57	7.71
8	1	60	50	50	11.52	50.13	2.26	108.58	4.91
12	1	60	50	50	11.33	71.54	3.19	115.80	5.17
8	3	60	50	50	10.64	26.41	1.18	171.60	7.68
12	3	60	50	50	10.28	35.54	1.59	172.57	7.71
10	2	40	75	25	10.96	42.19	1.88	155.06	6.91
10	2	40	75	25	10.96	42.19	1.88	155.06	6.91
10	2	40	75	25	10.96	42.19	1.88	155.06	6.91

5.3.2 Mechanical properties of the AA bauxite materials

AA materials made with bauxite alone.

The results indicate that the bauxite alone is suitable for synthesising geopolymers binders, without blending with FA or GGBS (Table 5-17-Table 5-18). Several bauxite geopolymers reached strengths comparable to the CEM II control specimens at 28 days, and they surpassed the flexural strength of the CEM II material, reaching values of c.10 MPa (vs 7 for CEM II).

The lowest NaOH molarity of 8M and increasing silicate content to $Na_2SiO_3/NaOH = 3$, shows the highest flexural strength and compressive strength. In all instances, strength increases between 28 and 90 days indicating a stable structure without metastable aluminates that can decrease strength over time.

Increasing curing temperature did not improve flexural strength (some reached lower values than the ambient cured specimens) and the improvement of compressive strength with rising curing temperature was erratic, the increase was sometimes insignificant and some values lowered. High curing temperature did not lower porosity or water absorption, and the density was similar to the specimens cured at ambient temperature. In contrast, increasing the silica content in the activator generally improved strength slightly enhancing density, but the porosity and pore connection didn't vary substantially. Rising the molar concentration of the NaOH activator from 8 to 12 M was detrimental to strength, with the effect is more evident at 90 days, and it didn't substantially affect the pore system.
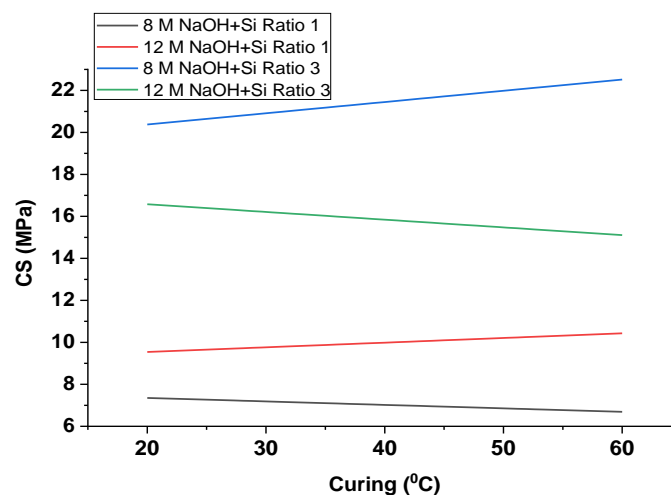
Figure 5-43 Compressive strength of the AA bauxite materials at 28 days.
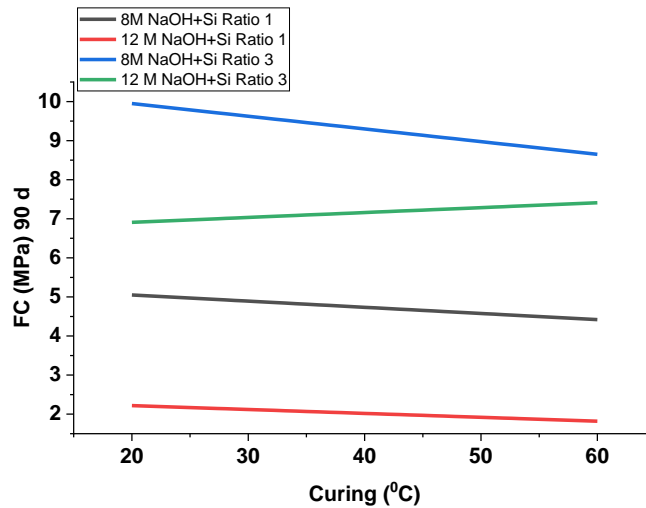
Figure 5-44 Flexural strength of the AA bauxite materials at 90 days.

AA materials made with bauxite and FA/GGBS.

In general, replacing bauxite with FA/GGBS increases strength and lowers porosity increasing density, and the effect is more pronounced as the % replacement grows (Table 5-17). The results evidenced the superior strength values of the 50% GGBS materials (Figure 5-45). However, the AA materials made with bauxite alone reached greater strengths, comparable to the materials with replacement, when the activator was Na_2SiO_3/ NaOH (8M) = 3, indicating that the bauxite needs a higher initial alkalinity to achieve a superior polymerization than when mixed with FA or GGBS (Figure 5-45).
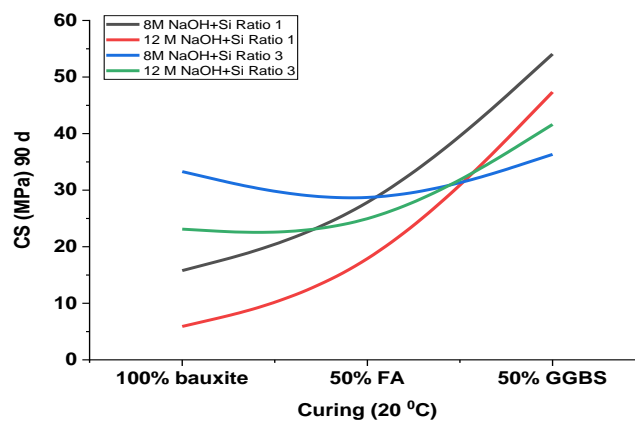
Figure 5-45 Variation of compressive strength (90 days) with % replacement.

In the FA-bauxite materials, increasing the curing temperature tends to rise the strength but the increase is not significant (Figure 5-47). Rising the silica content in the activator (Na_2SiO_3+ NaOH =3) enlarged the strength but the increase is erratic, and it didn't seem to affect the pore system and density in a significant manner. Similarly, the AA bauxite materials, increasing the concentration of the NaOH activator tends to lower strength and it has an inconsistent effect on the density and pore system of the materials. However, some of the values are similar.

In the GGBS-bauxite materials, the greatest strength values are achieved by the 50% GGBS materials activated with Na_2SiO_3/ NaOH (8M) = 1 cured at 60 degrees that reached over 90 MPa at 90 days (over 72 MPa at 28 days). Higher silica content in the activator tend to provide lower strength values however still high (36-53 MPa), and higher NaOH concentrations also provided outstanding values (42-71 MPa). Curing at 60 degrees rises the strength values (Figure 5-46). In some instances, the strength lowers between 28 and 90 days probably due to the initial presence of metastable aluminate hydrates.

Increasing the concentration of the NaOH activator lowering strength agrees with previous authors. Several authors claim that initially, during geopolymerisation, NaOH dissolves silica and aluminum ions, and later it balances the charge of the geopolymer network (Saraya and El-Fadaly, 2017). There is a tendency for the strength to lower as the NaOH molarity rises. This is probably due to the leaching of free cations to the surface of specimens, as observed on several specimens. An overly high dissolution at higher molarities, can result in free alkali ions becoming residues within the structure which slows down the geopolymerization reaction (Singh and Subramaniam, 2017; Das and Shrivastava, 2021).

The strength increase with rising the Na_2SiO_3/NaOH is often reported in geopolymers, and attributed to the more abundant silica in solution creating more Si-O-Si geopolymer bonds (stronger than Si-O-Al) improving geopolymerization and increasing strength (Jong and Brown, 1980; Gao *et al.*, 2014; Castillo *et al.*, 2021).

In all the AA bauxite materials, the porosity and density values are inconsistent as they seem to maintain or slightly raise over time in several mixes. However, as the Na_2SiO_3/NaOH increased, the pore volume and water absorption tend to lower. The water absorption values agree with the porosity indicating an open pore system. The results disagree with Huseien *et al.* (2016) who report that increased NaOH molarity in geopolymers enhances density and reduces void content resulting in an improved microstructure. However, the porosity values are

comparable with Thokchom *et al.* (2009) and Huseien *et al.* (2016) who stating porosity and water absorption values of 12.54–21.51% and 6.42-22.79% respectively for FA geopolymers.
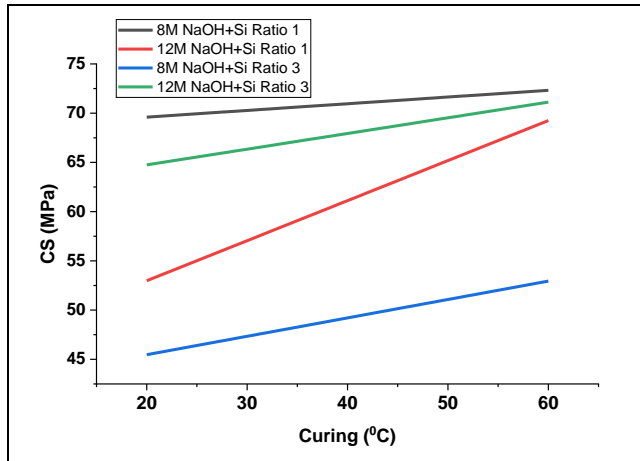
Figure 5-46 Effect of curing temperature in the AA bauxite 50% GGBS materials.	Figure 5-47 Effect of curing temperature in the AA bauxite 50% FA materials.
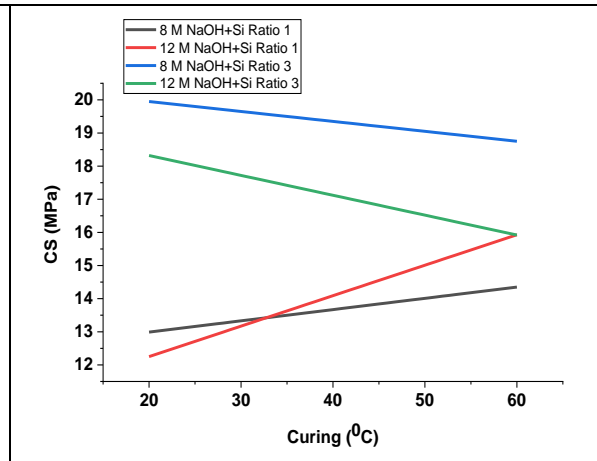
Table 5-17 Properties of AA bauxite materials at 28 and 90 days. FC (flexural strength), CS (compressive strength), P(porosity), BD (bulk density) and WA (water absorption).

Mix.	NaOH M	Na$_2$SiO$_3$/NaOH	T ^{0}C	FC (MPa)		CS (MPa)		P (%)		BD (kg/m^3)		WA (%)	
				28	90	28	90	28	90	28	90	28	90
100% bauxite	8	1	20	2.56	5.05	7.35	15.78	24.22	23.34	1909.24	1884.09	11.26	11.02
100% bauxite	12	1	20	2.78	2.22	9.54	5.90	19.45	23.47	1990.75	1890.53	8.90	11.04
100% bauxite	8	3	20	5.62	9.95	20.38	33.28	21.69	22.35	1977.13	1968.75	9.89	10.20
100% bauxite	12	3	20	4.54	6.91	16.58	23.11	20.68	22.14	1983.34	1976.81	9.44	10.07
100% bauxite	8	1	60	2.97	4.42	6.69	11.79	23.31	24.30	1914.26	1870.39	10.85	11.50
100% bauxite	12	1	60	2.31	1.82	10.43	4.98	21.80	23.31	1928.07	1879.91	10.16	11.03
100% bauxite	8	3	60	5.91	8.65	22.52	25.39	21.44	22.77	1925.84	1910.56	10.02	10.65
100% bauxite	12	3	60	5.05	7.41	15.11	15.46	22.39	23.23	1943.21	1949.63	10.33	10.64
100% bauxite	10	2	40	6.62	10.80	30.33	34.82	22.27	21.16	1957.21	1973.12	10.22	9.68
50% FA	8	1	20	3.93	8.08	12.99	24.31	17.69	21.46	2009.12	1971.25	8.09	9.82
50% FA	12	1	20	4.37	4.03	12.25	13.53	12.22	18.71	2074.10	1972.48	5.56	8.66
50% FA	8	3	20	5.49	8.53	19.95	25.66	17.69	19.83	2020.16	2017.44	8.05	8.95
50% FA	12	3	20	4.73	8.35	18.32	21.27	18.25	18.63	2032.06	2033.45	8.24	8.39
50% FA	8	1	60	5.04	6.92	14.35	14.27	19.79	21.87	1969.59	1932.52	9.13	10.17
50% FA	12	1	60	3.28	5.29	15.93	13.09	13.87	22.15	2048.99	1945.46	6.34	10.22
50% FA	8	3	60	5.20	9.02	18.75	26.32	20.41	20.81	1986.33	1971.89	9.32	9.54
50% FA	12	3	60	5.05	8.96	15.92	16.74	15.37	20.82	2041.77	1962.76	7.00	9.59
50% FA	10	2	40	5.09	9.54	23.28	30.23	20.92	18.99	2001.95	2030.60	9.46	8.55
25% FA	10	2	20	7.58	11.35	30.72	39.65	17.49	20.28	1995.92	1986.59	8.06	9.26
25% FA	10	2	40	6.55	11.63	29.79	31.92	12.00	18.00	2046.92	2003.54	8.75	9.71
25% FA	8	2	40	6.73	8.63	29.65	38.37	21.04	21.75	1983.81	1962.32	9.59	9.98
25% FA	12	2	40	5.82	9.62	21.25	32.48	20.25	21.47	2000.53	1994.52	9.19	9.72
25% FA	10	1	40	2.08	2.54	4.96	12.49	19.77	14.16	2012.20	2047.98	9.22	6.63
25% FA	10	3	40	5.54	8.67	20.23	26.23	17.38	20.10	2037.34	2019.31	7.86	9.05
25% FA	10	2	60	7.43	11.49	36.42	44.13	18.29	20.16	2000.04	1973.18	8.38	9.27
CEM II				6.02	7.33	37.18	46.67	7.31	8.51	2208.23	2323.52	3.21	3.85

Table 5-18 Properties of AA bauxite GGBS materials at 28 and 90 days. FC (flexural strength), CS (compressive strength), P(porosity), BD (bulk density) and WA (water absorption).

Mix.	NaOH M	Na$_2$SiO$_3$/NaOH	T ^{0}C	FC (MPa)		CS (MPa)		P (%)		BD (kg/m^3)		WA (%)	
				28	90	28	90	28	90	28	90	28	90
50% GGBS	8	1	20	10.40	4.67	69.59	54.07	10.59	16.25	2140.88	2060.48	4.7157	7.50
50% GGBS	12	1	20	8.33	3.75	52.98	47.34	8.72	14.80	2143.44	2081.78	3.9123	6.71
50% GGBS	8	3	20	7.18	7.95	45.47	36.33	12.93	18.46	2117.14	2042.49	5.7594	8.33
50% GGBS	12	3	20	7.73	5.45	64.75	41.62	17.04	16.47	2036.07	2082.23	7.7240	7.52
50% GGBS	8	1	60	9.41	10.70	72.32	90.10	10.26	5.01	2137.22	2298.91	4.5815	2.30
50% GGBS	12	1	60	9.06	8.07	69.25	55.37	8.99	15.15	2141.37	2077.04	4.0315	6.99
50% GGBS	8	3	60	7.94	7.34	52.98	37.83	13.39	15.18	2117.84	2046.76	5.9488	8.43
50% GGBS	12	3	60	8.49	7.90	71.12	56.12	16.31	18.74	2069.18	2075.77	7.3078	7.49
25% GGBS	10	2	40	8.17	7.09	44.55	40.27	16.07	17.03	2040.74	2079.05	7.3026	7.61
25% GGBS	10	2	40	6.66	8.40	39.30	39.18	15.63	16.40	2050.73	2187.12	7.0852	7.33
25% GGBS	10	2	40	6.82	7.95	39.68	39.73	16.11	16.20	2093.33	2080.04	7.5634	7.30

5.3.3 Microstructures of the AA bauxite materials

The SEM analysis was carried out in pastes aged 28 days. As shown in chapter 4, under the SEM, the remains of untransformed metakaolinite were evidenced in the pastes activated with lime. 800 °C bauxite was used to produce the AAMs, at this temperature, boehmite has transformed into amorphous alumina, and kaolinite has completely turned into reactive metakaolin.

Specimens with 50% FA and GGBS replacement which reached most outstanding property values were investigated, cured at 20 degrees. In both cases, the qualitative nature and resolution of the SEM was insufficient to determine specific changes in the nature and amount of the polymer cements with varying silica content and NaOH concentration in the activator. However, a general change in microstructure and the quality of the cements was evident from the study.

In the bauxite FA specimens, abundant low crystallinity cements were evident both coating FA particles and in the matrix, and filling voids. Some FA particles are totally covered with geopolymer gels and there are remnants of unreacted FA particles. Abundant pores are evident. The surfaces of some of the FA particles shows mullite needles, indicating partial geopolymerization. Some FA particles are broken and include abundant geopolymer gels grown inside so that they appear incorporated into the structure. Figure 5-48 shows the chemistry of the geopolymer gels in the AA bauxite materials with 50% FA replacement (NaOH 10M and $Na_2SiO_3/NaOH = 2$). The elemental composition (as percentage by weight) obtained from the EDX analysis of several representative areas in the geopolymer indicates that it is a low calcium phase (alumina–silicate gel) with minor Ca (~1-3%) and some sodium (4-11%) substitution.

| 2 µm | WD = 11.5 mm | Mag = 3.45 K X | Signal A = SE2 | Date :1 Apr 2022 |
| | File Name = sp sample 21.tif | | EHT = 5.00 kV | Time :14:12:28 |

Figure 5-48

| 2 µm | WD = 9.6 mm | Mag = 2.53 K X | Signal A = SE2 | Date :1 Apr 2022 |
| | File Name = sp sample 22.tif | | EHT = 15.00 kV | Time :14:27:30 |
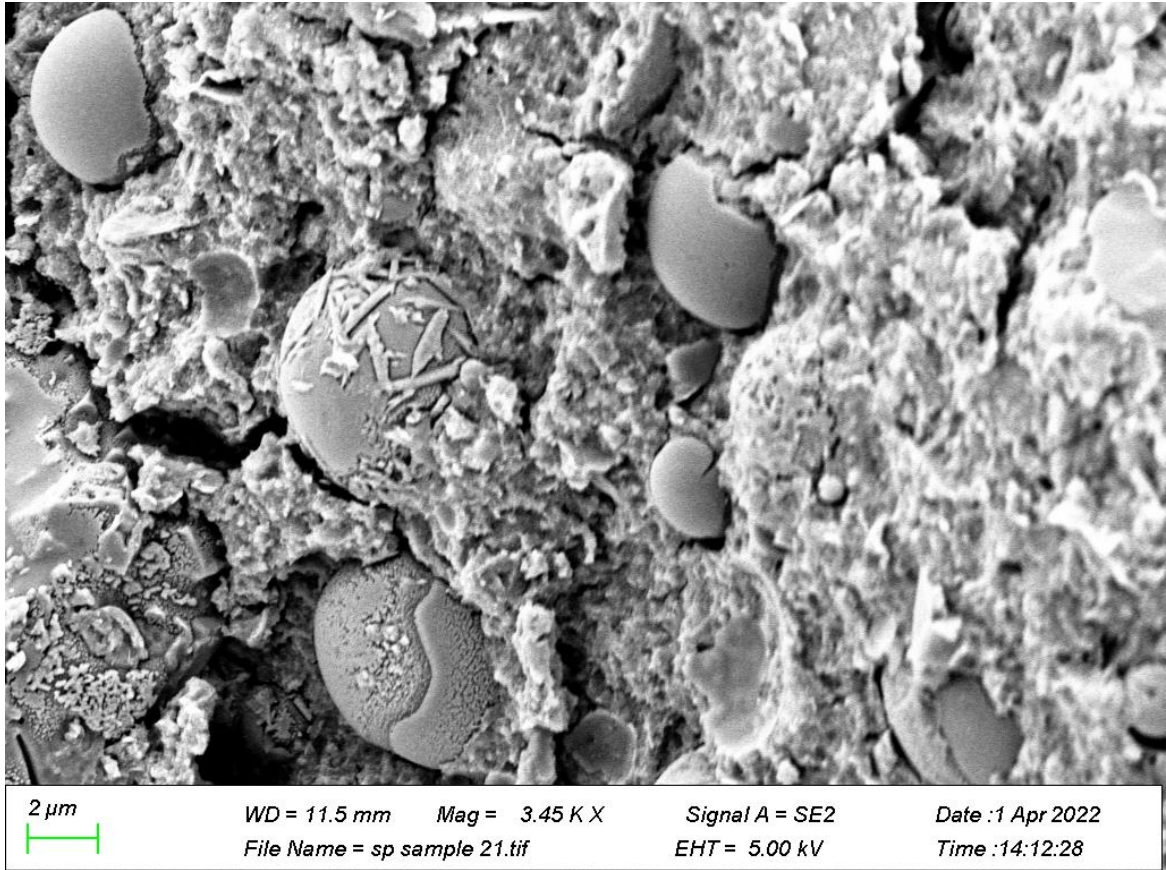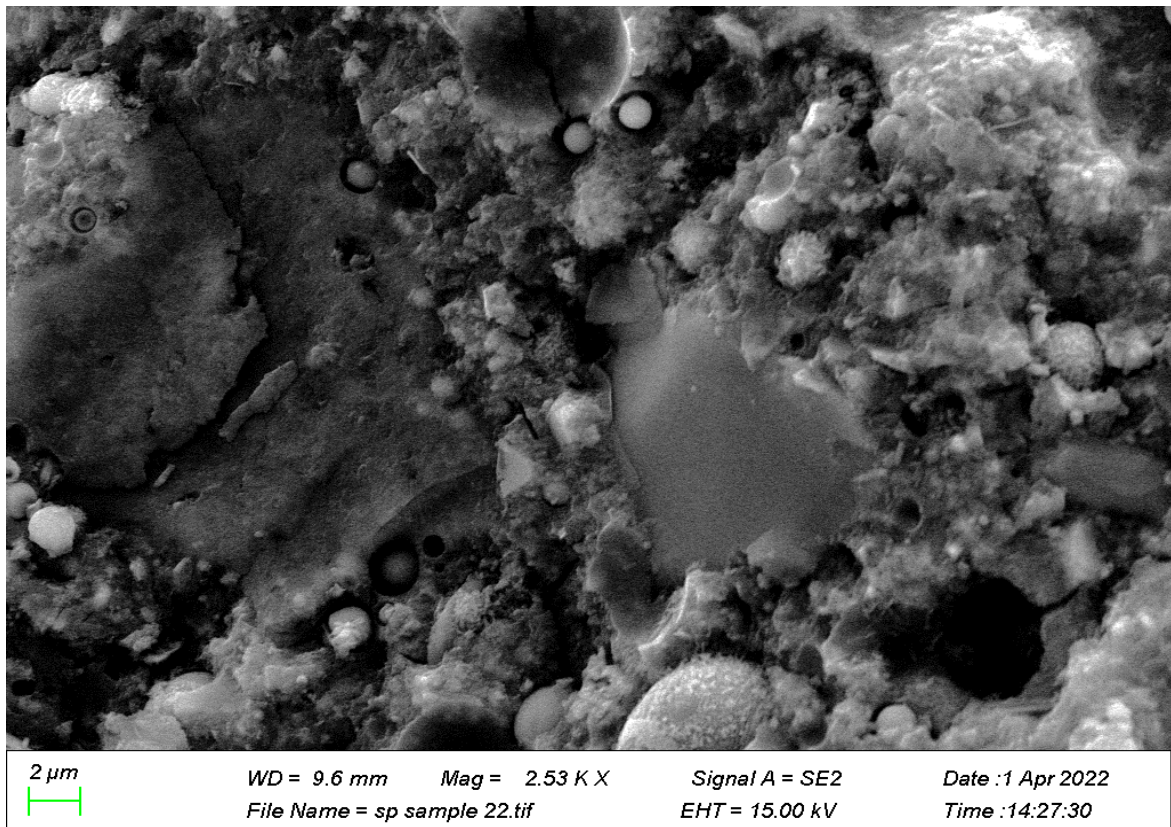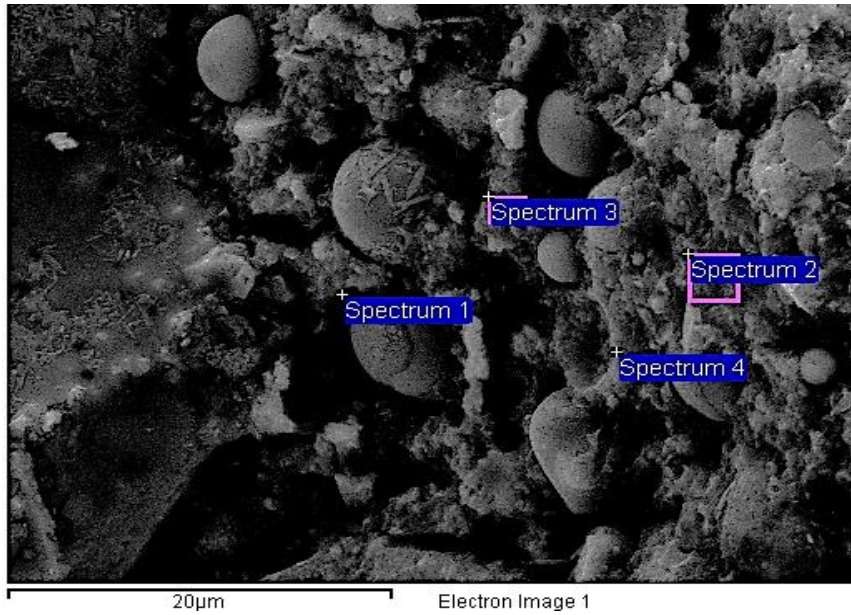
Figure 5-49

Figure 5-50 Location of the chemical composition of the geopolymers cements in the spectrums below- Figure 5-48.

Chemical composition of the geopolymer gels in Figure 5-48.
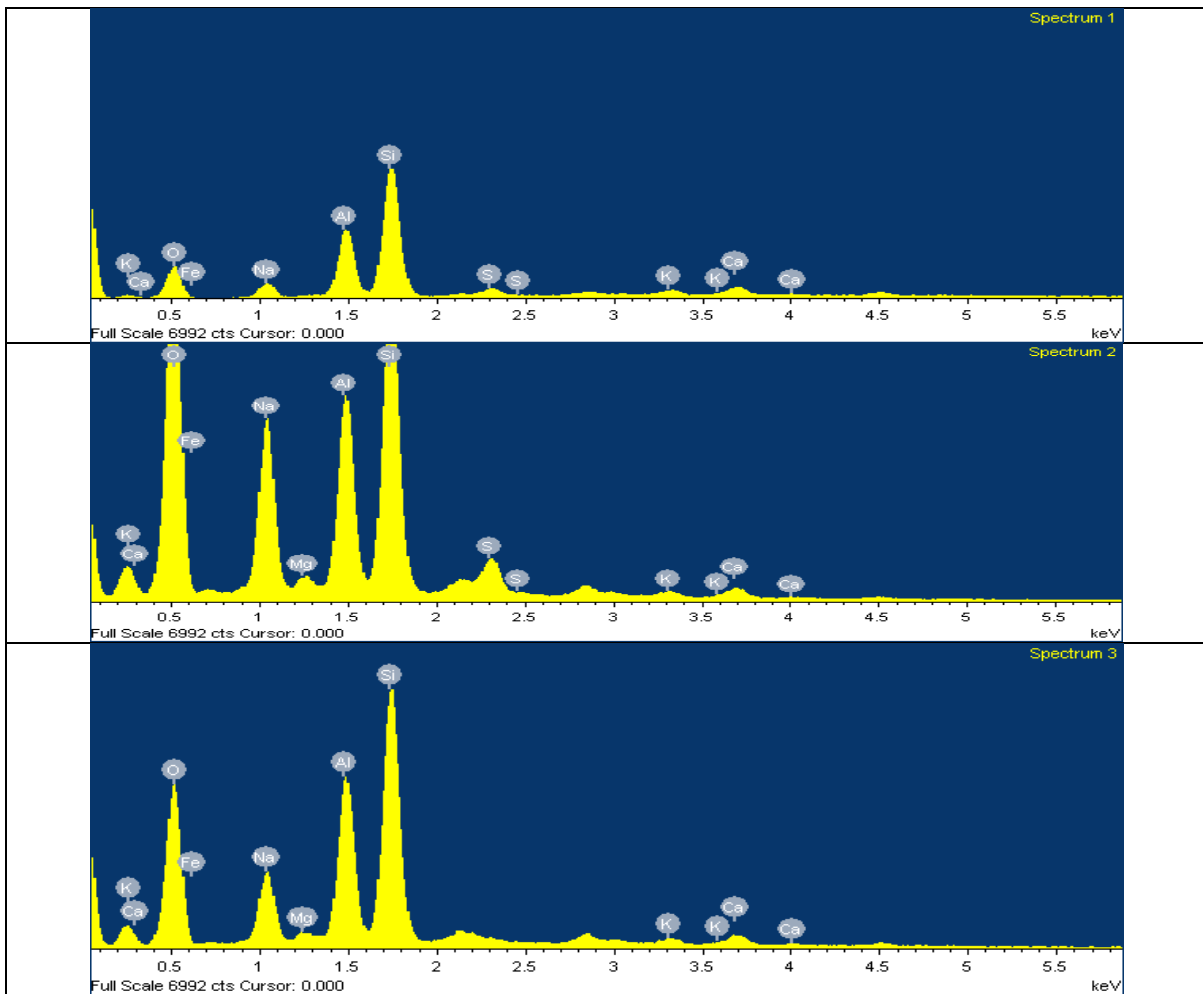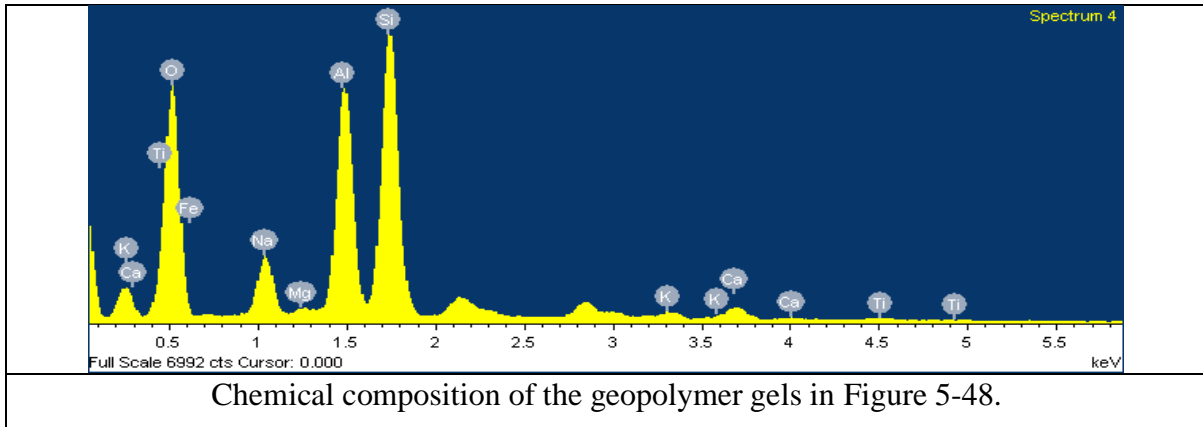
Table 5-19 Chemical composition (%wt) of the geopolymer gels in Figure 5-48.

Elements	O	Na	Mg	Al	Si	S	K	Ca	Ti	Fe
Spectrum 1	37.42	4.41	-	12.87	28.78	2.48	1.89	3.33	-	8.82
Spectrum 2	58.71	11.30	0.75	8.66	14.79	2.52	0.50	0.84	-	1.93
Spectrum 3	53.34	7.90	0.71	12.01	20.95	-	0.84	1.49	-	2.74
Spectrum 4	58.12	5.37	0.37	13.02	18.39	-	0.68	1.39	0.42	2.24

The bauxite 50% GGBS specimens, are finer grained and denser, with abundant cements coating particles and filling voids. The fine particles of GGBS also filled voids resulting in a dense microstructure agreeing with Yunsheng *et al.* (2007), who note that adding GGBS to metakaolin improved the pore structure of the geopolymeric matrix. However, clay mineral plates (probably kaolinite-metakaolin) were occasionally found unreacted - Figure 5-51.

The elemental composition (as percentage by weight), obtained from the EDX analysis of several representative areas in the geopolymer, indicates that it is a low-calcium phase similar to the one in the bauxite/FA geopolymer, however the Al content is greater. Therefore, the main cementing phase in an aluminate–silicate gel, with low-Ca and some sodium substitution.

Figure 5-51
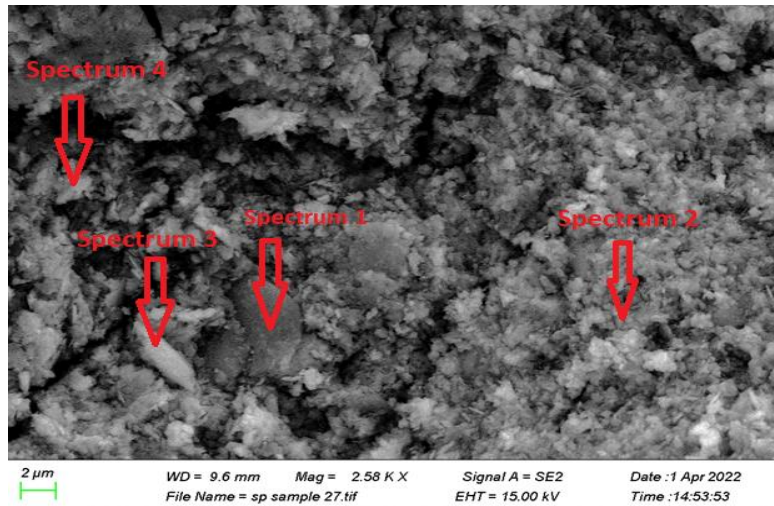
Figure 5-52

Table 5-20 Chemical composition of the geopolymer gels in Figure 5-53.

Elements	C	O	Na	Al	Si	K	Ca	Fe
Spectrum 1	11.53	48.88	1.43	21.45	15.66	-	0.5	0.54
Spectrum 2	-	51.89	3.79	29.28	12	0.13	1.16	1.74
Spectrum 3	-	54.93	2.64	24.67	16.22	-	0.79	0.75
Spectrum 4	-	50.64	3.75	31.79	10.13	0.15	1.65	1.9
average weight %	11.53	51.59	2.90	26.80	13.50	0.14	1.03	1.23

6. DESIGN OF ALKALI-ACTIVATED BAUXITE MATERIALS USING DESIGN OF EXPERIMENTS (DOE) ANALYSES

As explained in the methods (chapter 3) the Minitab software was used to undertake the DOE analysis. It generates different statistical reports and plots that illustrate the effects of the factors (or variables) on the outputs (or properties). As aforementioned, the main objective is to optimise the process by defining critical and non-critical relationships between factors and responses hence, optimise the settings of the process for best quality (Arnold, 2006). The statistical reports and plots generated by Minitab to determine the effect of factors (or variables) over outputs (or properties) are included in chapter 3. Minitab is the primary choice to do the DOE experiments due to the availability of a license from IT Services at Trinity College Dublin. As seen in methods, five responses or outputs of interest were determined including flexural strength, compressive strength, porosity, bulk density and water absorption; as well as four main factors (i-iv) at three levels each as follows:

i. NaOH 8 M (minimum level),10 M (centre level),and 12 M (maximum level);

ii. $Na_2SiO_3/NaOH = 1$ (minimum level), 2 (centre level) and 3 (maximum level);

iii. Curing temperature 20^0C (minimum level), 40^0C (centre level) and $60\ ^0C$ (max. level);

iv. % FA/GGBS at 0% (minimum level), 25% (centre level) and 50% (maximum level).

Two DOE methods were used in the analyses: Full factorial design and Response Surface Methodology (RSM). The full factorial design method measures the results with all combinations of experimental factors that can be used to run the experiments at all levels, and assumes that there is a linear relationship between each factor and the response. Accordingly, if the factor and response have a non-linear relationship, a factorial design for the particular study may produce a misleading result. When this was the case, the experiment was extended to Response surface methodology (RSM) (Al-Shalif, 2020). The RSM method is used to investigate non-linear factorial relationships obtained from the full factorial designs method, in order to fit the curves and analyse the data properly (Beg and Raza, 2021). It does this, by running further experiments and build up on the results obtained from the full factorial design method. As it can be seen from Table 6-1, some responses exhibit significant curvature indicating that factorial design is unsuitable. Therefore, the factorial design was upgraded to

RSM to fit the curves and analyse the responses properly. To this aim, 10 further mixes were added to increase the accuracy level of the model. The bauxite GGBS materials at 28 days show the responses with no-significant curvature, hence the full factorial design is sufficient.

Table 6-1 AA bauxite materials: factorial design for 19 experiments.

28 days AA bauxite blended with FA		
Response	**Curvature**	
flexural strength	0	Significant
compressive strength	0	Significant
porosity	0	Significant
water absorption	0	Significant
bulk density	0	Significant

90 days AA bauxite blended with FA		
Response	**Curvature**	
flexural strength	0.04	Significant
compressive strength	0.001	Significant
porosity	0	Significant
water absorption	0	Significant
bulk density	0	Significant

28 days AA bauxite blended with GGBS		
Response	**Curvature**	
flexural strength	0.063	Not significant
compressive strength	0.162	Not significant
porosity	0.117	Not significant
water absorption	0.310	Not significant
bulk density	0.134	Not significant

90 days AA bauxite blended with GGBS		
Response	**Curvature**	
flexural strength	0.005	Significant
compressive strength	0.001	Significant
porosity	0	Significant
water absorption	0	Significant
bulk density	0	Significant

As aforementioned, ANOVA (Analysis of Variance) is used to evaluate the fitness of the generated mathematical models of the five responses (flexural strength, compressive strength, porosity, water absorption, and bulk density) and their relationship with the four factors (NaOH molarity, Na_2SiO_3/NaOH, curing temperature and %FA/GGBS), and the P-value was used to

determine the results reliability (P-value $\leq$ 0.05, the results are reliable and vice versa). Consequently, the AA bauxite results are reliable- Table 6-2 and Table 6-3.

Additionally, the P-value of the ANOVA lack of fit is an additional method to confirm reliable results, the non-significant lack of fit is favourable, which means that the results are accurate and fit the experimental results (Igwegbe *et al.*, 2019) (Ahmadi *et al.*, 2018). Therefore, the P-Value of lack-of-fit > 0.05 means reliable results- Table 6-2 and Table 6-3.

Moreover, Table 6-2 and Table 6-3 show that the R² and adjusted R^2 values are in reasonable agreement at (76.15%–99.41%) and (64.18%–98.22%), respectively, suggesting a high correlation between the actual and adjusted values which means the value has a strong effect (Moore and Kirkland, 2007; Henseler *et al.,* 2009).

Table 6-2 ANOVA analysis model of AA bauxite- FA materials.

output variables	AA bauxite & FA blend									
	28 Days									
	FC		CS		P		BD		WA	
Source	P-Value	F-Value	P-Value	F-Value	P-Value	F-Value	P-Value	F-Value	P-Value	F-Value
P-value	0.00	13.96	0.00	23.23	0.00	7.98	0.00	15.08	0.00	12.28
Lack-of-Fit	0.92	0.38	0.06	8.62	0.10	5.22	0.12	4.50	0.73	0.70
R^2 (%)	86.87		92.81		79.08		85.78		85.33	
Adjusted R^2 (%)	80.65		88.81		69.18		80.10		78.39	
	90 Days									
output variables	FC		CS		P		BD		WA	
Source	P-Value	F-Value	P-Value	F-Value	P-Value	F-Value	P-Value	F-Value	P-Value	F-Value
P-value	0.00	12.89	0.00	37.68	0.00	6.57	0.00	19.26	0.00	7.98
Lack-of-Fit	0.70	0.76	0.08	5.91	0.20	2.96	0.09	5.46	0.07	6.50
R^2 (%)	85.93		93.78		75.69		86.52		76.15	
Adjusted R^2 (%)	79.26		91.29		64.18		82.03		66.61	
Flexural strength (FC), compressive strength (CS), porosity(P), bulk density and water absorption (WA).										

Table 6-3 ANOVA analysis model of AA bauxite - GGBS materials.

output variables	AA bauxite & GGBS blend									
	28 Days									
	FC		CS		P		BD		WA	
Source	P-Value	F-Value	P-Value	F-Value	P-Value	F-Value	P-Value	F-Value	P-Value	F-Value
P-value	0.00	21.96	0.00	83.91	0.00	56.48	0.00	20.36	0.00	21.63
Lack-of-Fit	0.73	0.61	0.47	1.32	0.06	19.08	0.50	1.33	0.08	11.19
R^2 (%)	96.48		99.41		97.29		91.05		95.58	
Adjusted R^2 (%)	92.09		98.22		95.57		86.58		91.16	
	90 Days									
output variables	FC		CS		P		BD		WA	
Source	P-Value	F-Value	P-Value	F-Value	P-Value	F-Value	P-Value	F-Value	P-Value	F-Value
P-value	0.00	8.48	0.00	17.44	0.00	9.53	0.00	7.82	0.00	8.84
Lack-of-Fit	0.59	0.92	0.18	2.30	0.11	3.05	0.65	0.81	0.15	2.64
R^2 (%)	80.06		90.65		87.73		83.50		85.12	
Adjusted R^2 (%)	70.62		85.45		78.53		72.83		75.50	

The DOE allows setting optimization goals using the response optimization tool. The optimization criteria were set to maximize the mechanical strengths and the density and minimize porosity and water absorption as shown in Table 6-4.

Table 6-4 Optimization parameters.

Response	Goal
Water absorption (WA), %	Minimum
Bulk density (BD), kg/m^3	Maximum
Porosity (P), %	Minimum
Compressive strength (CS), MPa	Maximum
Flexural strength (FC), MPa	Maximum

Table 6-5 Optimum mix for the AA bauxite - FA materials according to the DOE analyses.

	NaOH M	Na$_2$SiO$_3$/NaOH	Temperature	FA %
28 days	10	2	20	50
90 days	10	2	20	50

Table 6-6 Optimum mix for the AA bauxite - GGBS materials according to the DOE analyses.

	NaOH M	Na$_2$SiO$_3$/NaOH	Temperature	GGBS %
28 days	8	1	20	50
90 days	8	1	60	50

According to the DOE, the best curing temperature for AA bauxite FA materials (50%FA) is ambient temperature, and the property results are best at medium (10M) NaOH concentration. Medium silica contents in the activator (Na$_2$SiO$_3$/NaOH =2) enhance mechanical strength and microstructure in the bauxite-FA systems, whereas lower concentrations are needed in the bauxite-GGBS systems to optimise strength and microstructure (Tables 6-5, 6-6).

According to the DOE, the best AA bauxite GGBS materials (50%) would be produced at 60 °C curing temperature, and the property results are best at the lowest (8M) NaOH concentrations.

The optimum mixes delivered by the DOE in Table 6-5 and Table 6-6 were fabricated and tested in the laboratory. The laboratory experiments confirmed the software results as shown in Table 6-7 and Table 6-8. Therefore, the experimental methods are validated, as well as the method used for the modelled predictions for the AA materials in the range studied.

Table 6-7 Results of laboratory experiments run with the optimum mixes delivered by the DOE: AA bauxite-FA materials.

Responses	28 days		90 days	
	DOE software	Laboratory results	DOE software	Laboratory results
	Predicted results		Predicted results	
Flexural strength (MPa)	7.16	6.57	12.14	12.15
Compressive strength (MPa)	33.25	33.12	39.72	35.80
Porosity (%)	16.09	16.89	19.54	19.31
Water absorption (%)	7.46	8.10	8.64	8.81
Bulk density (kg/m^3)	2047.80	2025.17	2024.30	2000.32

Table 6-8 Results of laboratory experiments run with the optimum mixes delivered by the DOE: AA bauxite-GGBS materials.

Responses	28 days		90 days	
	DOE software	Laboratory results	DOE software	Laboratory results
	Predicted results		Predicted results	
Flexural strength (MPa)	9.70	9.35	9.87	8.95
Compressive strength (MPa)	66.55	60.41	77.44	75.80
Porosity (%)	10.66	9.95	10.15	9.20
Water absorption (%)	4.22	4.51	5.22	4.08
Bulk density (kg/m^3)	2148.55	2252.40	2131.32	2151.81

7. A COMPARATIVE STUDY OF THE ENVIRONMENTAL IMPACT OF SOME ALKALI-ACTIVATED AND TRADITIONAL MATERIALS

Construction is responsible for a significant percentage of the total greenhouse gas emissions worldwide. To restrict global warming, these emissions need to lower. Alkali-activated materials (AAMs) do not require clinker manufacturing but are produced at low temperatures, usually ranging from ambient to 100 °C. Furthermore, most AAMs are made with waste which further lowers their embodied energy as well as the raw material and fuel consumption used for their making. This chapter calculates the EE and carbon footprint (E_{CO2}) of alkali-activated materials made with industrial wastes, including red mud (RM), granulated blast furnace slag (GGBS), and bauxite. The values are compared with traditional PC products. The environmental impact calculated is set against the strength of the AAMs at 28 days to assist the design of mixes of lower impact.

As seen in the previous chapters (Chapter 4), some of the wastes used as precursors were pyro-processed to increase their reactivity. This involves energy use, and hence it raises the embodied carbon of the resultant materials. However, the lowest temperature that reported the greatest reactivity was chosen for pyro-processing, and the environmental impact due to the heat treatment is included in the environmental impact calculations as explained below.

7.1 ENVIRONMENTAL IMPACT OF CONSTRUCTION: PC AND AAMs.

Global warming and climate change are due to greenhouse gas emissions. The construction industry is one of the largest contributors to greenhouse gas emissions (GHG) and a great consumer of energy and non-renewable natural resources. A third of the world's GHG emissions come from buildings, which consume over 40% of the global energy consumed worldwide (Sbci, 2009).

CEN's Technical Committee 350 (CEN/TC 350 : 2012), was formed, under European Commission mandate, to provide a standardized method for the evaluation of the sustainability

of buildings and civil engineering works -Figure 7-1. Within the CEN/TC 350 : 2012 framework EN 15978 was published. As detailed below, this standard is used to assess the environmental performance of buildings and materials.

Sustainability of construction works CEN/TC 350		
Framework level BS EN 15643-1 (2010) *Sustainability Assessment of Buildings – General Framework* BS EN 15643-2 (2011) *Assessment of Buildings. Framework for the assessment of environmental performance*	**Building level** BS EN 15978 (2011) *Assessment of environmental performance of buildings. Calculation method* PD CEN/TR 17005 (2016) *Additional environmental impact categories and indicators – Background information and possibilities – Evaluation of the possibility of adding environmental impact categories and related indicators and calculation methods for the assessment of the environmental performance of buildings*	**Product level** BS EN 15804 (2012) +A2 (2019) *Environmental product declarations – Core rules for the product category of construction products* PD CEN/TR 16970 (2016) *Guidance for the implementation of EN 15804* BS EN 15942 (2011) *Environmental product declarations – Communication format business-to-business* PD CEN/TR 15941 (2010) *Environmental product declarations – Methodology for selection and use of generic data*

Figure 7-1 Framework of CEN/TC 350 sustainability of construction work (Gibbons and Orr, 2020).

The International Standard Organization (ISO/TS14067:2014) is also a relevant source providing the carbon footprint of products: their requirements and guidelines for quantification and communication. A carbon footprint measures the total GHG emissions produced by a person, organisation, event or product. GHGs are emitted throughout all the stages of the life cycle of a product, from raw material acquisition to production, use and end-of-life ISO/TS 14067: 2014. The embodied carbon is the carbon footprint of a material/structure. It is measured in kg of carbon dioxide equivalent ($kgCO_2e$) and includes the emissions of the six GHGs relative to one unit of CO_2.

A major contributor to climate change is carbon dioxide CO_2 which accounts for three-quarters of all GHGs (Nejat *et al.*, 2015). Most traditional construction materials carry a significant environmental impact because they require high energy inputs and nonrenewable materials for their production, contributing to material depletion, greenhouse gas emissions and climate change. The construction binder that generates the highest CO_2 emissions is Portland cement (PC) clinker, as it is the binder most widely used in construction. Hence, PC production is often blamed as the main contributor to greenhouse gas emissions worldwide. According to Metz *et*

al. (2005), the cement industry contributes approximately 7% of global carbon dioxide emissions.

There are two significant sources of CO_2 emissions in the PC industry: the decarbonisation of limestone and/or other carbonate rocks transforming into CaO, and the burning of fossil fuels that power the kilns where this process takes place. It is estimated that about 0.9–1.0 tonnes of CO_2/tonne of clinker require heat demand between 3500 to 5000 MJ per tonne of clinker, depending on the burning fuel type used (Deja et al., 2010). It is also estimated that 60 to 130 kilograms of fuel (oil) and around 110 kWh of electricity are needed to produce a tonne of cement in Europe, which contributes 4.3% of the total CO_2 emissions in 2019 (CEMBUREAU, 2020). Furthermore, the CO_2 emissions of the cement industry are not the only environmental impact of cement production but, as noted by García-Gusano *et al.*, (2015), photochemical ozone formation, acidification and fresh-water eutrophication can also be linked to the cement industry.

The CO_2 emissions from PC clinker production are a function of the energy efficiency of the calcination process and the type and consumption of fuel, with literature reporting a variation between 821.1 and 1150 kg CO_2/t clinker (Damineli *et al.*, 2010). A world average emission of 1 ton CO_2/t clinker is generally adopted, which in some cases is an overestimation because many producers currently have technologies to mitigate emissions, hence achieving emissions below 800 kg CO_2/t clinker (Damineli *et al.*, 2010).

CEM I is the PC which contains the most clinker (95%), hence it carries the greatest environmental impact. The reported global warming potential (GWP) of CEM I, measured for an average tonne of cement CEM I 52.5 (produced by 12 different companies across the 9 countries), is 874 kg CO_2e (Juarez and Finnegan, 2021). However, CEM I is hardly used in many countries in Europe because it is often over-specified for many applications, and it has a high environmental impact. CEM II is much more commonly used, which incorporates limestone as partial clinker substitution lowering environmental impact. However, the average tonne of CEM II still releases significant CO_2 into the atmosphere (631–769 kg CO_2e - Juarez and Finnegan, 2021). This is a lower emission than CEM I, however still enormous when compared to supplementary cementitious materials or pozzolans that can replace PC clinker.

As aforementioned, most of the environmental impact of PC is due to clinker production, which requires burning natural rocks at approximately 1400 °C releasing much CO_2 from the combustion of fuels and the decarbonization of carbonate rocks used as raw materials. Alkali-

activated materials (AAMs) do not require clinker manufacturing but are produced at low temperatures, usually ranging from ambient to 100 °C. Most AAMs are produced at ambient temperatures, and others with a small energy input that usually ranges between 60°C (curing) to 100°C (drying) or 400-600°C (thermal activation of certain wastes). Hence, they yield low carbon emissions and have low EE. Furthermore, most AAMs are made with industrial waste, which further lowers their EE as well as the raw material and fuel consumption for their making. The reduction in emissions, and the use of waste for the production of AAMs, can elicit their wide uptake in the markets (Shi *et al.,* 2003; Habert *et al.,* 2011; Unless *et al.*, 2015; Teh *et al.*, 2017).

Industrial by-products such as GGBS and ash residues such as FA, are used instead of PC clinker to produce AAMs. Tan *et al.*, (2020) demonstrated that FA in geopolymers can immobilise heavy metals and hazardous organic molecules via adsorption processes, in which heavy metal ions adhere to the binding surfaces of geopolymers referred to as adsorbates. These wastes contain abundant silicates and/or aluminates that can be activated with alkali metals. On successful activation, the wastes' active components generate Si^{4+}, Al^{3+}, and (sometimes) Ca^{2+} that become available to form cementing products. Most authors agree that AAMs have lower EE and carbon emissions than their equivalent PC products. Duxson *et al.*, (2007) calculated the CO_2 emissions of AA FA and/or metakaolin cements using the CO_2 evolved during the production of Na_2O and SiO_2 in the alkali process as the primary inputs and found savings of 80 % in CO_2 emissions when compared to PC. However, there is a great divergence of results due to both a disparity in the data used and the different formulations. Wimpenny, (2009); Provis *et al.,* (2009) state that the carbon footprint of AA binders is 30% of that of PC cement, but according to Zhang et al., (2017), the production of AA cement represents 60% lower values of energy and CO_2 emissions than PC. Pacheco-Torgal *et al.*, (2014) include several authors claiming 44-70% reductions in CO_2 emissions for several AAMs compared with similar PC mixes. Cunningham and Miller (2020) account for AAMs having 10%−80% lower EE than their equivalent PC materials. Davidovits and France (2018) state that geopolymers, a subset of AAMs where the binding phase is almost exclusively aluminosilicate, have a 10-20% lower carbon footprint than PC, while other geopolymer formulations (Habert *et al.,* 2010) have shown a 60% reduction in CO_2 emissions compared to their equivalent PC materials. More recently, Lolli and Kurtis (2021) completed life cycle analyses (LCA) studies concluding that AAMs display a 50% reduction in CO_2 intensity when compared to PC and

PC+SCM binders, while providing the required compressive strength for pavement applications (30 MPa).

The carbon emissions and EE of AAMs depend on their formulation. Ouellet-Plamondon and Habert (2015) state savings of up to 75% CO_2 emissions for certain formulations compared with their equivalent PC products. They also highlight additional environmental benefits such as reducing water use and no requirement for superplasticizer admixtures.

In AAMs, the main source of CO_2 impact are usually the activators. Na_2SiO_3 activators have a much greater environmental impact than NaOH (50–76% vs 8–31%) (Garces *et al.*, 2021). Alkali silicate production generally calcines silica and carbonated salts, and this is followed by dissolution in water, emitting abundant CO_2 and requiring high energy consumption. However, the CO_2 emission of the carbonates in this process is significantly lower per tonne than the CO_2 emissions of PC production, resulting in savings of up to 80% compared to PC manufacture (Gartner, 2004; Provis et al., 2014). The NaOH has lower CO_2 emissions and is typically produced via the chlor-alkali process in parallel with Cl_2. However, this has other environmental implications related to elements such as the mercury which is sometimes used in the process (Provis et al., 2014).

Ouellet-Plamondon and Habert (2015) claim that sodium silicate activators can contribute up to 80% of the total impact of an AAM. Anvekar *et al.,* (2014) report embodied energy 48% over the equivalent PC material, for certain AAM formulations, due to the energy required to manufacture the alkali activators. Several authors agree that the main source of CO_2 impact on AAMs in the production of sodium silicate activators is from sodium carbonate (Weldes and Lange 1969; Against *et al.,* 2014). However, the carbonate can be either mined from evaporate deposits or produced through the Solvay process, and mining implies 1/10th of the CO_2 production of the Solvay process. As a result, the impact of the sodium silicate activator is often overestimated (Lolli and Kurtis 2021).

Matheu *et al.,* (2015) state that the global warming potential of AAMs is approximately 25% lower than their PC equivalents. The authors demonstrated that, in ten LCA (Life cycle analysis) categories, (including global warming potential, acidification, human health, air pollutants, ecotoxicity, smog, natural resource depletion, indoor air quality, water intake and ozone depletion), AAMs have less impact than their equivalent PC materials. They found that, in seven categories, the AAMs impact was 40% lower than that of their PC equivalents. There were only two categories in which the PC material performed better: eutrophication and habitat

alteration, and they were attributed to the use of potassium-based activators. The potassium hydroxide used in the activating solution is the main cause of environmental impact because it can emit nutrients into the surrounding waterways (eutrophication) and hence alter habitats.

As the environmental impact of AAMs depends on their formulation, not only is it important to use activators of low impact, but it is also important to use wastes that do not require calcination or any other high-energy processing to render them reactive. As aforementioned, the processing of the wastes in this work is minimal, and the design of the AAMs tested is based in Chapter 4 which includes the properties of the raw and treated precursors which shows the minimum processing that renders maximum reactivity.

No current market data on AAMs was found. However, alkali activation is an old technology that was first patented by V.D. Glukhovskii and his team in the late 1950s (applied for in 1958 and listed in 1974- USSR 449894, Pub. No. 42, 1974- (Pacheco-Torgal et al. 2015). Subsequently, AAMs became very popular in the old U.R.S.S. According to Pacheco-Torgal et al. 2015, large water pipelines, cast building elements of different types, road slabs and air-field runways and breakwater blocks on sea shores were made with AAMs, showing outstanding durability and long-term strength gain. AAMs were advanced in the Soviet Union in the 70s and the 80s, Glukhovskii, Serykh, Pakhomov and other authors published widely in the Russian language, but no English translations prevented dissemination, and the technology didn't reach the world until later. Today's revival of AA technology is largely due to environmental problems.

7.2 CALCULATION OF EMBODIED ENERGY AND EMBODIED CARBON

Buildings include operational emissions (due to consuming energy for running the building) and embodied emissions or E_{CO2} (resulting from material production, construction, maintenance, repair, demolition and disposal). Up to recently, in both industry and legislation, priority was given to the operational emissions and the embodied carbon emissions were largely ignored. However, in recent years, the embodied carbon is finally being considered and related standards and tools have been produced. The standardised method most commonly used to assess the environmental impact of construction processes and products is the LCA which consists of five stages EN 15978 : 2011 and Figure 7-2. EN 15978 includes the whole life carbon analysis -LCA- of a building or material, including the embodied carbon of all building stages: from material production to demolition and disposal.

1- Production (cradle to gate): [stages $A1 - A3$], which include extraction of raw materials, transportation, and manufacturing.

2- Construction process (handover): [$A4 - A5$], which includes the transport of materials to the site.

3- Use: [$B1 - B5$], which includes replacement and maintenance.

4- End-of-life (cradle to grave): [$C1 - C4$], which includes demolition, disassembly, and disposal of materials, transportation of materials off-site, and disposal of materials.

5- Beyond the life cycle: [D], which includes 'cradle to grave' for the possible benefits of reusing and recycling.
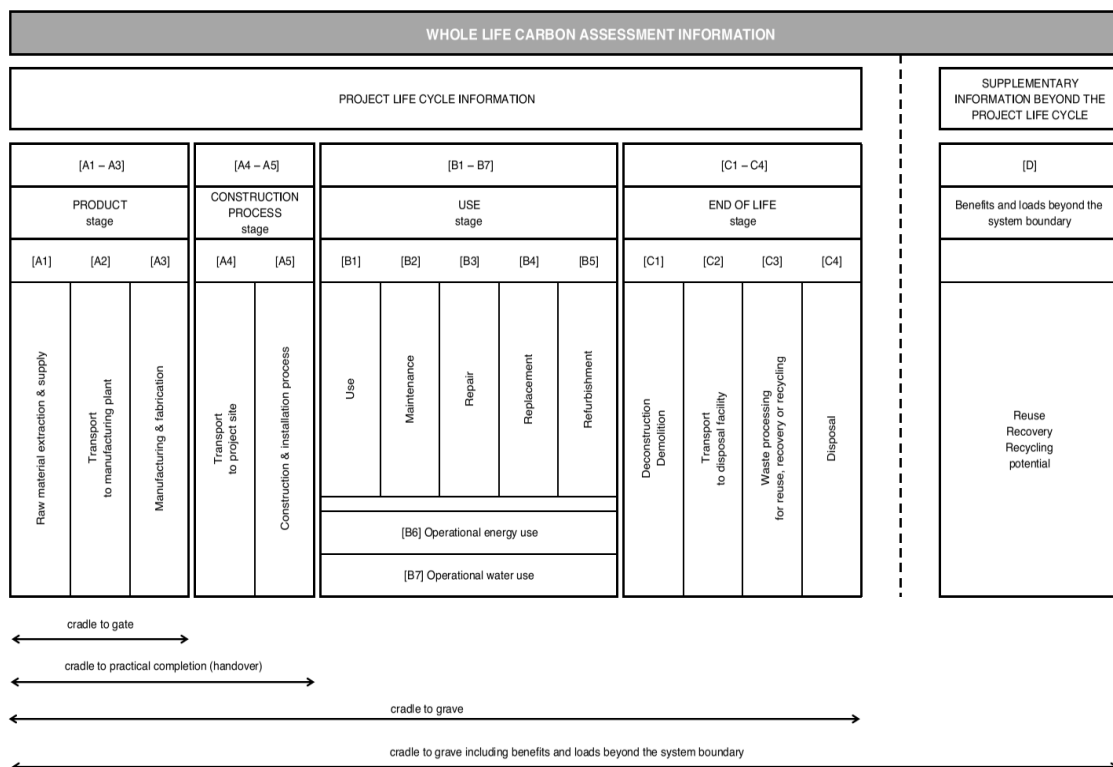
Figure 7-2 All the life cycle stages according to EN 15978.

In this research, we are calculating the embodied carbon of the production stage [stages A1–A3 in the LCA], or "cradle to gate", which includes raw material supply (including transport) and material production/manufacture. Here the E_{CO2} can be calculated from either detailed material specifications or taken from Environmental Product Declarations (EPDs) or well-known databases.

The carbon emissions of the product stage [A1–A3] in the whole life carbon assessment must be calculated by assigning suitable embodied carbon factors to the given material quantities. The environmental impact calculated according to the equation below:

[A1–A3] = Material quantity × Material embodied carbon factor

The embodied carbon factor was taken form relevant sources as explained below. When embodied carbon data were not available (e.g. for the bauxite), calculations were made by processing the data on energy consumption for material production provided by the producers.

The acceptable sources for embodied carbon factors that can be used in carbon assessments are standardised in EN 15978. One of the most common and acceptable sources of carbon factors are the environmental product declarations (EPDs) which are usually provided by material manufacturers. However, there are databases such as the Inventory of Carbon and Energy (ICE-RICS, 2012) that hold relevant information. The databases are more general rather than specific to a particular material, and they often compile data from various sources with wide variation in values. Hence, they can be less accurate and less specific to a particular project. This variation can led to a wide range of values that can cause inconsistent results.

Kaethner and Burridge (2012) in their review of worldwide LCA databases found that the embodied CO_2 value for concrete ranged from 59 to 202 $kgCO_2$/t. The values varied due to differing concrete specifications and PC production. Hammond and Jones (2008) completed a review of worldwide research and databases and found that the embodied carbon of concrete, for a cradle-to-gate boundary, ranged from 430 to 2750 $kgCO_2$/t depending on the amount of recycled steel used.

As aforementioned, the scenarios for the production stage which is subject to this study are usually defined in environmental product declarations (EPD's). However, no EPDs exist for the AAMs investigated, not even for some of the AAMs components. Therefore, for the different components of the AAMs, some values are taken from the databases and from the literature (Table 3.2 in Chapter 3), and other values are calculated with data provided by the producers as explained in Chapter 3 (Methods). The embodied energy and carbon of thermally activating the wastes was calculated when relevant. Similarly, the values for quarrying bauxite were also calculated.

This chapter calculates the EE and carbon footprint (E_{CO2}) of alkali-activated materials made with wastes including red mud (RM), granulated blast furnace slag (GGBS) and bauxite. The values are compared with equivalent PC products made with CEM II. The total embodied

energy (EE) expressed in MJ/kg and total embodied carbon - E_{CO2} - in $kgCO_2/kg$ were calculated. The EE and E_{CO2} of the AAMs are reported as the arithmetic mean of all the mixes investigated.

A high mechanical strength usually indicates a greater durability contributing to a long-lasting life for built structures. As a long-lasting functional life implies a lower environmental impact, the strength of the resultant AAMs is set against their environmental impact to optimize the design of alkali-activated materials for lower environmental impact. The strength of the AA RM and GGBS materials was measured experimentally, while the AA bauxite materials' strength comes from experimental data and optimization of the mix design modelled using software.

7.3 EMBODIED ENERGY AND EMBODIED CARBON OF AA RM MATERIALS

The RM is produced as a waste during the refining of bauxite to produce aluminium. As a by-product, the energy required for its manufacturing is zero. It is also produced locally. Therefore, no transport is accounted for at the production stage. The results confirm that the alkali activators are the main responsible for the environmental impact of AAMs. It can be seen from the results that rising the concentration and molar ratio of alkali activator increases the environmental impact. However, it does not significantly increase the strength, sometimes it even reduces the strength (Table 7-1). As shown in Table 7-2, the activator that most contributed to environmental impact is Na_2SiO_3. The arithmetic mean of the embodied energy and embodied carbon of the Na_2SiO_3 activator are 64.52% and 71.70 % respectively, much higher that the contribution of the NaOH activator at 10.77% and 22.53% respectively.

In the AA RM materials, the results also show that growing RM substitution with FA, from 30 to 50%, tends to nearly double the 28-day compressive strength of the resultant AAMs without increasing their environmental impact (Table 7-1). The same effect is evident for the GGBS replacement when the main activator is NaOH. However, when the activator is silica, the strength drops despite the increase of GGBS. The strength values are the arithmetic mean of 6 tests each, and the results are reliable, showing a small dispersion, with COVs ranging from 0.04 to 0.21 in the AA RM materials. COVs of their CEM II equivalent is 0.10.

Table 7-1 Compressive strength and environmental impact of the AA RM materials (3:1 - sand: RM/FA/GGBS). CS: COVs =0.04-0.21; 0.1 (CEM II).

	CS-28 day	RM	FA	GGBS	Sand	NaOH	Na$_2$SiO$_3$	Embodied Energy (total)	Embodied Carbon (total)	Density	Embodied Energy (total)	Embodied Carbon (total)
	(MPa)	(%)	(%)	(%)	(%)	(%)	(%)	(MJ/m^3)	(kgCO$_2$/m^3)	(kg/m^3)	(MJ/kg)	(kgCO$_2$/kg)
RM-1	4. 53	100	—	—	61.53	1.74	4.71	722.77	62.58	1873.94	0.39	0.03
RM-2	4.68	100	—	—	60.41	1.08	7.30	910.26	76.52	1873.94	0.49	0.04
RM-3	1.69	100	—	—	59.09	—	11.14	1190.43	96.58	1873.94	0.64	0.05
RM-FA-1	6.87	70	30	—	61.88	1.69	4.59	680.93	61.91	1995.82	0.34	0.03
RM-FA-2	10.85	70	30	—	60.75	1.05	7.12	863.95	75.56	1992.34	0.43	0.04
RM-FA-3	5.74	70	30	—	59.44	—	10.89	1137.48	95.18	1994.08	0.57	0.05
RM-FA-4	9.90	50	50	—	62.23	1.65	4.47	647.84	60.88	1973.04	0.33	0.03
RM-FA-5	11.54	50	50	—	61.11	1.02	6.95	826.16	74.21	2019.31	0.41	0.04
RM-FA-6	8.90	50	50	—	59.09	—	8.16	1147.26	98.46	1996.17	0.57	0.05
RM-GGBS-1	13.21	70	—	30	61.53	1.74	4.71	865.61	71.92	2051.75	0.42	0.04
RM-GGBS-2	9.52	70	—	30	60.75	1.05	7.12	1032.70	83.77	2056.36	0.50	0.04
RM-GGBS-3	8.02	70	—	30	59.44	—	10.89	1306.23	103.39	2041.23	0.64	0.05
RM-GGBS-4	27.48	50	—	50	61.88	1.69	4.59	944.91	76.35	2095.31	0.45	0.04
RM-GGBS-5	33.65	50	—	50	61.11	1.02	6.95	1107.41	87.89	2096.48	0.53	0.04
RM-GGBS-6	12.59	50	—	50	59.44	—	10.89	1401.46	109.62	2097.20	0.67	0.05
CEM II	37.18	—	—	—	46.37	—	—	1778.63	305.03	2208.23	0.81	0.14

Table 7-2 Embodied energy and carbon of each component as a percentage of the total (AA RM materials). *dried at 105 ^{0}C for 24 hrs + ground for 3 hrs + sintered at 300 ^{0}C for 3 hrs.

	EE						E_{CO_2}					
	*RM	FA	GGBS	sand	NaOH	Na$_2$SiO$_3$	RM	FA	GGBS	sand	NaOH	Na$_2$SiO$_3$
	(%)	(%)	(%)	(%)	(%)	(%)	(%)	(%)	(%)	(%)	(%)	(%)
RM-1	17.14	—	—	12.61	15.39	54.86	—	—	—	8.63	32.14	59.23
RM-2	13.61	—	—	10.01	7.71	68.68	—	—	—	7.06	16.58	76.37
RM-3	10.40	—	—	7.65	—	81.94	—	—	—	5.59	—	94.41
RM-FA-1	12.73	1.65	—	13.38	15.82	56.41	—	1.82	—	8.72	31.46	58.00
RM-FA-2	10.04	1.30	—	10.55	7.88	70.23	—	1.49	—	7.15	16.30	75.07
RM-FA-3	7.62	0.99	—	8.01	—	83.38	—	1.18	—	5.67	—	93.14
RM-FA-4	9.56	2.89	—	14.07	16.09	57.39	—	3.08	—	8.87	30.97	57.08
RM-FA-5	7.50	2.27	—	11.03	7.99	71.22	—	2.53	—	7.28	16.08	74.12
RM-FA-6	5.40	1.63	—	7.94	—	85.02	—	1.90	—	5.48	—	92.61
RM-GGBS-1	10.02	—	20.79	10.53	12.85	45.81	—	—	12.98	7.51	27.97	51.54
RM-GGBS-2	8.40	—	17.43	8.82	6.59	58.76	—	—	11.15	6.45	14.70	67.71
RM-GGBS-3	6.64	—	13.78	6.98	—	72.61	—	—	9.03	5.22	—	85.75
RM-GGBS-4	6.55	—	31.75	9.64	11.40	40.65	—	—	20.38	7.07	25.51	47.03
RM-GGBS-5	5.59	—	27.09	8.23	5.96	53.13	—	—	17.71	6.14	13.58	62.57
RM-GGBS-6	4.42	—	21.41	6.50	—	67.67	—	—	14.20	4.93	—	80.88
Arithmetic mean (%)	9.04	1.79	22.04	9.73	10.77	64.52	—	2.00	14.24	6.78	22.53	71.70

7.4 EMBODIED ENERGY AND EMBODIED CARBON OF AA GGBS MATERIALS

The AA GGBS materials, including NaOH-rich activators, can reach strengths comparable to their CEM II equivalents (~26 - 34 MPa compared with 37 MPa for CEM II)- Table 7-3. However, their environmental impacts are considerably lower.

The EE of the AA GGBS materials is 39.51 % lower than the CEM II and the E_{CO2} 78.57 % lower (Table 7-11). Therefore, the right activator can provide a similar strength at half the emissions and half the EE than a similar CEM II mix.

As shown in Table 7-4, the activator that most contributes to environmental impact is Na_2SiO_3. The highest contribution to E_{CO2} was by Na_2SiO_3 at 45.30%. The EE and E_{CO2} contribution of the Na_2SiO_3 activator were 33.85% and 45.30 % respectively, much higher than the NaOH activator contributions of 12.17% and 30.25%. Therefore, the right activator can provide a similar strength at half the emissions than similar CEM II products.

The results agree with the AA RM materials confirming that the alkali activators are the main materials responsible for the environmental impact, and that increasing the concentration and molar ratio of alkali activator increases the environmental impact but can lower strength.

The results also agree with previous authors. Bhardwaj and Kumar, (2019), in AA slag materials cured at ambient temperature, state that Na_2SiO_3 contributed 0.46 kgCO2e/kg and NaOH 0.0051 kgCO2e/kg. These are lower Na_2SiO_3 E_{CO2} values, and similar NaOH E_{CO2} values than the present study. Miraki *et al.* (2022) noted that NaOH produces the greatest amount of CO_2 (an average of 6.67 kg/m^3) in AAS activated with NaOH. Long *et al.*, (2017) found that Na_2SiO_3 consumed 8.5 MJ/kg of the total EE (3408.12 MJ/m^3) for AA slag materials, slightly higher values than the present study.

Table 7-3 Compressive strength and environmental impact of the alkali-activated GGBS materials (3:1 - sand: GGBS). COVs AA GGBS=0.01-0.48. * from (Kishar *et al.,* 2018). ** These values are higher than G1-G3 due to curing at 60 ^{0}C.

	Curing	GGBS	Sand	NaOH (6M)	Na$_2$SiO$_3$	CS	Embodied Energy (total)	Embodied Carbon (total)	*Density	Embodied Energy (total)	Embodied Carbon (total)
	(°C)	(%)	(%)	(%)	(%)	(MPa)	(MJ/m^3)	(kgCO$_2$/m^3)	(kg/m^3)	(MJ/kg)	(kgCO$_2$/kg)
G1	20	22.37	67.11	1.02	3.31	25.70	1019.61	73.61	2150	0.47	0.03
G2	20	22.37	67.11	2.55	—	17.56	840.75	63.58	2150	0.39	0.03
G3	20	21.74	65.22	—	6.85	5.21	1234.50	87.32	2150	0.57	0.04
G4	60	22.37	67.11	1.02	3.31	33.69	1066.69	73.61	2150	**0.50	0.03
G5	60	22.37	67.11	2.55	—	12.03	887.83	63.58	2150	**0.41	0.03
G6	60	21.74	65.22	—	6.85	2.92	1281.58	87.32	2150	**0.60	0.04
CEM II	20	—	46.37	—	—	37.18	1778.63	305.03	2208.23	0.81	0.14

Table 7-4 Embodied energy and carbon contribution of each material as a percentage of the alkali activated GGBS materials.

	EE				E$_{CO2}$			
	GGBS	sand	NaOH	Na$_2$SiO$_3$	GGBS	sand	NaOH	Na$_2$SiO$_3$
	(%)	(%)	(%)	(%)	(%)	(%)	(%)	(%)
G1	58.85	8.94	7.17	25.05	42.28	7.34	17.95	32.43
G2	71.36	10.84	17.80	—	48.95	8.49	42.55	—
G3	48.60	7.38	—	44.02	35.65	6.18	—	58.17
G4	56.25	8.54	6.85	23.94	42.28	7.34	17.95	32.43
G5	67.58	10.26	16.85	—	48.95	8.49	42.55	—
G6	46.82	7.11	—	42.40	35.65	6.18	—	58.17
Arithmetic mean (%)	58.24	8.85	12.17	33.85	42.29	7.34	30.25	45.30

7.5 EMBODIED ENERGY AND EMBODIED CARBON OF AA BAUXITE MATERIALS

To calculate the environmental impact of the AA bauxite materials, the values of quarrying the bauxite were first calculated. As aforementioned, bauxite is the principal ore for aluminium. Extraction is adjusted to local conditions and is carried out mechanically or with explosives. The environmental impact of producing aluminium from bauxite is high, and the GHG emissions arising from the process are an environmental concern. However, the bauxite mining emissions are negligible when compared to the rest of emissions generated during aluminium production. Georgitzikis *et al.* (2021) indicate that, of the total GHG emissions (16.6 tonnes of CO_2e per tonne of primary Al), electrolytic smelting is responsible for 12.8 tonnes while mining only accounts for 0.05 tonnes of CO_2e per tonne of Al. The majority of the emissions of aluminium production (61%) arise from the electricity that powers electrolysis during the smelting process, while the rest (39%) arise for all the other steps in production including mining, refining (or Al_2O_3 production) and semis production (i.e. sheet, strip, plate, profiles, rod and bar, tube, wire and forgings) (Georgitzikis *et al.,* 2021, based on data by the International Aluminium Institute -IAI- dating from 2020). On view of these results, and despite the wide use and numerous applications of aluminium in today's world, it can be argued that an alternative use for bauxite (other than Al production) would lower environmental impacts worldwide.

Norgate and Haque, (2010) carried out a comparative study of the environmental impact of mining operations, indicating that bauxite mining uses considerably less energy and has much lower impact than iron ore or copper concentrate mining. The impact categories considered gross energy requirement (or embodied energy) and GHG emissions expressed as global warming potential- GWP). The authors included: drilling equipment (explosive loader trucks and several types of drills run with electricity and diesel power); the energy consumed in the blasting process derived from the chemical energy contained in the blasting agents; excavators; pumping for dewatering; dump trucks; and auxiliary equipment such as dozers, graders, excavators and water tankers used for road construction, maintenance and dust suppression. The authors also considered crushing and grinding plants (usually powered by electricity generated onsite using diesel generator) and assorted physical separators when needed or just screening (for bauxite). They note than most of these assets use diesel fuel for their operation.

Their results evidenced that bauxite mining requires much lower energy (54.9 MJ/tonne) than mining copper and iron ore (at 8,329.0 and 152.7 MJ/tonne of ore respectively). Therefore, the embodied energy of mining bauxite is much lower than that of mining other ores. Furthermore, the authors state that the GWP of bauxite mining (4.9 kg CO_2e /t) is also much smaller than those of mining copper and iron ore (628.0 and 11.9 kg CO_2e /tore respectively) (Norgate and Haque, 2010).

The bauxite in this research is quarried in the Az Zabirah and Al Bai'tha mines. The Az Zabirah mine supplies kaolin to the phosphate industry and low-grade bauxite to local cement companies, while the Al Bai'tha is quarried for high-grade bauxite for aluminium production (Mujabar and Dajkumar, 2019). As mentioned in the methods, the bauxite was quarried from a deposit located in a remote desert area of central/northern Saudi Arabia, predominantly in the province of Ha'il. The Ma'aden's exploration area covers approximately 6,000 km^2. The Az Zabirah and Al Bai'tha mines are open-pit operations located approximately 20 km apart, North of the city of Qibah, in the Al Qassim and Hail provinces of central Saudi Arabia.

Details of the mining process were provided by (B.A.M. Sidiya, Kaolin Processing and Management Ma'aden, 2021). The mining process starts with stripping the overburden by bulldozer ripping and dozing. The strip waste is then loaded into dump trucks and hauled to dumps outside the pit. Once exposed, the bauxite is ripped and piled in heaps by bulldozer. The ore is then screened and blended to meet customer requirements in terms of size and chemistry. Finally, the product is loaded into trucks and dispatched to costumers. During overburden stripping, a 0.5 to 1 meter soil cap is removed with a bulldozer, loaded into trucks and sent to landfill. Following overburden removal, the bulldozer rips the bauxite layer (0.5 meter per pass) and gathers it in heaps. The mine utilizes Cat D9R bulldozers for both the overburden and the ore. The material is then hauled to blending areas for screening and blending. All the batches are sampled and analyzed for chemical specification. The screening is carried out using front end wheel loaders and mobile screens. The loaders collect the material passing the sieve and stockpile it as the final product. Auxiliary equipment includes one grader and one compactor for road maintenance.

Therefore, according to the producers, the primary energy used in bauxite quarrying and production is diesel fuel (B.A.M. Sidiya, Kaolin Processing and Management Ma'aden, 2021). The CO_2 emissions estimated based on the quantity of diesel used and the activity of the

Alzabirah mine, amount 3.3 kg CO_2/t bauxite. This calculation considers a diesel consumption of 3,144 l/day producing 8,237.3 kg CO_2.

The bauxite selected to produce the AAMs was grounded in a digital ball mill with 20 mm Ø stainless steel balls at 150 r.p.m. (24 hours, and then the fraction under 0.5 mm for 3 hours). The energy and emissions due to processing were calculated as explained in Chapter 3 (Methods) and included in the calculations below. The grounded bauxite was calcined at 800 ^{0}C. As aforementioned, this sintering temperature was selected because it yielded the best AAMs. Sintering at 800 ^{0}C has slightly raised the environmental impact but nearly doubled the strength compared to the equivalent CEM II product. The highest environmental impact of the bauxite processing was due to drying and sintering (0.06 MJ/kg); mining and grinding account for 0.007 MJ/kg and 0.006 MJ/kg respectively.

The results agree with the aforementioned literature; the Na_2SiO_3 is the main contributor to environmental impact (Table 7-6). As expected, the environmental impact values for the different mixes are similar due to the close composition and processing of the raw materials (Table 7-5). In general, increasing NaOH concentration and Na_2SiO_3 / NaOH ratio and rising curing temperatures enhances strength at the expense of the environmental impact. However, the results (Table 7-5) show that even the AA materials with the highest impacts (EE=0.62-0.64 MJ/kg) have outstanding strength (15-22 MPa), and that their impacts are small when compared with some of the most common construction materials used today such as blocks, steel, aluminium, glass and PC materials included below.

The environmental impact of the AA bauxite materials designated as best by the DOE was also calculated- Table 7-9 and Table 7-10. According to the results, the DOE software yielded the highest strengths and lowest embodied energy (EE=0.44-0.47 MJ/kg) when compared to the CEM II and the other AA bauxite specimens, and the DOE mixes have similar E carbon (0.04 kgCO_2/kg) than the other AA bauxite mixes.

Table 7-5 Compressive strength and environmental impact of the AA bauxite - FA materials (3:1 - sand: bauxite/FA).

Mix	NaOH M	Na$_2$SiO$_3$/ NaOH	Curing (^{0}C)	bauxite (%)	FA (%)	sand (%)	NaOH (%)	Na$_2$SiO$_3$ (%)	CS (MPa)	EE (total) (MJ/m^3)	E$_{CO_2}$ (total) (kgCO$_2$/m^3)	Density (kg/m^3)	EE (total) (MJ/kg)	E$_{CO_2}$ (total) (kgCO$_2$/kg)
1	8	1	20	100	—	58.34	2.69	5.83	7.35	986.91	88.05	1909.24	0.52	0.05
2	12	1	20	100	—	58.05	3.67	5.93	9.54	1065.94	101.30	1990.75	0.54	0.05
3	8	3	20	100	—	58.18	1.36	8.83	20.38	1165.52	96.93	1977.13	0.59	0.05
4	12	3	20	100	—	58.07	1.83	8.89	16.58	1204.02	103.32	1983.34	0.61	0.05
5	8	1	60	100	—	58.34	2.69	5.83	6.69	1034.00	88.05	1914.26	0.54	0.05
6	12	1	60	100	—	58.05	3.67	5.93	10.43	1113.03	101.30	1928.07	0.58	0.05
7	8	3	60	100	—	58.18	1.36	8.83	22.52	1212.61	96.93	1925.84	0.63	0.05
8	12	3	60	100	—	58.07	1.83	8.89	15.11	1251.10	103.32	1943.21	0.64	0.05
9	8	1	20	50	50	60.81	2.29	4.97	12.99	779.34)	74.33	2009.12	0.39	0.04
10	12	1	20	50	50	60.41	3.15	5.11	12.25	851.32	86.03	2074.1	0.41	0.04
11	8	3	20	50	50	60.56	1.17	7.58	19.95	932.21	82.30	2020.16	0.46	0.04
12	12	3	20	50	50	60.14	1.61	7.80	18.32	985.14	89.80	2032.06	0.48	0.04
13	8	1	60	50	50	60.81	2.29	4.97	14.35	826.43	74.33	1969.59	0.42	0.04
14	12	1	60	50	50	60.41	3.15	5.11	15.93	898.41	86.03	2048.99	0.44	0.04
15	8	3	60	50	50	60.56	1.17	7.58	18.75	979.30	82.30	1986.33	0.49	0.04
16	12	3	60	50	50	60.14	1.61	7.80	15.92	1032.23	89.80	2041.77	0.51	0.04
17	10	2	40	75	25	60.54	1.56	6.75	26.45	957.85	79.69	2066.07	0.46	0.04
18	10	2	40	75	25	60.54	1.56	6.75	27.76	957.85	79.69	2076.23	0.46	0.04
19	10	2	40	75	25	60.54	1.56	6.75	27.84	957.85	79.69	2077.62	0.46	0.04
20	8	2	40	75	25	60.08	1.61	6.96	29.65	984.90	82.57	1983.81	0.50	0.04
21	12	2	40	75	25	59.52	2.23	7.22	21.25	1055.13	92.81	2000.53	0.53	0.05
22	10	1	40	75	25	59.50	1.97	7.23	4.96	1038.81	89.77	2012.2	0.52	0.04
23	10	3	40	75	25	59.25	2.00	7.35	20.23	1054.78	91.50	2037.34	0.52	0.04
24	10	2	20	75	25	60.54	1.84	6.75	30.72	944.60	82.96	1995.92	0.47	0.04
25	10	2	60	75	25	60.54	1.84	6.75	36.42	991.69	82.96	2000.04	0.50	0.04
26	10	2	40	100	—	58.65	2.08	7.63	30.33	1131.90	94.98	1957.21	0.58	0.05
27	10	2	40	50	50	60.89	1.79	6.58	23.28	914.99	81.23	2001.95	0.46	0.04
28	10	2	40	75	25	60.54	1.56	6.75	27.85	957.85	79.69	2071.15	0.46	0.04
29	10	2	40	75	25	60.54	1.56	6.75	29.79	957.85	79.69	2046.92	0.47	0.04
CEM II	—	—	20	—	—	—	—	—	37.18	1778.63	305.03	2208.23	0.81	0.14

Table 7-6 Embodied energy and carbon of each component as a percentage of the total (AA bauxite/FA materials).

Mix	EE					E_{CO2}				
	bauxite	FA	sand	NaOH	Na$_2$SiO$_3$	bauxite	FA	sand	NaOH	Na$_2$SiO$_3$
	(%)	(%)	(%)	(%)	(%)	(%)	(%)	(%)	(%)	(%)
1	19.96	—	9.23	18.41	52.40	1.70	—	6.13	37.26	54.90
2	18.48	—	8.55	23.36	49.61	1.48	—	5.33	44.39	48.79
3	16.90	—	7.82	7.89	67.39	1.55	—	5.57	17.14	75.74
4	16.36	—	7.57	10.30	65.77	1.45	—	5.23	21.68	71.64
5	19.05	—	8.81	17.57	50.01	1.70	—	6.13	37.26	54.90
6	17.70	—	8.19	22.38	47.51	1.48	—	5.33	44.39	48.79
7	16.25	—	7.51	7.59	64.77	1.55	—	5.57	17.14	75.74
8	15.75	—	7.28	9.91	63.29	1.45	—	5.23	21.68	71.64
9	12.64	2.41	11.69	19.05	54.21	1.01	2.52	7.27	36.07	53.14
10	11.57	2.20	10.70	24.15	51.38	0.87	2.18	6.28	43.15	47.52
11	10.57	2.01	9.78	8.14	69.51	0.91	2.28	6.56	16.65	73.60
12	10.00	1.90	9.25	10.68	68.17	0.84	2.09	6.01	21.16	69.91
13	11.92	2.27	11.03	17.96	51.12	1.01	2.52	7.27	36.07	53.14
14	10.96	2.09	10.14	22.88	48.68	0.87	2.18	6.28	43.15	47.52
15	10.06	1.91	9.31	7.75	66.16	0.91	2.28	6.56	16.65	73.60
16	9.54	1.82	8.83	10.19	65.06	0.84	2.09	6.01	21.16	69.91
17	15.42	0.98	9.51	10.58	60.23	1.41	1.18	6.78	22.96	67.68
18	15.42	0.98	9.51	10.58	60.23	1.41	1.18	6.78	22.96	67.68
19	15.42	0.98	9.51	10.58	60.23	1.41	1.18	6.78	22.96	67.68
20	15.00	0.95	9.25	10.70	60.91	1.36	1.14	6.54	23.05	67.92
21	14.00	0.89	8.64	13.99	59.51	1.21	1.01	5.82	28.71	63.25
22	14.22	0.90	8.77	12.54	60.55	1.25	1.04	6.02	26.19	65.49
23	14.01	0.89	8.64	12.61	60.88	1.23	1.02	5.90	26.24	65.60
24	15.64	0.99	9.65	12.64	61.08	1.36	1.13	6.51	26.00	65.01
25	14.90	0.95	9.19	12.04	58.18	1.36	1.13	6.51	26.00	65.01
26	17.40	—	8.05	12.31	59.46	1.58	—	5.69	26.49	66.24
27	10.76	2.05	9.96	12.66	61.14	0.92	2.31	6.65	25.75	64.38
28	15.42	0.98	9.51	10.58	60.23	1.41	1.18	6.78	22.96	67.68
29	15.42	0.98	9.51	10.58	60.23	1.41	1.18	6.78	22.96	67.68
Arithmetic mean (%)	14.51	1.46	9.15	13.47	59.24	1.27	1.64	6.22	27.53	63.85

Table 7-7 Compressive strength and environmental impact of the AA bauxite - GGBS materials (3:1 - sand: bauxite/GGBS).

Mix	NaOH	Na₂SiO₃/NaOH	Curing	bauxite	GGBS	sand	NaOH	Na₂SiO₃	CS	Embodied Energy (total)	Embodied Carbon (total)	Density	Embodied Energy (total)	Embodied Carbon (total)
	M		(^{0}C)	(%)	(%)	(%)	(%)	(%)	(MPa)	(MJ/m^3)	(kgCO$_2$/m^3)	(kg/m^3)	(MJ/kg)	(kgCO$_2$/kg)
1	8	1	20	100	__	58.34	2.69	5.83	7.35	986.91	88.05	1909.24	0.52	0.05
2	12	1	20	100	__	58.05	3.67	5.93	9.54	1065.94	101.30	1990.75	0.54	0.05
3	8	3	20	100	__	58.18	1.36	8.83	20.38	1165.52	96.93	1977.13	0.59	0.05
4	12	3	20	100	__	58.07	1.83	8.89	16.58	1204.02	103.32	1983.34	0.61	0.05
5	8	1	60	100	__	58.34	2.69	5.83	6.69	1034.00	88.05	1914.26	0.54	0.05
6	12	1	60	100	__	58.05	3.67	5.93	10.43	1113.03	101.30	1928.07	0.58	0.05
7	8	3	60	100	__	58.18	1.36	8.83	22.52	1212.61	96.93	1925.84	0.63	0.05
8	12	3	60	100	__	58.07	1.83	8.89	15.11	1251.10	103.32	1943.21	0.64	0.05
9	8	1	20	50	50	60.99	2.26	4.91	69.59	1052.06	87.02	2140.88	0.49	0.04
10	12	1	20	50	50	60.24	3.19	5.17	52.98	1142.18	100.89	2143.44	0.53	0.05
11	8	3	20	50	50	60.38	1.18	7.68	45.47	1224.45	97.11	2117.14	0.58	0.05
12	12	3	20	50	50	60.31	1.59	7.71	64.75	1254.80	102.27	2036.07	0.62	0.05
13	8	1	60	50	50	60.99	2.26	4.91	72.32	1099.15	87.02	2137.22	0.51	0.04
14	12	1	60	50	50	60.24	3.19	5.17	69.25	1189.27	100.89	2141.37	0.56	0.05
15	8	3	60	50	50	60.38	1.18	7.68	52.98	1271.54	97.11	2117.84	0.60	0.05
16	12	3	60	50	50	60.31	1.59	7.71	71.12	1301.89	102.27	2069.18	0.63	0.05
17	10	2	40	75	25	60.19	1.88	6.91	44.55	1137.92	92.09	2040.74	0.56	0.05
18	10	2	40	75	25	60.19	1.88	6.91	39.30	1137.92	92.09	2050.73	0.55	0.04
19	10	2	40	75	25	60.19	1.88	6.91	39.68	1137.92	92.09	2093.33	0.54	0.04
CEM II	—	—	20	—	—	—	—	—	37.18	1778.63	305.03	2208.23	0.81	0.14

Table 7-8 Embodied energy and carbon of each component as a percentage of the total (AA bauxite/GGBS materials).

| Mix | EE | | | | | E_{CO2} | | | | |
| | bauxite | GGBS | sand | NaOH | Na_2SiO_3 | bauxite | GGBS | sand | NaOH | Na_2SiO_3 |
	(%)	(%)	(%)	(%)	(%)	(%)	(%)	(%)	(%)	(%)
1	19.96	—	9.23	18.41	52.40	1.70	—	6.13	37.26	54.90
2	18.48	—	8.55	23.36	49.61	1.48	—	5.33	44.39	48.79
3	16.90	—	7.82	7.89	67.39	1.55	—	5.57	17.14	75.74
4	16.36	—	7.57	10.30	65.77	1.45	—	5.23	21.68	71.64
5	19.05	—	8.81	17.57	50.01	1.70	—	6.13	37.26	54.90
6	17.70	—	8.19	22.38	47.51	1.48	—	5.33	44.39	48.79
7	16.25	—	7.51	7.59	64.77	1.55	—	5.57	17.14	75.74
8	15.75	—	7.28	9.91	63.29	1.45	—	5.23	21.68	71.64
9	9.36	28.52	8.66	13.90	39.56	0.86	17.88	6.21	30.34	44.71
10	8.62	26.27	7.98	18.27	38.86	0.74	15.43	5.35	37.35	41.13
11	8.04	24.50	7.44	6.29	53.72	0.77	16.03	5.56	14.32	63.32
12	7.85	23.91	7.26	8.26	52.72	0.73	15.22	5.28	18.30	60.47
13	8.96	27.29	8.29	13.30	37.87	0.86	17.88	6.21	30.34	44.71
14	8.28	25.23	7.66	17.55	37.33	0.74	15.43	5.35	37.35	41.13
15	7.75	23.59	7.17	6.06	51.73	0.77	16.03	5.56	14.32	63.32
16	7.57	23.04	7.00	7.96	50.81	0.73	15.22	5.28	18.30	60.47
17	13.00	13.18	8.01	10.81	52.24	1.22	8.45	5.86	24.13	60.34
18	13.00	13.18	8.01	10.81	52.24	1.22	8.45	5.86	24.13	60.34
19	13.00	13.18	8.01	10.81	52.24	1.22	8.45	5.86	24.13	60.34
Arithmetic mean (%)	12.94	21.99	7.92	12.71	51.58	1.17	14.04	5.63	27.05	58.02

Table 7-9 Compressive strength and environmental impact of the AA bauxite materials declared as optimum by the DOE compared with equivalent CEM II materials (3:1 - sand:bauxite/GGBS-FA).

	bauxite	FA	GGBS	Curing	NaOH	Na_2SiO_3	CS	Embodied Energy (total)	Embodied Carbon (total)	Density	Embodied Energy (total)	Embodied Carbon (total)
	(%)	(%)	(%)	(°C)	(%)	(%)	(MPa)	(MJ/m³)	(kgCO₂/m³)	(kg/m³)	(MJ/kg)	(kgCO₂/kg)
Bauxite+GGBS	50	—	50	20	2.26	4.91	60.41	1052.06	87.06	2252.40	0.47	0.04
Bauxite+FA	50	50	—	20	3.75	6.62	33.12	883.63	81.26	2025.17	0.44	0.04
CEM II	—	—	—	20	—	—	37.18	1778.63	305.03	2208.23	0.81	0.14

Table 7-10 Embodied energy and carbon contribution of the material components as a percentage of the total.

	EE						E_{CO2}					
	bauxite	GGBS	FA	sand	NaOH	Na_2SiO_3	bauxite	GGBS	FA	sand	NaOH	Na_2SiO_3
	(%)	(%)	(%)	(%)	(%)	(%)	(%)	(%)	(%)	(%)	(%)	(%)
Bauxite +GGBS	9.36	28.52	—	8.66	13.90	39.56	0.86	17.88	—	6.20	30.37	44.69
Bauxite +FA	11.15	—	2.12	10.31	13.11	63.31	0.92	—	2.31	6.64	25.77	64.35

Table 7-11 Summary of environmental impact vs strength results of AA RM, bauxite and GGBS materials compared with their CEM II (A/L) equivalents. EE (MJ/kg). E_{CO2} (kgCO₂/kg). COVs = 0.06 – 0.62. CEM II (A/L): EE= 0.81; E_{CO2}=0.14; CS=37MPa.

	AA RM			AA GGBS			AA Bauxite+GGBS			AA Bauxite + FA			AA Bauxite			DOE AA Bauxite + GGBS			DOE AA Bauxite + FA		
	EE	E_{CO2}	CS	EE	E_{CO2}	CS	EE	E_{CO2}	CS	EE	E_{CO2}	CS	EE	E_{CO2}	CS	EE	E_{CO2}	CS	EE	E_{CO2}	CS
Arithmetic mean	0.49	0.04	11.76	0.49	0.03	16.19	0.56	0.05	56.54	0.48	0.04	22.14	0.58	0.05	13.58	0.47	0.04	60.41	0.44	0.04	33.12

7.6 DISCUSSION

The AA bauxite-FA material projected as best by the DOE has the lowest environmental impact- Table 7-11. This is due to lower NaOH concentration, lower ratio of Na_2SiO_3/NaOH, and curing at ambient temperature.

The environmental impact of all the AAMs studied is lower than their CEM II equivalents. With the exception of the AA bauxite-GGBS materials, their strength is lower, however significant, and suitable for many applications.

The AA bauxite-GGBS materials are outstanding, not only in properties but also with regard to environmental impact, with an embodied energy and embodied carbon 30.86% and 64.29% (respectively) lower that their CEM II equivalents.

Manufacturing GGBS has higher EE and E_{CO2} than FA because it needs to be ground after quenching (Ostwal and Chitawadagi, 2014). Manufacturing GGBS requires 1 ton of 1300 MJ, with CO_2 emission of 0.07 tons (Cabeza *et al.,* 2013). Therefore, using GGBS as precursor elevates the environmental impact of AAMs. However, the AAMs including GGBS displayed high densities of outstanding strength. Therefore, it can be argued that the slight increase in environmental impact is offset with a superior durability that increases sustainability. Furthermore, the impact due to the inclusion of GGBS as precursor is still very small when compared with PC products, as the energy use to produce a 1 ton of PC is about 5000 MJ, with at least 1 ton of CO_2 emitted into the atmosphere.

The RM is produced as waste and contributes zero to embodied energy and carbon. However, RM drying, grinding, and sintering contributed to an average EE of 0.04 MJ/kg. 90% of the EE value of the AA bauxite materials is due to the processing of the bauxite including drying, grinding, and sintering, aimed at enhancing reactivity.

Based on the results, the main contributor to carbon emission and EE of the AAMs studied is the Na_2SiO_3 activator. This agrees with previous authors. However the % contributions assigned to the activator are slightly different due to the different formulations. Alsalman *et al.* (2021) note that the Na_2SiO_3 activator can contribute up to 48% and 42% (EE and E_{CO2} respectively) of the total impact of alkali-activated concrete. According to Mathew *et al.* (2013), Na_2SiO_3 accounts for 49% of the embodied energy of FA-GGBS geopolymer. The melting and drying processes of Na_2SiO_3 manufacturing is responsible for a high embodied

energy (Ostwal and Chitawadagi 2014). In addition, the production of Na_2SiO_3 evolves significant CO_2 into the atmosphere and it is a costly process (Torres and Puertas, 2017).

In contrast, the NaOH activator has lower EE and E_{CO2} as it is usually made in brine solution electrolysis which produces chlorine gas at the cathode and a weak alkali at the anode (Erixon, 1999). However, increasing the NaOH concentration led to an increase in EE and E_{CO2}.

The AAMs produced present values comparable to other AAMs in the literature (Table 7-12). The overall results show that even the AA materials with the highest impacts (EE=0.62-0.64 MJ/kg) have outstanding strength (15-22 MPa), and that their impacts are small when compared with some of the most common construction materials used today such as blocks, steel, aluminium, glass and PC materials (Table 7-13).

Table 7-12 EE and E_{CO2} values in the literature

Materials	EE	E_{CO2}	References
AA FA/PC materials (25% PC replacement with FA)	3.52 MJ/kg	-	Kalaw *et al.* (2016)
AA FA/PC materials (50% PC replacement with FA)	2.43 MJ/kg	-	
AAMs made with high-volume FA	881.2 MJ/m^3	45.5 kg CO_2/m^3	Faridmehr *et al.* (2021)
FA-silica fume geopolymer activated with NaOH (10-16% of FA)	1189.7 - 1729.8 MJ/m^3	-	Tempest *et al.* (2009)
AA slag, with 4% of Na_2O dosage at modulus of silica (MS=1.25)	4162 MJ	271 kg CO_2	Kumar et al., (2020)
(75:25) AA slag: FA, with 4% Na_2O at modulus of silica (MS=1.25)	3768 MJ	247 kg CO_2	
(50:50) AA slag: FA, with 4% Na_2O at modulus of silica (MS=1.25)	3374 MJ	223 kg CO_2	
(95:05) AA FA-RHA, activated with 12M Na_2SiO_3/NaOH = 0.5-1	1.64 MJ/kg	0.117 kg CO_2/kg	(Kalaw *et al.*, 2016)
(85:15) AA FA/ bottom ash, activated with 12M Na_2SiO_3/NaOH = 0.5-1	1.64 MJ/kg	0.117 kg CO_2/kg	
(85:10:05) AA FA/RHA activated 12M Na_2SiO_3/NaOH = 0.5-1	1.64 MJ/kg	0.117 kg CO_2/kg	

Table 7-13 Impact of some of the most common construction materials (Hammond and Jones 2011).

Material	Energy MJ/kg	Carbon kg CO_2/kg	Material density kg/m^3
Aggregate	0.083	0.0048	2240
PC Concrete (1:1.5:3)	1.11	0.159	2400
Bricks (common)	3	0.24	1700
Concrete block (Medium density)	0.67	0.073	1450
Aerated block	3.5	0.3	750
PC mortar (1:3)	1.33	0.208	-
Steel	20.1	1.37	7800
Stainless steel	56.7	6.15	7850
Expanded Polystyrene insul.	88.6	2.55	15–30
Polyurethane insulation (rigid)	101.5	3.48	30
Aluminium (33% recycled)	155	8.24	2700
Glass	15	0.85	2500
PVC	77.2	2.41	1380

8. CONCLUSIONS AND FURTHER RESEARCH

8.1 PRECURSORS

All the precursors are highly reactive. Not only they are pozzolanic, but they can also be successfully activated with alkali solutions of NaOH and silicate. The FA and GGBS comply with building standard requirements for the use of SCMs in PC.

The slag is a high-calcium precursor, all the others being low calcium. In addition, with the exception of the bauxite (with high alumina content of 53%), all the precursors show a medium alumina content (12-23%).

The GGBS shows outstanding qualities to produce AA binders being highly reactive and basic ($CaO+ MgO/SiO_2 =1.56$). Furthermore, it is highly amorphous, and has a CaO/SiO_2 ratio of 1.41 and a SiO_2/Al_2O_3 ratio of 0.34 which are considered suitable for alkali-activation.

The water demand is determined by the nature of the particles, mainly by the presence of layered structures, and their fineness rather than by the presence of carbon: the FA has the greatest carbon content and yet the lowest water demand, while the GGBS –which is the finest- and the bauxite have the highest water demand. As the water demand of the precursors to achieve specific workability is different, obtaining a workable mixture will require different volumes of activator solution, which will be difficult to control. Therefore, the activator ratio needs to be calculated by weight.

The RM is reactive mainly due to its layered phases gibbsite and boehmite (inherited from the parent bauxite), and its zeolite/feldepathoid phases: cancrinite, chantalite and sodalite, formed during the refining (Bayer) process. The Bayer process determined the reactivity of the RM:

- The Saudi RM is pozzolanic (not cementitious) because in Ma'adem the refining temperature (270°C) is low.
- The calcium oxide (CaO), added twice during refining, caused the occurrence of cancrinite which produces pozzolanic hydrates when the RM is activated with lime.

The Saudi RM is suitable for the production of AAMs and pozzolanic materials. It has high SiO$_2$ content and high alkalinity, the chloride and carbon contents are low and it doesn't include any toxic elements. It presents abundant specific surface area available for reaction, superior to commercial CEM II and other pozzolanic and cementitious materials such as FA and GGBS. The RM is moderately pozzolanic, and its activity is mainly due to the reaction of feldspathoid cancrinite and the formation of zeolitic and feldspathoid-based hydrates.

Thermal treatments enhance reactivity: the heated RMs make hydrated lime set two-three times faster than the lime alone. The RM sintered at 300-400°C sets the fastest, combines the most lime, and reached the greatest strengths and mechanical index.

The Saudi Arabian bauxite is highly reactive due to the layered atomic structures of its main components gibbsite, boehmite and kaolinite, which provide high specific surfaces (superior to CEM II and other pozzolanic and cementing materials such as FA and GGBS) and active hydroxyls that enhance adsorption, hence nucleation, precipitation and dissolution.

All the tests evidenced a high pozzolanic activity.

Heating, even at low temperature, significantly increases the SSA of the bauxite particles (at 300°C the SSA rises by over 60%).

Calcination, even at low temperature 300°C, increased reactivity due to the dehydroxylation of kaolinite. The 550°C bauxite (highest SSA) is the most active initially (hours-2 days) but at later ages, the 700°C -800°C bauxites (with the highest amorphous alumina content) are the most reactive reaching the highest strengths.

8.2 AA GGBS materials

The rheology and setting times are of the AA slag-materials are within practical limits, comparable to others in the literature. Cracking due to drying shrinkage, one of the challenges of AA materials, is hindered thanks to the high calcium content of the slag.

The Na$_2$SiO$_3$+NaOH activated GGBS materials showed the greatest strengths and microstructure. When cured at 60°C, they develop hydrogarnet–gehlenite hydrate cements that may be responsible for their high strength at 270 days (94MPa). The Na$_2$SiO$_3$ activator produces an excessive %Na$_2$O by mass of slag, and the NaOH activator produced an excessive alkalinity that lower strength.

The results agree with the chemistry and properties of the slag which suggests that it does not need an eminent alkalinity but it should be activated with either alkali silicates or low-concentration, alkali hydroxides. The GGBS is too reactive (too fine and amorphous) for a successful activation with high alkali hydroxide concentrations. Therefore, the best activator is a combination of Na_2SiO_3 and a low molarity ($< 6M$) alkali hydroxide.

Increasing the curing temperature to 60°C, enhances strength and microstructure when Na_2SiO_3+NaOH is the activator. In general early strengths (3, 7 days) increase but ultimate strengths (28, 270 days) either slighly increase or lower when compared with ambient-curing. The materials produced at ambient temperature are sound, and suitable for a wide range of applications.

8.3 AAM RM materials

All the AA RM materials achieved high strengths and some reached outstanding values. Even the materials made with RM alone reached significant flexural (up to 5 MPa) and compressive strengths (c.7 MPa).

Replacing RM with FA increased strength, and GGBS substitution increased strength further. The best RM materials were those with 50%GGBS replacement. They showed the highest density and shortest setting times, and the greatest strengths 39 – c.41 (activated with Na_2SiO_3 / 6M NaOH = 1 and 2.5 respectively).

The RM precursor welcomes silica content in the activator up to a certain threshold: increasing the silica content in the Na_2SiO_3 / 6M NaOH activator enhances strength, but using Na_2SiO_3 alone lowers it.

The microstructure of AAMs made with RM alone show little cements. However, when blended with FA and GGBS, cementing N-A-S-H hydrates are evident.

The AAMs made with RM alone did not resist laboratory weathering being particularly vulnerable to frost action. Replacing RM with FA increases durability but some specimens failed. In contrast, the AA RM materials blended with GGBS showed outstanding resilience, and those with 50% GGBS show better laboratory cycling resistance than their PC equivalents.

8.4 AAMs bauxite materials

The bauxite alone is suitable for synthesising geopolymers binders, reaching compressive strength up to c.35 MPa, but replacing bauxite with FA/GGBS increases strength and lowers porosity increasing density, and the effect is more pronounced as the % replacement grows.

According to the limited experiments, the best formulation for both the AA bauxite materials and the AA bauxite with FA replacement is curing at ambient temperature and activating with high silica content (Na_2SiO_3/NaOH = 3) and medium molarity (8M NaOH). The optimum mix for the AA bauxite - FA materials according to the DOE should be cured at ambient temperature, and have a slightly lower silica content (Na_2SiO_3/NaOH = 2) and higher molarity (NaOH 10M).

The GGBS-bauxite materials need a different formulation. The greatest strength (over 90 MPa at 90 days and over 72 MPa at 28 days) was achieved by the bauxite-50%GGBS materials activated with Na_2SiO_3/ NaOH (8M) = 1, cured at 60 degrees. The experimental conclusion agrees with the optimum mix forecasted by the DOE. The DOE validated the experimental methods and the method used for the modelled predictions for the AA materials in the range studied.

The cementing geopolymers of the AA bauxite materials are scarce when bauxite is used alone. However, when FA or GGBS are introduced, the main cementing phase in an aluminate–silicate gel, with low-Ca and some sodium substitution, with a greater Al content in the GGBS materials.

8.5 ENVIRONMENTAL IMPACT

Bauxite can create outstanding AAMs of low environmental impact. Using bauxite for AAM production, rather than for aluminium production, would lower environmental impact worldwide. Bauxite mining has a negligible environmental impact (3-5 kg CO_2e/t) when compared to even the low-impact PCs (CEM II releases 620-700 kg CO_2e/t).

The results evidence that, in alkali activation technology, an appropriate design leads to lower environmental impact and superior strength and microstructure. In the AA GGBS materials, the right activator procured a strength similar to the equivalent CEM II mixes at approximately half of their embodied energy and carbon emissions. Activators constitute the main environmental impact of AAMs. An excessive activator concentration or wrong molar ratio can increase the environmental impact while simultaneously lowering strength. Therefore, they must correctly selected and formulated.

Pyro-processing waste precursors at relatively low temperature can report great strength increase with a low increase in environmental impact: sintering the bauxite at 800 ºC slightly raised the environmental impact of the resultant material, but it nearly doubled the strength when compared to the equivalent CEM II product. The process of sintering bauxite consumes only 0.02 MJ/kg of energy, much less than the production of clinker, which according to Schorcht *et al.*, 2013, consumes 30 MJ/kg of energy during the calcination of limestone.

Blending, even with a high environmental impact precursor, can offset impact on account of a greatest durability: increasing FA in the AA RM materials, nearly doubles the 28-day compressive strength without increasing environmental impact. The GGBS slightly rises environmental impact but significantly increases strength and improves microstructure.

8.6 LIMITATIONS AND FURTHER RESEARCH

This research evidenced that a number of the AAMs designed and produced are quality materials that can be used in several applications such as structural frames, precast construction and paving units. The results also evidenced that the physical testing methods and analytical techniques used are adequate for AAMs. However, the standardisation and mass production of these materials is still undone. Therefore, further research into mass production and commercialisation is needed in order to introduce AAM into mainstream construction. Further investigation on the pore system of the AMMs investigated should be undertaken using BET (Brunauer–Emmett–Teller) or mercury porosimetry.

The properties and composition of precursors from different locations vary depending on the raw material and the production process. For example, not all the RMs in the world result from the Bayer refining process, and the Bayer process varies in different alumina producers. Therefore, a first step can be to establish limits and adequate ranges for certain elements in the

precursor including C, Ca, Al and Si. The alkali content and the content of anions (S, Cl, N) capable of forming salts should also be established.

A correspondence between the precursor composition and the most efficient activator needs to be established including activator type, concentration and ratio. Further research is also needed on leaching and toxicity to examine the potential impact of any leached heavy metals. It would also be relevant to conduct further research on the long-term durability of AAMs with regards to specific applications.

Water demand and workability are particularly important in alkali activation. In AAMs, to produce a workable mix, the precursor is mixed with the activator solution instead of water, and the demand is determined by the fineness, specific surface area and the structure/ porosity of the precursor particles. Therefore, the activator/solid ratio should be determined experimentally and calculated by weight.

The presence of minor elements in RM and bauxite (e.g., TiO_2 Fe_2O_3 and MgO), can affect the geopolymerization process and hence change material properties. This should be investigated as it can alter the materials properties in the long-term, and create environmental impact.

According to Alayed *et al.,* (2021), the structural concrete frames of Saudi Arabian villas typically account for 30-40% of the overall wall surface area. In addition, Saudi Arabia will require approximately 2.32 million new houses by 2020 due to growing population (Sidawi, 2009; Asif, 2016). This will rapidly increase the demand for materials. In light of the environmental benefits of AA RM and AA bauxite binders and their lower EE and E_{CO2}, onsite research should be conducted aimed at replacing current PC structural frames with the strongest AAMs in this research.

Appendix A. PAPERS PUBLISHED IN JOURNALS AND CONFERENCES

A.1 PUBLICATIONS

A.1.1 Journals

1- O. Alelweet and S. Pavia , An Evaluation of the Feasibility of Several Industrial Wastes and Natural Materials, as Precursors, for the Production of Alkali Activated Materials, *International Journal of Civil and Environmental Engineering* , 13, (12), 2019, p741 - 748.

2- Alelweet O, Pavia S, Lei Z, Pozzolanic and Cementing Activity of Raw and Pyro-Processed Saudi Arabian Red Mud (RM) Waste, *Recent Progress in Materials* , 3, (4), 2021, p139 – 164.

3- Alelweet O. and Pavia S., Durability of Alkali-Activated Materials Made with a High-Calcium, Basic Slag, *Recent Progress in Materials* , 3, (4), 2021, p19 – 45.

4- Alelweet O. and Pavia S., Pozzolanic and hydraulic activity of bauxite for binder production, *Journal of Building Engineering*, 51, 2022.

A.1.2 Conferences papers

1- O. Alelweet and S. Pavia , An evaluation of the feasibility of industrial wastes and natural materials, as precursors, for the production of alkali activated materials (AAMs), *ICNMTA 2019: XIII Int. Conf. on Civil, Structural and Construction Engineering*, *Barcelona*, *Dec. 16-17*, 2019.

2- O. Alelweet and S. Pavia, Potential of a low-calcium fly ash (FA) for the production of alkali-activated materials, *Civil Engineering Research in Ireland (CERI) Conference*, *Cork Institute of Technology* , *27- 28th August 2020*, edited by Ruane and Vesna Jaksic , 2020.

3- Alelweet O. and Pavia S., Fitness of a high-calcium slag for the production of alkali activated materials. , *CEES 2021 - International Conference on Construction, Energy, Environment and Sustainability.* , *Coimbra, Portugal*, *12-15 October 2021*, edited by Itecons - Instituto de Investigação e Desenvolvimento Tecnológico para a Construção, Energia, Ambiente e Sustentabilidade , ISBN: 978-989-54499-1-0, 2021.

4- O. Alelweet, S. Pavia , Long-Term Durability and Mechanical Performance of Alkali-Activated, Slag Cements. , *Global Summit on Civil, Architectural, and Environmental Engineering (GSCAEE2021)*, *Barcelona*, *July 19-21*, 2021.

5- O. Alelweet and S. Pavia, A comparative study of the environmental impact of alkali activated and traditional materials, *Civil Engineering Research in Ireland (CERI) Conference*, Trinity College Dublin, *25- 26th August 2022*.

A.2 AWARDs

1- 'Best paper award' at ICNMTA 2019: XIII Int. Conf. on Civil, Structural and Construction Engineering, Barcelona, Dec. 16-17: An Evaluation of the Feasibility of Several Industrial Wastes and Natural Materials as Precursors for the Production of Alkali Activated Materials. O Alelweet and S Pavia.

2- 'Best paper award', Durability of Alkali-Activated Materials Made with a High-Calcium, Basic Slag.

3- Alelweet O. and Pavia S., 'Book cover: Recent Progress in Materials.Durability of alkali-activated materials made with a high-calcium, basic slag', LIDSEN Publishing Inc., 2021.

4- Research excellence award (2021/2022) from Saudi cultural attache in the Republic of Ireland.

Appendix B. ANALYSIS AND OPTIMISATION OF THE DESIGN OF ALKALI-ACTIVATED BAUXITE USING DESIGN OF EXPERIMENTS (DOE)

This section shows the analysis of the design of experiments (DOE) used for AA bauxite, which were not included in Chapter 6.

B.1 ANALYSIS OF AA BAUXITE BLENDED WITH FA AT 28 DAYS

B.1.1 Flexural strength (28 FC)

As shown in Figure B-1 the Pareto chart demonstrates the magnitude of each input factor's standardised effect and the significance of the interaction found. The horizontal bars refer to the factors and interactions crossing the segmented vertical reference line that is treated as statistically significant.

The results show that the total number of single, double interaction and 2-way interaction terms was four. According to the results, ($Na_2SiO_3/NaOH* Na_2SiO_3/NaOH$) had the highest effect, followed by ($Na_2SiO_3/NaOH$), (T * T), and $Na_2SiO_3/NaOH*FA\%$ terms cross the reference line of the statistical significance located at 2.093, indicating that these effects are statistically significant.

Figure B-1 Pareto chart of the standardised effects for AA bauxite with FA of (28 FC) at a 95% confidence interval.

Figure B-2 shows the Probability plot of (28 FC) model that the data points are located between red lines. Furthermore, the P-Value is 0.406, which is greater than the significance level of 0.05, indicating that the data follows a normal distribution according to the null hypothesis (Alshalif *et al.*, 2021). The mean (28 FC) was 5.16 MPa, which lowers than control value (CEM II) by 14%.

Figure B-2 Probability plot of (28 FC) at 28 days.

Figure B-3 (A) and (B) show the main effects plots of (28 FC) responses. In our case, one term that has a significant effect on (28 FC) is $Na_2SiO_3/NaOH$, besides one interaction term, $Na_2SiO_3/NaOH*FA\%$, which are the significant factors with the most important influence on the response.

Figure B-3 (A), the increasing $Na_2SiO_3/NaOH$ from 1 to 2 has increased the (28 FC) from 3 to 7 MPa. However, further increases in $Na_2SiO_3/NaOH$ have decreased (28 FC) from 7 to 5 MPa.

Figure B-3 (B), the significant 2-way interaction of $Na_2SiO_3/NaOH*FA\%$ shows that a higher (28 FC) was obtained at average FA% and $Na_2SiO_3/NaOH$ levels. It is worth noting that higher levels of FA at 50% exhibited higher (28 FC) when $Na_2SiO_3/NaOH$ was at ratio 1. In contrast, the lower FA at 0% levels exhibited higher levels of (28 FC) when $Na_2SiO_3/NaOH$ was at higher levels at ratio 3.

Figure B-3 The main effect and interaction plot for (28 FC), main effect plot (A), and interaction plot (B) of bauxite and FA.

B.1.2 compressive strength (28 CS)

The distribution of ranking the model terms according to their significance is given in the following order: $Na_2SiO_3/NaOH* Na_2SiO_3/NaOH$ term was found to have the greatest impact on the 28 CS followed by $Na_2SiO_3/NaOH$, T*T and $Na_2SiO_3/NaOH*FA\%$, terms cross the reference line of the statistical significance located at 2.101 as presented in Pareto chart Figure B-4.
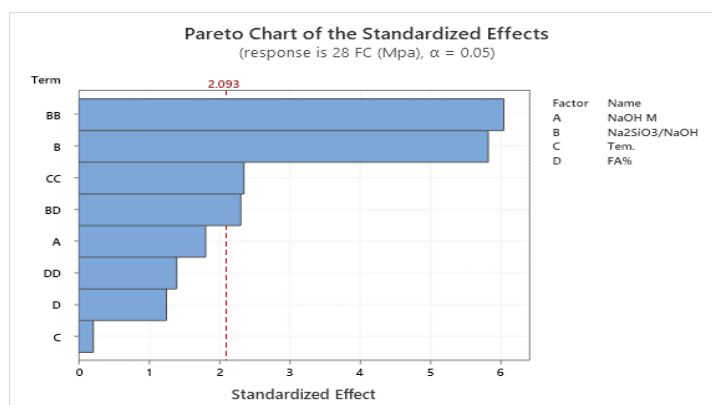

Figure B-4 Pareto chart of the standardised effects for AA bauxite with FA of (28 CS) at a 95% confidence interval.

From Figure B-5, it can be seen that the data points are approximately located between the red lines. The P-Value is 0.69, which is greater than the significance level, indicating that the data follows a normal distribution according to the null hypothesis. From Figure B-5, the mean value was 19.78 MPa, a lower control value (CEM II) by 47%.
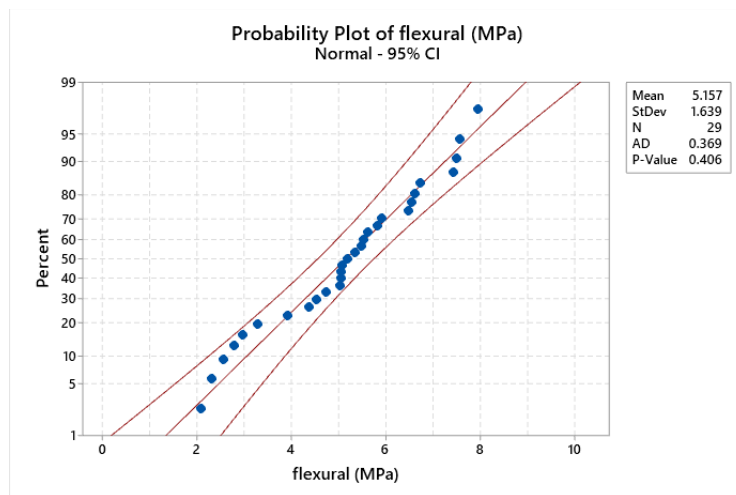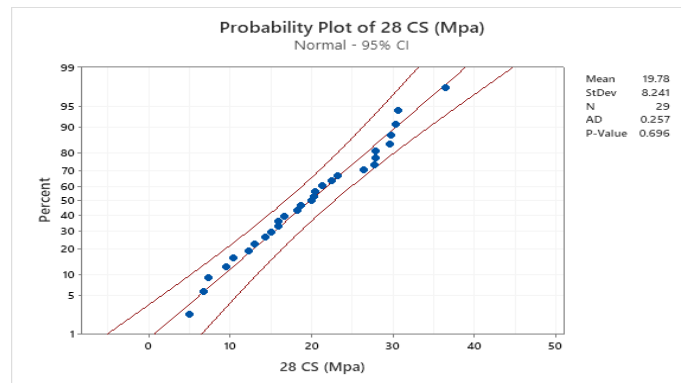

Figure B-5 Probability plot of (28 CS) at 28 days.

Figure B-6 (A) shows the main effects plots of 28 CS responses. In our case, one linear term has a significant effect, which is $Na_2SiO_3/NaOH$. The 28 CS was increased with increasing $Na_2SiO_3/NaOH$ up to 2.5 of $Na_2SiO_3/NaOH$, then the 28 CS decreased. Figure B-6 (B) shows the interaction factor between $Na_2SiO_3/NaOH$ at a higher level, and a lower level of FA% gives a higher strength at $Na_2SiO_3/NaOH$=2.5.
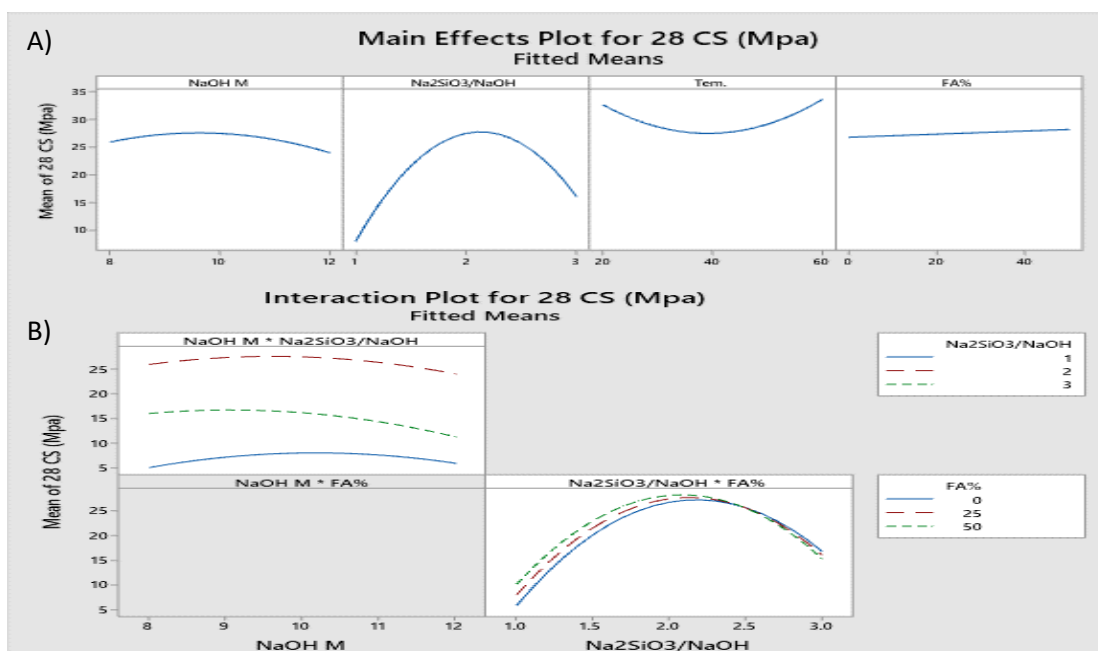
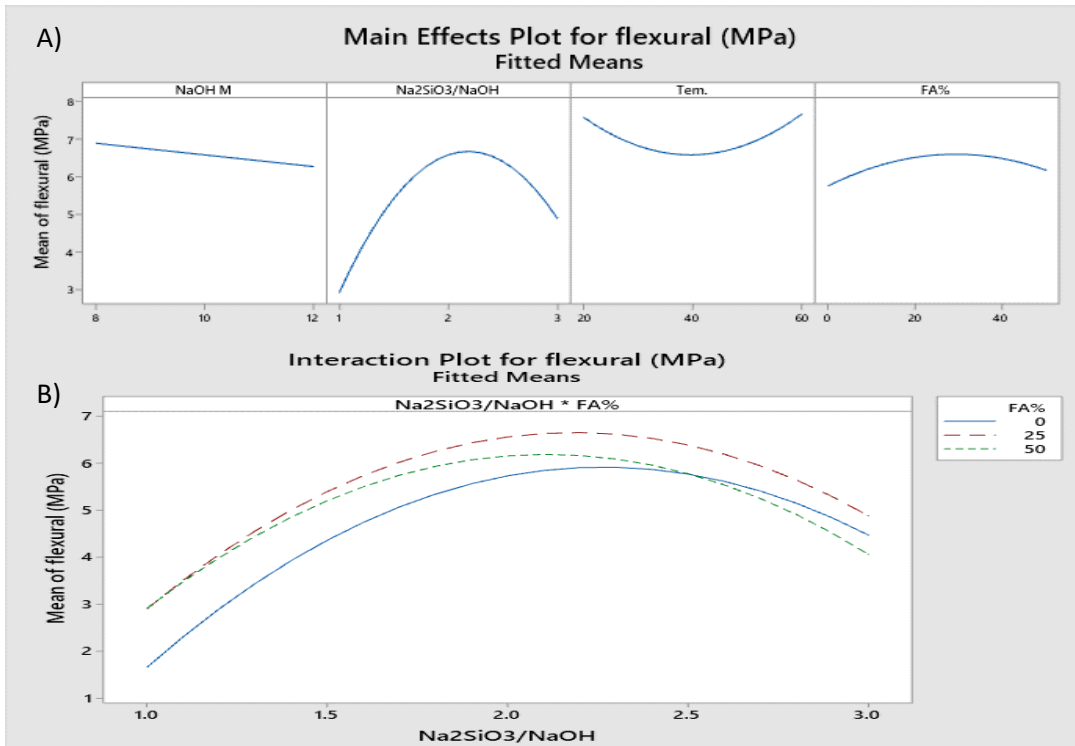
Figure B-6 The main effect and interaction plot for (28 CS), main effect plot (A), and interaction plot (B) of bauxite and FA.

B.1.3 porosity (28 P)

The greatest impact on the (28 P) was FA% followed by FA%*FA%, NaOH M and NaOH M*NaOH M, terms cross the reference line of the statistical significance located at 2.093 based in Pareto chart Figure B-7.

Figure B-7 Pareto chart of the standardised effects for AA bauxite with FA of (28 P) at a 95% confidence interval.

Figure B-8, the Probability plot of (28 P) shows the data is located very close to the straight red line, and the P-Value is 0.050, which is greater than the significance level of 0.05, indicating that the data follows a normal distribution according to the null hypothesis. According to the data, the mean porosity was 18.39%, which is higher than CEM II, which was 7.31%.
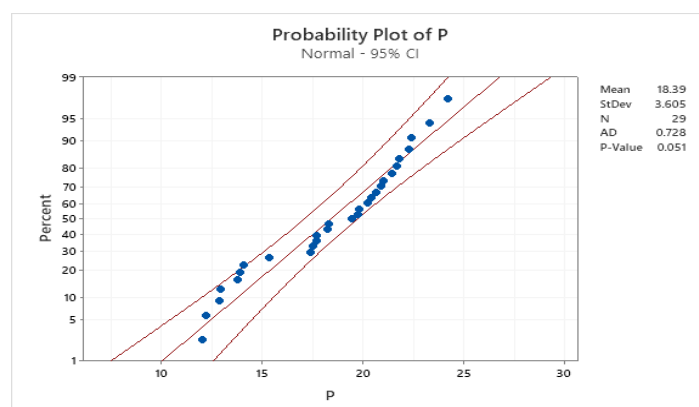
Figure B-8 Probability plot of (28 P) at 28 days.

Figure B-9 show the main effects plots of (28 P) response. The significant effects on P are NaOH M and FA%. The results show that increasing the porosity was decreased with

increasing NaOH M up to 10 M, then increased, as the same of FA%, which has the lower porosity at 25% and increases with increasing FA% replacement. However, the Na_2SiO_3/NaOH and T show that the variables have almost identical horizontal lines, indicating that there is no main effect for 28 P.
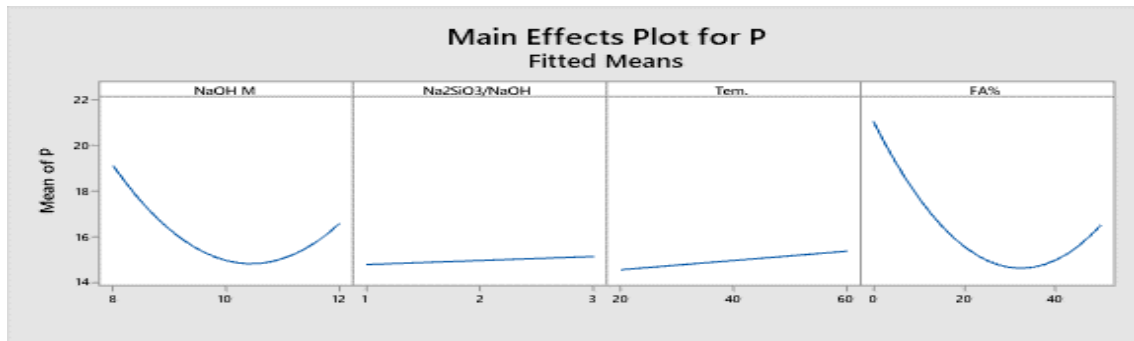
Figure B-9 The main effect and interaction plot for 28 P.

B.1.4 bulk density (28 BD)

The following is the distribution of ranking the model terms according to their significance, given in the following order as in Pareto chart Figure B-10: FA% term has the greatest effect on the 28 BD, followed by the FA%*FA%, NaOH M, NaOH M*NaOH M, and T, terms cross the reference line of the statistical significance located at 2.086.
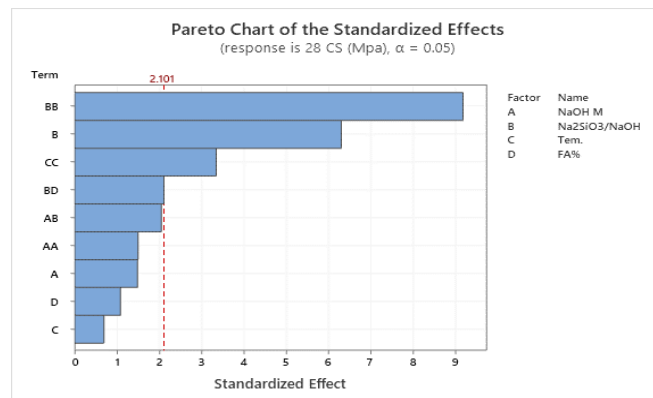

Figure B-10 Pareto chart of the standardised effects for AA bauxite with FA of (28 BD) at a 95% confidence interval.

Figure B-11 shows the Probability plot. The results show that the data points are approximately in a straight line. The P-Value is 0.56, which is greater than the significance level of 0.05,

meaning that the data follows a normal distribution as per the null hypothesis. The main BD was 2003 kg/m^3, a lower control value of 9%.
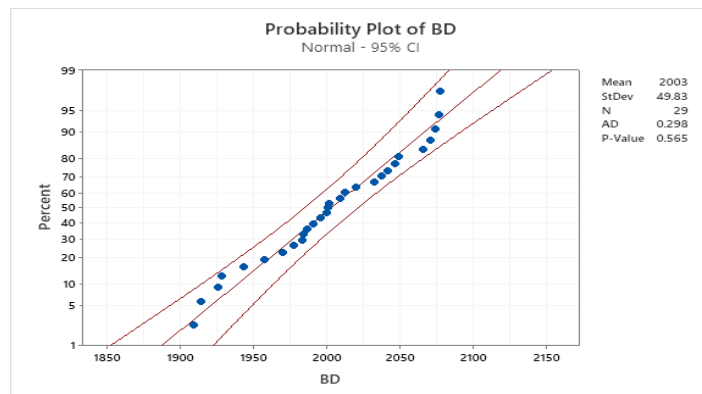
Figure B-11 Probability plot of (28 BD) at 28 days.

Figure B-12 shows the main effects plots of the 28 BD response. The significant effects on 28 BD are NaOH M and FA%. Since the results were shown at 10 M of NaOH and 25% FA replacement, the bulk density was higher (28 BD) at 2050 kg/m^3. However, the Na$_2$SiO$_3$/NaOH and T show that the variables have almost identical horizontal lines, indicating that there is no main effect for 28 BD.
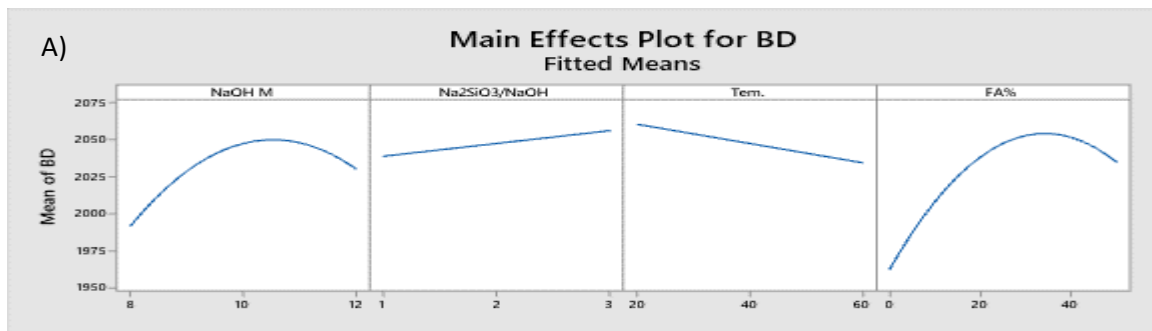
Figure B-12 The main effect and interaction plot for 28 BD.

B.1.5 water absorption (28 WA)

The distribution of ranking the model terms according to their significance is given in the following order as in Pareto chart Figure B-13: FA% had the most significant impact on the 28 WA, followed by FA%*FA%, NaOH M, NaOH M*NaOH M, and NaOH

M*Na$_2$SiO$_3$/NaOH, intersect the reference line of the statistical significance located at 2.093. Each factor's effect on the 28 WA.
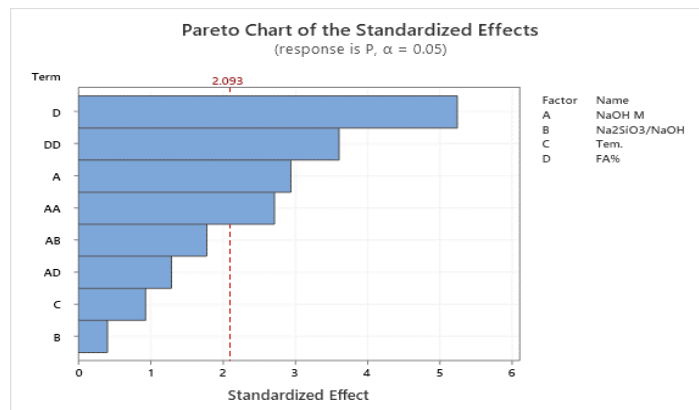

Figure B-13 Pareto chart of the standardised effects for AA bauxite with FA of (28 WA) at a 95% confidence interval.

Figure B-14 show the Probability plot that the data points are located between the red lines. Furthermore, the P-Value is 0.25, which is greater than the significance level of 0.05, indicating that the data follow a normal distribution according to the null hypothesis, and the mean value of 28 WA was 8.58%. In comparison, the CEM II was 3.21%.
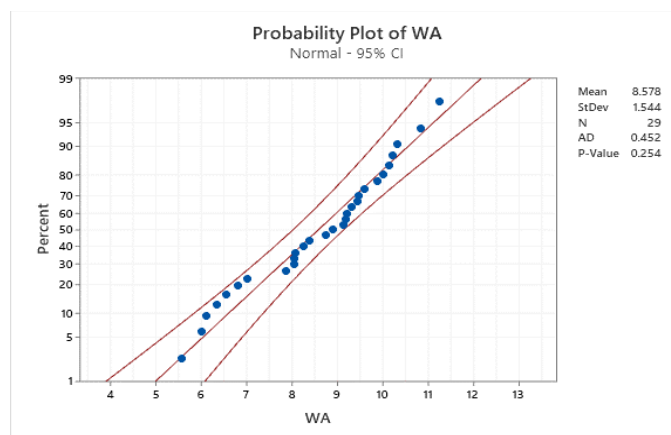
Figure B-14 Probability plot of (28 WA) at 28 days.

Figure B-15-(A), (B) shows the main effects plots of the 28 WA responses. In our case, two linear terms that significantly affect 28 WA are NaOH M and FA%. Consequently, in Figure B-15 (A), the lowest WA (7%) was recorded at 10 M NaOH and 30% FA, and the WA

increased after that. However, the $Na_2SiO_3/NaOH$ and T show that the variables have almost identical horizontal lines, indicating that there is no main effect for 28 WA.

The interaction between NaOH M and $Na_2SiO_3/NaOH$ as in Figure B-15 (B) shows that the lower level of 28 WA was recorded at 10 M when activated by a higher or lower ratio of $Na_2SiO_3/NaOH$.

Figure B-15 The main effect and interaction plot for 28 WA, main effect plot (A), and interaction plot (B) of bauxite and FA.

B.2 ANALYSIS OF AA BAUXITE BLENDED WITH FA AT 90 DAYS

B.2.1 flexural strength (90 FC)

The distribution of ranking the model terms in order of significance is shown in the following order as in Pareto chart Figure B-16: The $Na_2SiO_3/NaOH$ term was found to have the greatest impact on the 90 FC, followed by $Na_2SiO_3/NaOH* Na_2SiO_3/NaOH$, T*T, NaOH M, and the lower impact was FA%, which meets the reference line of the statistical significance located at 2.093.
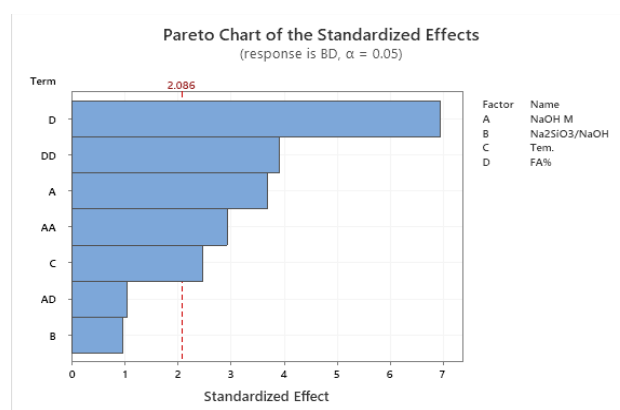
Figure B-16 Pareto chart of the standardised effects for AA bauxite with FA of (90 FC) at a 95% confidence interval.

From Figure B-17, it can be seen that the data points are located between the red lines in Probability plot. Furthermore, the P-Value is 0.129, which is greater than the significance level of 0.05, likely points to the data following a normal distribution according to the null hypothesis. Also, the mean FC was 7.60 MPa which is higher than CEM II by 4%.
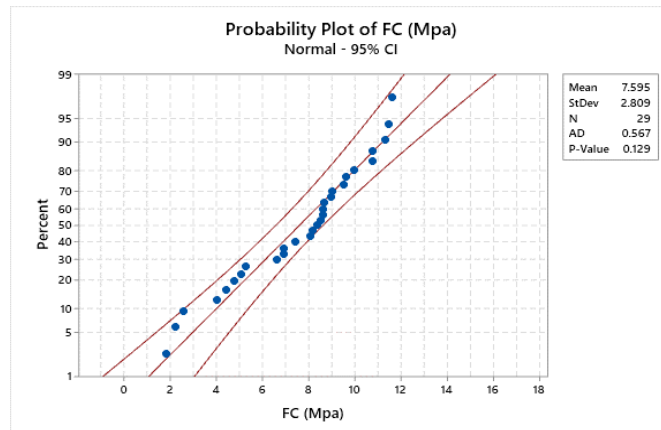
Figure B-17 Probability plot of (90 FC) at 90 days.

The main effects plots of the 90 FA responses are shown in Figure B-18 that terms significantly affect 90 FC: NaOH M, $Na_2SiO_3/NaOH$, T and FA%. Increasing NaOH M from 8 to 12 decreases the mean of 90 FC from 9 to 7 MPa. However, increasing $Na_2SiO_3/NaOH$ from 1 to 2 increases the mean of 90 FC from 3 to 9 MPa, and a further increase in $Na_2SiO_3/NaOH$ further decreases the mean of 90 FC from 8 to 6 MPa. Increasing T from 20 ^{0}C to 40 ^{0}C led to a decrease in the mean of 90 FC from 10 to 8 MPa. However, increasing T from 40 ^{0}C to 60 ^{0}C increased the mean of 90 FC from 8 to 10 MPa, and increasing FA% from 0 to 40% led to a slightly increased mean of 90 FC.
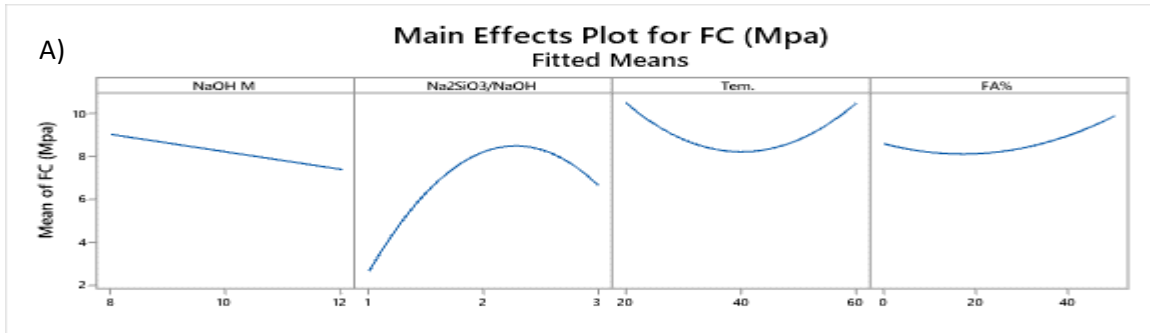
Figure B-18 The main effect and interaction plot for 90 FC.

B.2.2 compressive strength (90 CS)

The distribution of ranking the model terms according to their significance is given in the following order as in Pareto chart Figure B-19: The $Na_2SiO_3/NaOH$* $Na_2SiO_3/NaOH$ term was found to have the greatest impact on the 90 CS, followed by $Na_2SiO_3/NaOH$, NaOH M, T*T, $Na_2SiO_3/NaOH$*FA%, and the lower impact T, which crosses the reference line of the statistical significance located at 2.086.
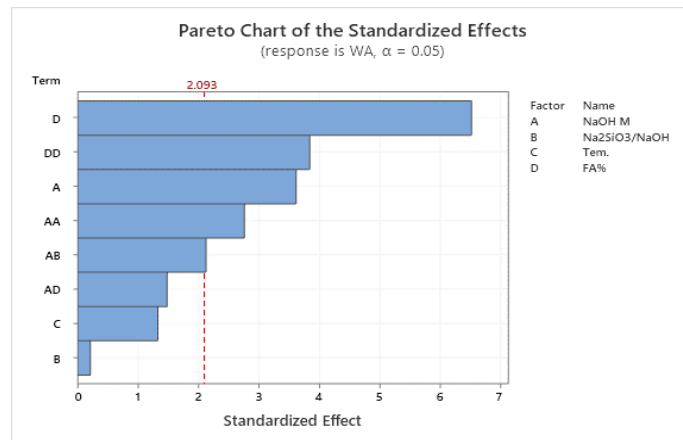

Figure B-19 Pareto chart of the standardised effects for AA bauxite with FA of (90 CS) at a 95% confidence interval.

From Probability plot Figure B-20, it can be seen that the data points are located between the red lines. The P-Value is 0.45, which is greater than the significance level of 0.05, indicating that the data follow a normal distribution according to the null hypothesis. The mean compressive strength was 24.03 MPa, which is lower than CEM II by 49%.
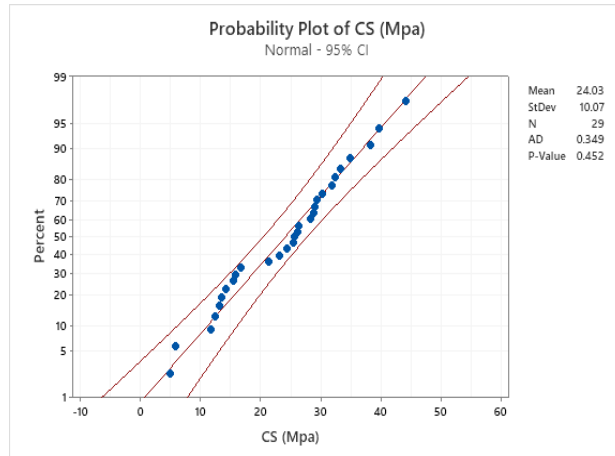
Figure B-20 Probability plot of (90 CS) at 90 days.

Figure B-21-(A), (B) shows the main and the interaction effects plots of the 90 CS responses. In our case, three terms that significantly affect 90 CS are NaOH M, Na_2SiO_3/NaOH, and T. As shown in Figure B-21-(A), increasing NaOH M decreases the mean of 90 CS slightly from 35 MPA to 28 MPa, and increasing Na_2SiO_3/NaOH from 1 to 2 increases the mean of 90 CS from 10 to 30 MPa. However, increasing Na_2SiO_3/NaOH from 2 to 3 decreases the mean of 90 CS to 20 MPa, and increasing T from 20 to 40 ^{0}C led to decreases in the mean of 90 CS from 40 to 30 MPa. However, increasing T from 40 to 60 ^{0}C led to an increasing the mean of 90 CS from 30 to 35 MPa, and the FA% show that the variable has almost identical horizontal lines, indicating that there is no main effect for of 90 CS.

The interaction plot in Figure B-21 (B) for Na_2SiO_3/NaOH and FA% shows that their interaction has affected the response differences between each factor's low, and high levels. When Na_2SiO_3/NaOH is at the lowest level of 1, a higher mean of 90 CS is obtained at the highest level of FA% (50), and the mean of 90 CS is increased by increasing Na_2SiO_3/NaOH from 1 to 2.5. However, when Na_2SiO_3/NaOH exceeds 2.5, the mean of 90 CS decreases and a higher mean of 90 CS (30 MPa) is obtained at the lowest level of FA% (0).
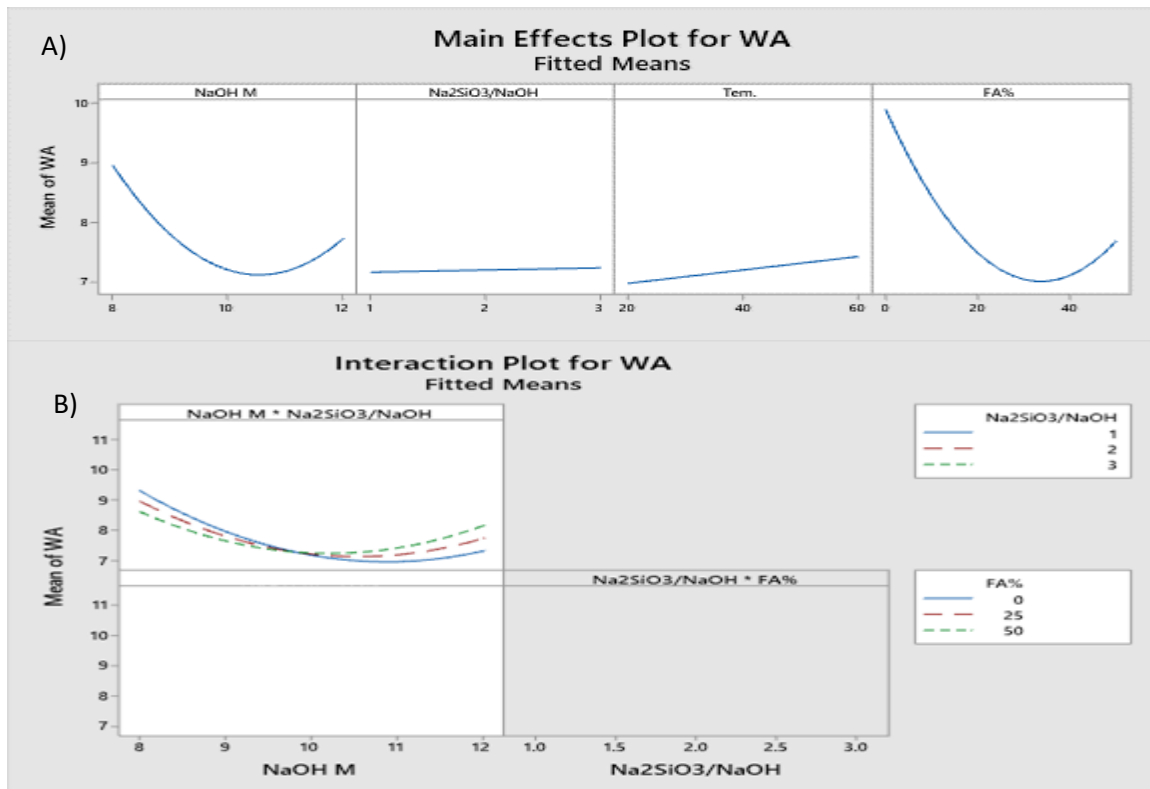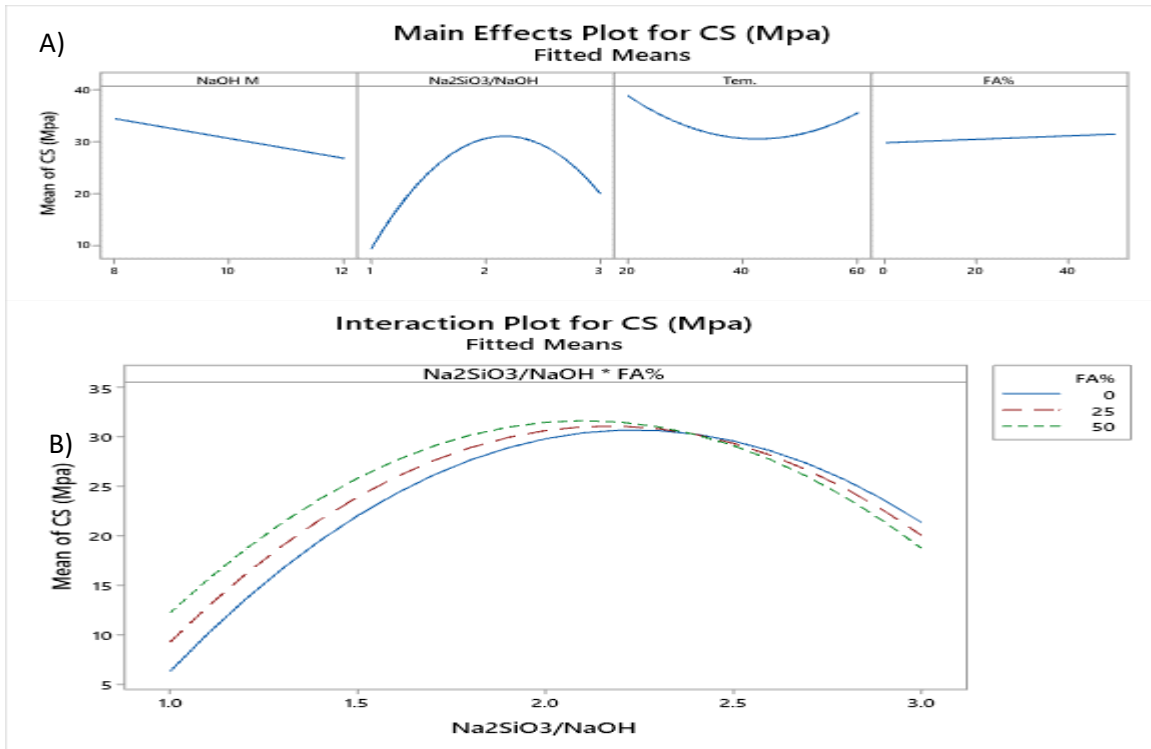
Figure B-21 The main effect and interaction plot for 90 CS, main effect plot (A), and interaction plot (B) of bauxite and FA.

B.2.3 porosity (90 P)

The distribution of ranking the model terms according to their significance can be seen with Pareto chart Figure B-22 as follows: The FA% term was found to have the most significant impact on the 90 P, followed by NaOH M*NaOH M and $Na_2SiO_3/NaOH$* $Na_2SiO_3/NaOH$, which cross the reference line of the statistical significance located at 2.093.
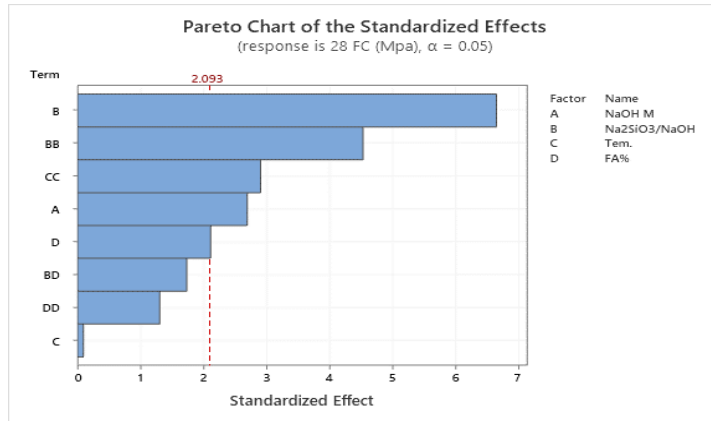

Figure B-22 Pareto chart of the standardised effects for AA bauxite with FA of (90 P) at a 95% confidence interval.

From Probability plot Figure B-23, it can be seen that the data points are located between red lines. However, only 1 point exceeded the limit, confirming that the error in the property plot at 90 P results. Consequently, the data analysis is highly accurate because the allowable error is below 10 % (Al-Shalif, 2020). The P-Value is 0.427, greater than the significance level of 0.05, this implies that the data follows a normal distribution according to the null hypothesis. The mean porosity was 20.83%, higher than CEM II, which was 8.51%.
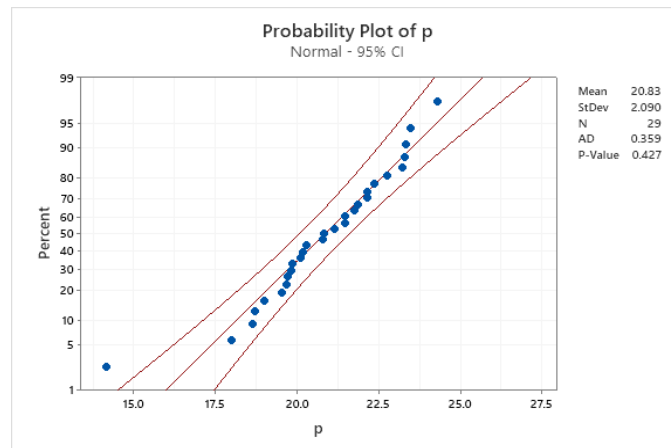
Figure B-23 Probability plot of (90 P) at 90 days.

Figure B-24 shows the main effects plots of the 90 FA responses. Increasing NaOH M from 8 to 10 decreases 90 P from 22 to 19%. However, increasing NaOH M from 10 to 12 increases 90 P from 19 to 22%, and increasing $Na_2SiO_3/NaOH$ from 1 to 2 increases 90 P from 18 to 20%. However, increasing $Na_2SiO_3/NaOH$ from 2 to 3 decreases 90 P. However, increasing the T from 20 to 40 ^{0}C led to a decrease of 90 P slightly. However, increasing T from 40 to 60 ^{0}C increases 90 P from 20 to 21, and increasing FA% by more than 40% decreases 90 P significantly from 21 to 19%.
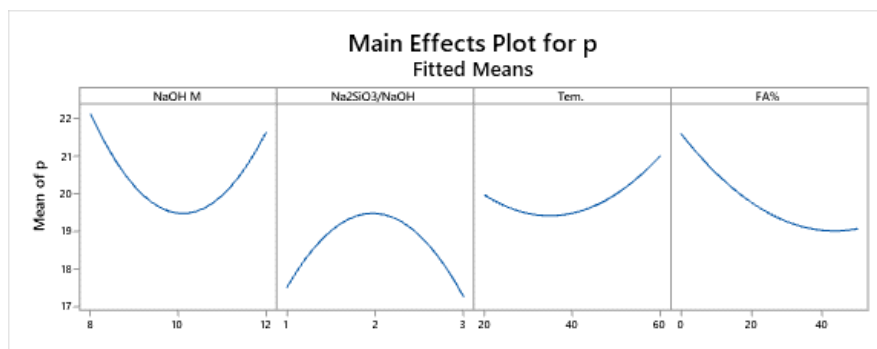
Figure B-24 The main effect plot for 90 P of bauxite and FA.

B.2.4 bulk density (90 BD)

The model terms' ranking according to their significance is given in the following order as in Pareto chart Figure B-25: The FA% term was found to have the greatest impact on the 90 BD, followed by $Na_2SiO_3/NaOH$, T, NaOH M*NaOH M, and T*T, crosses the reference line of the statistical significance located at 2.08.
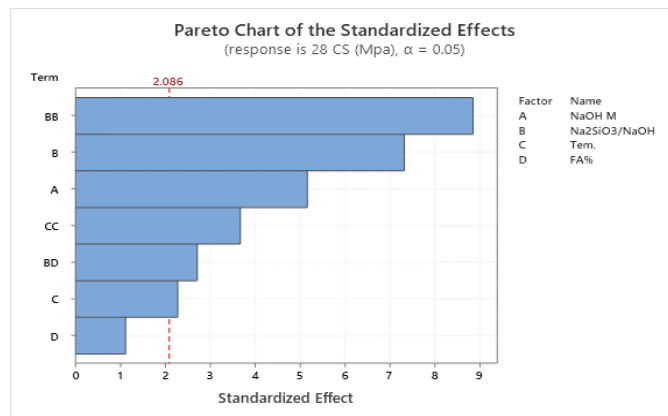

Figure B-25 Pareto chart of the standardised effects for AA bauxite with FA of (90 BD) at a 95% confidence interval.

From the Probability plot in Figure B-26, it can be seen that the data points are approximately on a straight line. The P-Value is 0.069, which is greater than the significance level of 0.05, indicating that the data follows a normal distribution according to the null hypothesis. The mean BD was 1970 kg/m^3, which was lower than CEM II by 7%.
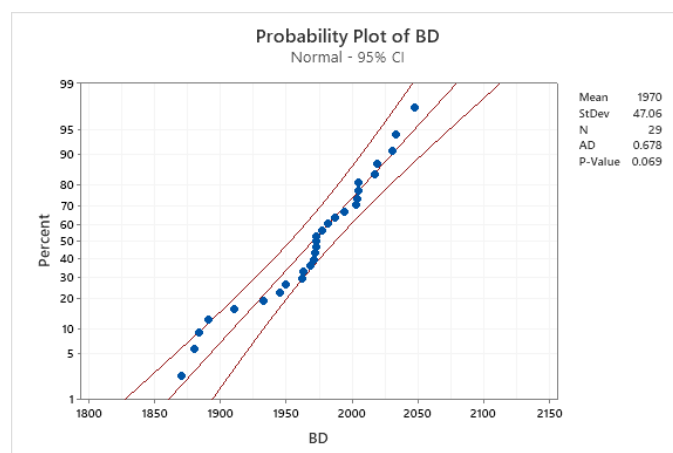
Figure B-26 Probability plot of (90 BD) at 90 days.

Figure B-27 shows the main effects plots of 90 BD responses. As shown, increasing NaOH M from 8 to 10 M increases the mean of 90 BD from 1970 to 2010 kg/m^3. However, increasing NaOH M from 10 to 12 decreases the mean of 90 BD from 2010 to 1980 kg/m^3. Moreover, increasing Na$_2$SiO$_3$/NaOH increased 90 BD from 1980 to 2030 Kg/m^3. In addition, increasing the T from 20 to 40 ^{0}C led to increasing the mean of 90 BD from 1990 to 2010 kg/m^3. However, increasing T from 40 to 60 ^{0}C decreases the mean of 90 BD from 2010 to 1960 kg/m^3, and increasing FA% increases the mean of 90 BD to recorded 2040 kg/m^3 at 50% FA.
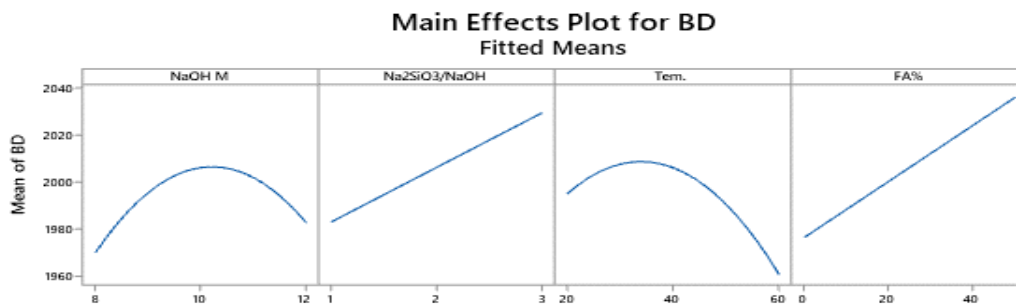
Figure B-27 The main effect plot for 90 BD of bauxite and FA.

B.2.5 water absorption (90 WA)

The distribution of ranking the model terms according to their significance is given in the following order as in Pareto chart Figure B-28: The FA% term was found to have the greatest impact on the 90 WA, followed by NaOH M*NaOH M, Na$_2$SiO$_3$/NaOH* Na$_2$SiO$_3$/NaOH, and T, which cross the reference line of the statistical significance located at 2.086. The effect of each factor on the 90 WA.
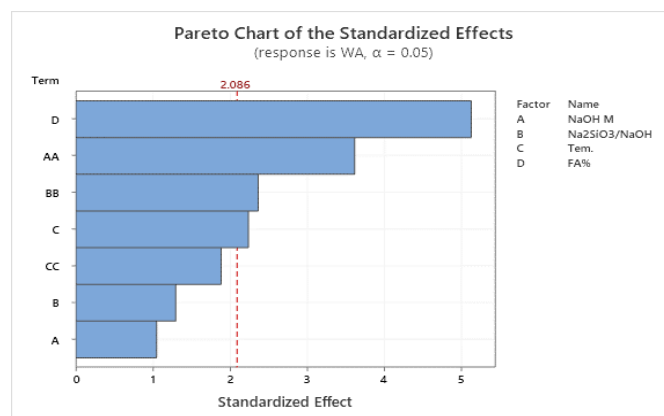
Figure B-28 Pareto chart of the standardised effects for AA bauxite with FA of (90 WA) at a 95% confidence interval.

From Probability plot Figure B-29, it can be seen that the data points are approximately on a straight line. The property plot at 90 WA resulted in only one point over the limit. Therefore, the data analysis is highly accurate since the allowable error is below 10%. The P-Value is 0.521, which is greater than the significance level of 0.05, 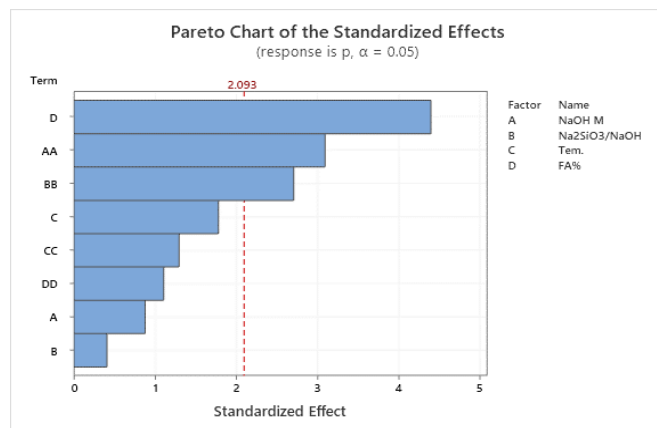indicating that the data follows a normal distribution according to the null hypothesis. The mean WA was 9.63%, while the WA of CEM II was 3.84%.
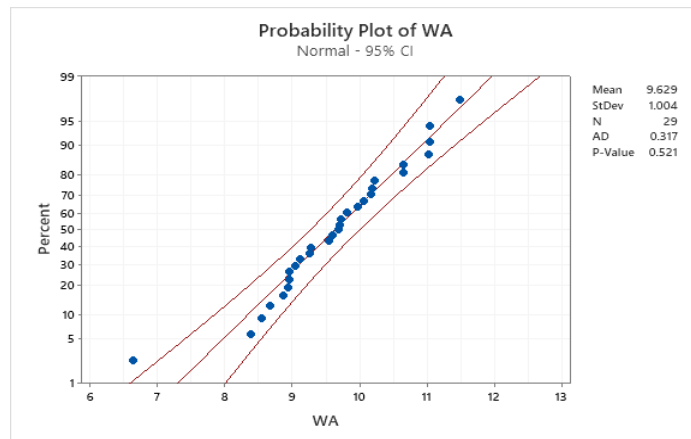
Figure B-29 Probability plot of (90 WA) at 90 days.

Figure B-30 shows the main effects plots of 90 WA responses. As shown, increasing NaOH M from 8 to 10M led to a decrease in the mean of 90 WA from 10.5 to 9 %. However, increasing NaOH M from 10 to 12 led to an increase in the mean of 90 WA from 9 to 10 %. However, increasing $Na_2SiO_3/NaOH$ led to increases in the mean of 90 WA, and a further decrease in $Na_2SiO_3/NaOH$ decreased the mean of 90 WA. In addition, increasing the T from 20 to 40 ^{0}C decreased WA slightly. However, increasing T from 40 to 60 ^{0}C raises the means of 90 WA from 9 to 10%. In addition, increasing FA% decreases the mean of 90 WA from 9.5 to 8% at 50% FA.
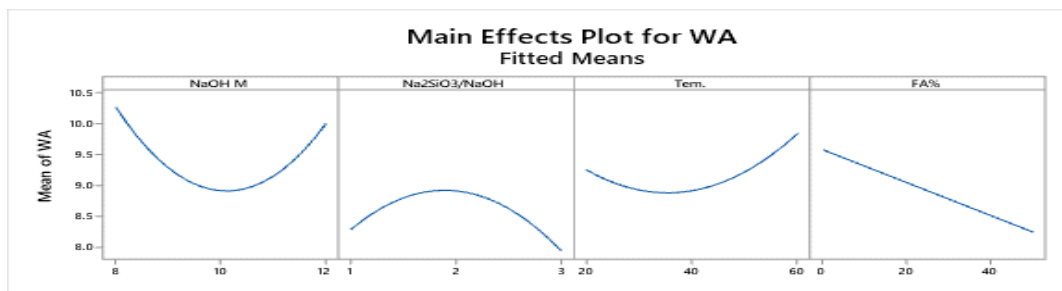
Figure B-30 The main effect plot for 90 WA of bauxite and FA.

B.3 ANALYSIS OF AA BAUXITE BLENDED WITH GGBS AT 28 DAYS

B.3.1 Flexural strength (28 FC)

The model terms' ranking according to their significance is given in the following order as the Pareto chart depicts in Figure B-31: The GGBS% term was found to have the greatest impact on the 28 FC, followed by $Na_2SiO_3/NaOH*GGBS\%$, which cross the reference line of the statistical significance located at 2.31.

Figure B-31 Pareto chart of the standardised effects for AA bauxite with GGBS of (28 FC) at a 95% confidence interval.

In terms of the Probability plot in Figure B-32, it can be identified that the data points are roughly on a straight line. The P-Value is 0.31, which is greater than the significance level of 0.05, this suggests that the data follows a normal distribution according to the null hypothesis. The mean FC was 6.42 MPa, which was higher than CEM II by 7%.
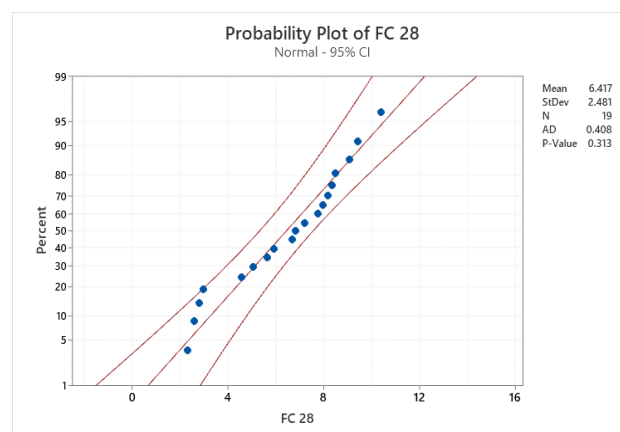
Figure B-32 Probability plot of (28 FC) at 28 days.

Figure B-33-(A), (B) shows the main effects plots and the interaction plot of 28 FC responses. For example, in Figure B-33-(A), the main effects plot for 28 FC shows that three terms (NaOH M, $Na_2SiO_3/NaOH$, and T) have approximately horizontal lines, indicating no main effect for the prementioned linear terms, and different levels of each factor affect the response the same. Meanwhile, the GGBS% term exhibited a non-horizontal line, indicating that it has a main effect. As seen, increasing GGBS% from 0 to 50 increased the mean of 28 FC from 4 to 9 MPa.

Figure B-33-(B) presents the interaction between factors. The interaction of $Na_2SiO_3/NaOH$ and GGBS% shows that at lower levels of $Na_2SiO_3/NaOH$, the highest of GGBS at 50% has higher means of 28 FC compared to the lowest GGBS at 0%. However, increasing $Na_2SiO_3/NaOH$ from 1 to 3 has decreased the mean of 28 FC at the highest of GGBS at 50% and increased the means of 28 FC at the lowest of GGBS.
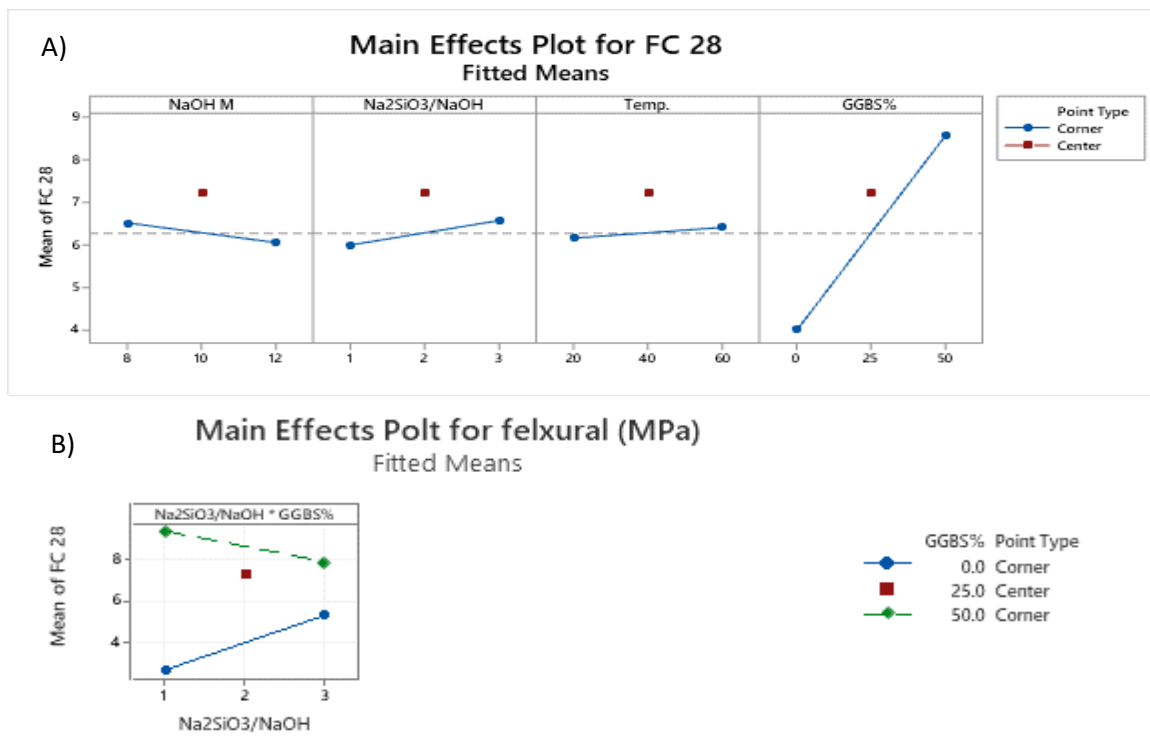
Figure B-33 The main effect and interaction plot for 28 FC, main effect plot (A), and interaction plot (B) of bauxite and GGBS.

B.3.2 compressive strength (28 CS)

The distribution of ranking represented with a Pareto chart of the model terms according to their significance is given in the following order as in Figure B-34 : The GGBS% term was found to have the greatest impact on the 28 CS followed by NaOH M*

Na$_2$SiO$_3$/NaOH*GGBS%, Na$_2$SiO$_3$/NaOH*GGBS%, Na$_2$SiO$_3$/NaOH*GGBS% , NaOH M* Na$_2$SiO$_3$/NaOH, T, and the lower effect of T*GGBS%, crosses the reference line of the statistical significance located at 2.45.

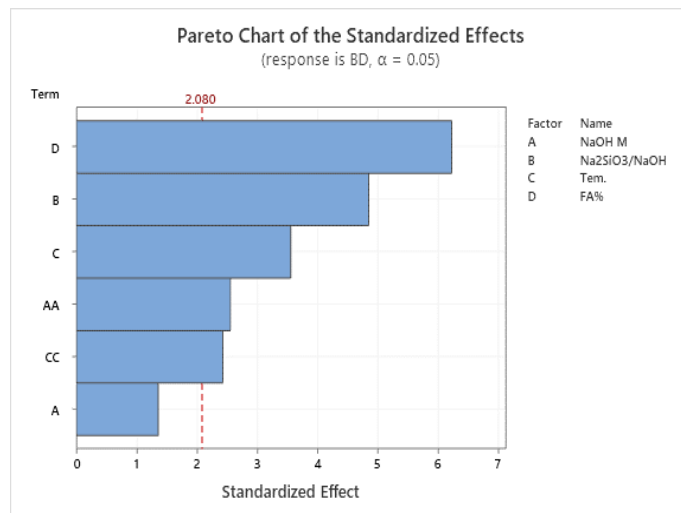

Figure B-34 Pareto chart of the standardised effects for AA bauxite with GGBS of (28 CS) at a 95% confidence interval.

The Probability plot, as shown in Figure B-35, shows that the data points are approximately on a straight line. The P-Value is 0.069, which is greater than the significance level of 0.05, suggesting that the data maintains a normal distribution according to the null hypothesis. The mean CS was 38.45 MPa, which was higher than PC by 3%.

Figure B-35 Probability plot of (28 CS) at 28 days.

Figure B-36-(A), (B) shows the main effects plots and the interaction plot of 28 CS responses. For example, in Figure B-36-(A), the main effects plot for 28 CS shows that three of the linear terms (NaOH M, Na$_2$SiO$_3$/NaOH, and T) have horizontal lines, indicating that there is no main effect for the prementioned linear terms, and different levels of each factor affect the response

the same. Meanwhile, the GGBS% term has exhibited a non-horizontal line, indicating that it has a main effect. As seen, increasing GGBS from 0 to 50% increased the mean of 28 CS from 20 to 50 MPa.

In Figure B-36-(B), the interaction of NaOH M and Na_2SiO_3/NaOH shows that the higher mean CS recorded 30 MPa when the higher and lower level of Na_2SiO_3/NaOH intersect at the centre of NaOH M, which was at 10 M.

The interaction of Na_2SiO_3/NaOH and GGBS% shows that at lower levels of Na_2SiO_3/NaOH, the highest of GGBS at 50% has higher means of 28 CS compared to the lowest GGBS at 0%. However, increasing Na_2SiO_3/NaOH from 1 to 3 has decreased the mean of 28 CS at the highest of 50% GGBS. On the other hand, increasing Na_2SiO_3/NaOH at a lower level of GGBS (0%) led to an increase the 28 CS.

The interaction of T and GGBS% indicated that higher means of 28 CS are obtained when GGBS is at the highest at 50%. However, the mean of 28 CS was increased when the T level increased from 20 to 60 ^{0}C. On the other hand, no change was seen at the lower of GGBS% between the highest and lowest levels of T.

Figure B-36 The main effect and interaction plot for 28 CS, main effect plot (A), and interaction plot (B) of bauxite and GGBS.

B.3.3 porosity (28 P)

The distribution of ranking the model terms according to their significance is given in the following order as in Pareto chart Figure B-37: The GGBS% term was found to have the greatest impact on the 28 P, followed by $Na_2SiO_3/NaOH*GGBS\%$, $Na_2SiO_3/NaOH$, and NaOH M* $Na_2SiO_3/NaOH$, converges with the reference line of the statistical significance located at 2.20.

Figure B-37 Pareto chart of the standardised effects for AA bauxite with GGBS of (28 P) at a 95% confidence interval.

The Probability plot in Figure B-38 shows that the data points are almost on a straight line. The P-Value is 0.262, which is greater than the significance level of 0.05, indicating that the data follows a normal distribution according to the null hypothesis. The mean P was 16.90%, and the P for CEM II was 7.31%.
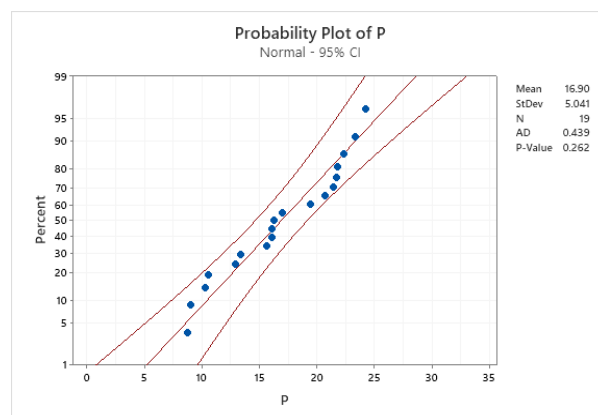
Figure B-38 Probability plot of (28 P) at 28 days.

Figure B-39- (A), (B) shows the main effects plots and the interaction plot of 28 P response. In Figure B-39- (A), the main effects plot for 28 P shows that two of the linear terms (NaOH M, and T) have horizontal lines. Meanwhile, the GGBS% and Na_2SiO_3/NaOH terms have exhibited non-horizontal lines, indicating the main effect. As seen, increasing GGBS from 0 to 50 % decreased the mean of 28 P from 22 to 12%. In addition, increasing Na_2SiO_3/NaOH from 1 to 3 elevated the mean of 28 P from 16 to 18%.

Figure B-39- (B) shows the interaction between factors. The interaction of NaOH M and Na_2SiO_3/NaOH indicated that a higher mean of 28 P was obtained when Na_2SiO_3/NaOH was at the highest at the ratio 3, which increased by increasing NaOH M level. On the other hand, in the lowest of Na_2SiO_3/NaOH at the ratio 1, the mean of 28 P was reduced by increasing the NaOH M level to the recorded 15% at NaOH 12M.

The interaction of Na_2SiO_3/NaOH and GGBS% shows that the lower GGBS% does not affect the increasing Na_2SiO_3/NaOH because the line is almost horizontal, which recorded a higher 28 P. However, increasing Na_2SiO_3/NaOH from 1 to 3 at 50% GGBS has increased the mean of 28 P from 10% to 15%.

Figure B-39 The main effect and interaction plot for 28 P, main effect plot (A), and interaction plot (B) of bauxite and GGBS.

B.3.4 bulk density (28 BD)

The model terms' ranking according to their significance is given in the following order as in the Pareto chart Figure B-40: The GGBS% term was found to have the most significant impact on the 28 BD, followed by $Na_2SiO_3/NaOH*GGBS\%$, which crosses the reference line of the statistical significance located at 2.18.

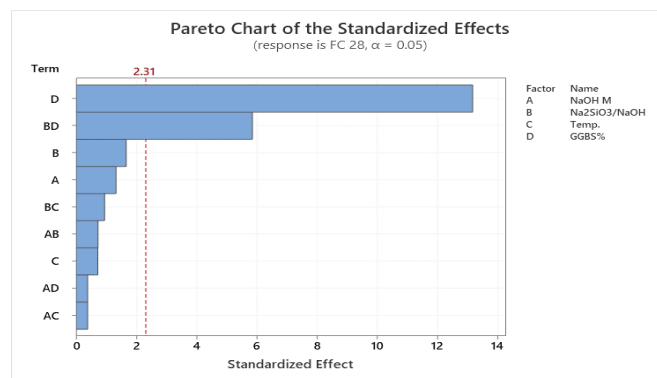Figure B-40 Pareto chart of the standardised effects for AA bauxite with GGBS of (28 BD) at a 95% confidence interval.

From the Probability plot in Figure B-41, it can be identified that the data points are nearly on a straight line. The P-Value is 0.097, which is more than the significance level of 0.05, meaning that the data follows a normal distribution according to the null hypothesis. The mean BD was 2035 kg/m^3, which was lower than CEM II by 37%.

Figure B-41 Probability plot of (28 BD) at 28 days.

Figure B-42- (A), (B) shows the main effects plots and the interaction plot of 28 BD response. In Figure B-42- (A), the main effects plot for BD shows that three of the terms (NaOH M, Na_2SiO_3/NaOH, and T) have almost horizontal lines, indicating that there is no main effect for the prementioned linear terms, and different levels of each factor affect the response the same. Meanwhile, the GGBS% term has exhibited a non-horizontal line, indicating that it has a main effect. As seen, increasing replacement of GGBS from 0 to 50% increased the mean of 28 BD from 1950 to 2100 kg/m^3.

Figure B-42- (B) presents the interaction between factors. The interaction of Na_2SiO_3/NaOH and GGBS% shows that at lower levels of GGBS at 0%, the mean of 28 BD increases with increasing Na_2SiO_3/NaOH. However, increasing Na_2SiO_3/NaOH from 1 to 3 has decreased the mean of 28 BD at a higher level of GGBS corner at 50% from 2150 kg/m^3 to 2075 kg/m^3.

Figure B-42 The main effect and interaction plot for 28 BD, main effect plot (A), and interaction plot (B) of bauxite and GGBS.

B.3.5 water absorption (28 WA)

The model terms' ranking according to their significance is given in the following order as in the Pareto chart Figure B-43: The GGBS% term was found to have the most significant impact on the 28 WA, followed by $Na_2SiO_3/NaOH*GGBS\%$ and $Na_2SiO_3/NaOH$, cross the statistical significance reference line located at 2.26.
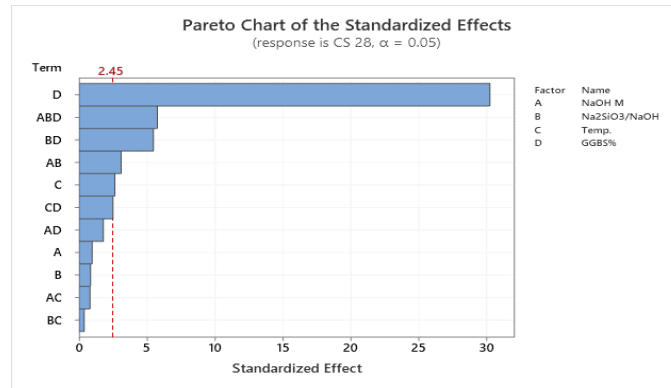

Figure B-43 Pareto chart of the standardised effects for AA bauxite with GGBS of (28 WA) at a 95% confidence interval.

From Probability plot Figure B-44, it can be seen that the data points are approximately in a straight line. The P-Value is 0.285, which is greater than the significance level of 0.05, indicating that the data follows a normal distribution according to the null hypothesis. The mean of WA was 7.73%, higher than CEM II, which was 3.21%.
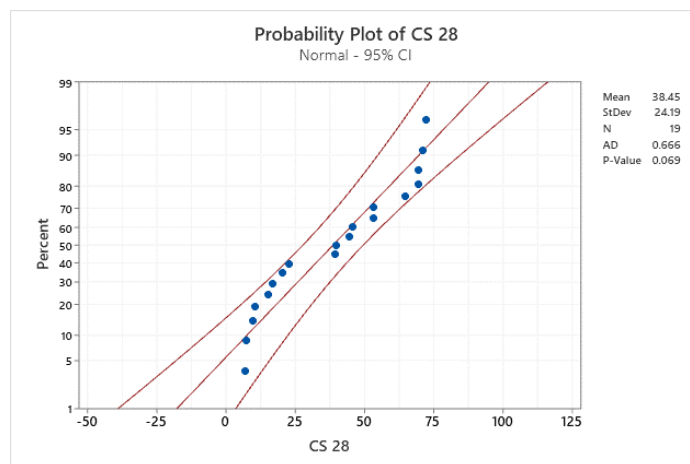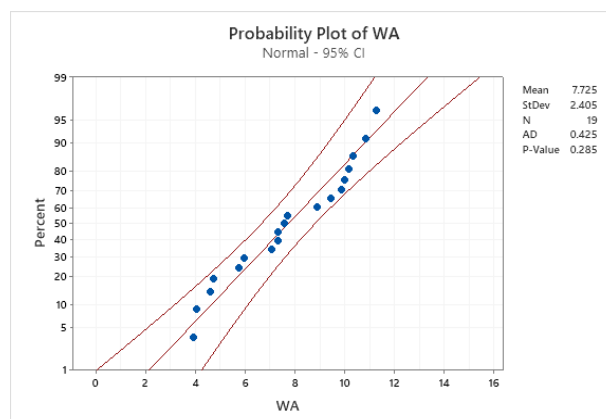

Figure B-44 Probability plot of (28 WA) at 28 days.

Figure B-45-(A), (B) shows the main effects plots and the interaction plot of 28 WA responses. In Figure B-45-(A), the main effects plot for WA shows that two of the terms (NaOH M, and T) have horizontal lines, indicating that there is no main effect for the prementioned linear terms, and different levels of each factor affect the response the same. Meanwhile, the Na_2SiO_3/NaOH and GGBS% terms have exhibited a non-horizontal line, indicating that it has a main effect. As shown, increasing Na_2SiO_3/NaOH from 1 to 3 raised the mean of 28 WA from 7 to 8%. In contrast, increasing the replacement of GGBS from 0 to 50% led to decreases in the mean of 28 WA from 10 to 5.5%.

Figure B-45-(B) shows the interaction between factors. The interaction of Na_2SiO_3/NaOH and GGBS% shows that at lower levels of Na_2SiO_3/NaOH, the lowest of GGBS at 0% has a higher mean of 28 WA compared to the highest GGBS at 50%. In contrast, the 28 WA increased by increasing Na2SiO3/NaOH at 50% GGBS.
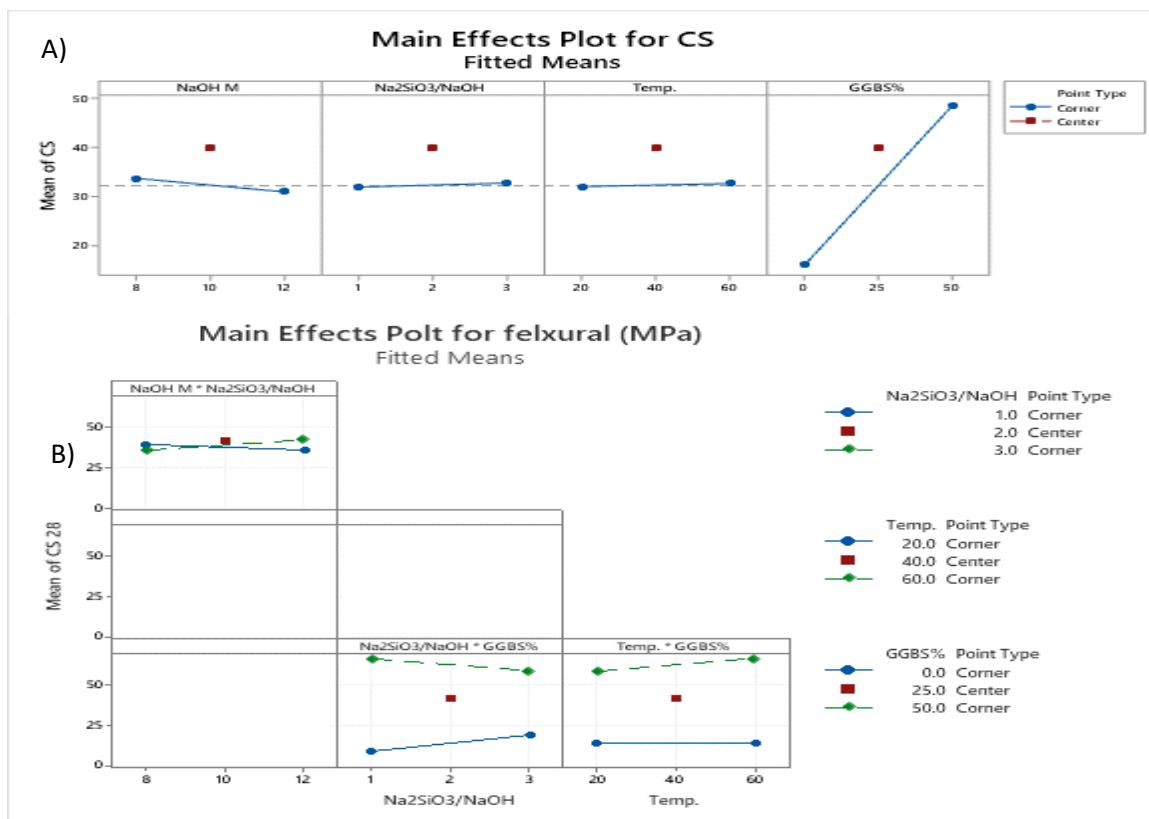

Figure B-45 The main effect and interaction plot for 28 WA, main effect plot (A), and interaction plot (B) of bauxite and GGBS.

B.4 ANALYSIS OF AA BAUXITE BLENDED WITH GGBS AT 90 DAYS

B.4.1 Flexural strength (90 FC)

The distribution of ranking the model terms according to their significance is given in the following order as in Pareto chart Figure B-46: The Na_2SiO_3/NaOH term was found to have the greatest impact on the 90 FC, followed by Na_2SiO_3/NaOH*GGBS%, NaOH M, T*GGBS%, and GGBS%*GGBS%, dissect the reference line of the statistical significance located at 2.093.
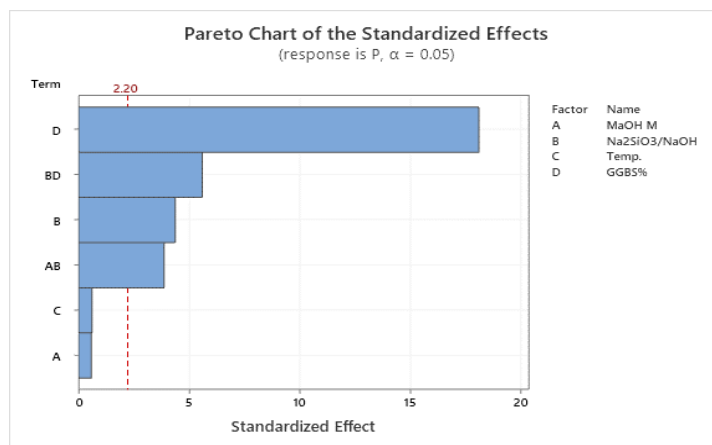

Figure B-46 Pareto chart of the standardised effects for AA bauxite with GGBS of (90 FC) at a 95% confidence interval.

The Probability plot in Figure B-47 shows the data points are approximately on a straight line. The P-Value is 0.097, which is more than the significance level of 0.05, this means that the data follow a normal distribution according to the null hypothesis. The mean FC was 7.46 MPa, which is higher than CEM II by 1%.


Figure B-47 Probability plot of (90 FC) at 90 days.

Figure B-48-(A), (B) show the main effects plots and the interaction plot of the 90 FC response. In our case, as shown in Figure B-48-(A), the NaOH M effect on 90 FA is linear, implying that increasing the NaOH M resulted in a decrease in 90 FC. On the other hand, at lower NaOH at 8 M, the FC was 9 MPa, while when increasing the NaOH to 12 M, the 90 FC was 7 MPa. In contrast, the 90 FC increased from 7 MPa with an increasing Na_2SiO_3/NaOH ratio to 9 MPa at a Na_2SiO_3/NaOH ratio of 3. In other words, 90 FC is directly proportional to the interaction of T and GGBS%. However, increasing T above 40 ^{0}C increases the mean of 90 FC from 8 to 10 MPa. In addition, increasing the replacement of GGBS from 0 to 20 % led to increasing the mean of 90 FC from 4 to 9 MPa. However, increasing GGBS above 20 % decreased 90 FC from 9 to 6 MPa.

Figure B-48-(B) show the interaction between factors. The interaction of Na_2SiO_3/NaOH and GGBS% shows a higher level of GGBS at 50% and a lower level of GGBS at 0% were intersected at 2.5 of Na_2SiO_3/NaOH to record the higher mean of 90 FC at 8 MPa. Also, the interaction of T and GGBS% shows that higher means of 90 FC are obtained at lower levels of T and the lowest level of GGBS%. Meanwhile, higher values for means of 90 FC are obtained at higher levels of both T and GGBS at 50%.

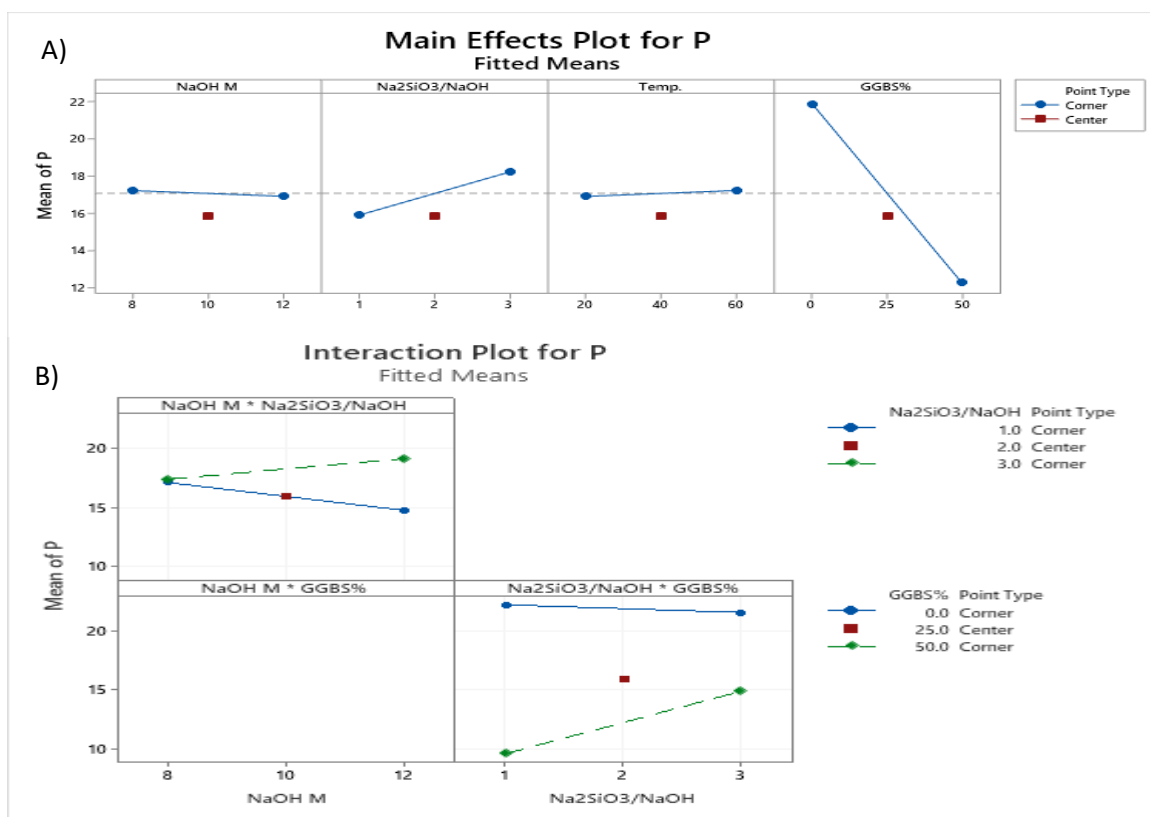
Figure B-48 The main effect and interaction plot for 90 FC, main effect plot (A), and interaction plot (B) of bauxite and GGBS.

B.4.2 compressive strength (90 CS)

The distribution of ranking the model terms according to their significance is given in the following order as in the Pareto chart Figure B-49: The GGBS% term was found to have the most significant impact on the 90 CS, followed by $Na_2SiO_3/NaOH*GGBS\%$, $T*GGBS\%$, and NaOH $M*Na_2SiO_3/NaOH$, which crosses the reference line of the statistical significance located at 2.10.
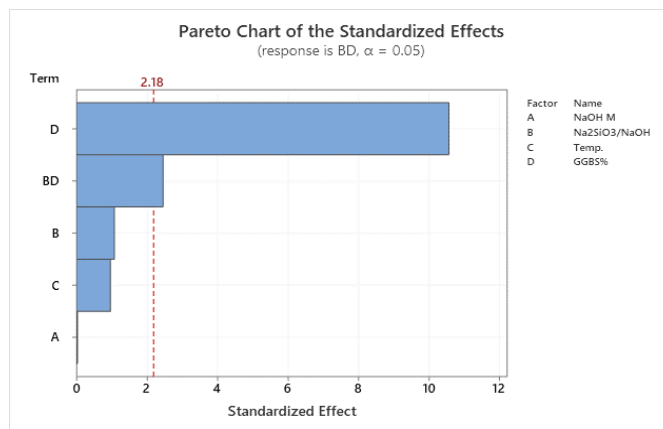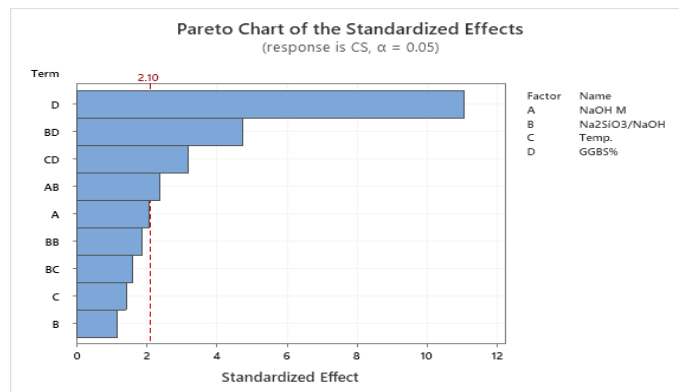

Figure B-49 Pareto chart of the standardised effects for AA bauxite with GGBS of (90 CS) at a 95% confidence interval.

The Probability plot in Figure B-50 highlights that the data points are approximately on a straight line. In 90 CS results, only one point exceeded the probability limit, this confirms that the error is normal. Since the allowable error is below 10%, the data analysis is highly accurate. The P-Value is 0.084, which is greater than the significance level of 0.05, tells us that the data follows a normal distribution in line with the null hypothesis. The mean CS was 35.17 MPa, which is lower than CEM II by 25%.
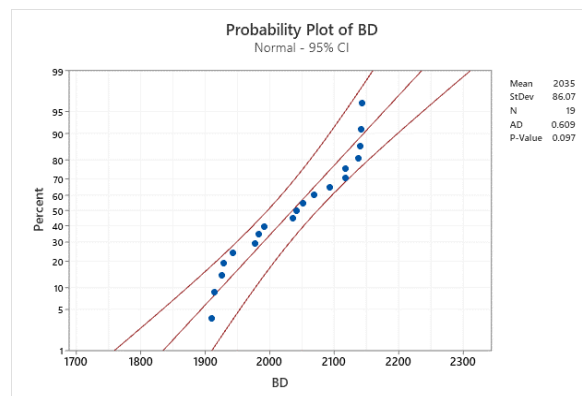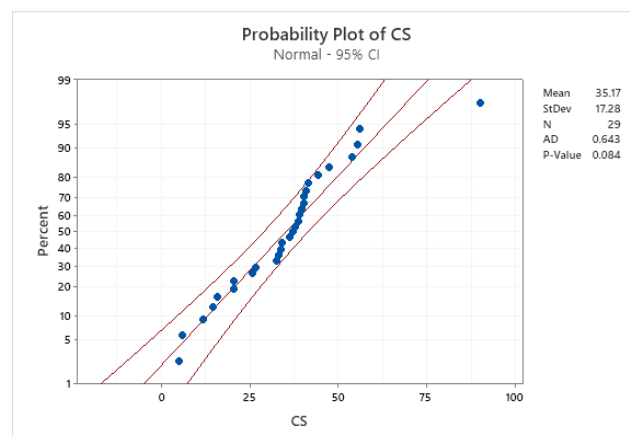

Figure B-50 Probability plot of (90 CS) at 90 days.

Figure B-51-(A), (B) shows the main effects plots and the interaction plot of 90 CS responses. The main effects plot for 90 CS, Figure B-51-(A), shows that NaOH M and T are close to horizontal lines, indicating that this interaction was weak between 35 MPa and 42 MPa. While the Na$_2$SiO$_3$/NaOH shows the parabolic curve of 90 CS, the higher 90 CS was recorded at Na$_2$SiO$_3$/NaOH=2, which was 40 MPa. On the other hand, increasing GGBS replacement led to increasing the 90 CS to 60 MPa at 50% of GGBS.

Figure B-51-(B) shows an interaction between factors. The interaction between NaOH M and Na$_2$SiO$_3$/NaOH shows the higher and lower level of Na$_2$SiO$_3$/NaOH intersecting at 10 M of NaOH to record the mean CS (25 MPa).

In an interaction between Na$_2$SiO$_3$/NaOH and GGBS%, the mean of CS decreased with increasing Na$_2$SiO$_3$/NaOH at a higher level of GGBS. In contrast, at the lower level of GGBS at 0%, the mean of CS increases with the increasing molarity of Na$_2$SiO$_3$/NaOH.

The interaction of T and GGBS% shows that at a higher level of GGBS at 50%, the mean of CS increases with increasing T. Nevertheless, at the lower level of GGBS at 0%, the mean of CS reduced with increasing T.
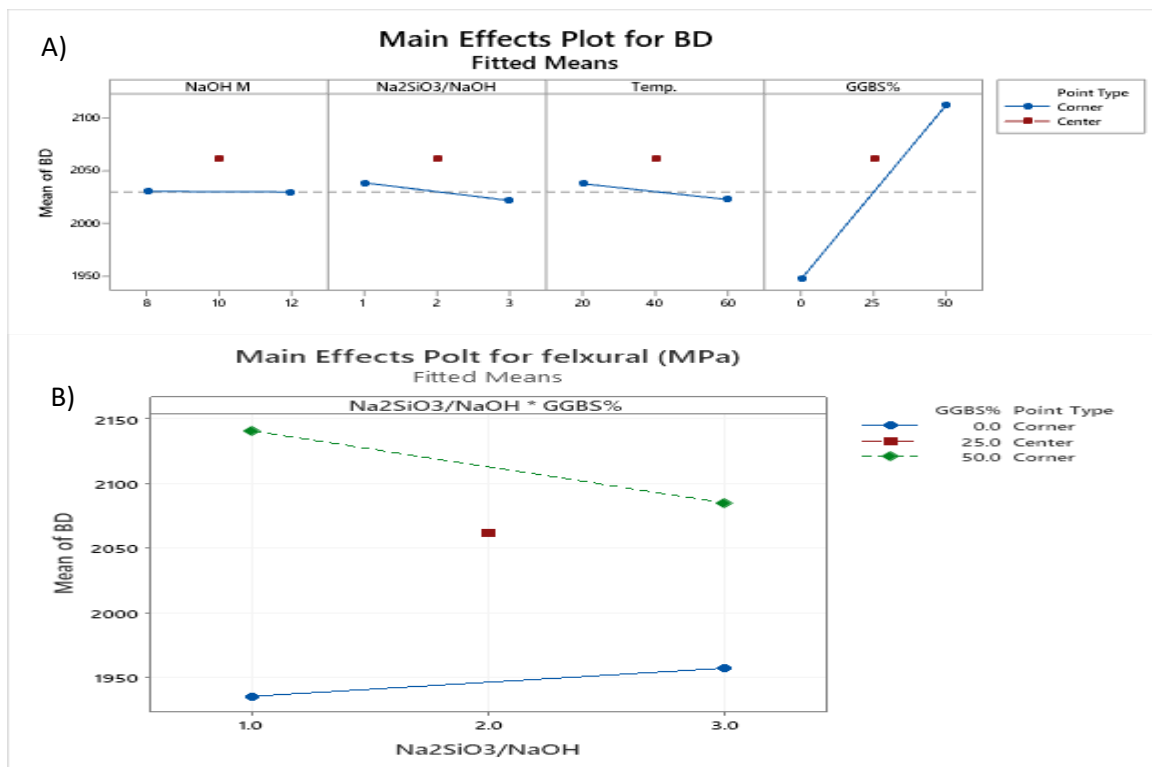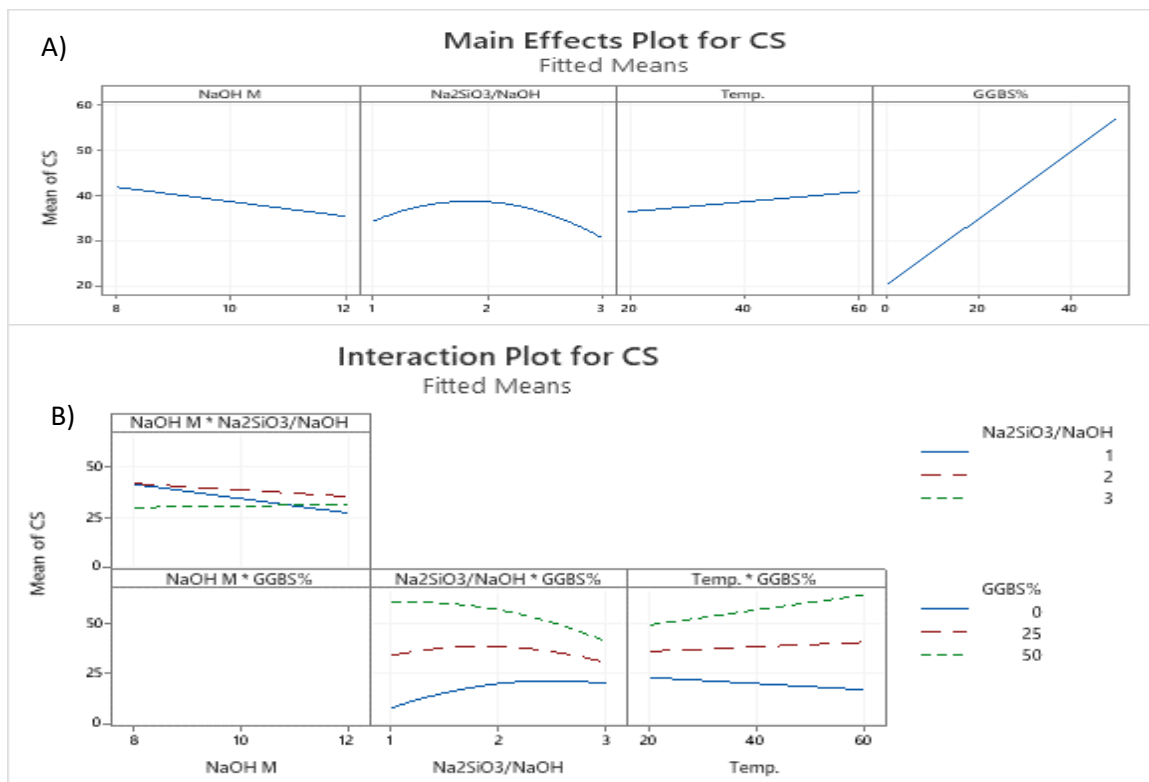

Figure B-51 The main effect and interaction plot for 90 CS, main effect plot (A), and interaction plot (B) of bauxite and GGBS.

B.4.3 porosity (90 P)

The distribution of ranking the model terms according to their significance is given in the following order as in Pareto chart Figure B-52: The GGBS% term was found to have the greatest impact on the 90 P followed by Na$_2$SiO$_3$/NaOH*GGBS%, NaOH M*T, and GGBS%* GGBS%, which crosses the reference line of the statistical significance located at 2.12.
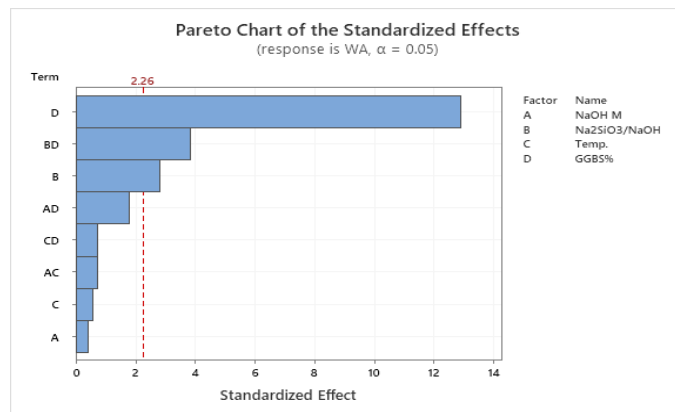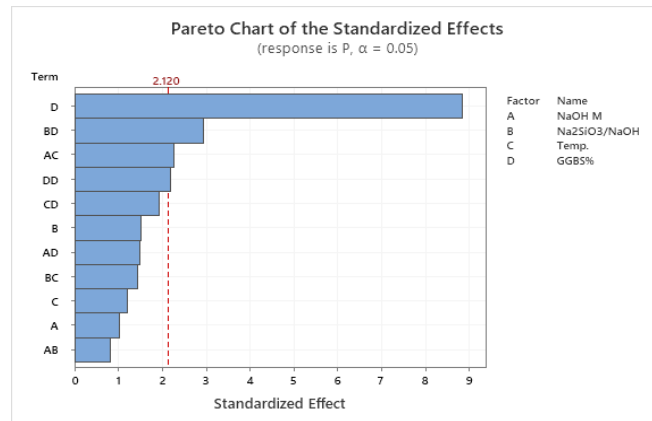

Figure B-52 Pareto chart of the standardised effects for AA bauxite with GGBS of (90 P) at a 95% confidence interval.

The Probability plot in Figure B-53, shows that the data points are approximately on a straight line. One point exceeded the probability limit, confirming that 90 P results are normal. As a result, the allowed error is below 10%, giving highly accurate results. The P-Value is 0.05, which is the same significance level of 0.05, indicating that the data follows a normal distribution according to the null hypothesis. The mean P was 19.15% higher than CEM II by double, which was 8.51.
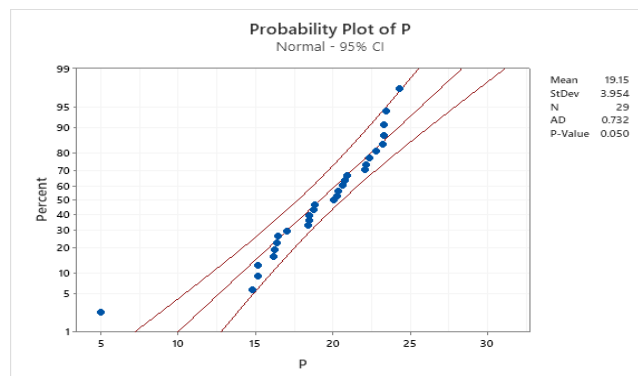

Figure B-53 Probability plot of (90 P) at 90 days.

Figure B-54-(A), (B) shows the main effects plots and the interaction plot of the 90 P response. In our case, one linear term that significantly affects 90 P is GGBS%. As shown in Figure B-54-(A), the main effects plot for 90 P, NaOH M, T, and Na_2SiO_3/NaOH have a horizontal line, indicating that they have no impact on 90 P. On the other hand, 90 P decreases with increasing the GGBS from 25 to 17% at a 50% level of GGBS.

Figure B-54-(B) shows the interaction between factors. The interaction between NaOH M and T shows the higher and lower levels of T intersecting at 11 M of NaOH to record 16% of 90 P.

The interaction between Na_2SiO_3/NaOH and GGBS% had a horizontal line at the lower level of GGBS%. In contrast, at GGBS 50%, the P increased with increasing Na_2SiO_3/NaOH.
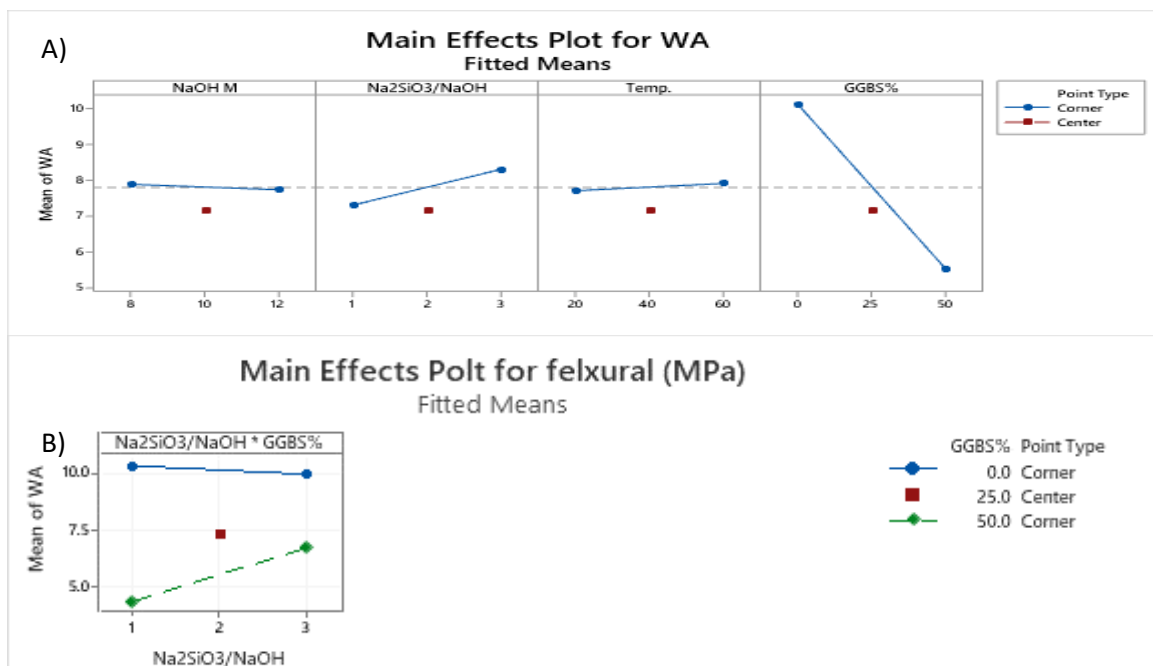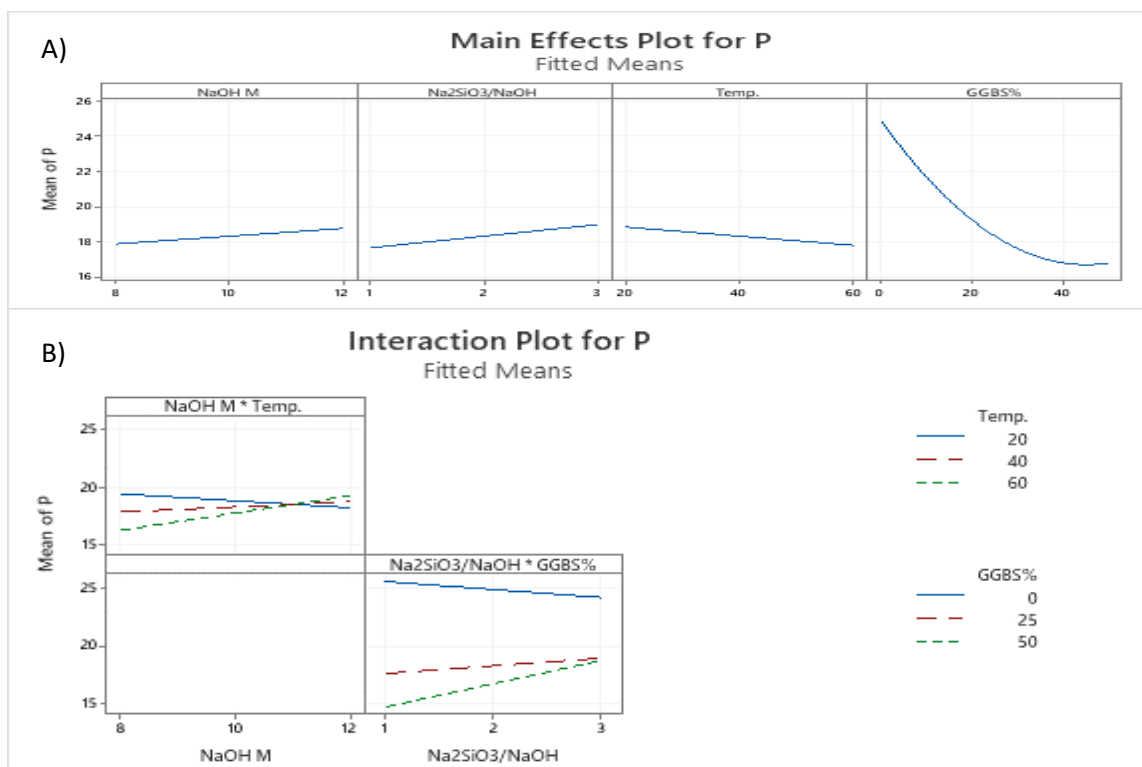

Figure B-54 The main effect and interaction plot for 90 P, main effect plot (A), and interaction plot (B) of bauxite and GGBS.

B.4.4 bulk density (90 BD)

The distribution of ranking the model terms according to their significance is given in the following order as in the Pareto chart Figure B-55: The GGBS% term was found to have the

most significant impact on the 90 BD, followed by GGBS%*GGBS% and Na$_2$SiO$_3$/NaOH* GGBS%, which crosses the reference line of the statistical significance located at 2.11.
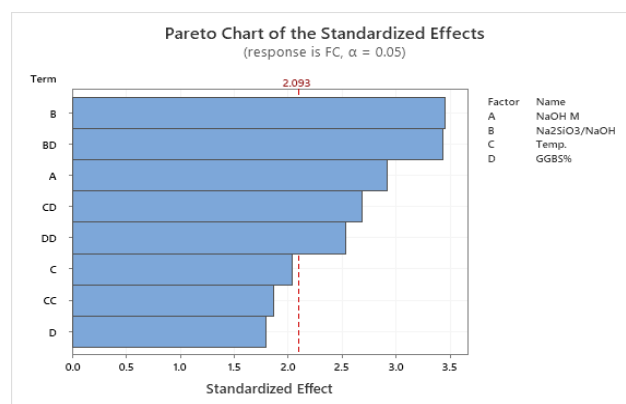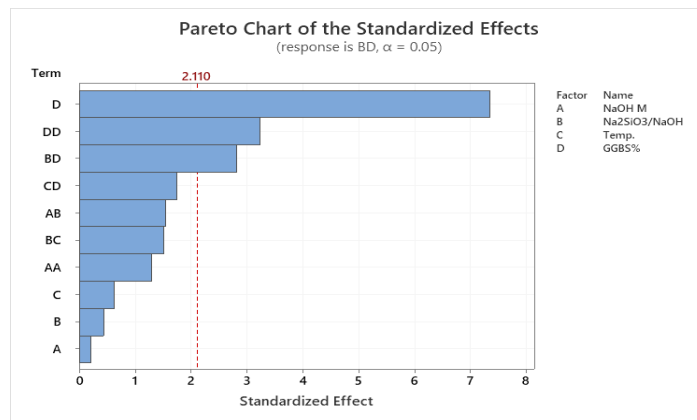

Figure B-55 Pareto chart of the standardised effects for AA bauxite with GGBS of (90 BD) at a 95% confidence interval.

The Probability plot in Figure B-56 illustrates that the data points are roughly on a straight line. However, only 2 points exceeded the probability limit, confirming that the error is normal in 90 BD results. Consequently, the data analysis is highly accurate because the allowable error is below 10 %. The P-Value is 0.133, which is more than the significance level of 0.05, implying that the data follows a normal distribution according to the null hypothesis. The means 90 BD was 2016 kg/m^3, lower than CEN II by 5%.
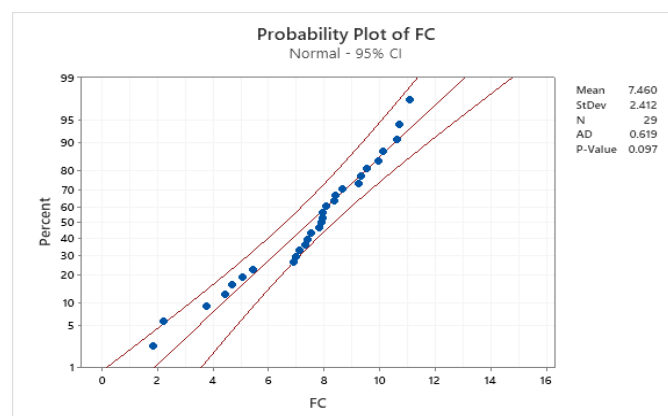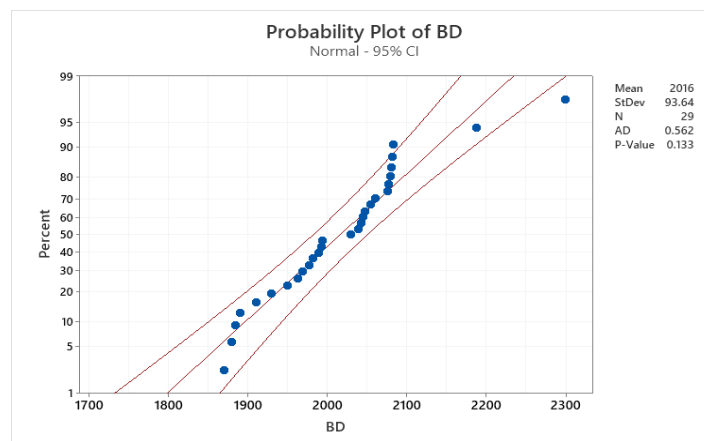

Figure B-56 Figure B-57 Probability plot of (90 BD) at 90 days.

Figure B-58 - (A), (B) shows the main effects plots and the interaction plot of 90 BD responses. In our case, one term that has a significant effect on 90 BD is GGBS%. This is shown in Figure B-58 - (A), the Na$_2$SiO$_3$/NaOH, and T have horizontal lines, and NaOH M shows a parabolic

curve which means mirror-symmetrical, indicating no main effect for the terms as mentioned above on 90 BD. On the other hand, increasing GGBS% from 0 to 35 has increased the 90 BD significantly, from 1800 kg/m^3 to the higher BD value of 2100 kg/m^3. However, increasing the GGBS by more than 35% resulted in a slight decrease in the 90 BD to record 2000 kg/m^3 at 50% GGBS.

At the centre level of GGBS at 25% in Figure B-58-(B), the interaction between Na$_2$SiO$_3$/NaOH and GGBS% had a horizontal line, indicating the main effect of GGBS at 25% does not affect the Na$_2$SiO$_3$/NaOH. However, the higher 90 BD was 2000 kg/m^3 at the higher level of GGBS% and lower level of Na$_2$SiO$_3$/NaOH, which was reduced by increasing Na$_2$SiO$_3$/NaOH. In contrast, at the lower level of GGBS at 0%, the 90 BD increased by increasing Na$_2$SiO$_3$/NaOH to record 1900 kg/m^3 at a higher level of Na$_2$SiO$_3$/NaOH.
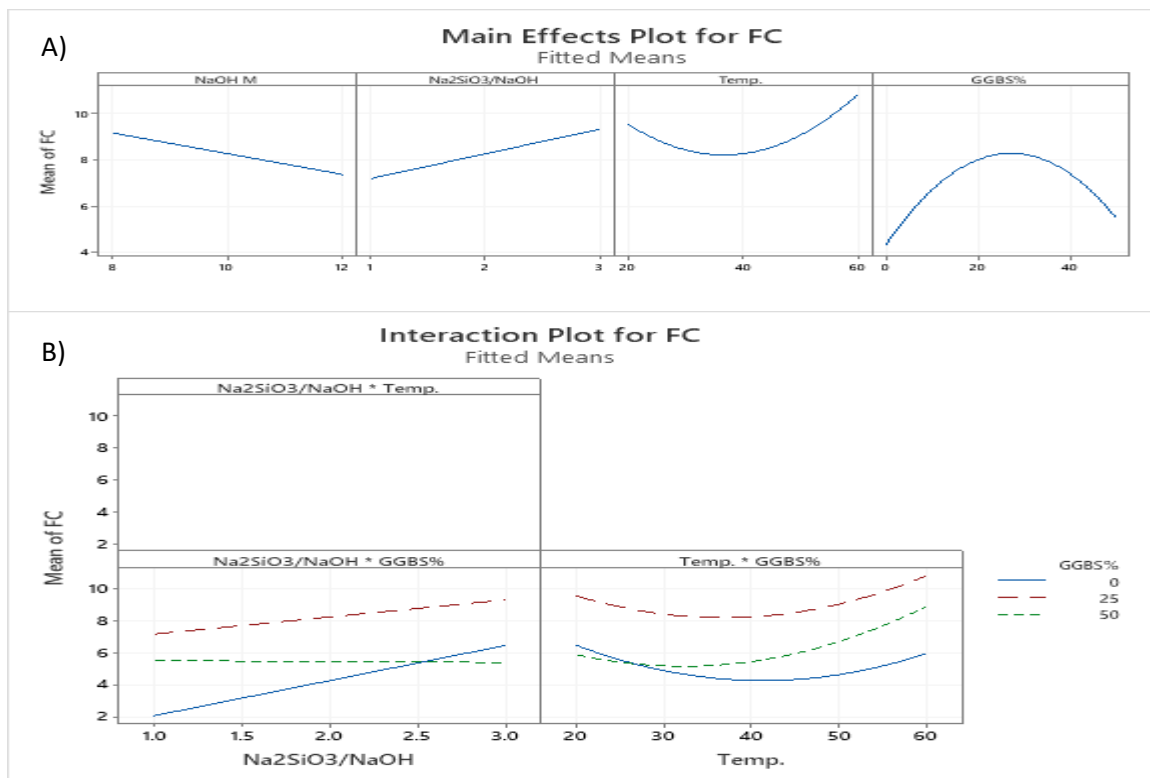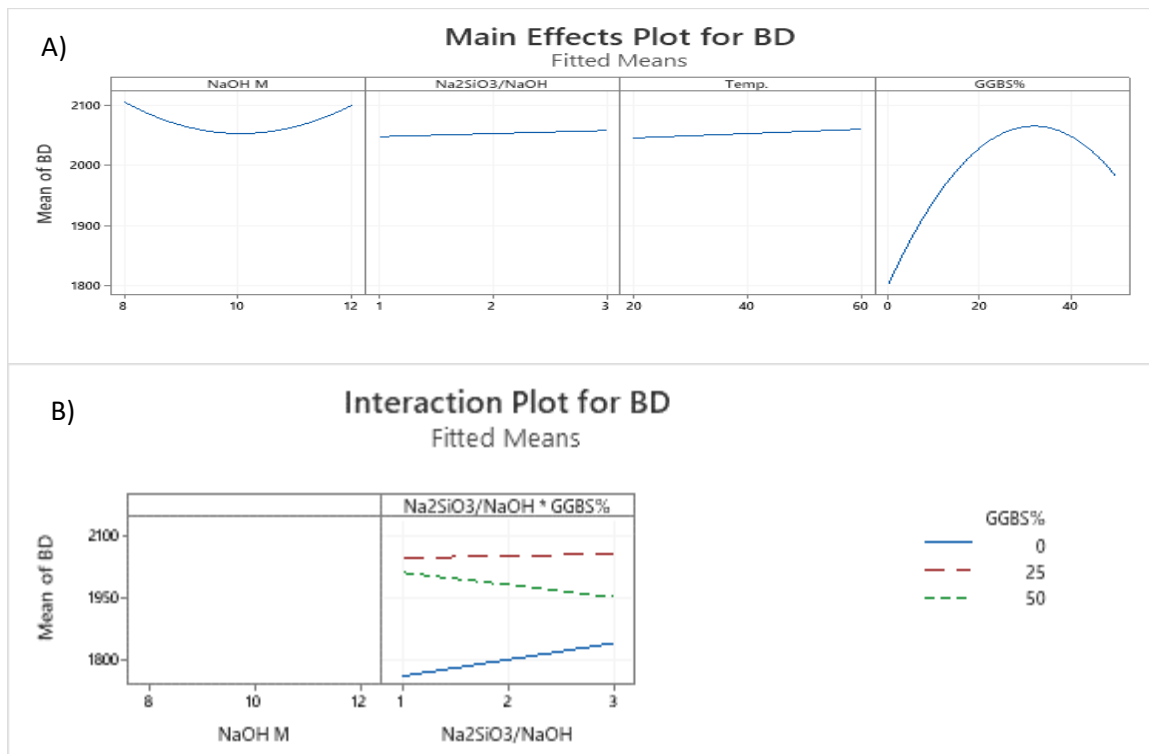

Figure B-58 The main effect and interaction plot for 90 BD, main effect plot (A), and interaction plot (B) of bauxite and GGBS.

B.4.5 water absorption (90 WA)

The model terms' ranking according to their significance is given in the following order as in Pareto chart Figure B-59: The GGBS% term was found to have the most significant impact on

the 90 WA, followed by Na$_2$SiO$_3$/NaOH*GGBS%, and GGBS%*GGBS%, which crosses the statistical significance line at 2.11.
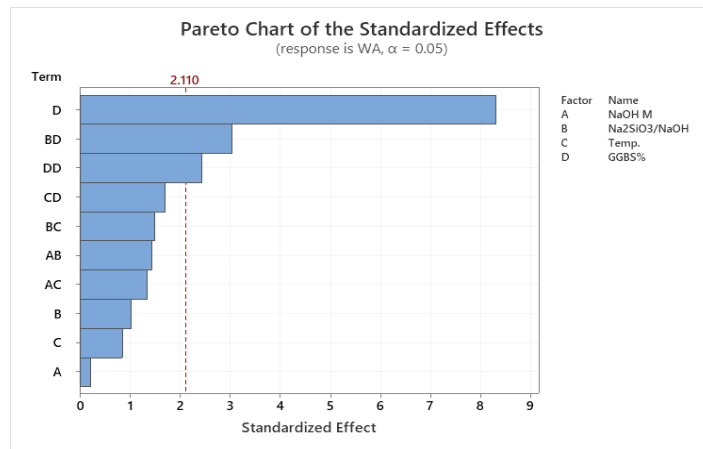
Figure B-59 Pareto chart of the standardised effects for AA bauxite with GGBS of (90 WA) at a 95% confidence interval.

From Probability plot Figure B-60, it can be seen that the data points are approximately on a straight line. There was only one point beyond the probability limit, which confirms the error is normal. Since the allowable error is below 10%, the data analysis is highly accurate. The P-Value is 0.115, which is greater than the significance level of 0.05, indicating that the data follows a normal distribution according to the null hypothesis. The mean WA was 8.80%, higher than CEM II, which was 3.85%.
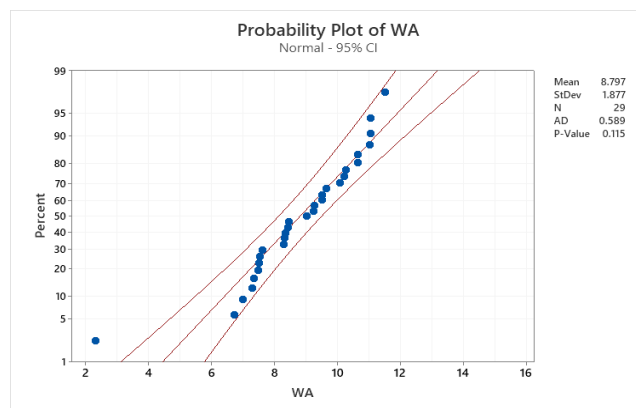
Figure B-60 Probability plot of (90 WA) at 90 days.

Figure B-61-(A),(B) shows the main effects plots and the interaction plot of 90 WA responses. In our case, one term that significantly affects 90 WA is GGBS%, besides one interaction term Na$_2$SiO$_3$/NaOH*GGBS% and one square term GGBS%*GGBS%, are the significant factors with the most important influence on the response. Figure B-61-(A) shows the main effects

248

plot for 90 WA. It shows that NaOH M, Na2SiO3/NaOH, and T have horizontal lines, indicating no main effect for the aforementioned linear terms on 90 WA. On the other hand, the mean 90 WA decreased with increasing GGBS replacing up to 50% to a record 8% of WA.

The interaction plot Figure B-61-(B) for 90 WA of Na_2SiO_3/NaOH and GGBS%, at the lower level of GGBS, the 90 WA decreased with increasing Na_2SiO_3/NaOH. Meanwhile, at a higher level of GGBS at 50%, the 90 WA increased with increasing Na_2SiO_3/NaOH.
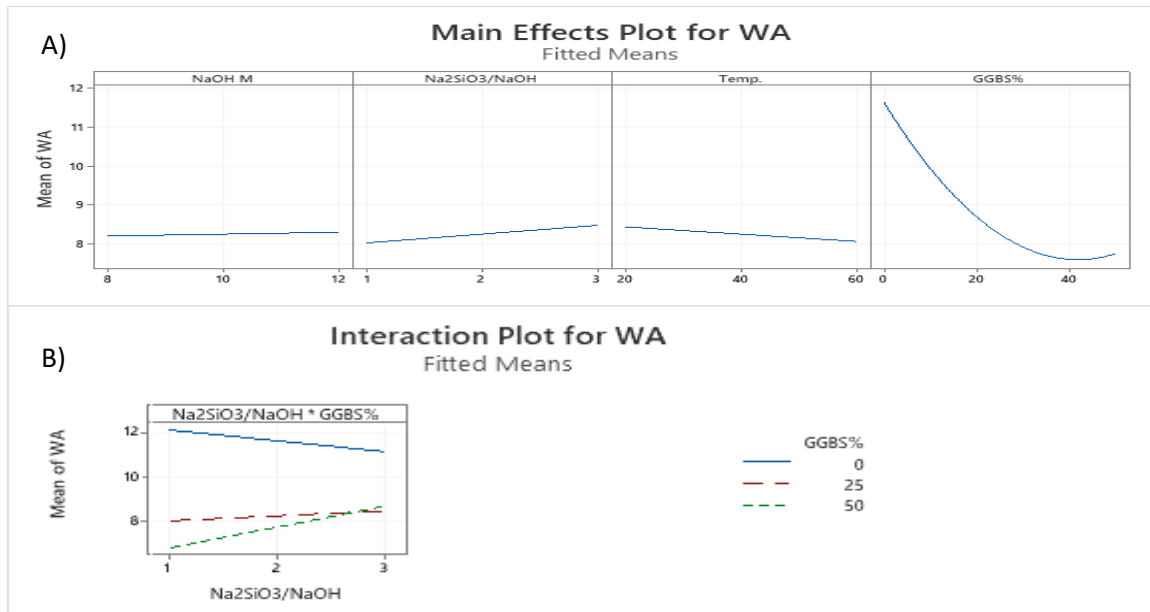
Figure B-61 The main effect and interaction plot for 90 BD, main effect plot (A), and interaction plot (B) of bauxite and GGBS.

Appendix C.

C1. Hydrated lime data sheet (CL90s)

PRODUCT SAFETY DATA SHEET

(Prepared in accordance with Annex II of the REACH Regulation (EC) 1907/2006)

1: Identification of the substance / preparation and of the company / undertaking

1.1: Identification of the substance or preparation

Substance Name	**Hydrated lime**
Synonyms	Slaked lime, Air slaked lime, Building lime, Fat lime, Chemical lime, Coarse Lime, Finishing lime, Mason's lime, Calcium dihydroxide, Calcium hydroxide, Calcium hydrate, Lime, Lime water, Bulk Hydrate, Hydrated Lime, Milk of Lime, Thick Lime Milk, Lime Putty, Bagged Hydrate, Hydrapure, White Rhino, White Rhino Hydrated Lime. *Please note that this list may not be exhaustive.*
Chemical Name and Formula	**Calcium dihydroxide – Ca(OH)$_2$**
Trade Name	**Hydrapure, White Rhino Hydrated Lime**
CAS N°	1305-62-0
EINECS N°	215-137-3
Molecular Weight	74,09

1.2: Use of the substance

Building material industry
Chemical industry
Agriculture
Biocidal use
Environmental protection (e.g. flue gas treatment, waste water treatment, sludge treatment)
Drinking water treatment
Feed, food and pharmaceutical industry
Civil engineering
Paper and paint industry
Glass industry

1.3: Company identification

Name	**Clogrennane Lime Ltd.**
Address	Clogrennane, Carlow.
Phone	059 9131811
Fax	059 9131607
Web	www.irishlime.ie
E-mail of competent person responsible for SDS in the MS or in the EU	jconnolly@clogrennane.ie

1.4: Emergency telephone

European Emergency N°	**112**
National centre for Prevention and Treatment of Intoxications N°	**01 8092566** **01 8379964** **npicdublin@beaumont.ie**
Emergency telephone at the company Available outside office hours	**00353 (0)879863618** ☒ **yes** ☐ **no**

250

C2. Calcium oxide (CaO)

ThermoFisher
SCIENTIFIC

SAFETY DATA SHEET

Creation Date 11-Jul-2014   Revision Date 31-Dec-2020   Revision Number 10

SECTION 1: IDENTIFICATION OF THE SUBSTANCE/MIXTURE AND OF THE COMPANY/UNDERTAKING

1.1. Product identifier

Product Description:	Calcium oxide
Cat No. :	C/2120/60
Synonyms	Lime
CAS-No	1305-78-8
EC-No.	215-138-9
Molecular Formula	Ca O
Reach Registration Number	-

1.2. Relevant identified uses of the substance or mixture and uses advised against

Recommended Use	Laboratory chemicals.
Sector of use	SU3 - Industrial uses: Uses of substances as such or in preparations at industrial sites
Product category	PC21 - Laboratory chemicals
Process categories	PROC15 - Use as a laboratory reagent
Environmental release category	ERC6a - Industrial use resulting in manufacture of another substance (use of intermediates)
Uses advised against	No Information available

1.3. Details of the supplier of the safety data sheet

Company	**UK entity/business name**
	Fisher Scientific UK
	Bishop Meadow Road, Loughborough,
	Leicestershire LE11 5RG, United Kingdom
	EU entity/business name
	Acros Organics BVBA
	Janssen Pharmaceuticalaan 3a
	2440 Geel, Belgium
E-mail address	begel.sdsdesk@thermofisher.com

1.4. Emergency telephone number

Tel: 01509 231166
Chemtrec US: (800) 424-9300
Chemtrec EU: 001 (202) 483-7616

SECTION 2: HAZARDS IDENTIFICATION

2.1. Classification of the substance or mixture

CLP Classification - Regulation (EC) No 1272/2008

Physical hazards

FSUC2120

C3. Chemical analysis test of CEM II

Platin Works Laboratory

Irish Cement
A CRH COMPANY

Chemical Analysis Test Report

Description of received samples:

Platin Works Portland Limestone Cement
CEM II/A-L 42,5N [0050-CPR-0028]

March, 2022

Content of report (analyses/tests):

SiO_2 *	17.30	[%]
Al_2O_3 *	4.68	[%]
Fe_2O_3 *	2.89	[%]
CaO *	62.10	[%]
Cl	Given on weekly reports	
SO_3	2.47	[%]
F.CaO	1.98	[%]
LOI :	6.50	[%]
Na_2O Eq (Alkali Equiv)	0.59	[%]
C_3A (by Bogue)	7.49	[%]

* Results reported in unignited format.

Page: 1 of 1

IRISH CEMENT LIMITED, Platin, Drogheda, Co. Louth, Ireland.
Tel: +353 0419876000

Sign: ....

C4. Saudi red mud

SAFETY DATA SHEET

1. Product and Company Identification

Material name	**Red Mud**
MSDS Number	REF-05
Version#	01
Revision date	April 3015.
CAS Number	Mixture
Product use	Waste, Reuse, Recycling
Recommended Restrictions	Naming conventions for this and similar materials vary between locations. Therefore, processes and compositions should be considered when selecting the proper Material Safety Data Sheet.
	Alkaline clay, red * Residue mud
Synonym(s)	Red Mud
Manufacturer	Ma'aden Aluminium
	Ras Al Khair Industrial City
	PO Box 11342
	Jubail Industrial City
	Eastern Province
	31961
	Kingdom of Saudi Arabia
	Ma'aden Aluminium: +966 (0)13 350-7000
Emergency Information	USA: Chemtrec: +1-703-527-3887 +1-800-424-9300 (24 Hour Emergency Telephone, multiple languages spoken

2. Hazards Identification

Emergency overview	Solid, moist, soil-like. Reddish-brown. Odorless. Non-combustible. Direct contact: Can cause severe irritation of the eyes and irritation of the skin. Dust: Can cause irritation of the upper respiratory tract.
Potential health effects	
Eyes	Direct contact: Can cause severe irritation and corrosive burns.
Skin	Direct contact: Can cause irritation especially when wet. Prolonged or repeated skin contact may cause severe irritation and dermatitis.
Inhalation	Material as received (moist, soil-like): Dust: Can cause irritation of the upper respiratory tract. Material if ground/milled to a fine powder: Chronic overexposures (airborne particles of respirable size): Can cause scarring of the lungs (silicosis) and lung cancer.
Ingestion	Can cause severe irritation.
Carcinogenicity and .Reproductive.Hazard	Material as received (moist, soil-like): Does not present any cancer or reproductive hazards. Material if ground/milled to a fine powder: Chronic overexposures (airborne particles of respirable size): Can present a cancer hazard (Silica, crystalline quartz).
Medical conditions aggravated by exposure to product	Asthma, chronic lung disease, and skin rashes.
Potential environmental effects	The product may affect the acidity (pH-factor) in water with risk of harmful effects to aquatic organisms.

3. Composition / Information on Ingredients

Composition comments   Complete composition is provided below and may include some components classified as non-hazardous.

Components	CAS#	Percent
Sodalite (3Na20.3Al203.6Si02.Na2S04)	CASNo. Not available	4 - 40
Alumino-goethite	CASNo. Not available	10 - 30
Hematite (Iron oxide)	1317-60-8	10- 30
Silica, crystalline quartzt	14808-60-7	0- 30
Tricalcium aluminate (3Ca0.Al203.6H20)	CASNo. Not available	2 - 20
Boehmite [Al(OH)O]	1318-23-6	0 - 20
Titanium dioxide	13463-67-7	2 - 15
Muscovite (K20.3Al203.6Si02.2H20)	1318-94-1	0 - 15
Calcium carbonate	1317-65-3	2 -10
Gibbsite [Al(OH)3]	21645-51-2	0-5
Kaolinite (Al203.2Si02.2H20)	1318-74-7	0-5
Sodium aluminate	1302-42-7	<1

Additional Information

4. First Aid Measures

First aid procedures

Eye contact	Immediately flush eyes with plenty of water for at least 20 minutes. Consult a physician immediately.
Skin contact	Wash with soap and water for at least 15 minutes. Get medical attention if irritation develops or persists.
Inhalation	Remove to fresh air. Check for clear airway, breathing, and presence of pulse. If breathing is difficult, provide oxygen. Loosen any tight clothing on neck or chest. Provide cardiopulmonary resuscitation for persons without pulse or respirations. Consult a physician.
Ingestion	If swallowed, dilute by drinking water. Recommend quantities up to 30 ml (Nl oz.) in children and 250 ml (N9 oz.) in adults. Never give anything by mouth to a victim who is unconscious or is having convulsions. Do NOT induce vomiting. Call a physician immediately.
Most important symptoms and effects, both acute and delayed	Upper respiratory tract irritation. Skin irritation. Eye irritation
Notes to physician	In case of shortness of breath, give oxygen.
General advice	Ensure that medical personnel are aware of the material(s) involved, and take precautions to protect themselves.

5. Fire Fighting Measures

General fire hazards	Non-combustible.
Extinguishing media	
Unsuitable extinguishing media	None known.
Protection of firefighters	
Special hazards arising from the substance or mixture	Not an explosion hazard.

254

C5. Saudi bauxite

MATERIAL SAFETY DATA SHEET (MSDS)

Bauxite (Natural Ore)

<table>
<tr><td colspan="2">Section 1: Identification of Substance /Mixture and Supplier</td></tr>
<tr><td>Product Name</td><td>: Low Grade Bauxite</td></tr>
<tr><td>Chemical Name</td><td>: Bauxite (Natural)</td></tr>
<tr><td>Chemical Formula</td><td>: Al2O3 H2O:SiO2</td></tr>
<tr><td>HS Code</td><td>: 26060010</td></tr>
<tr><td>Synonym</td><td>: Industrial Grade Bauxite, Cement Grade Bauxite, Laterite, Raw Bauxite Ore</td></tr>
<tr><td>Relevant Identified Use/Application</td><td>: Industrial applications, as an additive in Cement Manufacturing, raw material for Calcined Bauxite manufacturing, raw material for manufacturing of fire proof products</td></tr>
<tr><td>Company Identification</td><td>: Industrial Minerals Company (A Ma'aden Affiliate - Saudi Arabian Mining Company)</td></tr>
<tr><td>Address /Contacts</td><td>: 2869 Unit 1, Saudi Arabian Mining Company
Al-Madinah Al Munawarraha New Industrial City
Madinah 42524-6394, Kingdom of Saudi Arabia,
Tel No: +966 14 866 9107, Fax: +966 14 841 5378
E Mail: MIMCinfo@maaden.com.sa www.maaden.com.sa</td></tr>
</table>

Section 2: Composition / Information on Ingredients

Raw Bauxite composition is app. Al2O3 : 40 % min , SiO2 : 25 % Max , Fe2O3 : 20 % Max , TiO2 : 6 % Max , Rest Oxides : 5 % Max . Other ingredients no to be hazardous and not dangerous as per safe work criteria, make up the product concentration to 100%.

Composition reported in the oxide form but these do not necessarily exist within the magnesia as free uncombined oxides but as complex mineralogical phases

Hazard Symbols	: None Listed
Risk Phrases	: None Listed
Toxicology Data on Ingredients	: Not Applicable

Section 3: Hazards Identification

NOT CLASSIFIED AS HAZARDOUS / DANGEROUS

HAZCHEM CODE	: N/A
Routes of Entry	: Skin Contact / Eye Contact/ Inhalation/ Ingestion
EYES/SKIN	: May cause irritation of eyes / skin.
INHALATION	: May cause irritation of the upper respiratory passages. INGESTION

C6. Sodium silicate solution (Na₂SiO₃)

FREE delivery on orders over €250

lennox.ie

All Orders under €150 are subject to a order processing fee of €25
Orders between €0 and €250 (including those subject to the OP Fee)
will incur a carriage charge of:

1) €15 – Dublin area   2) €25 – Rest of Ireland

Terms and conditions apply. Deliveries are subject to scheduling on specific days.

Tel: +353 1 460 7602 | Fax: +353 1 450 7619 | Email: rebeca.castro@lennox.ie

Lennox Laboratory Supplies Ltd | www.lennox.ie

John F. Kennedy Drive | Naas Road | Co Dublin | D12FP79 | Ireland

Registered in Ireland No. 7217

Help our environment - please do not print this email unless really necessary

From: Omar Alelweet <alelweeo@tcd.ie>
Sent: 16 January 2020 15:44
To: Rebeca Decastroneves <Rebeca.Decastroneves@lennox.ie>
Subject: Re: Quotation 119607

Hi Rebeca

This is what i looking for Na2Sio3

- Viscosity * (cps) 800 to 1400

- Na2O (%) 14.00 to 17.00

- SiO2 (%) 31.00 to 35.00

- Total Solids 45 to 60

- Ratio (SiO2 / Na2O) 2.10 to 2.30 i prefer 2.2

- pH 11-14

C7. Sodium hydroxide (NaOH) – pearl

Product Overview   Documents

Gibco NaOH solutions offer more options for supply security and dual sourcing of the highest volume process liquid in bioprocessing manufacturing. Available in three different grades and two off-the-shelf sizes, these solutions provide outsourcing efficiencies to help reclaim time, space, and other core resources.

Features of Gibco NaOH solutions include:
- 0.1 M, 0.5 M, and 1 M concentrations
- Multi-compendial grade raw materials
- cGMP manufacturing to 21CFR820
- 20 L and 200 L ready-to-use single-use bioprocessing containers

Flexibility

Gibco NaOH solutions provide outsourcing efficiencies for customers manufacturing internally but seeking to partially outsource, as well as for customers with batch sizes that do not justify custom ordering and customers already outsourcing to Thermo Fisher Scientific but seeking additional flexibility. They are produced in the most commonly used concentrations and single-use containers.

Applications of Gibco NaOH solutions
- pH adjustment
- Facility/equipment sanitization
- Chromatography column cleaning, sanitization and storage

Specifications

Chemical Name or Material	Sodium Hydroxide
Shelf Life	12 months
CAS	1310-73-2
Appearance	Clear solution free of precipitate
Molecular Formula	NaOH
Concentration	0.1 M
Boiling Point	100 C
Synonym	Caustic soda, Acidity regulatory, Lye or Soda lye
Color	Clear solution
Melting Point	0 C
pH	≥12 to ≤14
Quantity	200 L
Endotoxin	≤1.0 EU/mL
Formula Weight	40
Percent Purity	95-100%
Grade	Compendial
Packaging	Bioprocess Container

REFERENCES

1. Abdul Rahim, R. H., Rahmiati, T., Azizli, K. A., Man, Z., Nuruddin, M. F., and Ismail, L. (2014) 'Comparison of Using NaOH and KOH Activated Fly Ash-Based Geopolymer on the Mechanical Properties', *Materials Science Forum*, 803(September), pp. 179–184. doi: 10.4028/www.scientific.net/msf.803.179.

2. Abdulaziz Al-Shalif, A. F. (2020) *Sequestration of carbon dioxide (CO$_2$) using bio-foamed concrete brick incorporating bacillus tequilensis bacteria*. Universiti Tun Hussein Onn Malaysia.

3. Abdullah, M. M. A. B., Kamarudin, H., Bnhussain, M., Ismail, K. N., Rafiza, A. R., and Zarina, Y. (2011) 'The relationship of NaOH molarity, Na2SiO3/NaOH ratio, fly ash/alkaline activator ratio, and curing temperature to the strength of fly ash-based geopolymer', *Advanced Materials Research*, 328–330, pp. 1475–1482. doi: 10.4028/www.scientific.net/AMR.328-330.1475.

4. Abdullah, M. M. A. B., Ming, L. Y., Yong, H. C., and Tahir, M. F. (2018) 'Clay Based Materials in Geopolymer Technology', in *Cement Based Materials*. doi: 10.5772/intechopen.74438.

5. Abdullah, M. M. A., Hussin, K., Bnhussain, M., Ismail, K. N., and Ibrahim, W. M. W. (2011) 'Mechanism and chemical reaction of fly ash geopolymer cement-a review', *Int. J. Pure Appl. Sci. Technol*, 6(1), pp. 35–44.

6. Achternbosch, M., Bräutigam, K. R., Hartlieb, N., Kupsch, C., Richers, U., Stemmermann, P. and Gleis, M. (2003) 'Heavy metals in cement and concrete resulting from the co-incineration of wastes in cement kilns with regard to the legitimacy of waste utilisation'*, Karlsruhe: Forschungszentrum Karlsruhe GmbH.

7. Adesina, A. (2020) 'Performance and sustainability overview of alkali-activated self-compacting concrete', *Waste Disposal and Sustainable Energy*, pp. 1–11.

8. Ahmadi, S., Mohammadi, L., Igwegbe, C. A., Rahdar, S., and Banach, A. M. (2018) 'Application of response surface methodology in the degradation of Reactive Blue 19 using H$_2$O$_2$/MgO nanoparticles advanced oxidation process', *International Journal of Industrial Chemistry*, 9(3), pp. 241–253.

9. Ahmaruzzaman, M. (2010) 'A review on the utilization of fly ash', *Progress in Energy and Combustion Science*, 36(3), pp. 327–363. doi: 10.1016/j.pecs.2009.11.003.

10. Ai, T., Zhong, D., Zhang, Y., Zong, J., Yan, X., and Niu, Y. (2021) 'The effect of red mud content on the compressive strength of geopolymers under different curing systems', *Buildings*, 11(7). doi: 10.3390/buildings11070298.

11. Al Bakri, A. M. M., Kamarudin, H., Nizar, I. K., Sandu, A. V., Binhussain, M., Zarina, Y., and Rafiza, A. R (2013) 'Design, processing and characterization of fly ash-based geopolymers for lightweight concrete application', *Revista de Chimie (Bucharest)*, 64(4), pp. 382–387.

12. Alayed, E., O'hegarty, R. and Kinnane, O. (2021) 'Thermal envelope analysis for new code compliance of Saudi Arabian dwellings', *Energy and Buildings*, 243, p. 110997. doi: 10.1016/j.enbuild.2021.110997.

13. Aldawsari, S., Kampmann, R., Harnisch, J., and Rohde, C. (2022) 'Setting Time, Microstructure, and

Durability Properties of Low Calcium Fly Ash/Slag Geopolymer: A Review', *Materials*. doi: 10.3390/ma15030876.

14. Al-Dubaisi, A. (2011) 'Development of Bauxite and Alumina Resources in the Kingdom of Saudi Arabia', in *Light Metals 2011*. Springer, pp. 23–28.

15. Alelweet, O. and Pavia, S. (2019) 'An Evaluation of the Feasibility of Several Industrial Wastes and Natural Materials as Precursors for the Production of Alkali Activated Materials', *International Journal of Civil and Environmental Engineering*, 13(12), pp. 741–748.

16. Alelweet, O. and Pavia, S. (2020) 'Potential of a low-calcium fly ash (FA) for the production of alkali-activated materials.', in *Civil EnginEEring rEsEarCh in irEland 2020*, pp. 162–168.

17. Alelweet, O. and Pavia, S. (2022) 'Pozzolanic and hydraulic activity of bauxite for binder production', *Journal of Building Engineering*, 51, p. 104186. doi: 10.1016/j.jobe.2022.104186.

18. Alelweet, O., Pavia, S. and Lei, Z. (2021) 'Pozzolanic and Cementing Activity of Raw and Pyro-Processed Saudi Arabian Red Mud (RM) Waste', *Recent Progress in Materials*, 3(4), pp. 1–1. doi: 10.21926/rpm.2104047.

19. Alex, T. C., Kumar, R., Roy, S. K., and Mehrotra, S. P. (2014) 'Mechanically induced reactivity of gibbsite: Part 1. Planetary milling', *Powder Technology*, 264, pp. 105–113. doi: 10.1016/j.powtec.2014.05.028.

20. Ali, M. B., Saidur, R. and Hossain, M. S. (2011) 'A review on emission analysis in cement industries', *Renewable and Sustainable Energy Reviews*, 15(5), pp. 2252–2261.

21. Allahverdi, A., Mehrpour, K. and Kani, E. N. (2008) 'Investigating the possibility of utilizing pumice-type natural pozzonal in production of geopolymer cement', *CERAMICS SILIKATY*, 52(1), p. 16.

22. Allahverdi, A., Najafi Kani, E. and Shaverdi, B. (2017) 'Carbonation versus efflorescence in alkali-activated blast-furnace slag in relation with chemical composition of activator', *International Journal of Civil Engineering*. Springer, 15, pp. 565–573.

23. Al-Mutairi, A. N., Galmed, M. A. and Aldamegh, K. S. (2015) 'Petrogenesis of the Az Zabirah south zone bauxite ore deposits, central northern Saudi Arabia', *Arabian Journal of Geosciences*, 8(4), pp. 2327–2339. doi: 10.1007/s12517-014-1347-5.

24. Alsalman, A., Assi, L. N., Kareem, R. S., Carter, K., and Ziehl, P. (2021) 'Energy and CO_2 emission assessments of alkali-activated concrete and Ordinary Portland Cement concrete: A comparative analysis of different grades of concrete', *Cleaner Environmental Systems*, 3(July), p. 100047. doi: 10.1016/j.cesys.2021.100047.

25. Alshalif, A. F., Irwan, J. M., Othman, N., Al-Gheethi, A. A., Shamsudin, S., and Nasser, I. M. (2021) 'Optimisation of carbon dioxide sequestration into bio-foamed concrete bricks pores using Bacillus tequilensis', *Journal of CO_2 Utilization*, 44(June 2020), p. 101412. doi: 10.1016/j.jcou.2020.101412.

26. Altan, E. and Erdoğan, S. T. (2012) 'Alkali activation of a slag at ambient and elevated temperatures', *Cement and Concrete Composites*, 34(2), pp. 131–139.

27. Aly, M. and Pavia, S. (2015) 'Mechanical and hygric properties of natural hydraulic lime (NHL) mortars with pozzolans', in *Third Conference on Smart Monitoring, Assessment and Rehabilitation of Civil Structures. SMAR*.

28. Aly, M. and Pavía, S. (2019) 'Limestone-filled, hydraulic-lime mortars for historic and traditional

fabrics.', in *In: 5th Historic Mortars Conference (HMC 2019), Pamplona, Spain, 19th-21st June, 2019. J I Alvarez, Dept. of Chemistry, University of Navarra*.

29. Andersson, R. and Gram, H.-E. (1987) 'Properties of alkali activated slag concrete', *Nordic concrete research*, (6), pp. 7–18.

30. Anvekar, S. R., Manjunatha, L. R., Anvekar, S. R., Sagari, S., and Archana, K. (2014) 'An Economic and Embodied Energy Comparison of Geo-polymer , Blended Cement and Traditional Concretes', *Journal of Civil Engineering Technology and Research*, 1(November), pp. 33–40.

31. Arif, E., Clark, M. W. and Lake, N. (2016) 'Sugar cane bagasse ash from a high efficiency co-generation boiler: Applications in cement and mortar production', *Construction and Building Materials*, 128, pp. 287–297.

32. Arnold, S. F. (2006) *Design of Experiments with MINITAB*, *The American Statistician*. doi: 10.1198/tas.2006.s46.

33. Asif, M. (2016) 'Growth and sustainability trends in the buildings sector in the GCC region with particular reference to the KSA and UAE', *Renewable and Sustainable Energy Reviews*, 55, pp. 1267–1273. doi: 10.1016/j.rser.2015.05.042.

34. ASTM C618 (2014) 'Standard Specification for Coal Fly Ash and Raw or Calcined Natural Pozzolan for Use in Concrete1', p. 5. doi: 10.1520/C0618.

35. ASTM C642 (2013) 'Standard test method for density, absorption, and voids in hardened concrete', *ASTM, ASTM International*.

36. Atasoy, A. (2005) 'An investigation on characterization and thermal analysis of the Aughinish red mud', *Journal of Thermal Analysis and Calorimetry*, 81(81), pp. 357–361.

37. Atiş, C. D., Bilim, C., Çelik, Ö., and Karahan, O. (2009) 'Influence of activator on the strength and drying shrinkage of alkali-activated slag mortar', *Construction and building materials*, 23(1), pp. 548–555.

38. Awoyera, P. and Adesina, A. (2019) 'A critical review on application of alkali activated slag as a sustainable composite binder', *Case Studies in Construction Materials*, 11, p. e00268.

39. Ayeni, O., Onwualu, A. P. and Boakye, E. (2021) 'Characterization and mechanical performance of metakaolin-based geopolymer for sustainable building applications', *Construction and Building Materials*, 272, p. 121938. doi: 10.1016/j.conbuildmat.2020.121938.

40. Azarsa, P. and Gupta, R. (2020) 'Freeze-Thaw Performance Characterization and Leachability of Potassium-Based Geopolymer Concrete', *Journal of Composites Science*, 4(2), p. 45. doi: 10.3390/jcs4020045.

41. Aziz, I. H., Abdullah, M. M. A. B., Salleh, M. A. A. M., and Sandu, A. V. (2020) 'The Incorporation of Sodium Hydroxide (NaOH) Concentration and CaO-Si Components on Ground Granulated Blast Furnace Slag Geopolymers.', in *IOP Conference Series: Materials Science and Engineering*. IOP Publishing, p. 12005.

42. B.A.M. Sidiya, K. P. and M. M. (2021) *Environmental Carbon Emissions of Bauxite Mining in the Mines of Az Zhabira, Kaolin Processing and Management*.

43. Bakharev, T. (2005) 'Resistance of geopolymer materials to acid attack', *Cement and Concrete Research*, 35(4), pp. 658–670. doi: 10.1016/j.cemconres.2004.06.005.

44. Bakharev, T., Sanjayan, J. G. and Cheng, Y. B. (2002) 'Sulfate attack on alkali-activated slag concrete', *Cement and Concrete Research*, pp. 211–216. doi: 10.1016/S0008-8846(01)00659-7.

45. Bakharev, T., Sanjayan, J. G. and Cheng, Y.-B. (2000) 'Effect of admixtures on properties of alkali-activated slag concrete', *Cement and Concrete Research*, 30(9), pp. 1367–1374.

46. Bakharev, T., Sanjayan, J. G. and Cheng, Y.-B. (2003) 'Resistance of alkali-activated slag concrete to acid attack', *Cement and Concrete research*, 33(10), pp. 1607–1611.

47. Bakharev, T., Sanjayan, Jay G and Cheng, Y.-B. (1999) 'Effect of elevated temperature curing on properties of alkali-activated slag concrete', *Cement and concrete research*, 29(10), pp. 1619–1625.

48. Bakharev, T., Sanjayan, Jay Gnananandan and Cheng, Y. B. (1999) 'Alkali activation of Australian slag cements', *Cement and Concrete Research*, 29(1), pp. 113–120. doi: 10.1016/S0008-8846(98)00170-7.

49. Bakharev, T., Sanjayan, Jay Gnananandan and Cheng, Y.-B. (1999) 'Alkali activation of Australian slag cements', *Cement and Concrete Research*, 29(1), pp. 113–120.

50. Barbosa, V. F. F., MacKenzie, K. J. D. and Thaumaturgo, C. (2000) 'Synthesis and characterisation of materials based on inorganic polymers of alumina and silica: Sodium polysialate polymers', *International Journal of Inorganic Materials*, 2(4), pp. 309–317. doi: 10.1016/S1466-6049(00)00041-6.

51. Bardossy, G. (1982) 'Karst Bauxites (Bauxite deposits on carbonate rocks) Budapest', in. Hungary.

52. Bárdossy, G. and Aleva, G. J. J. (1990) *Lateritic bauxites*. Elsevier Science Limited.

53. Barnes, P. and Bensted, J. (2002) *Structure and performance of cements*. CRC Press.

54. Bayat, A., Hassani, A. and Azami, O. (2020) 'Thermo- mechanical properties of alkali-activated slag–Red mud concrete', *Road Materials and Pavement Design*, 21(2), pp. 411–433. doi: 10.1080/14680629.2018.1500299.

55. Bayat, A., Hassani, A. and Yousefi, A. A. (2018) 'Effects of red mud on the properties of fresh and hardened alkali-activated slag paste and mortar', *Construction and Building Materials*, 167, pp. 775–790. doi: 10.1016/j.conbuildmat.2018.02.105.

56. BE EN 196-10 (2016) 'Methods of testing cement. Determination of the water-soluble chromium (VI) content of cement'. BSI, p. 37.

57. Beg, S. and Raza, K. (2021) 'Full Factorial and Fractional Factorial Design Applications in Pharmaceutical Product Development', in *Design of Experiments for Pharmaceutical Product Development*. Springer, pp. 43–53. doi: 10.1007/978-981-33-4717-5_4.

58. Benhelal, E., Zahedi, G., Shamsaei, E., and Bahadori, A. (2013) 'Global strategies and potentials to curb CO2 emissions in cement industry', *Journal of Cleaner Production*, 51, pp. 142–161. doi: 10.1016/j.jclepro.2012.10.049.

59. Berenguer, R., Lima, N., Valdés, A. C., Medeiros, M. H. F., Lima, N. B. D., Delgado, J. M. P. Q., and Rangel, B. (2020) 'Durability of Concrete Structures with Sugar Cane Bagasse Ash', *Advances in Materials Science and Engineering*. doi: 10.1155/2020/6907834.

60. Bergaya, Theng and Lagaly (2006) Handbook of Clay Science. Elsevier.

61. Bernal, S. A., Provis, J. L., Fernández-Jiménez, A., Krivenko, P. V., Kavalerova, E., Palacios, M., and Shi, C. (2014) *Alkali Activated Materials*. Available at: http://link.springer.com/10.1007/978-94-007-7672-2.

62. Bernal, S. A., Provis, J. L., Fernández-Jiménez, A., Krivenko, P. V., Kavalerova, E., Palacios, M., and

Shi, C. (2014) 'Binder chemistry–high-calcium alkali-activated materials', in *Alkali activated materials*. Springer, pp. 59–91.

63. Bernal, S. A., Provis, J. L., Walkley, B., San Nicolas, R., Gehman, J. D., Brice, D. G., and van Deventer, J. S (2013) 'Gel nanostructure in alkali-activated binders based on slag and fly ash, and effects of accelerated carbonation', *Cement and Concrete Research*, 53, pp. 127–144.

64. Bhardwaj, B. and Kumar, P. (2019) 'Comparative study of geopolymer and alkali activated slag concrete comprising waste foundry sand', *Construction and Building Materials*, 209, pp. 555–565.

65. Biglarijoo, N., Nili, M., Hosseinian, S. M., Razmara, M., Ahmadi, S., and Razmara, P. (2017) 'Modelling and optimisation of concrete containing recycled concrete aggregate and waste glass', Magazine of Concrete Research, 69(6), pp. 306–316.

66. Binici, H. and Aksoğan, O. (2006) 'Sulfate resistance of plain and blended cement', *Cement and Concrete Composites*, 28(1), pp. 39–46. doi: 10.1016/j.cemconcomp.2005.08.002.

67. Bish, D. L. and Post, J. E. (2018) *Modern powder diffraction*. Walter de Gruyter GmbH and Co KG.

68. Boden, T., Marland, G., Andres, B., and CO_2 emissions from fossil-fuel, G. (2011) 'burning, cement manufacture and gas flaring: Carbon dioxide information analysis center', *Oak Ridge National Laboratory, Oak Ridge, Tennessee, USA*.

69. Bortnovsky, O., and Dedecek, J. (2008) 'Metal ions as probes for characterization of geopolymer materials', *Journal of the American Ceramic Society*, pp. 3052–3057. doi: 10.1111/j.1551-2916.2008.02577.x.

70. Bouaissi, , A., Li, L. Y., Moga, L. M., Sandu, I. G., Abdullah, M. M. A. B., and Sandu, A. V. (2018) 'A review on fly ash as a raw cementitious material for geopolymer concrete', *Revista de Chimie*, 69(7).

71. Breck, Donald W and Breck, Donald Wesley (1973) *Zeolite molecular sieves: structure, chemistry, and use*. John Wiley and Sons.

72. Brigatti, M. F., Galan, E. and Theng, B. K. G. (2006) 'Structures and mineralogy of clay minerals', *Developments in clay science*, 1, pp. 19–86.

73. Brindley, G. W. and Lemaitre, J. (1987) 'Thermal, oxidation and reduction reactions of clay minerals.', *Monograph, Mineralogical Society*, (6), pp. 319–370.

74. Brough, A. R. and Atkinson, A. (2002) 'Sodium silicate-based, alkali-activated slag mortars: Part I. Strength, hydration and microstructure', *Cement and concrete research*, 32(6), pp. 865–879.

75. Brühne , S., Gottlieb, S., Assmus, W., Alig, E., and Schmidt, M. U. (2008) 'Atomic structure analysis of nanocrystalline boehmite AlO (OH)', *Crystal Growth and Design*, 8(2), pp. 489–493.

76. BS EN 1015-3 (1999) 'Methods of Test for Mortar for Masonry'.

77. BS EN 1377-3, B. (1990) 'Soils for civil engineering purposes'.

78. BS EN 15167-1 (2006) 'Ground granulated blast furnace slag for use in concrete, mortar and grout'.

79. BS EN 15978 (2011) 'Sustainability of construction works — Assessment of environmental performance of buildings — Calculation method', *BRITISH STANDARD*.

80. BS EN 196-1 (2016) 'Methods of testing cement'. BSI, p. 33.

81. BS EN 196-2 (2013) 'Method of testing cement - Part 2: Chemical analysis of cement'.

82. BS EN 196-3 (2016) 'Determination of Setting Times and Soundness'.

83. BS EN 197-1 (2011) 'Methods of testing cement', *European Standard*, p. 34.

84. BS EN 450-1 (2012) 'Fly ash for concrete'.

85. BS EN 459-1 (2015) 'Building Lime—Part 1: Definitions, Specifications and Conformity Criteria', *Brussels, Belgium: BSI*, 557, p. 52.

86. BS EN 933-2 (2020) 'BSI Standards Publication Tests for geometrical properties of aggregates Part 8 : Assessment of fines — Sand equivalent test'

87. BS EN C618 (2012) 'Supplementary cementitious materials', *Reviews in Mineralogy and Geochemistry*, 74, pp. 211–278. doi: 10.2138/rmg.2012.74.6.

88. Buchwald, a, Kaps, C. and Hohmann, M. (2003) 'Alkali-Activated Binders and Pozzolan Cement Binders – Compete Binder Reaction or Two Sides of the Same Story ?', *11th International Congress on the Chemistry of Cement.*, (May), pp. 1238–1247. Available at: http://www.uni-weimar.de/Bauing/bauchemie/Downloads/Bu-Ka-Ho-Manuscript-ICCC.pdf.

89. Buchwald, A., Tatarin, R. and Stephan, D. (2009) 'Reaction progress of alkaline-activated metakaolin-ground granulated blast furnace slag blends', *Journal of materials science*, 44(20), pp. 5609–5617.

90. Burciaga-Díaz, O. and Escalante-García, J. I. (2013) 'Structure, mechanisms of reaction, and strength of an alkali-activated blast-furnace slag', *Journal of the American Ceramic Society*, 96(12), pp. 3939–3948.

91. Cabeza, L. F., Barreneche, C., Miró, L., Morera, J. M., Bartolí, E., and Fernández, A. I. (2013) 'Low carbon and low embodied energy materials in buildings: A review', *Renewable and Sustainable Energy Reviews*, 23, pp. 536–542.

92. Canpolat, F. and Naik, T. R. (2011) 'Effect Of Curing Conditions On Strength And Durability Of High-Performance Concrete', *Scientia Iranica*, 24(2), pp. 183–186. doi: 10.24200/sci.2017.2419.

93. Castaldi, P., Silvetti, M., Enzo, S., and Deiana, S. (2011) 'X-ray diffraction and thermal analysis of bauxite ore-processing waste (red mud) exchanged with arsenate and phosphate', Clays and Clay Minerals, 59(2), pp. 189–199.

94. Castillo, H., Collado, H., Droguett, T., Sánchez, S., Vesely, M., Garrido, P., and Palma, S. (2021) 'Factors Affecting the Compressive Strength of Geopolymers: A Review', *Minerals*, 11(12), p. 1317.

95. CEMBUREAU (2020) 'The european cement association, Bulletin of the International Association of Engineering Geology - Bulletin de l', *Association Internationale de Géologie de l'Ingénieur*, 4(4), pp. 583–588.

96. Cement roadmap (2012) *International energy agency (IEA) and world business council for sustainable development (WBCSD).* Available at: www.iea.org/papers/2009/Cement_Roadmap_Foldout_WEB.pdf.

97. CEN/TC 350 (2012) 'CEN/TC 350 Sustainability of Construction Works'. Obtido em.

98. CENISO/TS 14067 (2014) *Greenhouse Gases: Carbon Footprint of Products: Requirements and Guidelines for Quantification and Communication.* International Organization for Standardization.

99. Chandra, S. (1996) *Waste materials used in concrete manufacturing.* Elsevier.

100. Chen, H. J., Shih, N. H., Wu, C. H., and Lin, S. K. (2019) 'Effects of the loss on ignition of fly ash on the properties of high-volume fly ash concrete', *Sustainability*, 11(9), p. 2704.

101. Chen, Tai-A. (2020) 'Optimum curing temperature and duration of alkali-activated glass inorganic binders', *Journal of the Chinese Institute of Engineers*, 43(6), pp. 592–602.

102. Cheng, H., Lin, K. L., Cui, R., Hwang, C. L., Chang, Y. M., and Cheng, T. W. (2015) 'The effects of SiO_2/Na_2O molar ratio on the characteristics of alkali-activated waste catalyst–metakaolin based

geopolymers', *Construction and Building Materials*, 95, pp. 710–720.

103. Cheng, X., Long, D., Zhang, C., Gao, X., Yu, Y., Mei, K., and Chen, Z. (2019) 'Utilization of red mud, slag and waste drilling fluid for the synthesis of slag-red mud cementitious material', *Journal of Cleaner Production*, 238, p. 117902.

104. Chengula, D. H. (2018) *Improving cementitious properties of blended pozzolan based materials for construction of low cost buildings in Mbeya region, Tanzania*. kassel university press GmbH.

105. Chindaprasirt, P., De Silva, P., Sagoe-Crentsil, K., and Hanjitsuwan, S. (2012) 'Effect of SiO_2 and Al_2O_3 on the setting and hardening of high calcium fly ash-based geopolymer systems', *Journal of Materials Science*, 47(12), pp. 4876–4883. doi: 10.1007/s10853-012-6353-y.

106. Chindaprasirt, P., Rukzon, S. and Sirivivatnanon, V. (2008) 'Effect of carbon dioxide on chloride penetration and chloride ion diffusion coefficient of blended Portland cement mortar', *Construction and Building Materials*. Elsevier, 22(8), pp. 1701–1707.

107. Chindaprasirt, Prinya De Silva, Pre Sagoe-Crentsil, Kwesi Hanjitsuwan, S. (2012) 'Effect of SiO_2 and Al_2O_3 on the setting and hardening of high calcium fly ash-based geopolymer systems', *Journal of Materials Science*, 47(12), pp. 4876–4883. doi: 10.1007/s10853-012-6353-y.

108. Choo, H., Lim, S., Lee, W., and Lee, C. (2016) 'Compressive strength of one-part alkali activated fly ash using red mud as alkali supplier', *Construction and Building Materials*, 125, pp. 21–28. doi: 10.1016/j.conbuildmat.2016.08.015.

109. Chowdhury, S., Mohapatra, S., Gaur, A., Dwivedi, G., and Soni, A (2021) 'Study of various properties of geopolymer concrete - A review', *Materials Today: Proceedings*, 46, pp. 5687–5695. doi: 10.1016/j.matpr.2020.09.835.

110. Cole, R. J. (1998) 'Energy and greenhouse gas emissions associated with the construction of alternative structural systems', *Building and Environment*, 34(3), pp. 335–348.

111. Collins, F. and Sanjayan, J. G. (2001) 'Microcracking and strength development of alkali activated slag concrete', *Cement and Concrete Composites*, pp. 345–352. doi: 10.1016/S0958-9465(01)00003-8.

112. Collins, Frank and Sanjayan, J. G. (2001) 'Early age strength and workability of slag pastes activated by sodium silicates', *Magazine of Concrete Research*, 53(5), pp. 321–326.

113. Coombs, D.S., Alberti, A., Armbruster, T., Artioli, G., C. and C. and Galli, E. (1997) 'Recommended nomenclature for zeolite minerals: Report of the subcommittee on zeolites of the International Mineralogical Association, Commission on New Minerals and Mineral Names', *Can Mineral*, 35, pp. 1571–1606.

114. Cornelis, R., Priyosulistyo, H. and Satyarno, I. (2018) 'The Investigation on Setting Time and Strength of High Calcium Fly Ash Based Geopolymer', in *Applied Mechanics and Materials*. Trans Tech Publ, pp. 158–164.

115. Cunningham, P. R. and Miller, S. A. (2020) 'Quantitative assessment of alkali-activated materials: environmental impact and property assessments', *Journal of Infrastructure Systems*, 26(3), p. 4020021.

116. Damineli, B. L., Kemeid, F. M., Aguiar, P. S., and John, V. M. (2010) 'Measuring the eco-efficiency of cement use', *Cement and Concrete Composites*, 32(8), pp. 555–562.

117. Das, S. K. and Shrivastava, S. (2021) 'Influence of molarity and alkali mixture ratio on ambient temperature cured waste cement concrete based geopolymer mortar', *Construction and Building*

Materials, 301, p. 124380.

118. Das, S. K., Banerjee, S. and Jena, D. (2013) 'A Review on Geo-polymer Concrete', 2(9), pp. 2785–2788.

119. Davidovits, J. (1991) 'Geopolymers: inorganic polymeric new materials.', *Journal of Thermal Analysis*, 37(8), pp. 1633–1656. doi: 10.1007/bf01912193.

120. Davidovits, J. (2015) 'False Values on CO_2 Emission for Geopolymer Cement/Concrete published In Scientific Papers', *Geopolymer Institute Library, Technical Paper*, 24, pp. 1–9.

121. Davidovits, J. and Cordi, S. A. (1979) 'Synthesis of new high temperature geo-polymers for reinforced plastics/composites', *Spe Pactec*, 79, pp. 151–154.

122. Davidovits, J. and France, S. (2018) 'Properties of Geopolymer Cements', in, pp. 131–149.

123. De Jong, B. and Brown Jr, G. E. (1980) 'Polymerization of silicate and aluminate tetrahedra in glasses, melts, and aqueous solutions—I. Electronic structure of H6Si2O7, H6AlSiO71−, and H6Al2O72−', *Geochimica et Cosmochimica Acta*, 44(3), pp. 491–511.

124. Diaz, E. I., Allouche, E. N. and Eklund, S. (2010) 'Factors affecting the suitability of fly ash as source material for geopolymers', *Fuel*, 89(5), pp. 992–996. doi: 10.1016/j.fuel.2009.09.012.

125. Dimas, D. D., Giannopoulou, I. P. and Panias, D. (2009) 'Utilization of alumina red mud for synthesis of inorganic polymeric materials', *Mineral Processing and Extractive Metallurgy Review*, 30(3), pp. 211–239. doi: 10.1080/08827500802498199.

126. Dodson, V. H. (1990) 'Pozzolans and the pozzolanic reaction', in *Concrete admixtures*. Springer, pp. 159–201.

127. Duxson, P. S. W. M., Mallicoat, S. W., Lukey, G. C., Kriven, W. M., and Van Deventer, J. S. (2007) 'The effect of alkali and Si/Al ratio on the development of mechanical properties of metakaolin-based geopolymers', *Colloids and Surfaces A: Physicochemical and Engineering Aspects*, 292(1), pp. 8–20. doi: 10.1016/j.colsurfa.2006.05.044.

128. Duxson, P., Fernández-Jiménez, A., Provis, J. L., Lukey, G. C., Palomo, A., and van Deventer, J. S (2007) 'Geopolymer technology: The current state of the art', *Journal of Materials Science*, 42(9), pp. 2917–2933. doi: 10.1007/s10853-006-0637-z

129. Duxson, P., Provis, J. L., Lukey, G. C., and Van Deventer, J. S. (2007). 'The role of inorganic polymer technology in the development of 'green concrete'. *cement and concrete research*, *37*(12), 1590-1597.

130. Duxson, P., Provis, J. L., Lukey, G. C., Mallicoat, S. W., Kriven, W. M., and Van Deventer, J. S. (2005) 'Understanding the relationship between geopolymer composition, microstructure and mechanical properties', *Colloids and Surfaces A: Physicochemical and Engineering Aspects*, 269(1–3), pp. 47–58. doi: 10.1016/j.colsurfa.2005.06.060.

131. Duxson, P., Provis, J. L., Lukey, G. C., Separovic, F., and van Deventer, J. S. (2005). 29Si NMR study of structural ordering in aluminosilicate geopolymer gels. *Langmuir*, *21*(7), 3028-3036.

132. EC (2010) *Windows Technical Background Report*, *Windows, Glazed Doors and Skylights. Report for the European Commission–DG Environment by AEA, Harwell*.

133. EI (2005) *Ecocem , GGBS Technical data sheet Technical data sheet*, *Innovation Powering Sustainability*.

134. El-Chabib, Hassan. (2020) 'Properties of SCC with supplementary cementing materials', in *Self-compacting concrete: Materials, properties and applications*. Elsevier, pp. 283–308.

135. Ellis, K., Alharbi, N., Matheu, P. S., Varela, B., and Hailstone, R. (2015) 'Durability of alkali activated blast furnace slag', *IOP Conference Series: Materials Science and Engineering*. doi: 10.1088/1757-899X/96/1/012004.

136. Elsayed, A. and Swan, C. (2007) 'Compression Behavior of Synthetic Lightweight Aggregates', *World of Coal Ash Conferences (WOCA)*. Available at: http://www.flyash.info/2007/143elsayed.pdf.

137. EPD, *Irish Green Building Council*. Available at: https://www.igbc.ie/epd-home/.

138. Erixon, M. (1999) *Centre for Environmental Assessment of Product and Material Systems*.

139. Escalante-García , J. I., Fuentes, A. F., Gorokhovsky, A., Fraire-Luna, P. E., and Mendoza-Suarez, G. (2003) 'Hydration products and reactivity of blast-furnace slag activated by various alkalis', *Journal of the American Ceramic Society*, 86(12), pp. 2148–2153.

140. European Environmental Agency (2019) *Economic losses from climate-related extremes, Indicator Assessment. Data and maps*. Available at: https://www.eea.europa.eu/downloads/92dcd5aa70764b63b092ee9ee5777fbb/1519722091/assessment-1.pdf.

141. Evans, K. (2016) 'The history, challenges, and new developments in the management and use of bauxite residue', *Journal of Sustainable Metallurgy*, 2(4), pp. 316–331.

142. Faridmehr, I., Nehdi, M. L., Nikoo, M., Huseien, G. F., and Ozbakkaloglu, T. (2021) 'Life-Cycle Assessment of Alkali-Activated Materials Incorporating Industrial Byproducts', *Materials*, 14(9), p. 2401.

143. Fatimah Azzahran Abdullah, S., Yun-Ming, L., Bakri, M. M. A., Cheng-Yong, H., Zulkifly, K., and Hussin, K. (2018) 'Effect of Alkali Concentration on Fly Ash Geopolymers', *IOP Conference Series: Materials Science and Engineering*, 343(1). doi: 10.1088/1757-899X/343/1/012013.

144. Fawer, M., Concannon, M. and Rieber, W. (1999) 'Life cycle inventories for the production of sodium silicates', *The International Journal of Life Cycle Assessment*, 4(4), pp. 207–212.

145. Feret, R. (1939) 'Slags for the manufacture of cement', *Rev. Mater. Constr. Tr. Publications*, pp. 1–145.

146. Fernández-Jiménez A. and Palomo A. (2003) 'Characterisation of fly ashes. *Potential reactivity as alkaline cements*', Fuel, 82, pp. 2259–2265. doi: 10.1016/S0016-2361(03)00194-7.

147. Fernández-Jiménez, A. and Puertas, F. (2001) 'Setting of alkali-activated slag cement. Influence of activator nature', *Advances in Cement Research*, 13(3), pp. 115–121.

148. Fernández-Jiménez, A. and Puertas, F. (2003) 'Effect of activator mix on the hydration and strength behaviour of alkali-activated slag cements', *Advances in Cement Research*, 15(3), pp. 129–136. doi: 10.1680/adcr.2003.15.3.129.

149. Fernández-Jiménez, A., García-Lodeiro, I. and Palomo, A. (2007) 'Durability of alkali-activated fly ash cementitious materials', *Journal of Materials Science*, 42(9), pp. 3055–3065.

150. Fernández-Jiménez, A., Palomo, J. G. and Puertas, F. (1999) 'Alkali-activated slag mortars: Mechanical strength behaviour', *Cement and Concrete Research*, 29(8), pp. 1313–1321. doi: 10.1016/S0008-8846(99)00154-4.

151. Fernández-Jiménez, A., Puertas, F., Sobrados, I., and Sanz, J. (2003) 'Structure of calcium silicate hydrates formed in alkaline-activated slag: Influence of the type of alkaline activator', *Journal of the American Ceramic Society*, 86(8), pp. 1389–1394. doi: 10.1111/j.1151-2916.2003.tb03481.x.

152. Fernández-Jiménez, A., Vallepu, R., Terai, T., Palomo, A., Ikeda, K.: Synthesis and thermal behavior of different aluminosilicate gels. *J. Non-Cryst. Solids* 352 , 2061–2066 (2006).

153. Ferone, C., Liguori, B., Capasso, I., Colangelo, F., Cioffi, R., Cappelletto, E., and Di Maggio, R. (2015) 'Thermally treated clay sediments as geopolymer source material', *Applied Clay Science*, 107, pp. 195–204. doi: 10.1016/j.clay.2015.01.027.

154. Ferreira da Costa Gardolinski, J. (2005) 'Interlayer grafting and delamination of kaolinite'.

155. Figueiredo, R. L. and Pavía, S. (2017) 'Pozzolanic properties of bottom ash and fly ash from a waste incinerator plant', in *COINVEDI, IV International Congress on Construction and Building Research, Universidad de La Laguna. Tenerife, Eds. Escuela Politécnica Superior de Ingeniería y Arquitectura*.

156. Figueiredo, R. L. and Pavía, S. (2018) 'Activity Of Fly Ashes From Waste Incinerators And The Sugar Industry In Lime Mortars And PasteS', in *7th Euro-American Congress on Construction Pathology, Rehabilitation Technology and Heritage Management.*, pp. 1422 – 1433.

157. Figueiredo, R. L. and Pavía, S. (2020) 'A study of the parameters that determine the reactivity of sugarcane bagasse ashes (SCBA) for use as a binder in construction', *SN Applied Sciences*, 2(9), pp. 1–15.

158. Fisher, G. L., Prentice, B. A., Silberman, D., Ondov, J. M., Biermann, A. H., Ragaini, R. C., and McFarland, A. R. (1978) 'Physical and Morphological Studies of Size-Classified Coal Fly Ash', *Environmental Science and Technology*, pp. 447–451. doi: 10.1021/es60140a008.

159. Fu, Y., Cai, L. and Yonggen, W. (2011) 'Freeze-thaw cycle test and damage mechanics models of alkali-activated slag concrete', *Construction and Building Materials*, 25(7), pp. 3144–3148. doi: 10.1016/j.conbuildmat.2010.12.006.

160. Gao, K., Lin, K. L., Wang, D., Hwang, C. L., Shiu, H. S., Chang, Y. M., and Cheng, T. W. (2014) 'Effects SiO_2/Na_2O molar ratio on mechanical properties and the microstructure of nano-SiO2 metakaolin-based geopolymers', *Construction and Building Materials*, 53, pp. 503–510.

161. Garces, J. I. T., Dollente, I. J., Beltran, A. B., Tan, R. R., and Promentilla, M. A. B. (2021) 'Life cycle assessment of self-healing geopolymer concrete', *Cleaner Engineering and Technology*, 4, p. 100147.

162. García-Gusano, , D., Herrera, I., Garraín, D., Lechón, Y., and Cabal, H. (2015) 'Life cycle assessment of the Spanish cement industry: implementation of environmental-friendly solutions', *Clean Technologies and Environmental Policy*, 17(1), pp. 59–73.

163. García-Lodeiro, I., Fernández-Jiménez, A. and Palomo, A. (2013) 'Variation in hybrid cements over time. Alkaline activation of fly ash-portland cement blends', *Cement and Concrete Research*, 52, pp. 112–122. doi: 10.1016/j.cemconres.2013.03.022.

164. Garcia-Lodeiro, I., Palomo, A. and Fernández-Jiménez, A. (2015) 'Crucial insights on the mix design of alkali-activated cement-based binders', in *Handbook of alkali-activated cements, mortars and concretes*. Elsevier, pp. 49–73.

165. Gartner, E. (2004) 'Industrially interesting approaches to "low-CO₂" cements', *Cement and Concrete research*, 34(9), pp. 1489–1498.

166. Gava, G. P. and Prude, L. R. (2007) 'Pozzolanic activity tests as a measure of pozzolans ' performance . Part 1', *Magazine of Concrete Research*, 59(10), pp. 729–734. doi: 10.1680/macr.2007.59.10.729.

167. Gebregziabiher, B. S., Thomas, R. and Peethamparan, S. (2015) 'Very early-age reaction kinetics and

microstructural development in alkali-activated slag', *Cement and concrete composites*, 55, pp. 91–102.

168. George, S. and Sofi, A. (2017) 'Enhancement of fly ash concrete by hydrated lime and steel fibres', *Materials Today: Proceedings*, 4(9), pp. 9807–9811.

169. Georgitzikis, K., Mancini, L., d'Elia, E., and Vidal-Legaz, B. (2021). Sustainability aspects of Bauxite and Aluminium.

170. Gibbons, O. P. and Orr, J. J. (2020) *How to calculate embodied carbon*. Institution of Structural Engineers.

171. Glukhovsky, V. D. (1959) 'Soil silicates', *Gosstroyizdat, Kiev*, 154.

172. Glukhovsky, V. D., Rostovskaja, G. S. and Rumyna, G. V (1980) 'High strength slag-alkaline cements', *Proceedings of the seventh international congress on the chemistry of cement*, 3, pp. 164–168.

173. Glukhovsky, Y. D., Rostovskaja, G. S. and Rumyna, G. V (1980) 'High-strength Slag-Alkaline Cements', in *VHIth Int. Cong. Chem. Cem.* V-164-168, pp. 164–168.

174. Gong, C. and Yang, N. (2000) 'Effect of phosphate on the hydration of alkali-activated red mud-slag cementitious material', *Cement and Concrete Research*, 30(7), pp. 1013–1016. doi: 10.1016/S0008-8846(00)00260-X.

175. Görhan, G. and Kürklü, G. (2014) 'The influence of the NaOH solution on the properties of the fly ash-based geopolymer mortar cured at different temperatures', *Composites Part B: Engineering*, 58, pp. 371–377. doi: 10.1016/j.compositesb.2013.10.082.

176. Görhan, G., Aslaner, R. and Şinik, O. (2016) 'The effect of curing on the properties of metakaolin and fly ash-based geopolymer paste', *Composites Part B: Engineering*, 97, pp. 329–335. doi: 10.1016/j.compositesb.2016.05.019.

177. Gräfe, M., Power, G. and Klauber, C. (2011) 'Bauxite residue issues: III. Alkalinity and associated chemistry', *Hydrometallurgy*, 108(1–2), pp. 60–79. doi: 10.1016/j.hydromet.2011.02.004.

178. Grapes, R. H. (2006) 'Anthropogenic Pyrometamorphism', *Pyrometamorphism*, pp. 191–218.

179. Ha, T. H., Muralidharan, S., Bae, J. H., Ha, Y. C., Lee, H. G., Park, K. W., and Kim, D. K. (2005) 'Effect of unburnt carbon on the corrosion performance of fly ash cement mortar', *Construction and Building Materials*, 19(7), pp. 509–515. doi: 10.1016/j.conbuildmat.2005.01.005.

180. Habert, G., D'Espinose De Lacaillerie, J. B. and Roussel, N. (2011) 'An environmental evaluation of geopolymer based concrete production: Reviewing current research trends', *Journal of Cleaner Production*, 19(11), pp. 1229–1238. doi: 10.1016/j.jclepro.2011.03.012.

181. Habert, G., D'Espinose de Lacaillerie, J. B., Lanta, E., and Roussel, N. (2010) 'Environmental evaluation for cement substitution with geopolymers', *2nd International Conference on Sustainable Construction Materials and Technologies*, pp. 1607–1615.

182. Hadjiivanov, K. (2014) 'Identification and characterization of surface hydroxyl groups by infrared spectroscopy', in *Advances in Catalysis*. Elsevier, pp. 99–318.

183. Hairi, S. N. M., Jameson, G. N., Rogers, J. J., and MacKenzie, K. J. (2015) 'Synthesis and properties of inorganic polymers (geopolymers) derived from Bayer process residue (red mud) and bauxite', *Journal of materials science*, 50(23), pp. 7713–7724.

184. Hajjaji, W., Andrejkovičová, S., Zanelli, C., Alshaaer, M., Dondi, M., Labrincha, J. A., and Rocha, F. (2013) 'Composition and technological properties of geopolymers based on metakaolin and red mud',

Materials and Design (1980-2015), 52, pp. 648–654.

185. Häkkinen, T. (1993) 'The influence of slag content on the microstructure, permeability and mechanical properties of concrete Part 1 Microstructural studies and basic mechanical properties', *Cement and Concrete Research*, 23(2), pp. 407–421. doi: 10.1016/0008-8846(93)90106-J.

186. Hameed, A. M., Rawdhan, R. R. and Al-Mishhadani, S. A. (2017) 'Effect of various factors on the manufacturing of geopolymer mortar', *Archives of Science*, 1(3), pp. 1–8.

187. Hammond, G. and Jones, C. (2011) 'Embodied Carbon: The Inventory of Carbon and Energy (ICE)', *A BSRIA Guide*, p. 136. Available at: http://www.ihsti.com/tempimg/57c152b-ENVIRO2042201160372.pdf%0Awww.bath.ac.uk/mech-eng/sert/embodied%0A.

188. Hardjito, D., Cheak, C. C., and Ing, C. L. (2008) 'Strength and Setting Times of Low Calcium Fly Ash-based Geopolymer Mortar Strength and Setting Times of Low Calcium Fly Ash-based Geopolymer Mortar', (May 2014), pp. 2–11. doi: 10.5539/mas.v2n4p3.

189. He, J., Jie, Y., Zhang, J., Yu, Y., and Zhang, G. (2013) 'Synthesis and characterization of red mud and rice husk ash-based geopolymer composites', *Cement and Concrete Composites*, 37(1), pp. 108–118. doi: 10.1016/j.cemconcomp.2012.11.010.

190. He, P., Wang, M., Fu, S., Jia, D., Yan, S., Yuan, J., and Zhou, Y. (2016) 'Effects of Si/Al ratio on the structure and properties of metakaolin based geopolymer', *Ceramics International*, 42(13), pp. 14416–14422. doi: 10.1016/j.ceramint.2016.06.033.

191. Heah, C. Y., Kamarudin, H., Al Bakri, A. M., Binhussain, M., Luqman, M., Nizar, I. K.,and Liew, Y. M. (2011) 'Effect of curing profile on kaolin-based geopolymers', *Physics Procedia*, 22, pp. 305–311.

192. Heah, C. Y., Kamarudin, H., Al Bakri, A. M., Bnhussain, M., Luqman, M., Nizar, I. K., and Liew, Y. M. (2012) 'Study on solids-to-liquid and alkaline activator ratios on kaolin-based geopolymers', *Construction and Building Materials*, 35, pp. 912–922. doi: 10.1016/j.conbuildmat.2012.04.102.

193. Heller-Kallai, L. (2006) 'thermally modified clay minerals', *Developments in clay science*, 1, pp. 289–308.

194. Helmuth, R. (1987) *Fly ash in cement and concrete*.

195. Hemmings, R. T. and Berry, E. E. (1987) 'On the glass in coal fly ashes: recent advances', *MRS Online Proceedings Library Archive*, 113.

196. Henseler, J., Ringle, C. M. and Sinkovics, R. R. (2009) 'The use of partial least squares path modeling in international marketing', in *New challenges to international marketing*. Emerald Group Publishing Limited.

197. Hepworth, N. and Goulden, M. (2008) 'Climate change in Uganda: Understanding the implications and appraising the response.'

198. Hewlett, Peter, and M. L. (2019) *Lea's chemistry of cement and concrete 5th edition*.

199. Higgins, D. D. (2003) 'Increased sulfate resistance of ggbs concrete in the presence of carbonate', *Cement and Concrete Composites*, 25(8), pp. 913–919. doi: 10.1016/S0958-9465(03)00148-3.

200. Hind, A. R., Bhargava, S. K. and Grocott, S. C. (1999) 'The surface chemistry of Bayer process solids: A review', *Colloids and Surfaces A: Physicochemical and Engineering Aspects*, 146(1–3), pp. 359–374. doi: 10.1016/S0927-7757(98)00798-5.

201. Hogan, F. J. (1982) 'Ground Granulated Blast Furnace Slag as a Cementitious Material', *Process*

Mineralogy II: Applications in Metallurgy, Ceramics and Geology, pp. 299–316.

202. Huang, C. H., Lin, S. K., Chang, C. S., and Chen, H. J. (2013) 'Mix proportions and mechanical properties of concrete containing very high-volume of Class F fly ash', *Construction and Building Materials*, 46, pp. 71–78.

203. Hughes, D. C. (1985) 'Sulphate resistance of OPC, OPC/fly ash and SRPC pastes: pore structure and permeability', *Cement and Concrete Research*, 15(6), pp. 1003–1012.

204. Hurt, R. H. and Gibbins, J. R. (1995) 'Residual carbon from pulverized coal fired boilers: 1. Size distribution and combustion reactivity', *Fuel*, 74(4), pp. 471–480.

205. Husaini, H., Cahyono, S. S. and Damayanti, R. (2014) 'UPGRADING OF TAYAN'S CRUDE BAUXITE USING ROTARY DRUM SCRUBBER', *Indonesian Mining Journal*, 17(1), pp. 40–52.

206. Huseien, G. F., Mirza, J., Ismail, M., Hussin, M. W., Arrifin, M. A. M., and Hussein, A. (2016) 'The Effect of Sodium Hydroxide Molarity and Other Parameters on Water Absorption of Geopolymer Mortars', *Indian Journal of Science and Technology*, 9(48). doi: 10.17485/ijst/2016/v9i48/109629.

207. Hwang, C. L. and Huynh, T. P. (2017) 'Characteristics of alkali-activated controlled low-strength material derived from red mud-slag blends', *Key Engineering Materials*, 753 KEM, pp. 343–348. doi: 10.4028/www.scientific.net/KEM.753.343.

208. ICE (2014) *Embodied Carbon-Inventory of Carbon and Energy (ICE)*. Available at: https://greenbuildingencyclopaedia.uk/wp-content/ uploads/2014/07/Full-BSRIA-ICE-guide.pdf.

209. Igwegbe, C. A., Mohmmadi, L., Ahmadi, S., Rahdar, A., Khadkhodaiy, D., Dehghani, R., and Rahdar, S. (2019) 'Modeling of adsorption of methylene blue dye on Ho-CaWO4 nanoparticles using response surface methodology (RSM) and artificial neural network (ANN) techniques', *MethodsX*, 6, pp. 1779–1797.

210. Ismail, K. N., Hussin, K., and Idris, M. S. (2007) *PHYSICAL, CHEMICAL and MINERALOGICAL PROPERTIES OF FLY ASH*, *Journal of Nuclear and Related Technology*.

211. Jianyong, L. and Yan, Y. (2001) 'A study on creep and drying shrinkage of high performance concrete', *Cement and Concrete Research*, 31(January), pp. 1203–1206. Available at: https://ac.els-cdn.com/S0008884601005397/1-s2.0-S0008884601005397-main.pdf?_tid=9d77eb64-c0ae-4fe0-8b6f-325f9c8aaf33andacdnat=1547563118_1c84bba24c4cb24958b857628d2f1f0c.

212. Jin, M., Zheng, Z., Sun, Y., Chen, L. and Jin, Z. (2016) 'Resistance of metakaolin-MSWI fly ash based geopolymer to acid and alkaline environments', *Journal of Non-Crystalline Solids*. Elsevier, 450, pp. 116–122.

213. Jones, R., McCarthy, M. and Newlands, M. (2011) 'Fly ash route to low embodied CO2 and implications for concrete construction', in *World of Coal Ash Conference, Denver, Colorado, USA*.

214. Juarez, R. I. C. and Finnegan, S. (2021) 'The environmental impact of cement production in Europe: A holistic review of existing EPDs', *Cleaner Environmental Systems*, 3, p. 100053.

215. Kalaw, M. E., Culaba, A., Hinode, H., Kurniawan, W., Gallardo, S., and Promentilla, M. A. (2016) 'Optimizing and characterizing geopolymers from ternary blend of philippine coal fly ash, coal bottom ash and rice hull ash', *Materials*. doi: 10.3390/MA9070580.

216. Kani, E. N. and Allahverdi, A. (2009) 'Effect of chemical composition on basic engineering properties of inorganic polymeric binder based on natural pozzolan', *Ceramics-Silikaty*, 53(3), pp. 195–204.

217. Karakoc, M. B., Türkmen, İ., Maraş, M. M., Kantarci, F., and Demirboğa, R. (2016) 'Sulfate resistance of ferrochrome slag based geopolymer concrete', *Ceramics International*, 42(1), pp. 1254–1260.

218. Kassa, A. E., Shibeshi, N. T., Tizazu, B. Z. and Prabhu, S. V. (2022) 'Characteristic investigations on Ethiopian kaolinite: effect of calcination temperature on pozzolanic activity and specific surface area', *Advances in Materials Science and Engineering*. Hindawi, 2022.

219. Ke, X., Bernal, S. A., Ye, N., Provis, J. L., and Yang, J. (2015) 'One-part geopolymers based on thermally treated red Mud/NaOH blends', *Journal of the American Ceramic Society*, 98(1), pp. 5–11. doi: 10.1111/jace.13231.

220. Keyte, L. M. (2009) 'Fly ash glass chemistry and inorganic polymer cements', in *Geopolymers*. Elsevier, pp. 15–36.

221. Khairul Nizar, I., Al Bakri, A. M., Abd Razak, R., Kamarudin, H., Abdullah, A., and Zarina, Y. (2014) 'Study on physical and chemical properties of fly ash from different area in Malaysia', *Key Engineering Materials*, pp. 985–989. doi: 10.4028/www.scientific.net/KEM.594-595.985.

222. Khairul, M. A., Zanganeh, J. and Moghtaderi, B. (2019) 'The composition, recycling and utilisation of Bayer red mud', *Resources, Conservation and Recycling*, 141, pp. 483–498. doi: 10.1016/j.resconrec.2018.11.006.

223. Khale, D. and Chaudhary, R. (2007) 'Mechanism of geopolymerization and factors influencing its development: A review', *Journal of Materials Science*, 42(3), pp. 729–746. doi: 10.1007/s10853-006-0401-4.

224. Kim, S. (2014) 'Engineering Sustainability of Mechanical Recycling of Carbon Fiber Composite Materials', p. 6. Available at: https://pdfs.semanticscholar.org/d163/547ee734c6ad16afd4fa8f6b33b899ae9af2.pdf.

225. Kishar, E., Ahmed, D. and Nabil, N. (2018) 'Geopolymer Cement Based on Alkali Activated Slag', *Journal of Scientific Research in Science*, 34(part1), pp. 538–552. doi: 10.21608/jsrs.2018.14709.

226. Klauber, C., Gräfe, M. and Power, G. (2011) 'Bauxite residue issues: II. options for residue utilization', *Hydrometallurgy*, 108(1–2), pp. 11–32. doi: 10.1016/j.hydromet.2011.02.007.

227. Kloprogge, J. T, H.D.Ruan and R.L.Frost (2002) 'THERMAL DECOMPOSITION OF BAUXITE MINERALS: INFRARED EMISSION SPECTROSCOPY OF GIBBSITE, BOEHMITE AND DIASPORE', *Journal of Materials Science*, 37(6), pp. 1121–1129. Available at: https://www.researchgate.net/publication/27463539%0AThermal.

228. Kloprogge, J. T. (2019) *Spectroscopic methods in the study of kaolin minerals and their modifications*. Springer.

229. Komnitsas, K. and Zaharaki, D. (2007) 'Geopolymerisation: A review and prospects for the minerals industry', *Minerals Engineering*, 20(14), pp. 1261–1277. doi: 10.1016/j.mineng.2007.07.011.

230. Krivenko, P. V (1994) 'Influence of physico-chemical aspects of early history of a slag alkaline cement stone on stability of its properties', in *1st International Conference on Reinforced Concrete Materials in Hot Climates*.

231. Krizan, D. and Zivanovic, B. (2002) 'Effects of dosage and modulus of water glass on early hydration of alkali–slag cements', *Cement and Concrete Research*, 32(8), pp. 1181–1188.

232. Kuenzel, C. and Ranjbar, N. (2019) 'Dissolution mechanism of fly ash to quantify the reactive

aluminosilicates in geopolymerisation', *Resources, Conservation and Recycling*, 150, p. 104421.

233. Kuhl, H. (1908) 'Slag Cement and Process of Making the Same. United States Patent Office; Patent No. 900,939'.

234. Kukko, H. and Mannonen, R. (1982) 'Chemical and mechanical properties of alkali-activated blast furnace slag (F-concrete)', *Nordic Concrete Research*, (1).

235. Kulkarni, S. (2018) 'Experimental Study on Red Mud , Fly Ash and GGBFS based Geopolymer Concrete', *International Journal of Engineering Research and Technology (IJERT)*, 7(2278–0181), pp. 107–111.

236. Kumar, A. and Kumar, S. (2013) 'Development of paving blocks from synergistic use of red mud and fly ash using geopolymerization', *Construction and Building Materials*, 38, pp. 865–871. doi: 10.1016/j.conbuildmat.2012.09.013.

237. Kumar, A., Saravanan, T. J., Bisht, K., and Kabeer, K. S. A. (2021) 'A review on the utilization of red mud for the production of geopolymer and alkali activated concrete', *Construction and Building Materials*, 302, p. 124170.

238. Kumar, B. S. C. and Ramesh, K. (2017) 'Experimental study on metakaolin and GGBS based geopolymer concrete', *International Journal of Engineering and Technology*, 9(2), pp. 341–349.

239. Kumar, C., Yaragal, S. C. and Das, B. B. (2020) 'Ferrochrome ash–Its usage potential in alkali activated slag mortars', *Journal of Cleaner Production*, 257, p. 120577.

240. Kumar, S., Kumar, R. and Bandopadhyay, A. (2006) 'Innovative methodologies for the utilisation of wastes from metallurgical and allied industries', *Resources, Conservation and Recycling*, pp. 301–314. doi: 10.1016/j.resconrec.2006.03.003.

241. Kyritsis, K., Meller, N. and Hall, C. (2009) 'Chemistry and Morphology of Hydrogarnets Formed in Cement-Based CASH Hydroceramics Cured at 200° to 350° C', *Journal of the American Ceramic Society*, 92(5), pp. 1105–1111.

242. Lagauche, M., Larmier, K., Jolimaître, E., Barthelet, K., Chizallet, C., Favergeon, L., and Pijolat, M. (2017) 'Thermodynamic characterization of the hydroxyl group on the γ-alumina surface by the energy distribution function', *The Journal of Physical Chemistry C*, 121(31), pp. 16770–16782.

243. Lawrence, C. and Hewlett, P. C. (1988) 'Lea's chemistry of cement and concrete', *Cap 9: Production of Low-Energy Cements*.

244. Lăzărescu, A., Mircea, C., Szilagyi, H., and Baeră, C. (2019) 'Mechanical properties of alkali activated geopolymer paste using different Romanian fly ash sources - Experimental results', *MATEC Web of Conferences*, 289. doi: 10.1051/matecconf/201928911001.

245. Le, V. Q., Do, M. Q., Hoang, M. D., Pham, V. T. H. Q., Bui, T. H., and Nguyen, H. T. (2018) 'Effect of alkaline activators to engineering properties of geopolymer-based materials synthesized from red mud', in *Key Engineering Materials*, pp. 508–512. doi: 10.4028/www.scientific.net/KEM.777.508.

246. Lecomte, I., Henrist, C., Liégeois, M., Maseri, F., Rulmont, A., and Cloots, R. (2006) '(Micro)-structural comparison between geopolymers, alkali-activated slag cement and Portland cement', *Journal of the European Ceramic Society*, 26(16), pp. 3789–3797.

247. Lee, N. K., Kim, E. M. and Lee, H. K. (2016) 'Mechanical properties and setting characteristics of geopolymer mortar using styrene-butadiene (SB) latex', *Construction and Building Materials*, 113, pp.

264–272. doi: 10.1016/j.conbuildmat.2016.03.055.

248. Lesik, S. A. (2018) *Applied statistical inference with MINITAB®*. Chapman and Hall/CRC.

249. Li, C., Sun, H. and Li, L. (2010) 'A review: The comparison between alkali-activated slag (Si + Ca) and metakaolin (Si + Al) cements', *Cement and Concrete Research*, 40(9), pp. 1341–1349. doi: 10.1016/j.cemconres.2010.03.020.

250. Li, G. and Wu, X. (2005) 'Influence of fly ash and its mean particle size on certain engineering properties of cement composite mortars', *Cement and Concrete Research*, 35(6), pp. 1128–1134. doi: 10.1016/j.cemconres.2004.08.014.

251. Liang, X. and Ji, Y. (2021) 'Mechanical properties and permeability of red mud-blast furnace slag-based geopolymer concrete', *SN Applied Sciences*, 3(1). doi: 10.1007/s42452-020-03985-4.

252. Liew, Y. M., Heah, C. Y., and Kamarudin, H. (2016) 'Structure and properties of clay-based geopolymer cements: A review', *Progress in Materials Science*, 83, pp. 595–629. doi: 10.1016/j.pmatsci.2016.08.002.

253. Liew, Y. M., Hussin, K., Al Bakri Abdullah, M. M., Binhussain, M., Musa, L., Khairul Nizar, I., and Heah, C. Y. (2013) 'Effect of curing regimes on metakaolin geopolymer pastes produced from geopolymer powder', in *Advanced Materials Research*. Trans Tech Publ, pp. 931–936.

254. Liew, Y. M., Kamarudin, H., Al Bakri, A. M., Bnhussain, M., Luqman, M., Nizar, I. K., and Heah, C. Y. (2012) 'Optimization of solids-to-liquid and alkali activator ratios of calcined kaolin geopolymeric powder', *Construction and Building Materials*, 37, pp. 440–451. doi: 10.1016/j.conbuildmat.2012.07.075.

255. Lin, C., Dai, W., Li, Z., and Sha, F. (2020) 'Performance and microstructure of alkali-activated red mud-based grouting materials under class F fly ash amendment', *Indian Geotechnical Journal*, 50(6), pp. 1048–1056.

256. Liu, W., Yang, J. and Xiao, B. (2009) 'Review on treatment and utilization of bauxite residues in China', *International Journal of Mineral Processing*, 93(3–4), pp. 220–231. doi: 10.1016/j.minpro.2009.08.005.

257. Liu, X., Zhang, N., Sun, H., Zhang, J., and Li, L. (2011) 'Structural investigation relating to the cementitious activity of bauxite residue - Red mud', *Cement and Concrete Research*, 41(8), pp. 847–853. doi: 10.1016/j.cemconres.2011.04.004.

258. Livi, C. N. and Repette, W. L. (2017) 'Effect of NaOH concentration and curing regime on geopolymer', *Revista IBRACON de Estruturas e Materiais*, 10, pp. 1174–1181.

259. LLC (2005) *Minitab*.

260. Lloyd, R. R., Provis, J. L. and Van Deventer, J. S. J. (2010) 'Pore solution composition and alkali diffusion in inorganic polymer cement', *Cement and Concrete Research*, 40(9), pp. 1386–1392.

261. Lolli, F. and Kurtis, K. E. (2021) 'Life Cycle Assessment of alkali activated materials: preliminary investigation for pavement applications', *RILEM Technical Letters*, 6, pp. 124–130.

262. Long, W. J., Wei, J. J., Gu, Y. C., and Xing, F. (2017) 'Research on dynamic mechanical properties of alkali activated slag concrete under temperature-loads coupling effects', *Construction and Building Materials*, 154, pp. 687–696.

263. Luga, E. (2015) 'Properties of fly ash and blast furnace slag geopolymer mortars'. Phd Thesis, Institute of Science, Erciyes University. https://tez. yok. gov .

264. Luxan, M. P. de, Madruga, F. and Saavedra, J. (1989) 'Rapid evaluation of pozzolanic activity of natural products by conductivity measurement', *Cement and concrete research*, 19(1), pp. 63–68.

265. Ma'aden (2014) *Delivering Results Responsibly, Ma'aden Annual Report*.

266. Ma'aden (2017) *Delivering Results Responsibly, Ma'aden Annual Report*.

267. Malki, A., Mekhalif, Z., Detriche, S., Fonder, G., Boumaza, A., and Djelloul, A. (2014) 'Calcination products of gibbsite studied by X-ray diffraction, XPS and solid-state NMR', *Journal of Solid State Chemistry*, 215, pp. 8–15.

268. Mallikarjuna Rao, G. and Gunneswara Rao, T. D. (2015) 'Final Setting Time and Compressive Strength of Fly Ash and GGBS-Based Geopolymer Paste and Mortar', *Arabian Journal for Science and Engineering*, 40(11), pp. 3067–3074. doi: 10.1007/s13369-015-1757-z.

269. Manfroi, E. P., Cheriaf, M. and Rocha, J. C. (2014) 'Microstructure, mineralogy and environmental evaluation of cementitious composites produced with red mud waste', *Construction and Building Materials*, 67, pp. 29–36. doi: 10.1016/j.conbuildmat.2013.10.031.

270. Manjunatha, G. S., Radhakrishna, Venugopal, K., and Maruthi, S. V. (2014) 'Strength characteristics of open air cured geopolymer concrete', *Transactions of the indian ceramic society*, 73(2), pp. 149–156.

271. Marchand, J., Odler, I. and Skalny, J. P. (2001) *Sulfate attack on concrete*. CRC Press.

272. Martín-Garrido, M., Teresa Molina-Delgado, M. and Martínez-Ramírez, S. (2020) 'A comparison between experimental and theoretical Ca/Si ratios in C–S–H and C–S (A)–H gels', *Journal of Sol-Gel Science and Technology*, 94(1), pp. 11–21.

273. Marvila, M. T., Azevedo, A. R. G. de and Vieira, C. M. F. (2021) 'Reaction mechanisms of alkali-activated materials', *Revista IBRACON de Estruturas e Materiais*, 14(3). doi: 10.1590/s1983-41952021000300009.

274. Marvila, M. T., de Azevedo, A. R. G., de Oliveira, L. B., de Castro Xavier, G., and Vieira, C. M. F. (2021) 'Mechanical, physical and durability properties of activated alkali cement based on blast furnace slag as a function of %Na_2O', *Case Studies in Construction Materials*, 15(October), p. e00723. doi: 10.1016/j.cscm.2021.e00723

275. Massazza, F. (1998) 'Pozzolana and pozzolanic cements', *Lea's chemistry of cement and concrete*, 4, pp. 471–631.

276. Massazza, F. (2002) 'Properties and applications of natural pozzolanas', *Structure and performance of cements*, pp. 326–352.

277. Massazza, F. (2007) *Pozzolana and pozzolanic cements.-Lea's chemistry of cement and concrete, Fourth Edi. Lea's Chem Cem Concr.* B978-0-7506-6256-7.50022-9.2007.

278. Matheu, P. S., Ellis, K. and Varela, B. (2015) 'Comparing the environmental impacts of alkali activated mortar and traditional portland cement mortar using life cycle assessment', in *IOP Conference Series: Materials Science and Engineering*. IOP Publishing, p. 12080.

279. Mathew, B. J., Sudhakar, M. and Natarajan, C. (2013) 'Strength , Economic and Sustainability Characteristics of Coal Ash – GGBS Based Geopolymer Concrete', *International Journal Of Computational Engineering Research*, pp. 207–212.

280. Mathews, P. G. (2005) 'Design of Experiments with MINITAB', *The American Statistician*, 60(2), p. 521. Available at: http://qualitypress.asq.org.

281. Medri, V., Fabbri, S., Dedecek, J., Sobalik, Z., Tvaruzkova, Z., and Vaccari, A. (2010) 'Role of the morphology and the dehydroxylation of metakaolins on geopolymerization', *Applied Clay Science*, 50(4), pp. 538–545

282. Mehta, P. K. (1977) 'Properties of blended cements made from rice husk ash', in *Journal Proceedings*, pp. 440–442.

283. Mellado, A., Catalán, C., Bouzón, N., Borrachero, M. V., Monzó, J. M., and Payá, J. (2014) 'Carbon footprint of geopolymeric mortar: study of the contribution of the alkaline activating solution and assessment of an alternative route', *RSC advances*, 4(45), pp. 23846–23852

284. Memon , F. A., Nuruddin, M. F., Khan, S., Shafiq, N. A. S. I. R., and Ayub, T. (2013) 'Effect of sodium hydroxide concentration on fresh properties and compressive strength of self-compacting geopolymer concrete', *Journal of Engineering Science and Technology*, pp. 44–56.

285. Metz, B., Davidson, O., De Coninck, H. C., Loos, M., and Meyer, L. (2005) *IPCC special report on carbon dioxide capture and storage*. Cambridge: Cambridge University Press.

286. Minnick, L. J., Webster, W. C. and Purdy, E. J. (1971) 'Predictions of the effect of fly ash in Portland cement mortar and concrete', *Journal of Materials*.

287. Miraki, H., Shariatmadari, N., Ghadir, P., Jahandari, S., Tao, Z., and Siddique, R. (2022) 'Clayey soil stabilization using alkali-activated volcanic ash and slag', *Journal of Rock Mechanics and Geotechnical Engineering*, 14(2), pp. 576–591.

288. Mishra, B. and Gostu, S. (2017) 'Materials sustainability for environment: Red-mud treatment', *Frontiers of Chemical Science and Engineering*, 11(3), pp. 483–496. doi: 10.1007/s11705-017-1653-z.

289. Mohd Mortar, N. A., Abdullah, M. M. A. B., Abdul Razak, R., Abd Rahim, S. Z., Aziz, I. H., Nabiałek, M., Jaya, R. P., Semenescu, A., Mohamed, R. and Ghazali, M. F. (2022) 'Geopolymer Ceramic Application: A Review on Mix Design, Properties and Reinforcement Enhancement', *Materials*. MDPI, 15(21), p. 7567.

290. Montgomery, D. C. (2017) *Design and analysis of experiments*. John wiley and sons.

291. Moore, D. S. and Kirkland, S. (2007) *The basic practice of statistics*. WH Freeman New York.

292. Moranville-Regourd, M. (1998) 'Cements made from blastfurnace slag', *Lea's chemistry of cement and concrete*, 4, pp. 633–674.

293. MRPI (2013) *Environmental Product Declaration for Ecocem GGBS cement, in accordance with EN 15804 "Sustainability of construction works - Environmental product declarations - Core rules for the product category of construction products"*, *MRPI (milieu relevante product informatie)*. Available at: https://www.igbc.ie/wp-content/uploads/2017/09/MRPI-certificate-EPD-Ecocem-GGBS.pdf.

294. Mudgal, M., Singh, A., Chouhan, R. K., Acharya, A., and Srivastava, A. K. (2021) 'Fly ash red mud geopolymer with improved mechanical strength', *Cleaner Engineering and Technology*, 4(August 2020), p. 100215. doi: 10.1016/j.clet.2021.100215.

295. Mujabar, P. S. and Dajkumar, S. (2019) 'Mapping of bauxite mineral deposits in the northern region of Saudi Arabia by using Advanced Spaceborne Thermal Emission and Reflection radiometer satellite data', *Geo-spatial Information Science*, 22(1), pp. 35–44.

296. Mukiza, E., Zhang, L., Liu, X., and Zhang, N. (2019) 'Utilization of red mud in road base and subgrade materials: A review', *Resources, Conservation and Recycling*, pp. 187–199. doi:

10.1016/j.resconrec.2018.10.031.

297. Muraleedharan, M. and Nadir, Y. (2021) 'Factors affecting the mechanical properties and microstructure of geopolymers from red mud and granite waste powder: A review', *Ceramics International*, 47(10), pp. 13257–13279.

298. Mustafa Al Bakri Abdullah, M. M., Kamarudin, H., Ismail, K. N., Bnhussain, M., Zarina, Y., and Rafiza, A. R. ((2012) 'Correlation between Na2SiO3/NaOH ratio and fly ash/alkaline activator ratio to the strength of geopolymer', *Advanced Materials Research*, 341–342, pp. 189–193. doi: 10.4028/www.scientific.net/AMR.341-342.189.

299. Mustafa Al Bakria, Kamarudin, H., Bin Hussain, M., Nizar, I. K., Zarina, Y., and Rafiza, A. R. (2011) 'The effect of curing temperature on physical and chemical properties of geopolymers', *Physics Procedia*, 22, pp. 286–291. doi: 10.1016/j.phpro.2011.11.045.

300. Mustafa, M. M., Al-Bassam, K. S. and Al-Ani, T. M. (2019) 'KARST BAUXITE DEPOSITS OF NORTH HUSSAINIYAT AREA, WESTERN DESERT, IRAQ: AN OVERVIEW', *Iraqi Bulletin of Geology and Mining*, (8), pp. 125–146.

301. Mustofa, M. and Pintowantoro, S. (2017) 'The Effect of Si/Al Ratio to Compressive Strength and Water Absorption of Ferronickel Slag-based Geopolymer', *IPTEK Journal of Proceedings Series*, p. 167. doi: 10.12962/j23546026.y2017i2.2334.

302. Najafi Kani, E. and Allahverdi, A. (2009) 'Effects of curing time and temperature on strength development of inorganic polymeric binder based on natural pozzolan', *Journal of Materials science*, 44(12), pp. 3088–3097.

303. Najafi Kani, E., Allahverdi, A. and Provis, J. L. (2012) 'Efflorescence control in geopolymer binders based on natural pozzolan', *Cement and Concrete Composites*, pp. 25–33. doi: 10.1016/j.cemconcomp.2011.07.007.

304. Narayanan, A., Toropov, V. V., Wood, A. S., and Campean, I. F. (2007) 'Simultaneous model building and validation with uniform designs of experiments', *Engineering Optimization*, 39(5), pp. 497–512. doi: 10.1080/03052150701399978.

305. Nasr, D., Pakshir, A. H. and Ghayour, H. (2018) 'The influence of curing conditions and alkaline activator concentration on elevated temperature behavior of alkali activated slag (AAS) mortars', *Construction and Building Materials*, 190, pp. 108–119.

306. Nath, P. and Sarker, P. K. (2014) 'Effect of GGBFS on setting, workability and early strength properties of fly ash geopolymer concrete cured in ambient condition', *Construction and Building materials*, 66, pp. 163–171.

307. NBR 15895 (2010) 'Método Chapelle Materiais pozolânico - Determinagáo do teor modificado de hidróxido de cálcio fixado.', *Associação Brasileira de Normas Técnicas*, p. 209.

308. Nejat, P., Jomehzadeh, F., Taheri, M. M., Gohari, M., and Majid, M. Z. A. (2015) 'A global review of energy consumption, CO_2 emissions and policy in the residential sector (with an overview of the top ten CO_2 emitting countries)', *Renewable and sustainable energy reviews*, 43, pp. 843–862.

309. Nematollahi, B. and Sanjayan, J. (2014) 'Efficacy of Available Superplasticizers on Geopolymers Efficacy of Available Superplasticizers on Geopolymers', (June). doi: 10.19026/rjaset.7.420.

310. Newton, I. (2014). *Minitab cookbook*. Packt Publishing Ltd.

311. Ngo, S. H., Huynh, T. P., Le, T. T. T., and Mai, N. H. T. (2018) 'Effect of high loss on ignition-fly ash on properties of concrete fully immersed in sulfate solution', in *IOP conference series: materials science and engineering*. IOP Publishing, p. 12007.

312. Nmiri, A., Hamdi, N., Yazoghli-Marzouk, O., Duc, M., and Srasra, E. (2017) 'Synthesis and characterization of kaolinite-based geopolymer: Alkaline activation effect on calcined kaolinitic clay at different temperatures', *J. Mater. Environ. Sci*, 8(2), pp. 276–290.

313. Norgate, T. and Haque, N. (2010) 'Energy and greenhouse gas impacts of mining and mineral processing operations', *Journal of Cleaner Production*, 18(3), pp. 266–274. doi: 10.1016/j.jclepro.2009.09.020.

314. Novak, C., Pokol, G., Izvekov, V., and Gal, T. (1990) 'Studies on the reactions of aluminium oxides and hydroxides', *Journal of thermal analysis*, 36(5), pp. 1895–1909.

315. Ollivier, J. P., Maso, J. C. and Bourdette, B. (1995) 'Interfacial transition zone in concrete', *Advanced cement based materials*, 2(1), pp. 30–38.

316. Osborn, E. F., Roeder, P. L. and Ulmer, G. C. (1969) 'Part I—Phase equilibria at solidus temperatures in the quaternary system CaO-MgO-Al2O3-SiO2 and their bearing on optimun composition of blast furnace slag and on slag properties', *Bulletin of the Earth and Mineral Sciences Experiment Station; The Pennsylvania State University: State College, PA, USA*.

317. Ostwal, T. and Chitawadagi, M. V (2014) 'Experimental investigations on strength, durability, sustainability and economic characteristics of geopolymer concrete blocks', *International Journal of Research in Engineering and Technology*, 3(6), pp. 115–122.

318. Ouellet-Plamondon, C. and Habert, G. (2015) 'Life cycle assessment (LCA) of alkali-activated cements and concretes', in *Handbook of alkali-activated cements, mortars and concretes*. Elsevier, pp. 663–686.

319. Pacheco-Torgal, F. and Jalali, S. (2010) 'Influence of sodium carbonate addition on the thermal reactivity of tungsten mine waste mud based binders', *Construction and Building Materials*, 24(1), pp. 56–60.

320. Pacheco-Torgal, F., Castro-Gomes, J. and Jalali, S. (2008) 'Alkali-activated binders: A review. Part 1. Historical background, terminology, reaction mechanisms and hydration products', *Construction and Building Materials*, 22(7), pp. 1305–1314. doi: 10.1016/j.conbuildmat.2007.10.015.

321. Pacheco-Torgal, Fernando (2014) 'Handbook of Alkali-Activated Cements, Mortars and Concretes', *Handbook of Alkali-Activated Cements, Mortars and Concretes*, pp. 1–830. doi: 10.1016/C2013-0-16511-7.

322. Pacheco-Torgal, Fernando, Labrincha, J., Leonelli, C., Palomo, A., and Chindaprasit, P. (2014) *Handbook of alkali-activated cements, mortars and concretes*. Elsevier.

323. Paglia, G., Buckley, C. E., Rohl, A. L., Hart, R. D., Winter, K., Studer, A. J., and Hanna, J. V. (2004) 'Boehmite Derived γ-Alumina System. 1. Structural Evolution with Temperature, with the Identification and Structural Determination of a New Transition Phase, γ′-Alumina', *Chemistry of Materials*, 16(2), pp. 220–236. doi: 10.1021/cm034917j.

324. Palomo, A., Alonso, S., Fernández-Jiménez, A., Sobrados, I., Sanz, J.: Alkaline activation of fly ashes: NMR study of the reaction products. *J. Am. Ceram. Soc.* 87 (6), 1141–1145 (2004).

325. Palomo, A., M. Grutzeck, and M. B. (1999) 'Alkali-activated fly ashes: a cement for the future. Cement and concrete research', *Cement and Concrete Research*, 29(8):, pp. 1323-1329.

326. Pan, Z. H., Feng, Y., & Yang, N. R. (1998) 'Solid alkali-slag-red mud cementitious material', *J. Nanjing*

Univ. Chem. Technol, 20(2), pp. 34–38.

327. Pan, Z., Fang, Y. and Zhao, C. (1999) 'Research on alkali activated slag-red mud cement preparation', *Bull. Chin. Ceram. Soc*, 18(3), pp. 34–39.

328. Pan, Z., Li, D., Yu, J., and Yang, N. (2003) 'Properties and microstructure of the hardened alkali-activated red mud-slag cementitious material', *Cement and Concrete Research*, 33(9), pp. 1437–1441. doi: 10.1016/S0008-8846(03)00093-0.

329. Passaglia, E. and Rinaldi, R. (1984) 'Katoite, a new member of the Ca_3Al_2 (SiO_4) $_3$-Ca_3Al_2 (OH) $_{12}$ series and a new nomenclature for the hydrogrossular group of minerals', *Bulletin de Minéralogie*, 107(5), pp. 605–618.

330. Patankar, S. V and Jamkar, S. S. (2017) 'Effect of Concentration of Alkaline Solutions on the Development of Geopolymer Mortar', in.

331. Pavía S. (2008) 'A petrographic study of the technology of hydraulic mortars at masonry bridges, harbours and mill ponds'., Concrete Research and Bridge Infrastructure Symp., Galway, December 2008, edited by Cannon E., West, R. and Fanning P. , Galileo Editions, 2008, p 253 – 264.

332. Pavia S. and Caro S. (2006) 'Aplicaciones del estudio petrográfico de morteros en la conservación del patrimonio': *Morteros de La Rioja, Tierra y Tecnologia,* 28, 2006.

333. Pavia S. and Caro S. (2007) 'Petrographic microscope investigation of mortar and ceramic technologies for the conservation of the built heritage.', Proc. SPIE Vol. 6618, *Optics for Arts, Architecture, and Archaeology*. Munich, July 2007.

334. Pavía S. and Caro S. (2008) 'An investigation of Roman mortar technology through the petrographic analysis of archaeological material', *Construction and Building Materials.*, 22, (8), 2008, p 1807 – 1811.

335. Pavia Santamaria, S. and Bolton, J. R. (1997) 'Laboratory studies of the interaction between bedding and pointing mortars and building stones', *Internationale Zeitschrift für Bauinstandsetzen= International journal for restoration of buildings and monuments*, 3(3), pp. 253–267.

336. Pavía, S. and Aly, M. (2019) 'Sustainable, Hydraulic-Lime-Limestone Binders for Construction', *Advances in Civil Engineering Materials*, 8(3), pp. 235–254.

337. Pavía, S. and Condren, E. (2008) 'Study of the durability of OPC versus GGBS concrete on exposure to silage effluent', *Journal of Materials in Civil Engineering*, 20(4), pp. 313–320. doi: 10.1061/(ASCE)0899-1561(2008)20:4(313).

338. Pavía, S., Walker, R., Veale, P., and Wood, A. (2014) 'Impact of the properties and reactivity of rice husk ash on lime mortar properties', *Journal of materials in civil engineering*, 26(9), p. 4014066.

339. Paya, J., Borrachero, M. V., Monzo, J., Peris-Mora, E., and Amahjour, F. (2001) 'Enhanced conductivity measurement techniques for evaluation of fly ash pozzolanic activity', *Cement and Concrete Research*, 31, pp. 41–49.

340. Pedersen, K. H., Jensen, A. D. and Dam-Johansen, K. (2010) 'The effect of low-NOx combustion on residual carbon in fly ash and its adsorption capacity for air entrainment admixtures in concrete', *Combustion and Flame*, 157(2), pp. 208–216.

341. Pelisser, F., Guerrino, E. L., Menger, M., Michel, M. D., and Labrincha, J. A. (2013) 'Micromechanical characterization of metakaolin-based geopolymers', *Construction and Building Materials*, 49, pp. 547–553. doi: 10.1016/j.conbuildmat.2013.08.081.

342. Pera, J., Boumaza, R. and Ambroise, J. (1997) 'Development of a pozzolanic pigment from red mud', *Cement and Concrete Research*, 27(10), pp. 1513–1522.

343. Petrakis, E. and Komnitsas, K. (2022) 'Effect of Grinding Media Size on Ferronickel Slag Ball Milling Efficiency and Energy Requirements Using Kinetics and Attainable Region Approaches', *Minerals*, 12(2), p. 184.

344. Pontikes, Y. and Angelopoulos, G. N. (2013) 'Bauxite residue in cement and cementitious applications: Current status and a possible way forward', *Resources, Conservation and Recycling*, 73, pp. 53–63. doi: 10.1016/j.resconrec.2013.01.005.

345. Poppe, L. J., Paskevich, V. F., Hathaway, J. C., and Blackwood, D. S. (2001) 'A laboratory manual for X-ray powder diffraction', *US Geological Survey open-file report*, 1(041), pp. 1–88.

346. Praveen Kumar, V. V., Prasad, N. and Dey, S. (2020) 'Influence of metakaolin on strength and durability characteristics of ground granulated blast furnace slag based geopolymer concrete', *Structural Concrete*, 21(3), pp. 1040–1050.

347. Provis, J. L. and Bernal, S. A. (2014) 'Geopolymers and related alkali-activated materials', *Annual Review of Materials Research*, 44, pp. 299–327. doi: 10.1146/annurev-matsci-070813-113515.

348. Provis, J. L. and van Deventer, J. S. J. (2007) 'Geopolymerisation kinetics. 2. Reaction kinetic modelling', *Chemical Engineering Science*, 62(9), pp. 2318–2329. doi: 10.1016/j.ces.2007.01.028.

349. Provis, J. L. and Van Deventer, J. S. J. (2013) *Alkali activated materials: state-of-the-art report, RILEM TC 224-AAM*. Springer Science and Business Media.

350. Provis, J. L. and van Deventer, J. S. J. (2014) *STAR 224-AAM Alkali Activated Materials*, *Rilem Tc 224*. doi: 10.1007/978-94-007-7672-2.

351. Provis, J. L. and Van Deventer, Jannie Stephanus Jakob (2009) *Geopolymers: Structures, processing, properties and industrial applications*, *Geopolymers: Structures, Processing, Properties and Industrial Applications*. doi: 10.1533/9781845696382.

352. Provis, J. L., Muntingh, Y., Lloyd, R. R., Xu, H., Keyte, L. M., Lorenzen, L., and van Deventer, J. S. (2007) 'Will geopolymers stand the test of time', in *Ceramic Engineering and Science Proceedings*, pp. 235–248.

353. Provis, J. L., Myers, R. J., White, C. E., Rose, V., and Van Deventer, J. S. (2012) 'X-ray microtomography shows pore structure and tortuosity in alkali-activated binders', *Cement and Concrete Research*, 42(6), pp. 855–864. doi: 10.1016/j.cemconres.2012.03.004.

354. Provis, J. L., Palomo, A. and Shi, C. (2015) 'Advances in understanding alkali-activated materials', *Cement and Concrete Research*, 78, pp. 110–125.

355. Provis, J. L., Walls, P. A. and van Deventer, J. S. J. (2008) 'Geopolymerisation kinetics. 3. Effects of Cs and Sr salts', *Chemical Engineering Science*, 63(18), pp. 4480–4489. doi: 10.1016/j.ces.2008.06.008.

356. Provis, John L. and van Deventer, J. S. J. (2007) 'Geopolymerisation kinetics. 1. In situ energy-dispersive X-ray diffractometry', *Chemical Engineering Science*, 62(9), pp. 2309–2317. doi: 10.1016/j.ces.2007.01.027.

357. Provis, John L., and Jannie SJ Van Deventer, E. (2014) *Alkali activated materials: state-of-the-art report, RILEM TC 224-AAM*. Springer Science and Business Media,2013.

358. Puertas, F., Gutierrez, R. D., Fernández-Jiménez, A., Delvasto, S., and Maldonado, J (2002) 'Alkaline

cement mortars. Chemical resistance to sulfate and seawater attack', *Materiales de Construccion*, pp. 55–71. doi: 10.3989/mc.2002.v52.i267.326.

359. Puertas, F., Martínez-Ramírez, S., Alonso, S., and Vázquez, T (2000) 'Alkali-activated fly ash/slag cements: strength behaviour and hydration products', *Cement and concrete research*, 30(10), pp. 1625–1632.

360. Purdon, A. O. (1940) 'The action of alkalis on blast-furnace slag', *Journal of the Society of Chemical Industry*, 59(9), pp. 191–202.

361. Qureshi, M. N. and Ghosh, S. (2014) 'Alkali-Activated Blast furnace Slag as a Green Construction Material', *IOSR Journal of Mechanical and Civil Engineering*, pp. 24–28.

362. Rafidah, A., Nurulhuda, A., Azrina, A., Suhaila, Y., Anwar, I. S., and Syafiq, R. A. (2014) 'Comparison design of experiment (DOE): Taguchi method and full factorial design in surface roughness', *Applied Mechanics and Materials*, 660, pp. 275–279. doi: 10.4028/www.scientific.net/AMM.660.275.

363. Rahier, H., Van Mele, B., Biesemans, M., Wastiels, J., and Wu, X. (1997) 'Low-temperature synthesized aluminosilicate glasses: Part III Influence of the composition of the silicate solution on production, structure and properties', *Journal of Materials Science*, 32(9), pp. 2237–2247. doi: 10.1023/A:1018563914630.

364. Rajesh, D. V. S. P., Narender Reddy, A., Venkata Tilak, U., and Raghavendra, M. (2013) 'Performance of alkali activated slag with various alkali activators', *International Journal of Innovative Research, Engineering and Technology*, 2, pp. 378–386.

365. Ramachandran, V. S. (1976) 'Hydration of cement—role of triethanolamine', *Cement and Concrete research*, 6(5), pp. 623–631.

366. Razak, S., Zainal, F. F. and Shamsudin, S. R. (2020) 'Effect of porosity and water absorption on compressive strength of fly ash based geopolymer and OPC Paste', in *IOP Conference Series: Materials Science and Engineering*. IOP Publishing, p. 12035.

367. Reddy, P. comm J. (2010) *Ecocem*.

368. Rees, C., Lukey, G. C. and Van Deventer, J. S. J. (2004) 'The role of solid silicates on the formation of geopolymers derived from coal ash', in *International symposium of research students on material science and engineering*, pp. 20–22.

369. RICS (2012) 'Methodology to calculate embodied carbon of materials', *Royal Institution of Chartered Surveyors S and Construction Standards*, (1st), pp. 1–33. Available at: https://www.fgould.com/uk-europe/articles/embodied-carbon-q-sean-lockie-director-carbon-and-.

370. RILEM, T. (1980) 'Recommended Tests to Measure the Deterioration of Stone and to Assess the Effectiveness of Treatment Methods', *Materials and Structures*, pp. 175–253.

371. Risdanareni, P., Ekaputri, J. J. and Triwulan (2015) 'The influence of alkali activator concentration to mechanical properties of geopolymer concrete with trass as a filler', *Materials Science Forum*, 803, pp. 125–134. doi: 10.4028/www.scientific.net/MSF.803.125.

372. Rivas Mercury, J. M., Cabral, A. A., Paiva, A. E. M., Angélica, R. S., Neves, R. F., and Scheller, T. (2011) 'Thermal behavior and evolution of the mineral phases of Brazilian red mud', *Journal of Thermal Analysis and Calorimetry*, 104(2), pp. 635–643.

373. Rodríguez, E., Bernal, S., De Gutiérrez, R. M., and Puertas, F. (2008) 'Alternative concrete based on

alkali-activated slag', *Materiales de Construcción*, 58(291), pp. 53–67.

374. Rosenqvist, J. (2002) 'Surface chemistry of Al and Si (hydr) oxides, with emphasis on nano-sized gibbsite (α-Al (OH) 3)'.

375. Rovnaník, P. (2010) 'Effect of curing temperature on the development of hard structure of metakaolin-based geopolymer', *Construction and Building Materials*, 24(7), pp. 1176–1183. doi: 10.1016/j.conbuildmat.2009.12.023.

376. Roy D M (1999) 'Alkali activated cements, opportunities and challenges', *Cement and concrete Research*, 29, pp. 249–254.

377. Rożek, P., Król, M. and Mozgawa, W. (2019) 'Geopolymer-zeolite composites: A review', *Journal of Cleaner Production*, 230, pp. 557–579. doi: 10.1016/j.jclepro.2019.05.152.

378. Safety data sheet (2014), 'Science Lab.com'. Available at: https://www.sciencecompany.com/Sodium-Silicate-Solution-16oz-P6375.aspx.

379. Sagawa, Y., Ota, S., Harada, K., Nishizaki, T., and Goda, H. (2015) 'Utilization of fly ash with higher loss on ignition for geopolymer mortar', in *Advanced Materials Research*. Trans Tech Publ, pp. 614–620.

380. Sakulich, A. R., Anderson, E., Schauer, C., and Barsoum, M. W. (2009) 'Mechanical and microstructural characterization of an alkali-activated slag/limestone fine aggregate concrete', *Construction and Building Materials*, 23(8), pp. 2951–2957.

381. Samarakoon, M. H., Ranjith, P. G., Rathnaweera, T. D., and Perera, M. S. A. (2019) 'Recent advances in alkaline cement binders: A review', *Journal of Cleaner Production*, 227, pp. 70–87. doi: 10.1016/j.jclepro.2019.04.103.

382. San Nicolas, R., Bernal, S. A., de Gutiérrez, R. M., van Deventer, J. S., and Provis, J. L. (2014) 'Distinctive microstructural features of aged sodium silicate-activated slag concretes', *Cement and Concrete Research*, 65, pp. 41–51. doi: 10.1016/j.cemconres.2014.07.008.

383. San Nicolas, R., Bernal, S. A., de Gutiérrez, R. M., van Deventer, J. S., and Provis, J. L. (2016) 'Determination of Excess Sodium Hydroxide in Geopolymer by Volumetric Analysis', *Procedia Engineering*, 148, pp. 298–301. doi: 10.1016/j.proeng.2016.06.621.

384. Saraya, M. E.-S. I. and El-Fadaly, E. (2017) 'Preliminary study of alkali activation of basalt: effect of NaOH concentration on geopolymerization of basalt', *Journal of Materials Science and Chemical Engineering*, 5(11), pp. 58–76.

385. Sarkar, M. and Majumdar, P. (2011) 'Application of response surface methodology for optimization of heavy metal biosorption using surfactant modified chitosan bead', *Chemical Engineering Journal*, 175, pp. 376–387.

386. SBCI, U. (2009) 'Buildings and climate change: Summary for decision-makers', *United Nations Environmental Programme, Sustainable Buildings and Climate Initiative, Paris*, pp. 1–62.

387. SCA (2013) *COMPRESSIVE AND FLEXURAL STRENGTH*, *Slag Cement Association*. https://www.slagcement.org/.

388. Scheetz, B. E. and Earle, R. (1998) 'Utilization of fly ash', *Current Opinion in Solid State and Materials Science*, 3(5), pp. 510–520.

389. Schorcht, F., Kourti, I., Scalet, B. M., Roudier, S. and Sancho, L. D. (2013) 'Best available techniques

(BAT) reference document for the production of cement, lime and magnesium oxide', European Commission Joint Research Centre Institute for Prospective Technological Studies, Luxembourg.

390. Scrivener, K. L. and Capmas, A. (1998) 'Lea's chemistry of cement and concrete', *Calcium aluminate cements*, p. 69.

391. Scrivener, K. L., Bentur, A. and Pratt, P. L. (1988) 'Quantitative characterization of the transition zone in high strength concretes', *Advances in Cement Research*, 1(4), pp. 230–237.

392. Sglavo, V. M., Campostrini, R., Maurina, S., Carturan, G., Monagheddu, M., Budroni, G., and Cocco, G. (2000) 'Bauxite 'red mud'in the ceramic industry. Part 1: thermal behaviour', Journal of the European Ceramic Society, 20(3), pp. 235–244.

393. Sha, W. and Pereira, G. B. (2001) 'Differential scanning calorimetry study of ordinary Portland cement paste containing metakaolin and theoretical approach of metakaolin activity', *Cement and Concrete Composites*, 23(6), pp. 455–461.

394. Shi, C. (1996) 'Strength, pore structure and permeability of alkali-activated slag mortars', *Cement and Concrete Research*, 26(12), pp. 1789–1799. doi: 10.1016/S0008-8846(96)00174-3.

395. Shi, C. (2001) 'An overview on the activation of reactivity of natural pozzolans', *Canadian Journal of Civil Engineering*, 28(5), pp. 778–786. doi: 10.1139/cjce-28-5-778.

396. Shi, C. and Qian, J. (2000) 'High performance cementing materials from industrial slags—a review', *Resources, Conservation and Recycling*, 29(3), pp. 195–207.

397. Shi, C. and Xie, P. (1998) 'Interface between cement paste and quartz sand in alkali-activated slag mortars', *Cement and Concrete Research*, 28(6), pp. 887–896.

398. Shi, C., Grattan-Bellew, P. E. and Stegemann, J. A. (1999) 'Conversion of a waste mud into a pozzolanic material', *Construction and Building materials*, 13(5), pp. 279–284.

399. Shi, C., Krivenko, P. V and Roy, D. (2006) ',,Alkali-activated cements and concretes" Taylor and Francis', *London, New York*.

400. Shi, C., Roy, D. and Krivenko, P. (2003) *Alkali-activated cements and concretes*. CRC press.

401. Shi, Caijun, Della Roy, and P. K. (2003) *Alkali-activated Cements and Concretes*, *Alkali-activated cements and concretes. CRC press*.

402. Shon, C.-S. and Kim, Y.-S. (2013) 'Evaluation of West Texas natural zeolite as an alternative of ASTM Class F fly ash', *Construction and Building Materials*. Elsevier, 47, pp. 389–396.

403. Sidawi, B. (2009) 'Hindrances to the financing of affordable housing in Kingdom of Saudi Arabia', *Emirates Journal for Engineering Research*, 14(1), pp. 73–82.

404. Silva, P. De Sagoe-Crenstil, K. Sirivivatnanon, V. (2007) 'Kinetics of geopolymerization: Role of Al2O3 and SiO2', *Cement and Concrete Research*, 37(4), pp. 512–518. doi: 10.1016/j.cemconres.2007.01.003.

405. Singh, G. V. P. B. and Subramaniam, K. V. L. (2017) 'Evaluation of sodium content and sodium hydroxide molarity on compressive strength of alkali activated low-calcium fly ash', *Cement and Concrete Composites*, 81, pp. 122–132.

406. Singh, N. (2018) 'Fly Ash-Based Geopolymer Binder: A Future Construction Material', *Minerals*, 8(7), p. 299. doi: 10.3390/min8070299.

407. Singh, P. S., Trigg, M., Burgar, I., and Bastow, T. (2005) 'Geopolymer formation processes at room temperature studied by 29Si and 27Al MAS-NMR', *Materials Science and Engineering A*, 396(1–2), pp.

392–402. doi: 10.1016/j.msea.2005.02.002.

408. Singh, S. P., Samantasinghar, S. and Sindhuja, D. (2018) 'Stabilization of Red Mud Using Ground Granulated Blast Furnace Slag by Geopolymerization Technique', pp. 338–350. doi: 10.1007/978-3-319-61612-4_28.

409. Singh, S., Aswath, M. U. and Ranganath, R. V. (2018) 'Effect of mechanical activation of red mud on the strength of geopolymer binder', *Construction and Building Materials*, 177, pp. 91–101. doi: 10.1016/j.conbuildmat.2018.05.096.

410. Singh, S., Biswas, R. Das and Aswath, M. U. (2016) 'Experimental study on red mud based geopolymer concrete with fly ash and GGBS in ambient temperature curing', *Int. J. Adv. Mech. Civ. Eng. Issn*, 3, pp. 2394–2827.

411. Singh, Smita, M. U. Aswath, and R. V. R. (2016) 'EFFECT OF CURING METHODS ON THE PROPERTY OF RED MUD BASED GEOPOLYMER MORTAR', *International Journal Of Engineering And Computer Science*, (October). doi: 10.18535/ijecs/v5i7.09.

412. Sisol, M., Drabová, M. and Mosej, J. (2014) 'Alkali activation of fresh and deposited black coal fly ash with high loss on ignition', *Gospodarka Surowcami Mineralnymi*, 30.

413. Škvára, F., Kopecký, L., Myšková, L., Šmilauer, V., Alberovská, L., and Vinšová, L. (2009) 'Aluminosilicate polymers - Influence of elevated temperatures, efflorescence', *Ceramics - Silikaty*, pp. 276–282.

414. Song, S., Sohn, D., Jennings, H. M., and Mason, T. O. (2000) 'Hydration of alkali-activated ground granulated blast furnace slag', *Journal of materials science*, 35(1), pp. 249–257.

415. Songpiriyakij, S., Kubprasit, T., Jaturapitakkul, C., and Chindaprasirt, P. (2007) 'Compressive strength and degree of reaction of biomass- and fly ash-based geopolymer', *Ceramics International*, 44(4), pp. 14416–14422. doi: 10.1016/j.conbuildmat.2009.09.002.

416. Srikanth, S., Ray, A. K., Bandopadhyay, A., Ravikumar, B., and Jha, A. (2005) 'Phase constitution during sintering of red mud and red mud–fly ash mixtures', *Journal of the American Ceramic Society*, 88(9), pp. 2396–2401.

417. StevenSon, M. and Panian, L. (2009) 'Sustainability through strength', *Concrete international*, 31(3), pp. 34–39.

418. Steveson, M. and Sagoe-Crentsil, K. (2005) 'Relationships between composition, structure and strength of inorganic polymers', *Journal of materials science*, 40(8), pp. 2023–2036.

419. Strydom, C. a. and Swanepoel, J. C. (2002) 'Utilisation of fly ash in a geopolymeric material', *Applied Geochemistry*, 17(8), pp. 1143–1148. doi: 10.1016/S0883-2927(02)00005-7.

420. Survey, U. S. G. (2009) *Mineral commodity summaries, 2009*. Government Printing Office.

421. Szabó, L., Hidalgo, I., Císcar, J. C., Soria, A., and Russ, P. (2003) 'Energy consumption and CO2 emissions from the world cement industry', *European Commission Joint Research Centre, Report EUR*, 20769.

422. Szklorzová, H. and Bílek, V. (2008) 'Influence of alkali ions in the activator on the performance of alkali-activated mortars', in *Proceedings of the 3rd International Symposium on Non-traditional Cement and Concrete*, pp. 777–784.

423. Talling, B. and Brandstetr, J. (1989) 'Present state and future of alkali-activated slag concretes', *Special*

Publication, 114, pp. 1519–1546.

424. Talling, B. and Krivenko, P. (1996) 'Blast furnace slag-the ultimate binder', in *Waste materials used in concrete manufacturing*. Elsevier, pp. 235–289.

425. Tan, T. H., Mo, K. H., Ling, T.-C. and Lai, S. H. (2020) 'Current development of geopolymer as alternative adsorbent for heavy metal removal', *Environmental Technology & Innovation*. Elsevier, 18, p. 100684.

426. Taylor, H. F. W. (1997) *Cement chemistry*. Thomas Telford London.

427. Tchamba, A. B., Melo, U. C., Kamseu, E., Yongue, R., and Njopwouo, D. (2010) 'THERMAL AND SINTERING BEHAVIOUR OF BAUXITES FROM HALEO-DANIELLE, MINIM-MARTAP(CAMEROON)', *Industrial Ceramics(Italy)*, 30(1), pp. 21–26.

428. Teh, S. H., Wiedmann, T., Castel, A., and de Burgh, J. (2017) 'Hybrid life cycle assessment of greenhouse gas emissions from cement, concrete and geopolymer concrete in Australia', *Journal of Cleaner Production*, 152, pp. 312–320.

429. Tempest, B., Sanusi, O., Gergely, J., Ogunro, V., and Weggel, D. (2009) 'Compressive strength and embodied energy optimization of fly ash based geopolymer concrete', in *world of coal ash (WOCA) conference*, pp. 1–17.

430. Temuujin, J. and van Riessen, A. (2009) 'Effect of fly ash preliminary calcination on the properties of geopolymer', *Journal of Hazardous Materials*, pp. 634–639. doi: 10.1016/j.jhazmat.2008.08.065.

431. Ter Teo, P., Seman, A. A., Basu, P., and Sharif, N. M. (2016) 'Characterization of EAF steel slag waste: The potential green resource for ceramic Tile production', *Procedia Chemistry*, 19, pp. 842–846.

432. Thannimalay, L., Yusoff, S. and Zawawi, N. Z. (2013) 'Life cycle assessment of sodium hydroxide', *Aust. J. Basic Appl. Sci*, 7(2), pp. 421–431.

433. Thokchom, S., Ghosh, P. and Ghosh, S. (2009) 'Effect of water absorption, porosity and sorptivity on durability of geopolymer mortars', *Journal of Engineering and Applied Sciences*, 4(7), pp. 28–32.

434. Thomas, M. D. A. (2007) *Optimizing the use of fly ash in concrete*. Portland Cement Association Skokie, IL, USA.

435. Toniolo, N. (2019) *Novel geopolymers incorporating silicate waste*. Friedrich-Alexander-Universität Erlangen-Nürnberg (FAU).

436. Torres-Carrasco, M. and Puertas, F. (2017) 'Alkaline activation of different aluminosilicates as an alternative to Portland cement: alkali activated cements or geopolymers', *Revista Ingenieria de Construccion*, 32(2), pp. 5–12.

437. Türker, H. T., Balçikanli, M., Durmuş, İ. H., Özbay, E., and Erdemir, M. (2016) 'Microstructural alteration of alkali activated slag mortars depend on exposed high temperature level', *Construction and Building Materials*, 104, pp. 169–180.

438. Unklesbay, N., Biedrzycki, K. and Unklesbay, K. (1988) 'Bentonite models of turkey rolls enable energy comparisons of electric and gas convection ovens', *International Journal of Hospitality Management*, 7(2), pp. 131–138.

439. Van Deventer, , J. S., Provis, J. L., Duxson, P., and Brice, D. G. (2010) 'Chemical research and climate change as drivers in the commercial adoption of alkali activated materials', *Waste and Biomass Valorization*, 1(1), pp. 145–155. doi: 10.1007/s12649-010-9015-9.

440. Van Jaarsveld, J. G. S., Van Deventer, J. S. J. and Lukey, G. C. (2002) 'The effect of composition and temperature on the properties of fly ash- and kaolinite-based geopolymers', *Chemical Engineering Journal*, pp. 63–73. doi: 10.1016/S1385-8947(02)00025-6.

441. Varshneya, A. K. (1994) 'Flat Glass', *Fundamentals of Inorganic Glasses", Academic Press, Inc., Boston*, pp. 534–540.

442. Velandia, D. F., Lynsdale, C. J., Provis, J. L., Ramirez, F., and Gomez, A. C. (2016) 'Evaluation of activated high volume fly ash systems using Na2SO4, lime and quicklime in mortars with high loss on ignition fly ashes', *Construction and Building Materials*, 128, pp. 248–255.

443. Vieira Coelho, H. Souza Santos, P.K. Kiyohara, P. (2002) 'Surface area and crystal morphology of alumina powders by thermal activation of a gibbsite precursor prepared by a new procedure', in *CBECIMAT*, pp. 1534–1538.

444. Wahlström, M., Teittinen, T., Kaartinen, T. and van Cauwenberghe, L. (2019) 'Hazardous substances in construction products and materials: PARADE. Best practices for Pre-demolition Audits ensuring high quality RAw materials'. EIT RawMaterials.

445. Wainwright, P. J. and Rey, N. (2000) 'The influence of ground granulated blastfurnace slag (GGBS) additions and time delay on the bleeding of concrete', *Cement and Concrete Composites*, 22(4), pp. 253–257.

446. Walker, R. and Pavía, S. (2010) 'Behaviour and Properties of Lime-Pozzolan Pastes', *8th International Masonry Conference, Dresden, July 2010*, pp. 353–362.

447. Walker, R. and Pavía, S. (2011) 'Physical properties and reactivity of pozzolans, and their influence on the properties of lime-pozzolan pastes', *Materials and Structures/Materiaux et Constructions*, 44(6), pp. 1139–1150. doi: 10.1617/s11527-010-9689-2.

448. Wallemacq, P. and House, R. (2018) 'Economic losses, poverty and disasters: 1998-2017', *UNDRR and CRED*, p. 31. Available at: https://www.unisdr.org/files/61119_credeconomiclosses.pdf.

449. Wan, Q., Rao, F., Song, S., García, R. E., Estrella, R. M., Patino, C. L., and Zhang, Y. (2017) 'Geopolymerization reaction, microstructure and simulation of metakaolin-based geopolymers at extended Si/Al ratios', *Cement and Concrete Composites*, 79, pp. 45–52.

450. Wang, H., Li, H. and Yan, F. (2005) 'Synthesis and mechanical properties of metakaolinite-based geopolymer', *Colloids and Surfaces A: Physicochemical and Engineering Aspects*, 268(1–3), pp. 1–6. doi: 10.1016/j.colsurfa.2005.01.016.

451. Wang, S. D. and Scrivener, K. L. (1995) 'Hydration products of alkali activated slag cement', *Cement and Concrete Research*, 25(3), pp. 561–571. doi: 10.1016/0008-8846(95)00045-E.

452. Wang, S. D., Pu, X. C., Scrivener, K. L., and Pratt, P. L. (1995) 'Alkali-activated slag cement and concrete: a review of properties and problems', *Advances in cement research*, 7(27), pp. 93–102.

453. Wang, Shao-Dong, Karen L. Scrivener, and P. L. P. (1994) 'factors affecting the strength of alkali-activated slag', *Cement and concrete Research*, 6(24), pp. 1033–1043. Available at: https://www.pnas.org/content/pnas/76/1/170.full.pdf.

454. Wang,Y., Liu, X., Tang, B., Li, Y., Zhang, W., and Xue, Y. (2021) 'Effect of Ca/(Si+ Al) on red mud based eco-friendly revetment block: Microstructure, durability and environmental performance', *Construction and Building Materials*, 304, p. 124618.

455. Watling, L., Pembroke, A. and Lind, H. (1975) 'Alkali-Activated Red Mud and Construction and Demolition Waste-Based Components: Characterization and Environmental Assessment'.

456. Watt, J. D. and Thorne, D. J. (1965) 'Composition and pozzolanic properties of pulverised fuel ashes. I. Composition of fly ashes from some British power stations and properties of their component particles', *Journal of applied chemistry*, 15(12), pp. 585–594.

457. Weldes, H. H. and Lange, K. R. (1969) 'Properties of soluble silicates', *Industrial and Engineering Chemistry*, 61(4), pp. 29–44. doi: 10.1021/ie50712a008.

458. Wianglor, K., Sinthupinyo, S., Piyaworapaiboon, M., and Chaipanich, A. (2018) 'Effect of metakaolin replaced granulated blast furnace slag on fresh and early strength properties of geopolymer mortar', *Ain Shams Engineering Journal*, 9(4), pp. 1557–1566. doi: 10.1016/j.asej.2016.11.011.

459. Wimpenny, D. (2009) 'Low Carbon Concrete – Options for the Next Generation of Infrastructure Concrete Solutions 09 Paper 4a-1', *Concrete Solutions 09*, (February), pp. 1–10.

460. Wu,Y., Lu, B., Bai, T., Wang, H., Du, F., Zhang, Y., and Wang, W. (2019) 'Geopolymer, green alkali activated cementitious material: Synthesis, applications and challenges', *Construction and Building Materials*, 224(206), pp. 930–949. doi: 10.1016/j.conbuildmat.2019.07.112.

461. Xing, J., Zhao, Y., Qiu, J., and Sun, X. (2019) 'Microstructural and mechanical properties of alkali activated materials from two types of blast furnace slags', *Materials*, 12(13), p. 2089.

462. Xu, G. and Shi, X. (2018) 'Characteristics and applications of fly ash as a sustainable construction material: A state-of-the-art review', *Resources, Conservation and Recycling*, 136, pp. 95–109.

463. Xu, H. and Deventer, J. S. J. Van (2000) 'The geopolymerisation of alumino-silicate minerals'.

464. Xu, H. and Van Deventer, J. S. J. (2003) 'Effect of source materials on geopolymerization', *Industrial and Engineering Chemistry Research*, 42(8), pp. 1698–1706. doi: 10.1021/ie0206958.

465. Yalçın, N. and Sevinç, V. (2000) 'Utilization of bauxite waste in ceramic glazes', *Ceramics International*, 26(5), pp. 485–493.

466. Yang, Jiakuan, and X. (2008) 'Development of unsintered construction materials from red mud wastes produced in the sintering alumina process', *Construction and Building Materials*, 22(12), pp. 2299–2307.

467. Yang, M., Zheng, Y., Li, X., Yang, X., Rao, F., and Zhong, L. (2022) 'Durability of alkali-activated materials with different C–S–H and N-A-S-H gels in acid and alkaline environment', *Journal of Materials Research and Technology*, 16, pp. 619–630. doi: 10.1016/j.jmrt.2021.12.031.

468. Yankwa Djobo, J. N. Y., Elimbi, A., Tchakouté, H. K., and Kumar, S. (2016) 'Mechanical properties and durability of volcanic ash based geopolymer mortars', *Construction and Building Materials*, pp. 606–614. doi: 10.1016/j.conbuildmat.2016.07.141.

469. Yao, Z. T., Ji, X. S., Sarker, P. K., Tang, J. H., Ge, L. Q., Xia, M. S., and Xi, Y. Q. (2015) 'A comprehensive review on the applications of coal fly ash', *Earth-Science Reviews*, pp. 105–121. doi: 10.1016/j.earscirev.2014.11.016.

470. Ye, H., Cartwright, C., Rajabipour, F., and Radlińska, A. (2017) 'Understanding the drying shrinkage performance of alkali-activated slag mortars', *Cement and Concrete Composites*, 76, pp. 13–24.

471. Ye, J., Zhang, W. and Shi, D. (2017) 'Properties of an aged geopolymer synthesized from calcined ore-dressing tailing of bauxite and slag', *Cement and Concrete Research*, 100, pp. 23–31. doi: 10.1016/j.cemconres.2017.05.017.

472. Ye, N., Yang, J., Ke, X., Zhu, J., Li, Y., Xiang, C., and Xiao, B. (2014) 'Synthesis and characterization of geopolymer from bayer red mud with thermal pretreatment', *Journal of the American Ceramic Society*, 97(5), pp. 1652–1660. doi: 10.1111/jace.12840.

473. Ye, N., Zhu, J., Liu, J., Li, Y., Ke, X., and Yang, J. (2012) 'Influence of thermal treatment on phase transformation and dissolubility of aluminosilicate phase in red mud', *MRS Online Proceedings Library*, 1488(1), pp. 88–93.

474. Yip, C. K. and Van Deventer, J. S. J. (2003) 'Microanalysis of calcium silicate hydrate gel formed within a geopolymeric binder', *Journal of Materials Science*, 38(18), pp. 3851–3860. doi: 10.1023/A:1025904905176.

475. Yunsheng, Z., Wei, S., Qianli, C., and Lin, C. (2007) 'Synthesis and heavy metal immobilization behaviors of slag based geopolymer', *Journal of Hazardous Materials*, pp. 206–213. doi: 10.1016/j.jhazmat.2006.09.033.

476. Zerfu, K. and Ekaputri, J. J. (2016) 'Review on alkali-activated fly ash based geopolymer concrete', in *Materials Science Forum*. Trans Tech Publ, pp. 162–169.

477. Zhang, J., Li, S., Li, Z., Liu, C., and Gao, Y. (2020) 'Feasibility study of red mud for geopolymer preparation: effect of particle size fraction', *Journal of Material Cycles and Waste Management*, 22(5), pp. 1328–1338. doi: 10.1007/s10163-020-01023-4.

478. Zhang, M., El-Korchi, T., Zhang, G., Liang, J., and Tao, M (2014) 'Synthesis factors affecting mechanical properties, microstructure, and chemical composition of red mud-fly ash based geopolymers', *Fuel*, 134, pp. 315–325. doi: 10.1016/j.fuel.2014.05.058.

479. Zhang, M., Zhao, M., Zhang, G., Sietins, J. M., Granados-Focil, S., Pepi, M. S., and Tao, M. (2018) 'Reaction kinetics of red mud-fly ash based geopolymers: Effects of curing temperature on chemical bonding, porosity, and mechanical strength', *Cement and Concrete Composites*, 93(July), pp. 175–185. doi: 10.1016/j.cemconcomp.2018.07.008.

480. Zhang, M.-H., Lastra, R. and Malhotra, V. M. (1996) 'Rice-husk ash paste and concrete: some aspects of hydration and the microstructure of the interfacial zone between the aggregate and paste', *Cement and concrete Research*, 26(6), pp. 963–977.

481. Zhang, X., Cui, W., Hu, J. Z., Wang, H. W., Prange, M. P., Wan, C., and Rosso, K. M. (2019) 'Transformation of Gibbsite to Boehmite in Caustic Aqueous Solution at Hydrothermal Conditions', *Crystal Growth and Design*, 19(10), pp. 5557–5567. doi: 10.1021/acs.cgd.9b00468.

482. Zhang, Y. J., Zhao, Y. L., Li, H. H., and Xu, D. L. (2008) 'Structure characterization of hydration products generated by alkaline activation of granulated blast furnace slag', *Journal of materials science*, 43(22), pp. 7141–7147.

483. Zhang, Z., Zhu, Y., Yang, T., Li, L., Zhu, H., and Wang, H. (2017) 'Conversion of local industrial wastes into greener cement through geopolymer technology: A case study of high-magnesium nickel slag', *Journal of Cleaner Production*, 141, pp. 463–471.

484. Zhang, Z., Wang, H., Zhu, Y., Reid, A., Provis, J. L., and Bullen, F. (2014) 'Using fly ash to partially substitute metakaolin in geopolymer synthesis', *Applied Clay Science*, 88–89, pp. 194–201. doi: 10.1016/j.clay.2013.12.025.

485. Zhao, H., Deng, Y., Harsh, J. B., Flury, M., and Boyle, J. S. (2004) 'Alteration of kaolinite to cancrinite

and sodalite by simulated Hanford tank waste and its impact on cesium retention', *Clays and Clay Minerals*, 52(1), pp. 1–13.

486. Zhihua P, Dongxu L, Jian Y, and N. Y. (2002) 'Hydration products of alkali-activated slag red mud', *Cementitious Material.:*, 32(5), pp. 357-362.

487. Zhuang, X. Y., Chen, L., Komarneni, S., Zhou, C. H., Tong, D. S., Yang, H. M., Yu, W. H. and Wang, H. (2016) 'Fly ash-based geopolymer: clean production, properties and applications', *Journal of Cleaner Production*. Elsevier, 125, pp. 253–267.